Transport Phenomena of Solutes in Dense Polymer Membranes

by

Yi-hung Lin

A dissertation submitted to the Graduate Faculty of
Auburn University
in partial fulfillment of the
requirements for the Degree of
Doctor of Philosophy

Auburn, Alabama
May 10, 2025

Keywords: Ion exchange membranes, Membrane science, Polymer chemistry, Solute transport, Transport phenomena

Approved by

Bryan S. Beckingham, Chair, Associate Professor of Chemical Engineering, Auburn University
Tae-Sik Oh, Associate Professor of Chemical Engineering, Auburn University
Michael P. Howard, Assistant Professor of Chemical Engineering, Auburn University
Cassandra Porter, Assistant Professor of Chemical Engineering, Auburn University
Dong-Joo Kim, Reader, Alumni Professor of Materials Engineering, Auburn University

Abstract

Ion exchange membranes (IEMs) are indispensable materials with diverse applications in energy and environmental technologies, such as fuel cells, water desalination, water purification, and electrochemical CO2 reduction systems. IEMs facilitate selective ion transport while maintaining charge balance, minimizing undesired crossover of species, and ensuring efficient separation processes. However, the development of IEMs is hindered by several challenges. A key issue is the trade-off between ionic conductivity and selectivity, where enhancing one often compromises the other. Additionally, the undesired crossover of reactants or byproducts can significantly diminish system efficiency and product purity. Compounding these issues is an incomplete understanding of the structure-property relationships that govern membrane behavior, limiting the ability to design tailored membranes for specific applications. To address these challenges, this study investigates (1) single and co-transport solute behavior across various IEMs, (2) solute transport characteristics in membranes with comparable water volume fractions, and (3) the impact of different polymer structures on solute transport. In anion exchange membranes (AEMs), we observed that the co-permeation of alcohol and carboxylate ions decreases, while the co-permeation of two carboxylates exhibits competitive transport. However, the water volume fraction generally has the most significant influence on transport behavior. Different monomers impart distinct physicochemical properties to the membrane, substantially affecting solute transport.

Acknowledgments

I deeply appreciate Dr. Beckingham for providing me the opportunity to begin my research journey as a master's student and for trusting me to continue as a Ph.D. student. I am especially grateful for the rigorous training I received under his guidance. His unwavering support and dedication to my success have been invaluable, and I feel fortunate to have had such a supportive mentor during this transformative chapter of my life.

I would like to express my deepest gratitude to Dr. Howard, Dr. Porter, Dr. Oh, and the Dr. Kim for serving as my committee members and providing invaluable guidance and feedback to refine my dissertation. I am especially thankful to Luca for the mentorship and support during the early stages of my research journey, which laid a strong foundation for my work. I am also appreciative of Pravin for his assistance and contributions to the lab.

My heartfelt thanks go to Elaine, Bonnie, and Emma for their dedicated support with administrative tasks. I am incredibly grateful to my past and present lab mates—Tom, Vinita, Yorae, Harrish, Adam, Sarah, John, and Riana—for their support throughout this journey. I extend my gratitude to McKenna, Braden, Camylle, and Logan for giving me the opportunity to be their mentor.

I would also like to give a warm shout-out to all my friends from Taiwan and Auburn. Thank you all for the support! Finally, my deepest thanks go to my wife, Shuqi, for her unwavering support, encouragement, thoughtfulness, and companionship. Without you, none of this would have been possible. I am equally grateful to my parents, brother, and parents-in-law for their steadfast support and trust throughout this journey.

Table of Contents

Abstract 2

Acknowledgments 3

Table of Contents 4

List of Tables 11

List of Figures 15

List of Abbreviations 26

Chapter 1: Introduction 32

1.1. Motivation 32

1.2. Objectives and Goal 33

1.2.1. Single and Co-transport of Ethanol and Carboxylate in AEMs 34

1.2.2. Single and Co-transport of Methanol and Acetate in CEMs 35

1.2.3. Effect of Acrylate and Methacrylate Backbone Linkages in IEMs 36

1.2.4. Salt Transport in Zwitterionic Membranes 37

1.2.5. Impact of Crosslinker on Physiochemical Properties and Transport Behavior in AEMs 38

1.2.6. Transport Behavior Differences between CEMs Containing SPMAK and MPS 39

1.2.7. Isolating the Impact of Water Volume Fraction in AEMs 40

1.2.8. Phenyl Acrylate-Based IEMs for Direct Urea Fuel Cell 41

1.3. Organization of this Dissertation 42

1.4. References 44

Chapter 2: Background 46

2.1. Membrane Technology 46
2.2. Application of IEMs 49
2.2.1. Photoelectrochemical CO2 Reduction Cells (PEC-CRC) 49
2.2.2. Direct Urea Fuel Cells (DUFC) 51
2.3. Transport Mechanisms in Dense Polymer Membranes 52
2.3.1. Free Volume Theory 52
2.3.2. Solution-Diffusion Model 54
2.3.3. Yasuda's Model 57
2.3.4. Donnan Theory 58
2.3.5. Mackie-Meares Model 60
2.3.6. Manning's Theory 61
2.4. Tradeoff relationship in polymer membranes 62
2.5. References 65
Chapter 3: Materials and Experimental Methods 71
3.1. Materials 71
3.2. Synthesis of Polymer Membranes 72
3.2.1. UV Photopolymerization 73
3.2.2. Thermal Polymerization 75
3.3. Membrane Characterization 80
3.3.1. Water Content and Polymer Density 80
3.3.2. Dimensional Swelling 82
3.3.3. Ion Exchange Capacity 83

3.3.4. Fixed Charge Concentration and Density 84
3.3.5. Ionic Conductivity 85
3.3.6. Mechanical Properties 85
3.3.7. Crosslink Density 86
3.3.8. Thermal Properties 87
3.3.9. Contact Angle 87
3.4. Counterion Exchange 88
3.5. Transport Properties 89
3.5.1. Permeability 89
3.5.2. Solubility 92
3.6. References 94
Chapter 4: Single and Co-transport of Ethanol and Carboxylate in AEMs 97
4.1. Introduction 97
4.2. Results and Discussion 102
4.2.1. Water Uptake, Density, and Water Volume Fraction 103
4.2.2. Counterion Conversion, Ionic Conductivity, and IEC 105
4.2.3. Permeation 108
4.2.4. Sorption 111
4.2.5. Diffusion 116
4.3. Conclusions 124
4.4. References 126
Chapter 5: Single and Co-transport of Methanol and Acetate in CEMs 132

5.1. Introduction 132
5.2. Results and Discussion 135
5.2.1. Ionic Conductivity and IEC of Membranes 137
5.2.2. Membrane Water Volume Fraction 139
5.2.3. Storage Modulus 141
5.2.4. Membrane Permeability 143
5.2.5. Membrane Solubility 148
5.2.6. Membrane Diffusivity 152
5.3. Conclusions 156
5.4. References 157
Chapter 6: Effect of Acrylate and Methacrylate Backbone Linkages in IEMs 162
6.1. Introduction 162
6.2. Results and Discussion 165
6.2.1. Water Volume Fraction 166
6.2.2. Ionic Conductivity 167
6.2.3. Young's Modulus 167
6.2.4. MeOH and KOFm Permeability 169
6.2.5. MeOH and KOFm Sorption Coefficients 170
6.2.6. Relative Permittivity 173
6.3. Conclusions 175
6.4. References 177
Chapter 7: Salt Transport in Zwitterionic Membranes 180

7.1. Introduction 180
7.2. Results and Discussion 182
7.2.1. Membrane Characterization 183
7.2.2. Mechanical Characterization 185
7.2.3. Salt Permeability 186
7.2.4. Salt Solubility 188
7.2.5. Salt Diffusivity 190
7.3. Conclusions 191
7.4. References 193
Chapter 8: Impact of Crosslinker on Physicochemical Properties and Transport Behavior in AEMs 197
8.1. Introduction 197
8.2. Results and Discussion 199
8.2.1. Membrane Physiochemical Properties 201
8.2.2. Salt Permeability 209
8.2.3. Salt Solubility 211
8.2.4. Salt Diffusivity 213
8.3. Conclusions 214
8.4. References 216
Chapter 9: Transport Behavior Differences between CEMs Containing SPMAK and MPS 220
9.1. Introduction 220
9.2. Results and Discussion 222

9.2.1. Membrane Water Content 223
9.2.2. Membrane Characterization 225
9.2.3. Salt Permeability 229
9.2.4. Salt Solubility 230
9.2.5. Salt Diffusivity 231
9.3. Conclusions 233
9.4. References 234
Chapter 10: Isolating the Impact of Water Volume Fraction in AEMs 237
10.1. Introduction 237
10.2. Results and Discussion 238
10.2.1. Membrane water content and charge content 240
10.2.2. Membrane Characterization 242
10.2.3. Salt Permeability 244
10.2.4. Salt Solubility 248
10.2.5. Salt Diffusivity 254
10.3. Conclusions 256
10.4. References 258
Chapter 11: Phenyl Acrylate-Based IEMs for Direct Urea Fuel Cells 262
11.1. Introduction 262
11.2. Results and Discussion 265
11.2.1. Young's Modulus and Storage Modulus 268
11.2.2. Water Volume Fraction 272

11.2.3. IEC and Ionic Conductivity of Membranes 273
11.2.4. Direct Urea Fuel Cell 277
11.2.5. Urea Permeability 281
11.3. Conclusions 283
11.4. References 284
Chapter 12: Conclusion and Recommendations 289
12.1. Conclusions 289
12.2. Recommendations for Future Work 295
12.2.1. Multi-Solute Transport in IEMs 295
12.2.2. Isolating Water Volume Fraction Effect 297
12.2.3. Next Generation of IEMs 298
12.3. References 300

List of Tables

Table 3.1. Membrane properties from pre-polymerization mixtures in Chapter 4. 74

Table 3.2. Membrane characteristics from pre-polymerization mixtures in Chapter 5. 75

Table 3.3. Pre-polymerization mixture compositions in Chapter 6. 76

Table 3.4. Pre-polymerization mixture compositions in Chapter 7. 76

Table 3.5. Pre-polymerization mixtures compositions in Chapter 8. 77

Table 3.6. Pre-polymerization mixtures compositions in Chapter 9. 77

Table 3.7. Composition of Pre-polymerization mixtures in Chapter 10. 78

Table 3.8. Membrane characteristics from pre-polymerization mixtures in Chapter 11. 79

Table 4.1. Membrane properties from pre-polymerization mixtures. 102

Table 4.2. Water uptake, dry polymer density, and water volume fraction of all films. 104

Table 4.3. Weight percent (wt.%) of AEMs (A8, A12, and AMVN) in Cl^- and HCO_3^- forms. . 106

Table 4.4. Water uptake, dry polymer density, and water volume fraction of all films. 106

Table 4.5. Normalized film thickness to hydrated membrane after permeability measurements. 109

Table 4.6. Volume of hydrated films and volume of swollen films (mm^3) after sorption experiments were measured from photographs and a digital caliper. Normalized to the volume of the hydrated films. 112

Table 4.7. Volume fraction among the solution, EtOH ($\boldsymbol{\emptyset e}$)-carboxylate salt ($\boldsymbol{\emptyset c}$), inside the membranes after sorption experiments, where the remaining is the volume fraction of water ($\boldsymbol{\emptyset w}$) from the solution. 113

Table 4.8. Solute diffusivities of select species in water (× 10^5 cm^2/s) at 25 ºC in the dilute condition. 118

Table 4.9. Water volume fractions ($\emptyset_w$) and solution volume fractions ($\emptyset_s$) of films after sorption experiments, where the remaining is the polymer volume fraction ($\emptyset_p$) from the dry polymer density..... 119

Table 5.1. Membrane characteristics from pre-polymerization mixtures. 137

Table 5.2. Measured Conductivities and IECs..... 138

Table 5.3. Water uptake, dry polymer density, water volume fraction, crosslink density, and glass transition temperature of all membranes..... 140

Table 5.4. Normalized film thickness to hydrated membrane after permeability measurements. 146

Table 5.5. Volume of swollen membranes. 152

Table 6.1. Glass transition temperature (T_g) values of dry polymer films. 165

Table 6.2. Water Volume Fractions, Ionic Conductivities (Cl^- Conductivity for PA/A and PA/MA and K^+ Conductivity for PA/S and PA/SM), and Young's Moduli of All Films. 166

Table 6.3. The volume fraction of solutes (MeOH and/or KOFm), water, and polymer after equilibration with single solute solutions (1 M MeOH or 1 M KOFm) or a mixed solute solution (1 M MeOH and 1 M KOFm). The polymer volume fraction is the remaining volume fraction in these swollen materials. All measurements were made at room temperature, and all values were measured in triplicate (standard deviations are reported). 172

Table 6.4. Relative permittivity values at 45 MHz of hydrated films before and after equilibration with either 1 M MeOH, 1 M KOFm, or a mixed solute solution containing 1 M MeOH and 1 M

KOFm. All measurements were made at room temperature, and all values were measured in triplicate (standard deviations are reported). 175
Table 7.1. Pre-polymerization mixture compositions. 182
Table 7.2. Water uptake, dry polymer density, and ionic conductivity of all films. 185
Table 8.1. Pre-polymerization mixtures compositions. 200
Table 8.2. Water uptake, dry polymer density, and water volume fraction of all membranes. .. 203
Table 8.3. Young's Modulus and ion exchange capacity of all membranes. 205
Table 9.1. Pre-polymerization mixtures compositions. 222
Table 9.2. Water uptake, dry polymer density, and water volume fraction. 224
Table 9.3. Membrane Characterization. 226
Table 10.1. Composition of Pre-polymerization mixtures. 239
Table 10.2. Water uptake, dry polymer density, water volume fraction, ionic conductivity, fixed charge concentration, and fixed charge density. 241
Table 10.3. Glass transition temperature, ionic conductivity, and Young's modulus. 244
Table 11.1. Membrane characteristics from pre-polymerization mixtures. 267
Table 11.2. Young's modulus, dry polymer density, water volume fraction, ionic conductivity, and ion exchange capacity of CEMs and AEMs 271
Table 11.3. Ionic Conductivity and Ion Exchange Capacity of CEMs and AEMs. 275
Table 11.4. Maximum Power Density and Voltage at the Maximum Power Density 279
Table 11.5. The volumetric ratio between solvated films (Solutions: 0.33, 1, 2, and 3 M Urea) and hydrated films (VS/VH) was measured via the photograph-caliper method at 25 °C, where the surface area of each film was measured from a digital photograph coupled with the ImageJ

software and the film thickness was measured with a digital caliper by taking the average of 5 random points..... 282

List of Figures

Figure 2.1. Classification of membrane filtration processes based on pore size and their separation targets [8]. 47

Figure 2.2. Schematic description of CEM and AEM. 48

Figure 2.3. Diagram illustrating the PEC-CRC system. 50

Figure 2.4. Schematic diagram of a DUFC [22]. 51

Figure 2.5. schematic illustration of solute transport through a hydrated dense membrane. 53

Figure 2.6. Schematic representation of the concentration gradient in a hydrated dense membrane. 55

Figure 2.7. Schematic depiction of diffusion cell setup..... 58

Figure 2.8. Schematic depiction of electrostatic repulsion in AEM. 59

Figure 3.1. Schematic depiction of the membrane synthesis process. 74

Figure 3.2. a) ATR-FTIR spectra of methanol at varying concentrations, and b) the linear least-squares regression of absorbance against concentration at 1018 cm^{-1}. The error bars in the figure are smaller than the symbols representing the data points[34]. 90

Figure 3.3. An example of ATR-FTIR absorbance as a function of MeOH concentration at wavenumbers 1018 cm^{-1} (△, red), 1044 cm^{-1} (▽, blue), 1350 cm^{-1} (◁, green), and 1414 cm^{-1} (▷, yellow). 91

Figure 3.4. Schematic diagram of sorption-desorption experiment. 93

Figure 4.1. Schematic depiction of a carboxylate salt diffusion in (A,D) cation exchange membranes (i.e. PEGDA-AMPS and Nafion® 117), (B,E) crosslinked PEGDA (i.e. A0) and (C,F) anion exchange membranes (i.e. P8, P12, and AMVN) in (A-C) single and (D-F) co-diffusion with

an alcohol (MeOH or EtOH). Figures are reprinted from [28, 30, 32] with permission from Elsevier, Wiley, and MDPI. 99

Figure 4.2. (A, B) Synthetic scheme of (A) crosslinked PEGDA, A0, and (B) crosslinked PEGDA-APTA, A8 and A12. (C) Schematic of Selemion AMVN, functionalized polystyrene-divinylbenzene (PS-DVB)-based film. 100

Figure 4.3. Molecular structure of (A) EtOH (4.5 Å), (B) carboxylate ions, OFm^- (5.9 Å) and OAc^- (7.4 Å) and (C) cations, K^+ (6.6 Å) and Na^+ (7.2 Å), where kinetic diameters are stated for EtOH and hydrated diameters are stated for ions. Carbons are shown in grey, oxygens are shown in red, hydrogens are shown in white, K^+ is shown in a darker purple, and Na^+ is shown in a lighter purple. 103

Figure 4.4. Ionic conductivity as a function of inverse water volume fraction for A8, A12 (filled markers), and AMVN (empty markers) in Cl^- (diamonds, ◇) and in HCO_3^- (squares, □). The line is a regression on a series of ImPPO- χ AEMs and Selemion® AMV from the literature [16]. 107

Figure 4.5. (A) Permeabilities to EtOH, ○, in single permeation. (B) Permeabilities to KOFm (△, red), NaOFm (▽, orange), KOAc (▷, blue) and NaOAc (◁, purple) in single permeation. Each data point is the average of 3 experiments with error bars corresponding to the standard deviation. 109

Figure 4.6. (A) Permeabilities to EtOH in co-permeation with KOFm (△, red), NaOFm (▽, orange), KOAc (▷, blue), and NaOAc (◁, purple). (B) Permeabilities to KOFm (△, red), NaOFm

(▽, orange), KOAc (▷, blue), and NaOAc (◁, purple) in co-permeation with EtOH. Each data point is the average of 3 experiments with error bars corresponding to the standard deviation. 111

Figure 4.7. (A) Solubilities to EtOH, ○, in single sorption. (B) Solubilities to KOFm (△, red), NaOFm (▽, orange), KOAc (▷, blue) and NaOAc (◁, purple) in single sorption. Each data point is the average of 3 experiments with error bars corresponding to the standard deviation. 112

Figure 4.8. (A) Solubilities to EtOH in co-sorption with KOFm (△, red), NaOFm (▽, orange), KOAc (▷, blue) and NaOAc (◁, purple). (B) Solubilities to KOFm (△, red), NaOFm (▽, orange), KOAc (▷, blue) and NaOAc (◁, purple) in co-sorption with EtOH. Each data point is the average of 3 experiments with error bars corresponding to the standard deviation. 115

Figure 4.9. (A) Diffusivities to EtOH, ○, in single diffusion. The solid line is the Mackie-Meares′ fit. (B) Diffusivities to KOFm (△, red), NaOFm (▽, orange), KOAc (▷, blue) and NaOAc (◁, purple) in single diffusion. The lines are the Mackie-Meares' fits, KOFm (solid line, red), NaOFm (dot-dashed, orange), KOAc (dashed, blue), and NaOAc (dotted, purple). 117

Figure 4.10. (A) Diffusivities to EtOH, ○, in co-diffusion with KOFm (△, red), NaOFm (▽, orange), KOAc (▷, blue) and NaOAc (◁, purple). The solid line is the Mackie-Meares' fit. (B) Diffusivities to KOFm (△, red), NaOFm (▽, orange), KOAc (▷, blue) and NaOAc (◁, purple) in co-diffusion with EtOH. The lines are the Mackie-Meares' fits, KOFm (solid line, red), NaOFm (dot-dashed, orange), KOAc (dashed, blue), and NaOAc (dotted, purple). 122

Figure 4.11. Schematic depiction of a carboxylate salt diffusion in charge neutral crosslinked PEGDA and anion exchange membranes in single and co-diffusion with alcohol. 125

Figure. 5.1. Illustration of KOAc diffusion in (A-C) single and (D-F) co-diffusion with MeOH. (A,D) PEGDA-SPMAK, (B,E) PEGDASPMAK/PEGPEA, and (C,F) PEGDA-PEGPEA. 135

Figure 5.2. Scheme of prepared (A) binary-SPMAK films, P-S, (B) binary-phenyl films, P-E and P-G, and (C) ternary films, P-S/E and P-S/G..... 136

Figure 5.3. Ionic conductivity of P-S, ◯, P-S/E, △, and P-S/G, ◁. Standard deviations are denoted by error bars and lines provided as a guide. 138

Figure 5.4. Water volume fraction of (A) P-S, ◯, (B) P-E, △, (C) P-G, ◁, (D) P-S/E, △, and (E) P-S/G, ◁. The error bars show the standard deviation and all lines are a guide to the eye. 141

Figure 5.5. Storage modulus of (A) P-S, ◯, (B) P-E, △, (C) P-G, ◁, (D) P-S/E, △, and P-S/G, ◁. The error bars show the standard deviation and all lines are a guide to the eye. 143

Figure 5.6. Permeabilities of all films to (A-E) MeOH and KOAc measured in one-component (solid line) and two-component (dashed), which consist of (A) P-S (red, one: ◯ and two: ×), (B) P-E (green, one: △ and two: ▽), (C) P-G (blue, one: ◁ and two: ▷), (D) P-S/E (green, one: △ and two: ▽), and (E) P-S/G (blue, one: ◁ and two: ▷) films. The error bars show the standard deviation and all lines are a guide to the eye. 147

Figure 5.7. Glass transition temperature (T_g, °C) of (A-C) binary films (P-S, P-E, and P-G) and (D,E) ternary films (P-S/E and P-S/G). 148

Figure 5.8. Solubilities of all films to (A-E) MeOH and KOAc measured in one-component (solid line) and two-component (dashed), which consist of (A) P-S (red, one: ◯ and two: ×), (B) P-E (green, one: △ and two: ▽), (C) P-G (blue, one: ◁ and two: ▷), (D) P-S/E (green, one: △ and

two: ▽), and (E) P-S/G (blue, one: ◁ and two: ▷) films. The error bars show the standard deviation and all lines are a guide to the eye. 151
Figure 5.9. (A-C) MeOH and (D-F) KOAc diffusivities of (A,D) binary films (P-S, P-E, and P-G), (B,E) P-S/E films, and (C,F) P-S/G films. Single diffusivities are shown in solid lines with filled markers (E: ▲, G: ◀, and S: ●) and co-diffusivities are shown in dashed lines with empty markers(E: ▽, G: ▷, and S: ×). The error bars show the standard deviation and all lines are a guide to the eye. 155
Figure 6.1. Scheme of prepared PA/A, PA/MA, PA/S, and PA/SM hydrogels. 165
Figure 6.2. Stress-strain curves for (a) PA/A, (b) PA/MA, (c) PA/S, and (d) PA/SM. 168
Figure 6.3. (a) MeOH permeabilities in single (blue) in mixed solute permeation with KOFm (green) and (b) KOFm permeabilities in single (red) in mixed solute permeation with MeOH (orange) as a function of water volume fraction. 170
Figure 6.4. (a) MeOH sorption coefficients in single (blue) in mixed solute sorption with KOFm (green) and (b) KOFm sorption coefficients in single (red) in mixed solute sorption with MeOH (orange) as a function of water volume fraction. 171
Figure 6.5. (a) Relative permittivity values (at 45 MHz) of all films in water (cyan) and after equilibration with 1 M MeOH (blue). (b) Relative permittivity values of all films after equilibration with 1 M KOFm (red) and a mixed solute solution containing 1 M MeOH and 1 M KOFm (purple). 175
Figure 6.6. Schematic depiction of different rigidity hydrated film interaction with water and formate. 176
Figure 7.1. Synthetic scheme of PA-SBMA membrane. 182

Figure 7.2. Representative FTIR spectra for each membrane composition..... 183
Figure 7.3. (a) Water volume fraction as functions of SBMA content. (b) Water volume fraction as function of Young's modulus. 185
Figure 7.4. Representative stress–strain curves for (solid) SX-10 and (dotted) SX-20 films 186
Figure 7.5. (a) Correlation between permeability and water volume fraction in MBAA 10 zwitterionic polymer. (b) Correlation between permeability and water volume fraction in MBAA 20 zwitterionic polymers. The average of three experiments is shown by each data point, and the error bars represent the standard deviation 187
Figure 7.6. (a) Effect of SBMA content on the salt solubility to MBAA 10 films. (b) Effect of SBMA content on the salt solubility to MBAA 20 films. The average of three experiments is shown by each data point, and the error bars represent the standard deviation. Lines are guides to the eye. 189
Figure 7.7. Correlation of diffusivity and water volume fraction in zwitterionic polymers. (a) Effect of water volume fraction on the monovalent salt diffusivity. (b) Effect of water volume fraction on the divalent salt diffusivity..... 190
Figure 7.8. Schematic depiction of ionic interactions between the ammonium and sulfonate groups in both low and high SBMA content. 192
Figure 8.1. Synthetic scheme of crosslinked MBAA-PA-APTA and PEGDA-PA-APTA membranes. 200
Figure 8.2. Water volume fraction as functions of APTA content. 202
Figure 8.3. Effect of copolymer composition on water contact angle for all membranes. 205
Figure 8.4. Glass transition temperature as a function of APTA content for all membranes. 206

Figure 8.5. Ionic conductivity as a function of APTA content of A12/P8, A8/P12, A12/M8, and A8/M12 membranes..... 207
Figure 8.6. Representative stress–strain curves for (A) PEGDA-contained membranes and (B) MBAA-contained membranes. 209
Figure 8.7. (A) The correlation between permeability and APTA content is demonstrated for A0/P20, A8/P12, and A12/P8. (B) The correlation between permeability and APTA content is demonstrated for A0/M20, A8/M12, and A12/M8. The data points reflect the average of three experiments, and the standard deviation is depicted by the error bars. 211
Figure 8.8. (A) The impact of APTA content on salt solubility in A0/P20, A8/P12, and A12/P8. (B) The impact of APTA content on salt solubility in A0/M20, A8/M12, and A12/M8. Each data point represents the average of three experiments, with error bars indicating the standard deviation. 212
Figure 8.9. The correlation between diffusivity and water volume fraction. 214
Figure 9.1. Synthetic scheme of PA/PEGDA/SPMAK and PA/PEGDA/MPS..... 223
Figure 9.2. Water volume fraction of PA/PEGDA/SPMAK (circle), PA/PEGDA (square) and PA/PEGDA/MPS (triangle). Each data point represents the average of measurements from three separate membranes, while the error bars indicate the extent of the standard deviation..... 225
Figure 9.3. Glass transition temperature as a function of PEGDA content for all membranes.. 228
Figure 9.4. Stress-strain curves for (a) SPMAK-contained films and (b) MPS-contained films. 229
Figure 9.5. (a) Permeabilities of charge neutral film and films containing SPMAK to KOAc, KOFm, NaOAc, and NaOFm. (b) Permeabilities of films containing MPS to KOAc, KOFm,

NaOAc, and NaOFm. Each data point represents the average of three experiments, with error bars indicating the standard deviation. 230

Figure 9.6. (a) Solubilities of charge neutral film and films containing SPMAK to salts. (b) solubility of films containing MPS to salts. Each data point represents the average of three experiments, with error bars indicating the standard deviation. 231

Figure 9.7. Diffusivity of (a) charge neutral film and films containing SPMAK (b) films containing MPS to all salts. Each data point represents the average of three experiments, with error bars indicating the standard deviation 232

Figure 10.1. Synthetic scheme of PA/MBAA/APTA and PA/MBAA/AETAC 240

Figure 10.2. Fixed charge density and water volume fraction are plotted against the mol% of charge monomer in the pre-polymerization solution. Fixed charge density is shown in black color, while water volume fraction is depicted in blue color. Circles (○) represent membranes containing APTA, triangles (▽) represent membranes containing AETAC, and crosses (╳) denote neutral membranes. 242

Figure 10.3. Single solute permeability as a function of fixed charge density is presented. Blue markers indicate APTA-containing membranes, red markers indicate AETAC-containing membranes, and black markers represent neutral membranes. Potassium formate is represented by triangles (▽), potassium acetate by crosses (✕), and potassium bicarbonate by circles (○). ... 246

Figure 10.4. The co-permeation of two solutes is illustrated as a function of fixed charge density. (a) APTA-containing and neutral membrane (b) AETAC-containing and neutral membrane. Co-permeation results for potassium acetate and potassium formate are shown in blue, potassium

acetate and potassium bicarbonate in red, and potassium formate and potassium bicarbonate in black. Symbols represent each solute: potassium formate with triangles (▽), potassium acetate with crosses (×), and potassium bicarbonate with circles (○). 248

Figure 10.5. The deswelling ratio of membranes conducting single-solute solubility is shown, with blue markers for APTA-containing membranes, red markers for AETAC-containing membranes, and black markers for neutral membranes. Potassium formate is indicated by triangles (▽), potassium acetate by crosses (×), and potassium bicarbonate by circles (○). 249

Figure 10.6. Single solute solubility as a function of fixed charge density is presented. Blue markers indicate APTA-containing membranes, red markers indicate AETAC-containing membranes, and black markers represent neutral membranes. Potassium formate is represented by triangles (▽), potassium acetate by crosses (×), and potassium bicarbonate by circles (○). ... 251

Figure 10.7. The deswelling ratio of membranes during co-sorption is illustrated, with blue markers representing APTA-containing membranes, red markers for AETAC-containing membranes, and black markers for neutral membranes. A square (□) indicates potassium acetate and potassium formate, a star (✻) represents potassium acetate and potassium bicarbonate, and a triangle (△) stands for potassium formate and potassium bicarbonate. 252

Figure 10.8. The co-sorption of two solutes as a function of fixed charge density is illustrated. (a) APTA-containing and neutral membrane (b) AETAC-containing and neutral membrane. Co-sorption results for potassium acetate and potassium formate are shown in blue, potassium acetate and potassium bicarbonate in red, and potassium formate and potassium bicarbonate in black.

Symbols represent each solute: potassium formate with triangles (▽), potassium acetate with crosses (×), and potassium bicarbonate with circles (○). 253

Figure 10.9. Single solute diffusivity as a function of fixed charge density is presented. Blue markers indicate APTA-containing membranes, red markers indicate AETAC-containing membranes, and black markers represent neutral membranes. Potassium formate is represented by triangles (▽), potassium acetate by crosses (×), and potassium bicarbonate by circles (○). ... 255

Figure 10.10. The co-diffusion of two solutes as a function of fixed charge density is illustrated. (a) APTA-containing and neutral membrane (b) AETAC-containing and neutral membrane. Co-diffusion results for potassium acetate and potassium formate are shown in blue, potassium acetate and potassium bicarbonate in red, and potassium formate and potassium bicarbonate in black. Symbols represent each solute: potassium formate with triangles (▽), potassium acetate with crosses (×), and potassium bicarbonate with circles (○). 256

Figure 11.1. Scheme of prepared PA/A, PMA/A, PA/M, and PMA/M organogels. 266

Figure 11.2. Stress-strain curves of (A) commercial CEM(Nafion 117, red solid) and AEM (FAA-Br, blue dashed), (B) PA/A, (C) PMA/A, (D) PA/M, and (E) PMA/M, where the MBAA (cross-linker) contents are specified as 5 (red solid), 10 (blue dashed), 20 (green dot-dashed), and 30 (orange dotted) mol %. 269

Figure 11.3. Young' s modulus of (A) CEMs, PA/A (○, red, solid line) and PMA/A (□, orange, dashed line). Young' s modulus of (B) AEMs, PA/M(○, blue, solid line) and PMA/M (□, purple,

dashed line). Each data point is the average of three membranes with error bars corresponding to the standard deviation. Lines are present as a guide to the eye. 270
Figure 11.4. Water volume fractions of (A) CEMs, PA/A (◯, red) and PMA/A (□, orange). Water volume fractions of AEMs, (B) PA/M (◯, blue) and PMA/M (□, purple) and (C) FAA-Br, FAA-OH, PA/M-30-Cl, and PA/M-30-OH. Each data point is the average of three membranes with error bars corresponding to the standard deviation..... 273
Figure 11.5. Theoretical IECs (solid lines) of (A) PA/A (red, ◯) and (B) PMA/A (orange, □) and (C) PA/M (◯, blue) and (D) PMA/M (□, purple). Measured IECs (dashed lines) of (A) PA/A (red, ×), (B) PMA/A (orange, ◊), (C) PA/M (×, blue), and (D) PMA/M (◊, purple). Lines are present as a guide to the eye. 276
Figure 11.6. Ionic conductivities of (A) CEMs, PA/A (◯, red, solid line) and PMA/A (□, orange, dashed line), and (B) AEMs, PA/M (◯, blue, solid line) and PMA/M (□, purple, dashed line). Lines are present as a guide to the eye. (C) Ionic conductivities of FAA in Br^- form (blue) and OH^- form (purple) and PA/M-30 in Cl^- form (blue) and OH^- form (purple). Each data point is the average of three membranes with error bars corresponding to the standard deviation. 277
Figure 11.7. Schematic diagram of a direct urea fuel cell. 278
Figure 11.8. Power density and OCV, in initial voltage, of (A, C) FAA-OH and (B, D) PA/M-30-OH at (A, B) 20 and (C, D) 50 °C. 280
Figure 11.9. Urea permeabilities of (A) FAA-OH and (B) PA/M-30-OH at 25 ˚C (dashed, blue, ◯) and 55 ˚C (solid line, black, □) at 1, 2, and 3 M urea. Lines are present as a guide to the eye. 282

List of Abbreviations

IEMs	Ion exchange membranes
AEMs	Anion exchange membranes
CEMs	Cation exchange membranes
CO_2	Carbon dioxide
CO	Carbon monoxide
CH_4	Methane
C_2H_4	Ethylene
$HCOO^-$	Formate
CH_3COO^-	Acetate
QA	Quaternary ammonium
PEGDA	Poly(ethylene glycol) diacrylate
SPMAK	3-Sulfopropyl methacrylate potassium
PEA	Phenoxyethyl acrylate

PEGPEA	Poly(ethylene glycol) phenyl ether acrylate
OAc^-	Acetate
MeOH	Methanol
CO_2RCs	CO2 reduction cells
SPAK	3-Sulfopropyl acrylate potassium
AETAC	[2-(Acryloyloxy)-ethyl]trimethylammonium chloride
MAETAC	(Methacryloyloxy)ethyl trimethylammonium chloride
PA	Phenyl acrylate
SBMA	Sulfobetaine methacrylate
MBAA	Methylenebisacrylamide
APTA	(3-acrylamidopropyl) trimethylammonium chloride
OFm^-	Formate
PMA	Phenyl methacrylate
AMPS	2-Acrylamido-2-methyl-1-propanesulfonic acid
MACC	Methacroylcholine chloride

DMFCs	Direct methanol fuel cells
DUFCs	Direct urea fuel cells
MPS	2-Methyl-2-propene-1-sulfonic acid sodium
MF	Microfiltration
UF	Ultrafiltration
NF	Nanofiltration
RO	Reverse osmosis
ED	Electrodialysis
RED	Reverse electrodialysis
N_2	Nitrogen
H_2O	Water
PALS	Positron annihilation lifetime spectroscopy
NaCl	Sodium chloride
LiCl	Lithium chloride
KCl	Potassium chloride

$MgCl_2$	Magnesium chloride
NH_4Cl	Ammonium chloride
$CaCl_2$	Calcium chloride
NaOH	Sodium hydroxide
KOAc	Potassium acetate
K_2CrO_4	Potassium chromate
$AgNO_3$	Silver nitrate
FAA	Fumasep FAA-3-50
EtOH	Ethanol
HCl	Hydrochloric acid
KOH	Potassium hydroxide
AIBN	2,2′-Azobis(2-methylpropionitrile)
DMSO	Dimethyl sulfoxide
NaOFm	Sodium formate
$NiCl_2$	Nickel chloride

HCPK	1-Hydroxycyclohexyl phenyl ketone
NaOAc	Sodium acetate
KOFm	Potassium formate
$KHCO_3$	Potassium bicarbonate
DI	Deionized
IEC	Ion exchange capacity
EIS	Electrochemical impedance spectroscopy
H^+	Protons
DSC	Differential scanning calorimeter
T_g	Glass transition temperature
SEM	Scanning electron microscope
EDS	Energy dispersive spectroscopy
Cl^-	Chloride
Br^-	Bromide
ATR-FTIR	Attenuated total reflectance-fourier transform infrared

HPLC	High-performance liquid chromatography
AA	Acrylic acid
HEMA	Hydroxyethyl methacrylate
DMF	Dimethylformamide
THF	Tetrahydrofuran
NMP	N-methyl-2-pyrrolidone
TMPTA	Trimethylolpropane triacrylate
TMPTMA	Trimethylolpropane trimethacrylate
PETA	Pentaerythritol tetraacrylate
PETMA	Pentaerythritol tetramethacrylate

Chapter 1: Introduction

1.1. Motivation

Carbon dioxide (CO_2) plays a vital role in regulating global temperatures through the greenhouse effect. The rapid growth of the human population and the reliance on fossil fuels for energy production have exacerbated CO_2 emissions, intensifying the energy crisis and global warming [1, 2]. The increased concentration of CO_2 has led to negative environmental impacts, including rising sea levels, and extreme weather events [3, 4]. However, artificial photosynthetic technologies, such as photoelectrochemical CO_2 reduction cells (PEC-CRC), have emerged as a promising solution to address this global challenge. PEC-CRC systems can convert CO_2 into a range of products, including carbon monoxide (CO), methane (CH_4), ethylene (C_2H_4), formate ($HCOO^-$), acetate (CH_3COO^-), and valuable chemical fuels like methanol and ethanol, which serve as carbon-neutral energy sources. [5-8]. This technology offers a dual advantage by lowering atmospheric CO_2 levels while providing a method for sustainable energy production. These chemical fuels are critical for mitigating fossil fuel consumption and addressing the energy crisis, making PEC-CRC a transformative technology in the fight against climate change. A key component of PEC-CRC systems is the IEMs, which facilitate electrolyte transport, maintain charge balance, and prevent CO_2 reduction product crossover between electrodes [9-11]. A major challenge with this approach is the lack of IEMs capable of effectively reducing the crossover of CO_2 reduction products dissolved in the electrolyte. This crossover results in unwanted oxidation

of these products back into CO_2 and other by-products. Beyond PEC-CRC, IEMs are indispensable in various electrochemical applications, including fuel cells [12, 13], electrodialysis[14, 15], and redox flow batteries[16, 17], highlighting their widespread importance in advancing sustainable technologies. However, the performance of IEMs is often constrained by challenges such as low ion selectivity, limited understanding of multi-solute transport behavior, and insufficient knowledge of membrane structure-property relationships. These limitations hinder the optimization of electrochemical systems and highlight the need for a deeper understanding of IEMs. Advancing research on these membranes is essential for developing next-generation membranes tailored to specific applications, paving the way for breakthroughs in PEC-CRC and other electrochemical technologies.

1.2. Objectives and Goal

The primary objective of this dissertation research was to deepen the understanding of ion transport behavior, including permeability, solubility, and diffusivity, between aqueous salt solutions and IEMs. Advancing molecular insights in this area provides a foundation for the rational design of high-performance membranes for water purification and energy generation applications. To achieve this goal, this dissertation employed a combination of experimental and theoretical approaches. Transport properties and physicochemical characteristics of both commercial and synthesized AEMs and CEMs were systematically measured. These experimental findings were then utilized to develop and validate a theoretical framework that links solute transport to membrane structure-property relationships. This framework exhibited predictive

capabilities, offering a powerful tool for understanding and optimizing membranes tailored to specific applications

The following sections provide an overview of the work in this dissertation broken into discrete sections that form subsequent Chapters. In order to investigate these complex systems a series of membrane manipulations were performed and those membranes studied for particular solutes and solute mixtures. These manipulations included controlling membrane water content, varying crosslinker density, adjusting charge monomer content, and incorporating different monomers and functional groups. This was done in an attempt to isolate particular membrane features and/or physiochemical properties and thereby extract structure-property relationships. For instance, isolating the impact of water content helps eliminate permeability differences attributed to variations in free volume. Additionally, incorporating different monomers allows for examining how structural changes influence the membrane's physicochemical properties, such as water content, mechanical strength, and transport behavior. The following sections provide additional details of these efforts that form this dissertation.

1.2.1. Single and Co-transport of Ethanol and Carboxylate in AEMs

Investigating the transport behavior of two-solute mixtures in hydrated dense membranes is critical for advancing PEC-CRC technologies. A deeper understanding of the mechanisms governing the movement of CO_2 reduction products, such as formate, acetate, and ethanol, is essential for optimizing system performance. AEMs are integral to PEC-CRC systems due to their ability to transport key electrolytes like bicarbonates. However, their concurrent facilitation of carboxylate transport poses a significant challenge, hindering overall efficiency. Developing

AEMs tailored for selective ion and electrolyte transport is therefore crucial for enhancing the performance of electrochemical devices. This study examines the transport properties of formate and acetate, along with their co-transport behavior with ethanol, in two types of AEMs: (1) a crosslinked membrane based on poly(ethylene glycol) diacrylate (PEGDA), functionalized with a quaternary ammonium (QA) charged monomer, and (2) Selemion® AMVN. Through the systematic synthesis of AEMs and commercial AEM, physicochemical and transport experiments were conducted to investigate the following research questions in Chapter 4:

1. The impact of counter ions on water content and ionic conductivity.
2. The transport order of carboxylate ions and alcohols.
3. Study the transport behavior of alcohols and carboxylate ions in AEMs under single and binary solute conditions.

1.2.2. Single and Co-transport of Methanol and Acetate in CEMs

CO_2 reduction cells are advanced systems designed to convert CO_2 into valuable chemicals, such as methanol (MeOH) and acetate (OAc^-), at the cathode. A critical challenge in these devices is the development of IEMs that facilitate ion-selective transport—specifically protons in the case of CEMs—while minimizing the crossover of CO2 reduction products. Understanding the multi-solute transport behavior of these species is essential for designing effective membranes. Our previous work demonstrated that acetate diffusivity increases in sulfonated CEMs when co-diffusing with MeOH, suggesting that charge screening of electrostatic interactions by MeOH influences this behavior [18]. In this study, 12 chemically dissimilar crosslinked membranes were fabricated via photopolymerization using a crosslinker (PEGDA), a sulfonate-containing

comonomer, 3-sulfopropyl methacrylate potassium (SPMAK), and a phenyl-containing comonomer either phenoxyethyl acrylate (PEA, n=1) or poly(ethylene glycol) phenyl ether acrylate (PEGPEA, n=3). Through the systematic synthesis of CEMs, physicochemical and transport experiments were performed to address the following research questions in Chapter 5:

1. The hydrophobic pendant phenyl groups influence ionic conductivity at a consistent charge content.
2. Investigating the impact of varied sidechain length, PEA (n = 1) and PEGPEA (n = 3), on the multi-solute transport of MeOH and KOAc.
3. Impact of interactions between (1) mobile MeOH (partially hydrophobic) and PEGPEA (hydrophobic) chains and (2) SPMAK (hydrophilic) and PEGPEA on the observed transport behavior.

1.2.3. Effect of Acrylate and Methacrylate Backbone Linkages in IEMs

In CO_2 reduction cells (CO_2RCs), IEMs play a critical role in suppressing the crossover of CO_2 reduction products while facilitating the selective transport of electrolytes. However, several crosslinked films, such as PEGDA-based IEMs, often exhibit low toughness, which has restricted their application. Tuning the polymer rigidity within the membrane is essential for achieving controlled transport of organic solutes in dense, hydrated membranes. In this study, we investigate the mixed solute transport behavior of methanol and formate in a series of robust phenyl acrylate-based crosslinked IEMs. These membranes include CEMs functionalized with quaternary ammonium (QA^+)-containing monomers, such as 3-sulfopropyl acrylate potassium (SPAK) or 3-sulfopropyl methacrylate potassium (SPMAK), and AEMs functionalized with sulfonate (SO_3^-)-

containing monomers, such as [2-(Acryloyloxy)-ethyl]trimethylammonium chloride (AETAC) or 2-(Methacryloyloxy)ethyl trimethylammonium chloride (MAETAC). Among these charged monomers, AETAC and SPAK feature acrylates in their backbones, while MAETAC and SPMAK have methacrylates in their backbones. Using systematically synthesized IEMs, we conducted physicochemical and transport experiments to address the following research questions in Chapter 6:

1. The effect of acrylate and methacrylate backbone linkages on polymer chain flexibility, mechanical properties, water content, and transport behavior.
2. The impact of introducing different quaternary carbons as structural modifications on water content, as well as single and mixed solute transport
3. Evaluate the effect of organic solutes on the membrane's hydrogen-bonding environment through relative permittivity measurements.

1.2.4. Salt Transport in Zwitterionic Membranes

Produced water, a by-product of industrial activities such as hydraulic fracturing for enhanced oil recovery, presents significant environmental challenges due to the presence of various metal ions that must be removed before disposal to prevent contamination of water resources. Membrane separation processes, which utilize selective transport properties or absorption-swing techniques with membrane-bound ligands, offer a promising and efficient solution for extracting or collecting these harmful contaminants. This study investigates the transport of a variety of metal ions, including Na^+, Li^+, K^+, Ca^{2+}, Ni^{2+}, and Mg^{2+}, through crosslinked polymer membranes synthesized using a hydrophobic monomer (phenyl acrylate, PA), a zwitterionic hydrophilic

monomer (sulfobetaine methacrylate, SBMA), and a crosslinker (methylenebisacrylamide, MBAA). Six distinct zwitterionic membranes were systematically synthesized, and physicochemical and transport experiments were performed to address the following research questions in Chapter 7:

1. The relationship between PA, SBMA, and MBAA in terms of physicochemical properties, including water content, ionic conductivity, and mechanical characteristics.
2. The permeability, solubility, and diffusivity ranking of LiCl, NaCl, KCl, $CaCl_2$, $MgCl_2$, and $NiCl_2$ in zwitterionic membranes.
3. The transport behavior of solutes within zwitterionic membranes.

1.2.5. Impact of Crosslinker on Physiochemical Properties and Transport Behavior in AEMs

CO2 reduction cells are advanced devices designed to convert CO2 into valuable chemicals such as formate (OFm^-) and acetate (OAc^-) at the cathode. A critical challenge in these systems is developing IEMs that facilitate charge carrier transport between electrodes while minimizing the crossover of CO2 reduction products. This study focuses on the synthesis and characterization of crosslinked neutral membranes and AEMs composed of PA and (3-acrylamidopropyl) trimethylammonium chloride (APTA), crosslinked with PEGDA, n=13, or MBAA. By systematically synthesizing 4 distinct APTA-containing AEMs and 2 neutral membranes, we evaluated their water volume fraction, mechanical properties, ionic conductivity, ion exchange capacity, water contact angle, glass transition temperature, permeability, and solubility to investigate the following research questions in Chapter 8:

1. Understanding the underlying causes of physicochemical differences, including water volume fraction, polymer chain flexibility, dimensional swelling, and contact angle, resulting from variations in crosslinker type and content.
2. Evaluating the mechanical properties of membranes crosslinked with MBAA versus those crosslinked with PEGDA.
3. Influence of polymer chain mobility on transport behavior as a result of crosslinker variation.

1.2.6. Transport Behavior Differences between CEMs Containing SPMAK and MPS

Current membranes face challenges in effectively blocking carboxylate ions, such as formate and acetate, which are byproducts of CO_2 electrochemical reduction, from crossing over. Understanding the factors that govern ion transport within membranes is therefore essential for designing tailored solutions. This research focuses on comparing SPMAK and 2-methyl-2-propene-1-sulfonic acid sodium (MPS) to investigate the relationships between monomers, crosslinkers, and charged monomers. Through a systematic approach, a series of 9 membranes with controlled chemical compositions were synthesized, utilizing SPMAK and MPS as charged monomers to modify membrane properties. Through experiments evaluating water content, water contact angle, glass transition temperature, ionic conductivity, mechanical properties, and transport behavior, the following questions will be explored in Chapter 9:

1. Influence of crosslinker, hydrophobic monomer, and charge monomer ratios on physicochemical properties.

2. How the different monomers influence the flexibility, rigidity, and overall structural integrity of the membranes.
3. Investigation and comparison of transport behavior in CEMs containing SPMAK and MPS, analyzing how the chemical composition, monomer structure, and membrane properties affect permeability, solubility, and diffusivity for carboxylate ions.

1.2.7. Isolating the Impact of Water Volume Fraction in AEMs

Electrochemical reactions often involve multiple electrolytes, and membrane transport in these systems typically includes interactions between various solutes. The presence of one solute within the membrane can significantly influence the diffusion and sorption behavior of other solutes. In complex systems where multiple solutes diffuse simultaneously through hydrated, dense polymer membranes, understanding these interactions becomes challenging. Among various factors, water volume fraction plays a critical role in transport behavior. Moreover, systematically synthesizing membranes with varying properties while maintaining comparable water volume fractions to study solute transport in IEMs remains difficult, leaving the transport behavior poorly understood. This study investigates the individual and binary solute transport behaviors of potassium formate, acetate, and bicarbonate ions in both neutral membranes and quaternary ammonium-functionalized AEMs with phenyl acrylate polymer backbones.By systematically synthesizing a neutral membrane and two types of AEMs incorporating APTA and AETAC with varying charge monomer content while maintaining comparable water volume fractions, this study aims to address the following questions in Chapter 10:

1. Single and co-transport behavior of solutes and their transport order within membranes with comparable water volume fractions.
2. The effects of Donnan exclusion, fixed charge density and solute-membrane interactions on permeability, solubility, and diffusivity behavior.
3. Influence of amide and ester groups in charge monomers on physicochemical properties and transport behavior.

1.2.8. Phenyl Acrylate-Based IEMs for Direct Urea Fuel Cell

IEMs play a critical role in direct fuel cells, including direct methanol fuel cells (DMFCs) and direct urea fuel cells (DUFCs). Although commercially available IEMs, such as FAA-3-50, deliver reasonable power densities in these systems, they suffer from significant methanol or urea crossover, which undermines device performance. This challenge drives the development of advanced IEMs designed to minimize fuel crossover. Most IEMs are composed of linear copolymers combining a hydrophobic monomer and a hydrophilic monomer with charged functional groups. These designs typically require non-woven backing for structural support and make it challenging to incorporate pendant functional groups that could effectively suppress crossover effects. In this study, we synthesize crosslinked IEMs with enhanced mechanical toughness by incorporating MBAA as a crosslinker, hydrophobic monomers PA or phenyl methacrylate (PMA), and charged monomers. For CEMs, we used 2-acrylamido-2-methyl-1-propanesulfonic acid (AMPS), a negatively charged monomer with sulfonate functional groups. For AEMs, we employed methacroylcholine chloride (MACC), a positively charged monomer featuring a quaternary ammonium group. To assess their suitability for fuel cell applications, we

performed a series of physicochemical evaluations, including measurements of water volume fraction, mechanical properties, ionic conductivity, DUFC performance, and urea transport experiments. These investigations addressed the following research questions outlined in Chapter 11:

1. Influence of methyl groups, varying charged monomers, and crosslinker content on mechanical properties, water volume fraction, and ionic conductivity.
2. Performance comparison of synthesized AEMs and commercial membranes in DUFC operation at 20°C and 50°C, focusing on maximum power density and voltage output.
3. Urea permeability of synthesized AEMs at 1, 2, and 3 molar urea concentrations, compared to commercial membranes at 25°C and 55°C.

1.3. Organization of this Dissertation

This dissertation begins with an introduction of the motivation to emphasize the importance of IEMs for various electrochemical applications and environments. Then each project's objectives and motivation were briefly introduced. Chapter 2 provides an overview of membrane technology, introducing pertinent background and various types of membranes. Moreover, Chapter 2 emphasizes the applications of IEMs and presents detailed derivations of theoretical transport models and theories that are utilized in the subsequent chapters. Chapter 3 outlines the materials utilized in this dissertation, details the polymer synthesis methods, and describes the experimental techniques employed to characterize the physicochemical and transport properties of the membranes. Chapters 4 through 11 provide a comprehensive exploration of various transport behaviors and factors influencing IEMs: Chapter 4 examines ethanol and carboxylate transport,

both individually and in two-solute systems in AEMs, detailing their transport behavior. Chapter 5 investigates methanol and acetate transport, including single and co-transport scenarios in CEMs. Chapter 6 explores the effects of acrylate and methacrylate components on the physiochemical properties and transport behavior of IEMs. Chapter 7 focuses on metal ion transport in zwitterionic membranes. Chapter 8 identifies crosslinker as a critical factor impacting the physiochemical and transport properties of membranes. Chapter 9 analyzes the influence of two distinct charge monomers, SPMAK and MPS, on transport behavior in CEMs. Chapter 10 examines the transport behavior of carboxylate ions by isolating the role of water volume fraction which significantly dominates the transport behavior in membranes. Chapter 11 showcases phenyl acrylate-based IEMs with enhanced mechanical properties for use in DUFC. Chapter 12 concludes the study with a conclusion and recommendations for future research.

1.4. References

[1] A.M. Omer, The energy crisis, the role of renewable and global warming, Greener Journal of Environment Management and Public Safety 1(1) (2012) 038-07.

[2] S. Singh, Energy crisis and climate change: Global concerns and their solutions, Energy: crises, challenges and solutions (2021) 1-17.

[3] W.K. Michener, E.R. Blood, K.L. Bildstein, M.M. Brinson, L.R. Gardner, Climate change, hurricanes and tropical storms, and rising sea level in coastal wetlands, Ecological applications 7(3) (1997) 770-801.

[4] M.K. Van Aalst, The impacts of climate change on the risk of natural disasters, Disasters 30(1) (2006) 5-18.

[5] M.R. Singh, A.T. Bell, Design of an artificial photosynthetic system for production of alcohols in high concentration from CO 2, Energy & Environmental Science 9(1) (2016) 193-199.

[6] K. Ma, O. Yehezkeli, E. Park, J.N. Cha, Enzyme mediated increase in methanol production from photoelectrochemical cells and CO2, ACS Catalysis 6(10) (2016) 6982-6986.

[7] S. Castro, J. Albo, A. Irabien, Continuous conversion of CO2 to alcohols in a TiO2 photoanode-driven photoelectrochemical system, Journal of Chemical Technology & Biotechnology 95(7) (2020) 1876-1882.

[8] D.J. Miller, F.A. Houle, Membranes for Solar Fuels Devices, in: I.D. Sharp, H.A. Atwater, H.-J. Lewerenz (Eds.), Integrated Solar Fuel Generators, The Royal Society of Chemistry2018, p. 0.

[9] J.M. Kim, Y.-h. Lin, B. Hunter, B.S. Beckingham, Transport and co-transport of carboxylate ions and ethanol in anion exchange membranes, Polymers 13(17) (2021) 2885.

[10] J.M. Kim, Y.-h. Lin, S.M. Bannon, G.M. Geise, B.S. Beckingham, Improved Structural Stability of Charged Hydrogels under Organic CO2 Reduction Products: Effect of Acrylate and Methacrylate Backbone Linkages, The Journal of Physical Chemistry C 127(22) (2023) 10826-10832.

[11] J.M. Kim, Y.-H. Lin, P.P. Aravindhan, B.S. Beckingham, Impact of hydrophobic pendant phenyl groups on transport and co-transport of methanol and acetate in PEGDA-SPMAK cation exchange membranes, Chemical Engineering Research and Design 185 (2022) 418-429.

[12] J.M. Kim, Y. Wang, Y.-h. Lin, J. Yoon, T. Huang, D.-J. Kim, M.L. Auad, B.S. Beckingham, Fabrication and Characterization of Cross-Linked Phenyl-Acrylate-Based Ion Exchange

Membranes and Performance in a Direct Urea Fuel Cell, Industrial & Engineering Chemistry Research 60(41) (2021) 14856-14867.

[13] J. Yoon, J.M. Kim, Y.-h. Lin, G.M. Geise, B.S. Beckingham, D.-J. Kim, Impact of a Novel Nickel-Based Catalyst and Phenyl-Acrylate-Based Anion-Exchange Membrane in a Direct Urea Fuel Cell, Energy & Fuels 38(13) (2024) 12274-12281.

[14] G.M. Geise, M.A. Hickner, B.E. Logan, Ionic resistance and permselectivity tradeoffs in anion exchange membranes, ACS applied materials & interfaces 5(20) (2013) 10294-10301.

[15] S. Al-Amshawee, M.Y.B.M. Yunus, A.A.M. Azoddein, D.G. Hassell, I.H. Dakhil, H.A. Hasan, Electrodialysis desalination for water and wastewater: A review, Chemical Engineering Journal 380 (2020) 122231.
[16] A.Z. Weber, M.M. Mench, J.P. Meyers, P.N. Ross, J.T. Gostick, Q. Liu, Redox flow batteries: a review, Journal of applied electrochemistry 41 (2011) 1137-1164.
[17] X. Li, H. Zhang, Z. Mai, H. Zhang, I. Vankelecom, Ion exchange membranes for vanadium redox flow battery (VRB) applications, Energy & Environmental Science 4(4) (2011) 1147-1160.
[18] J.M. Kim, B.M. Dobyns, R. Zhao, B.S. Beckingham, Multicomponent transport of methanol and acetate in a series of crosslinked PEGDA-AMPS cation exchange membranes, Journal of Membrane Science 614 (2020) 118486.

Chapter 2: Background

2.1. Membrane Technology

Membranes provide several advantages over traditional separation techniques, making them a preferred choice in many applications. Membrane separation processes typically require less energy than conventional thermal techniques such as distillation, which involve energy-intensive phase changes and higher operational costs [1]. Membranes have a smaller carbon footprint due to their ability to operate at ambient temperature and pressure. Moreover, their high selectivity enables precise and efficient separation of specific molecules or ions based on size, charge, or chemical properties.

Membrane filtration processes are widely utilized across various industries, including water treatment, food processing, medical applications, and energy production[2-6]. Figure 2.1 illustrates the classification of membrane filtration processes into microfiltration (MF), ultrafiltration (UF), nanofiltration (NF), and reverse osmosis (RO) based on the size of particles or molecules they separate and the pore size of the membrane [6, 7]. Microfiltration is designed to remove larger particles, such as bacteria and suspended solids, and ultrafiltration separates viruses and proteins. Nanofiltration and reverse osmosis work at the molecular level, separating salts and organic compounds [6, 7]. This broad filtration spectrum highlights the adaptability of membranes in tackling various separation and purification challenges.

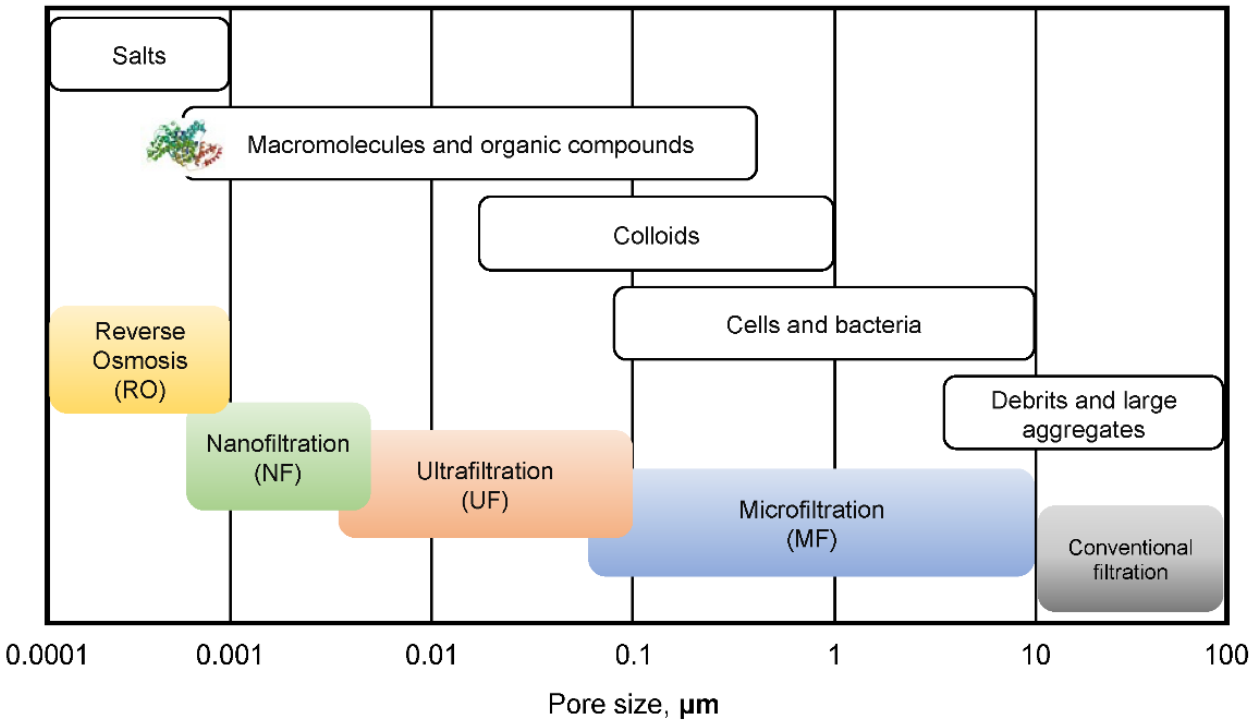

Figure 2.1. Classification of membrane filtration processes based on pore size and their separation targets [8].

IEMs are a specialized class of membranes that feature charged groups on the polymer backbone, enabling selective ion transport and high ionic conductivity. IEMs are typically classified into CEMs and AEMs, depending on the type of ions they transport, as illustrated in Figure 2.2. In electrochemical systems such as fuel cells and PEC-CRC, IEMs facilitate charge balance by allowing the movement of counterions while preventing the crossover of reactants and products [9, 10]. This selective transport is crucial for maintaining system efficiency and minimizing energy losses. For example, CEMs used in photoelectrochemical cells are tailored to optimize the transport of positively charged species while restricting negatively charged byproducts like carboxylate ions [11].

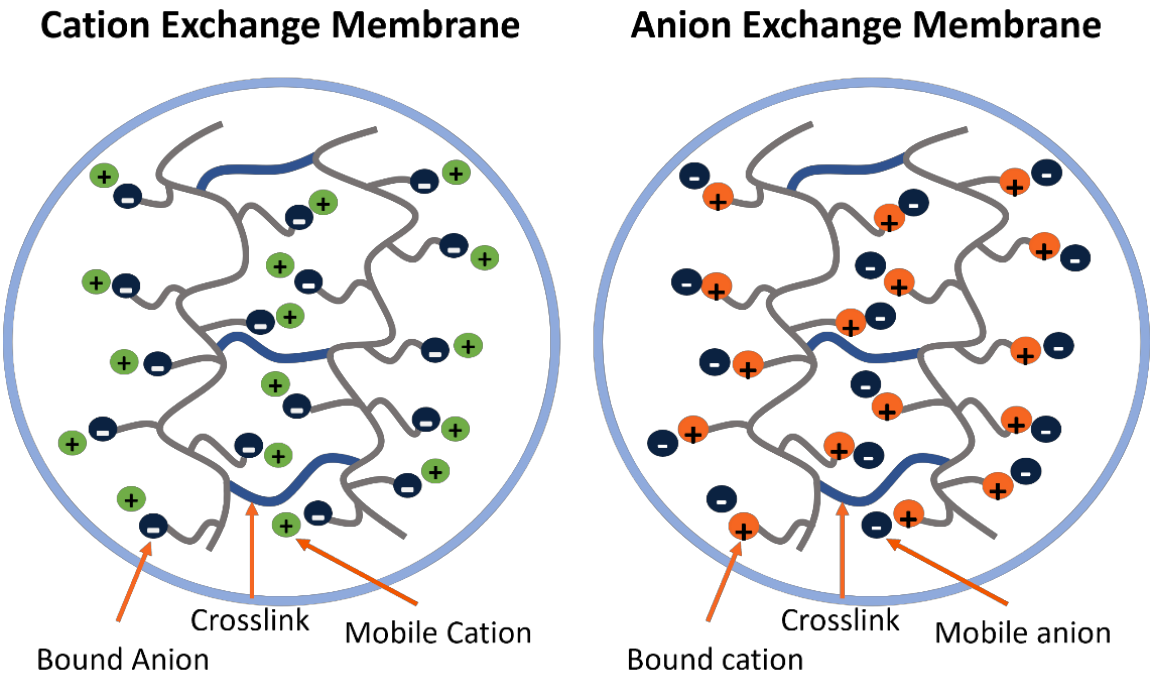

Figure 2.2. Schematic description of CEM and AEM.

Moreover, zwitterionic membranes are another type of membrane that contain both positive and negative charges while being charge-neutral. These membranes are recognized for their unique properties, including resistance to fouling and high water retention [12]. The balanced charge distribution enables them to exhibit excellent ion conductivity and selective ion transport, making them suitable for applications such as water desalination, fuel cells, and biomedical devices [13]. The structure-property relationships and physicochemical properties of these membranes are critical parameters influencing their transport performance. However, a fundamental understanding of the relationship between IEMs physicochemical and transport properties is still lacking. This dissertation aims to address this knowledge gap, with further details provided in the following chapter.

2.2. Application of IEMs

IEMs have attracted significant research attention since the last century due to their broad range of applications across various industries. In electrochemical technologies such as electrodialysis (ED) and reverse electrodialysis (RED), polymer electrolyte fuel cells, direct methanol fuel cells (DMFCs), redox flow batteries, and water electrolysis, IEMs are essential for separating and transporting ions between the anode and cathode, helping to balance electron flow in the external circuit. This has driven growing global interest in IEMs as a solution to energy and environmental challenges. In this study, we focus on the common electrolytes and solutes generated during the PEC-CRC and DUFU processes.

2.2.1. Photoelectrochemical CO2 Reduction Cells (PEC-CRC)

The PEC-CRC is an innovative technology designed to address two critical global challenges: mitigating CO_2 levels in the atmosphere and producing sustainable energy [14]. PEC-CRC uses solar energy as a driving force to facilitate the conversion of carbon dioxide (CO_2) into chemical fuels such as hydrogen, hydrocarbons, and multi-carbon oxygenates like methanol and ethanol [15-17]. These fuels can serve as carbon-neutral alternatives to fossil fuels, offering a pathway toward achieving energy sustainability. A PEC-CRC system consists of three essential components. The first is the photoelectrodes, which are crucial for generating and managing photogenerated charges, enabling CO_2 reduction at the photocathode and oxygen evolution at the photoanode [15]. The second is the IEMs, which prevent product crossover, transfer ions to maintain charge balance, and separate cathodic and anodic reactions [11, 18, 19]. The third

component is the CO_2 feeding system, which is necessary to address the low solubility of CO_2 in aqueous solutions[15]. Figure 2.3 shows the schematic diagram of PEC-CRC. Although PEC-CRC systems are straightforward and highly integrated, they face challenges such as low product purity, difficulties in producing target chemicals, and preventing the crossover of CO_2 reduction products [9, 10]. Ongoing research focuses on understanding solute transport within IEMs to address the limitations and enhance the feasibility of PEC-CRC.

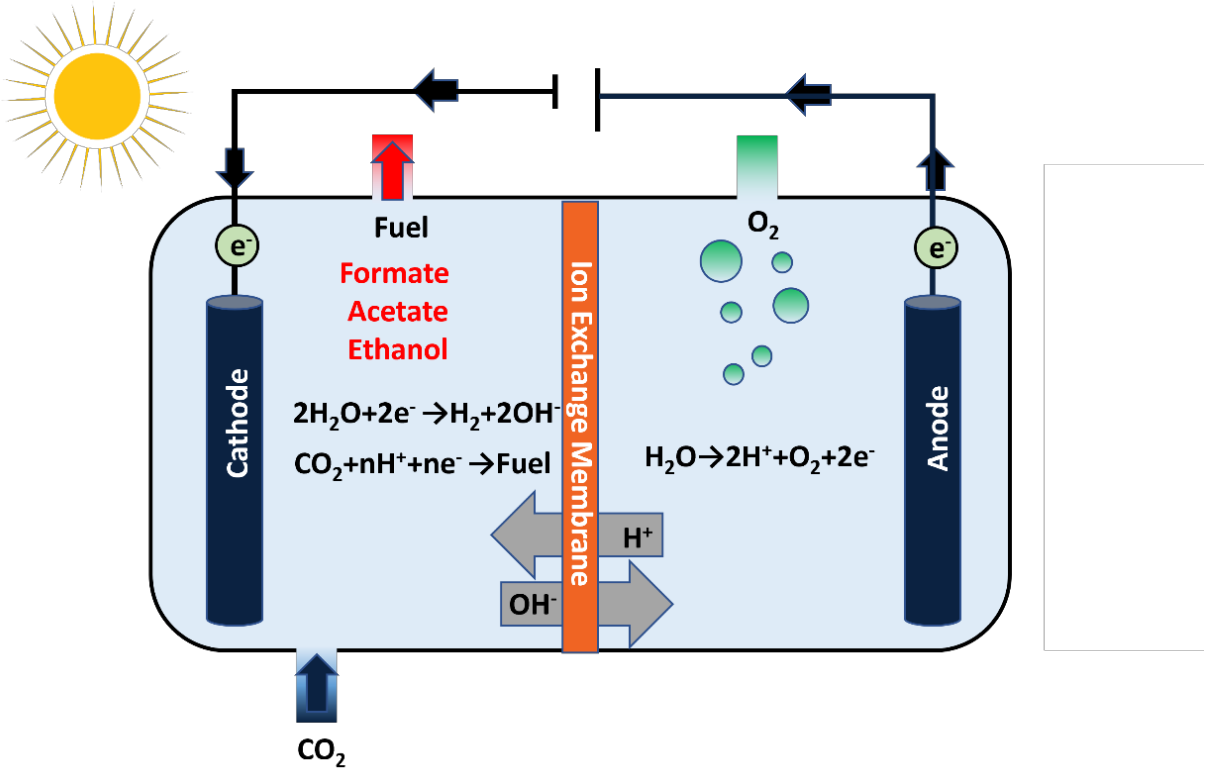

Figure 2.3. Diagram illustrating the PEC-CRC system.

2.2.2. Direct Urea Fuel Cells (DUFC)

Urea is a non-toxic compound with a high energy density and can be easily stored and transported [20]. Figure 2.4 presents the schematic diagram of the DUFC. In DUFCs, urea is electrochemically oxidized in an alkaline medium, producing carbon dioxide (CO_2), nitrogen (N_2), water (H_2O), and electricity. This process enables efficient electricity generation, positioning DUFCs as a promising solution for sustainable energy. However, to enhance DUFC performance, three main challenges must be addressed: (1) increasing catalytic activity by alloying catalysts or enhancing their surface area, (2) boosting the theoretical open circuit voltage (OCV), and (3) minimizing the crossover of urea to the cathode side of the cell, particularly at higher concentrations [21]. Overcoming these challenges can improve the efficiency and practicality of DUFCs, making them a viable option for clean energy production.

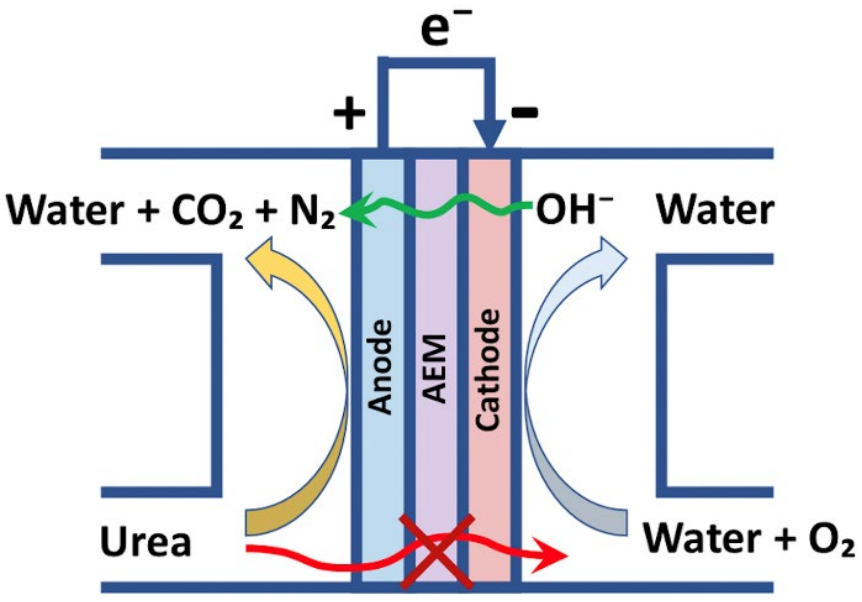

Figure 2.4. Schematic diagram of a DUFC [22].

2.3. Transport Mechanisms in Dense Polymer Membranes

Membrane separation mechanisms can be classified into several types. One common mechanism is size-based separation, which is fundamental to MF, UF, and NF, RO[23, 24]. In this mode, separation occurs based on the size of particles or molecules relative to the membrane's pore size. Molecules or particles smaller than the pore size pass through, while larger particles are retained on the membrane surface or trapped within its pores. RO also relies on the ion exchange mechanism for solute separation. Charged membranes selectively transport ions based on their charge. Counter-ions (those opposite in charge to the membrane's fixed groups) are mobile and selectively transported, while co-ions are excluded due to electrostatic repulsion [25]. Additionally, solute transport within RO membranes is governed by the solution-diffusion mechanism, which is complex and strongly influenced by the physicochemical properties of the membrane and the solutes. The following section will focus on hydrate-dense RO membrane transport mechanisms, which separate solutes primarily based on their charge and the interplay between membrane structure and solute properties.

2.3.1. Free Volume Theory

The free volume theory is critical for understanding transport phenomena in hydrated dense polymer membranes. It explains how small molecules, such as water and ions, move through dense polymer matrices. Free volume refers to the molecular-scale spaces between polymer chains that are not occupied by polymer segments [26], which are crucial for molecular diffusion and influence membrane separation performance. The free volume theory has been widely utilized to

estimate the diffusion coefficients of permeants through polymeric membranes [27-29]. Figure 2.5 shows the permeant solute molecules diffuse through these spaces, hopping between transient gaps created by thermal and segmental motion within the polymer structure [30]. The extent of free volume is affected by factors such as polymer chain flexibility, crosslinking density, and crystallinity, with amorphous regions having greater free volume than crystalline ones [31-33]. Temperature also impacts free volume, as higher temperatures increase polymer chain mobility, enhancing diffusion rates but potentially reducing selectivity[31, 34].

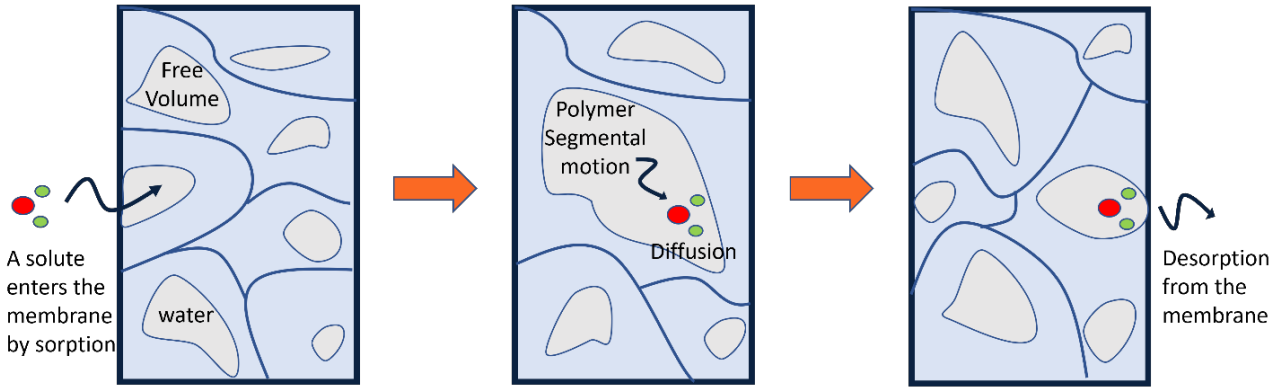

Figure 2.5. schematic illustration of solute transport through a hydrated dense membrane.

Positron Annihilation Lifetime Spectroscopy (PALS) is one of the most reliable methods for directly measuring free volume in polymeric materials [35-37]. This technique is based on a quantum model where positronium atoms form within free volume cavities and interact with the surrounding electron density. The local electron density is then correlated with the size of the micro-voids in the polymer [38]. Although PALS can directly measure free volume in dense polymer membranes, positrons can interact with ion exchange functional groups, altering their lifetimes and potentially affecting the accuracy of free volume calculations [39]. Therefore, the

most practical and direct method for approximating the free volume within the membrane is through water content measurement, which will be discussed in Chapter 3.

2.3.2. Solution-Diffusion Model

Permeant transport through porous membranes follows the pore-flow model, whereas transport through dense (nonporous) membranes driven by a concentration gradient is governed by the solution-diffusion mechanism [40-42]. The solution-diffusion model is widely applied to characterize water and salt transport in dense membranes, assuming independent diffusion of water and salt through the membrane. Moreover, water and salt selectivity are determined by the differences in the solubility and diffusivity of water and salt through the membrane. According to this model, salt molecules first absorb into the upstream side of the membrane, where the concentration is higher. They then diffuse through the membrane along the concentration gradient and desorb from the downstream side, as shown in Figure 2.6.

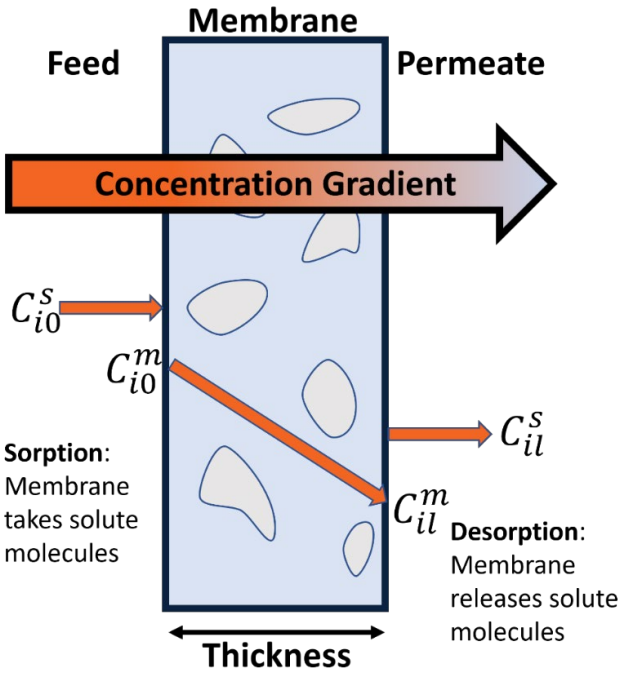

Figure 2.6. Schematic representation of the concentration gradient in a hydrated dense membrane.

The solution-diffusion model is based on thermodynamic principles, with the concentration gradient serving as its driving force. Accordingly, Fick's first law is expressed as follows:

$$J_i = -D_i \cdot \frac{dc_i}{dx} \tag{2.1}$$

where J_i represents the flux of permeant i, D_i is the diffusivity, c_i denotes the molar concentration, and x is the dimension of length. By substituting x with the membrane thickness, the equation becomes:

$$J_i = -D_i \frac{c_{io(m)} - c_{il(m)}}{l} \tag{2.2}$$

where $c_{io(m)}$ represents the concentration of solute i on the feed side of the membrane, $c_{il(m)}$ is the concentration of solute i on the permeate side of the membrane, and l denotes the thickness

of the membrane (Figure 2.6). Since our experimental method measures solute concentration in the solution rather than within the membrane, the chemical potential of the feed and the feed side of the membrane are assumed to be equal, resulting in:

$$\gamma_{io} c_{io} = \gamma_{io(m)} c_{io(m)} \tag{2.3}$$

Where γ_{io} and $\gamma_{io(m)}$ represent the activity coefficient of permeant i on the feed side and the feed side of the membrane, respectively. The solubility of solute i, K_i, can be used to replace the ratio of activity coefficients, $\gamma_{io}/\gamma_{io(m)}$. This process is then repeated on the permeate side of the membrane. Thus.

$$c_{io(m)} = K_i \cdot c_{io} \tag{2.4}$$

$$c_{il(m)} = K_i \cdot c_{il} \tag{2.5}$$

By substituting Equations 2.4 and 2.5 into Equation 2.2, the result is:

$$J_i = D_i K_i \frac{(c_{io} - c_{il})}{l} \tag{2.6}$$

Under pseudo-steady-state conditions, the integral salt permeability coefficient, P_i, represents the steady-state salt flux normalized by the membrane thickness and the driving force. This coefficient can be expressed as a combination of two terms: the salt sorption coefficient, K_i, a thermodynamic parameter quantifying the solutes' ability to sorb to or desorb from the membrane interfaces, and the concentration-averaged diffusion coefficient, D_i, a kinetic parameter describing the rate at which solutes traverse the membrane [41, 43]. The relationship is defined as follows:

$$P_i = K_i \times D_i \tag{2.7}$$

$$J_i = P_i \frac{(c_{io} - c_{il})}{l} \tag{2.8}$$

2.3.3. Yasuda's Model

Membrane permeability can be assessed by measuring the solute flux across the membrane under the influence of a chemical potential gradient (concentration gradient) and normalizing this flux by the membrane's thickness and transport area [10]. To measure membrane permeability, diffusion cells are typically employed; as shown in Figure 2.7. A membrane of known thickness is positioned between two diffusion half-cells, each with a precisely defined orifice. These half-cells are temperature-controlled to minimize any temperature gradients. The donor chamber is filled with a solution of known concentration, while the receiver chamber is filled with ultrapure water. The concentration increase in the receiver chamber is monitored over time as the solute permeates through the membrane [10, 44].

Yasuda's model is the most widely recognized framework for describing solute permeation through hydrated dense membranes. Permeability can be determined using the following equation:

$$ln\left[1 - 2\frac{c_{il}(t)}{c_{io}(0)}\right] = -2\frac{A}{Vl}P_i t \tag{2.9}$$

where $c_{il}(t)$ represents the concentration of solute i in the receiver chamber at time t, $c_{io}(0)$ is the initial concentration of solute i in the donor chamber, A is the cross-sectional area available for solute transport through the membrane, V is the solution volume in both the donor and receiver chambers, l is the membrane thickness. Utilizing the permeability as an adjustable parameter, the permeability is calculated from the time-resolved concentration data [10, 44].

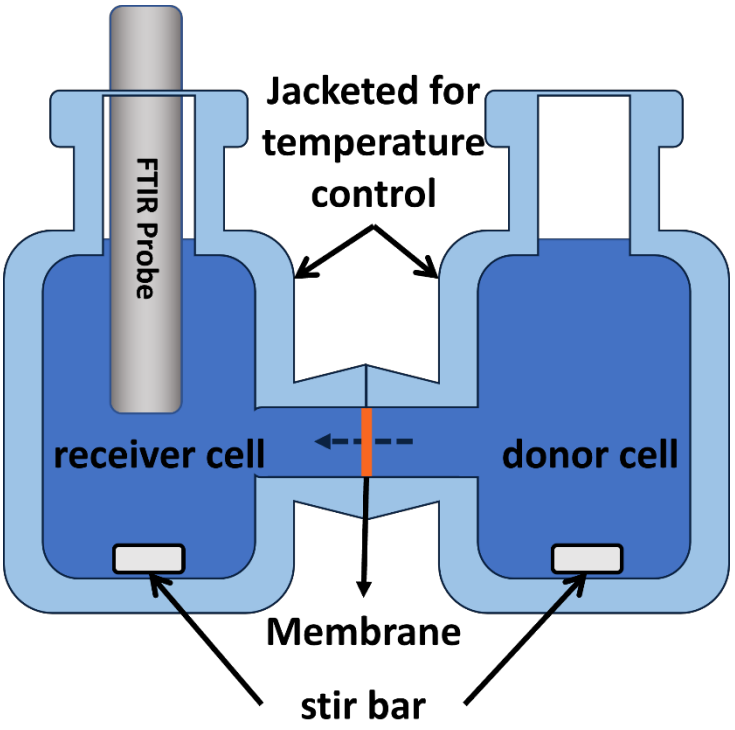

Figure 2.7. Schematic depiction of diffusion cell setup.

2.3.4. Donnan Theory

Donnan exclusion theory describes the behavior of ions in the presence of charged membranes, particularly IEMs. These membranes contain fixed charge groups that are bound to the polymer structure, allowing the permeation of counter-ions (ions of opposite charge to the fixed charges) while largely excluding co-ions (ions with the same charge as the fixed charges) [25, 45, 46]. When IEMs are placed between two ionic solutions, due to the presence of fixed ions and the condition of electroneutrality, an unequal distribution of ions exists in a charged polymer, creating a concentration gradient across the membrane. This gradient leads to the development of an electrostatic potential difference, referred to as the Donnan potential, at the membrane/solution

interface. The Donnan potential serves as the driving force for ion transport, influencing which ions can permeate the membrane and how they are distributed across the membrane. It specifically works to exclude co-ions from entering the membrane [47]. Figure 2.8 illustrates the electrostatic repulsion of co-ions in AEM.

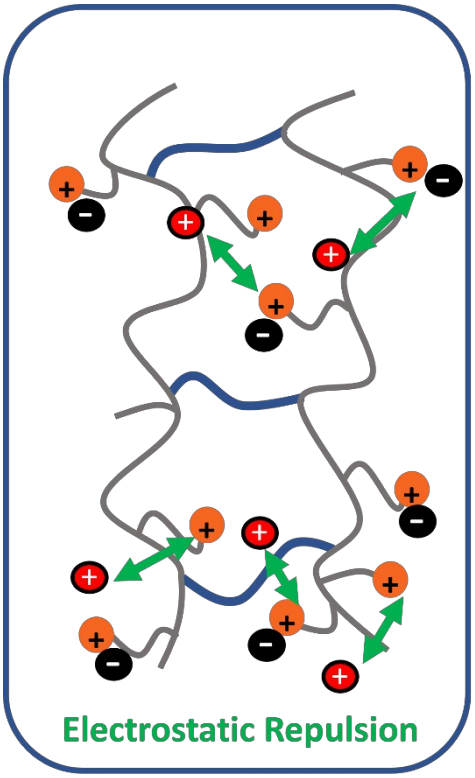

Figure 2.8. Schematic depiction of electrostatic repulsion in AEM.

This phenomenon is particularly important for processes like electrodialysis, where selective ion transport is critical for maintaining functions. The extent of Donnan exclusion is influenced by factors such as the fixed charge density of the membrane, the ionic strength of the solutions on either side of the membrane, and the size and charge of the ions involved. Higher fixed charge densities or greater differences in ionic strength across the membrane lead to stronger

exclusion of co-ions. Despite the extensive theoretical and practical use of Donnan exclusion, direct measurement of the Donnan potential has remained challenging due to the lack of effective interfacial experimental techniques [48]. This limitation has hindered the development of more selective membranes for specific ions. The ongoing development of advanced membrane technologies and experimental methods to measure the Donnan potential will be critical for enhancing the selectivity and efficiency of ion separation processes.

2.3.5. Mackie-Meares Model

The Mackie-Meares model provides a foundational framework for understanding ion diffusion in membranes by emphasizing tortuosity as the primary factor affecting ion transport and offering a simple method to estimate ion diffusion coefficients [49]. It assumes that ions diffuse within membranes similarly to how they move in aqueous solutions but must follow a more intricate path due to the presence of polymer chains acting as physical barriers. In this model, ions retain their intrinsic mobility properties from salt solutions, but the reduced effective transport area and increased path complexity (tortuosity) slow their movement across the membrane. Consequently, the diffusion of small molecules in swollen membranes is significantly lower than in pure solvents due to these combined effects of tortuosity and reduced transport area. To quantify tortuosity, the Mackie-Meares model employed a statistical approach assuming a random distribution of polymer chains, resulting in a relationship that depends solely on the membrane's water volume fraction. The Mackie-Meares model can be expressed as below:

$$D_i = D_{0,i}\left(\frac{\emptyset_w}{2-\emptyset_w}\right)^2 \tag{2.10}$$

where D_i is the diffusivity of a membrane to a solute i, $D_{0,i}$ is the solute i diffusivity in pure water and $\emptyset_w$ is the water volume fraction. While the model provides valuable insights, particularly for predicting co-ion diffusion coefficients in highly hydrated polymers and neutral membranes, it oversimplifies the effects of electrostatic interactions and fixed charge group dynamics, limiting its accuracy for counterion transport. Counterions, which remain closer to fixed charge groups, are more influenced by electrostatic interactions, making their diffusion behavior harder to predict with this model. Despite its limitations, the model remains a useful tool for estimating diffusion behavior in membranes with high water content. Additionally, its prediction that diffusion coefficients become zero at a water volume fraction of zero is unrealistic, limiting the model's applicability to membranes with significant water content.

2.3.6. Manning's Theory

Manning's theory explains ion diffusion in aqueous solutions containing both polyelectrolytes and ions. It assumes that polyelectrolyte chains generate inhomogeneous electric fields, which alter the ion diffusion pathways. To model these interactions, Manning applied the Debye–Hückel approximation to characterize the electric field produced by the charged polymer chains [50, 51]. Moreover, in this model, it is assumed that condensed counterions are immobilized. However, Manning acknowledged that while these condensed counterions may have some ability to move along the length of the polyelectrolyte chain, they are not free to detach and move away from the chain easily [14, 52, 53]. For instance, electric field-driven transport is primarily governed by counterion movement [54], allowing for a more flexible assumption regarding the mobility of condensed counterions. In Manning's model, polyelectrolyte chains are represented as infinite line

charges with uniformly spaced charged groups along their length, and the linear charge density is quantified by the Manning parameter, ξ [51, 55, 56].

$$\xi = \frac{e^2}{4\pi\varepsilon_0\varepsilon kTb} = \frac{\lambda_B}{b} \tag{2.11}$$

where e represents the elementary charge, ε_0 denotes the permittivity of free space, ε is the relative permittivity of the membrane phase (static dielectric constant), k is Boltzmann's constant, T is the absolute temperature, b is the average spacing between fixed charge groups along the polymer chain, and λ_B refers to the Bjerrum length. When the Manning parameter exceeds a critical threshold ($\xi = 1$), counterions condense onto the polymer chain, neutralizing its fixed charge groups and reducing the Manning parameter to the critical value [51]. The remaining uncondensed counterions are relatively free to move. This phenomenon, known as counterion condensation, arises in polyelectrolyte solutions due to the overlapping electric fields generated by closely spaced fixed charges [51, 57]. Conversely, if the Manning parameter is below the critical value, counterion condensation does not occur [51].

2.4. Tradeoff relationship in polymer membranes

Water content in polymer membranes significantly impacts solute transport behavior, ionic conductivity, and mechanical properties of the polymer [58, 59]. Factors such as the type of counterion, pre-polymerization solvent content, degree of crosslinking, external solution salt concentration, and fixed charge group concentration can all affect and regulate the membrane's water content. Higher water uptake in hydrated polymers is typically accompanied by excessive swelling and increased free volume within the polymer matrix, which enhances solute transport

behavior [42, 60, 61]. According to free volume theory, membranes with greater water content provide more space for solute movement, resulting in elevated solute diffusion coefficients and improved permeability [60, 62, 63]. The expanded free volume reduces restrictions on solute transport, facilitating their passage through the membrane. Additionally, membranes with high water content often exhibit higher ionic conductivity but suffer from reduced mechanical strength. This is because increased water content decreases the fixed charge concentration, further boosting the solute diffusion coefficient [22, 59, 64]. However, excessive swelling can compromise the membrane's structural integrity, leading to mechanical instability and reduced durability [65].

Pre-polymerization solvent is the most straightforward factor influencing membrane water content. As the solvent content in the pre-polymerization solution increases, more void spaces are created within the membrane structure [66]. Introducing a crosslinker into the polymer matrix helps mitigate this effect by increasing the crosslink density, making the polymer network more rigid. This reduces water content, limits swelling, and prevents the polymer chains from dissolving, thereby enhancing the membrane’s mechanical stability [54, 67]

The incorporation of charged functional groups into a polymer chain generally increases its water affinity and absorption capacity [43, 68, 69]. This behavior is attributed to the hydrophilic nature of ionic groups on the polymer backbone, which attract and are surrounded by water molecules [54]. While enhancing ion exchange capacity is a primary objective for IEMs, polymers made exclusively from monomers with fixed charge groups tend to be highly water-soluble, rendering them unsuitable for membrane formation. Additionally, membrane water uptake is affected by the type of counterions present, as different counterions exhibit distinct hydration numbers and binding affinities to the fixed functional groups [63, 70, 71].

The water content of a membrane also depends on the salt concentration in the surrounding solution [54, 72, 73]. As the external salt concentration rises, the thermodynamic activity of water in the solution decreases, leading to reduced water uptake by the polymer matrix. In general, water absorption by polymers increases with higher water activity, as described by models like the Flory–Huggins theory [74]. Consequently, higher salt concentrations result in a reduction of the polymer's water content, a process often referred to as osmotic deswelling.

While the above sections detail some of what is known, much remains to be understood concerning how the distinct properties of different functional groups, crosslinkers, and monomers influence membrane characteristics and their interactions. Additionally, most studies focus on investigating the transport behaviors of membranes with varying water content. Given the profound impact of water content on transport properties, systematically synthesizing membranes with comparable water volume fractions could offer deeper insights into these mechanisms.

2.5. References

[1] M. Mulder, Basic principles of membrane technology, Springer science & business media2012.

[2] O.T. Iorhemen, R.A. Hamza, J.H. Tay, Membrane bioreactor (MBR) technology for wastewater treatment and reclamation: membrane fouling, Membranes 6(2) (2016) 33.

[3] B.T. Konvensional, A review of oilfield wastewater treatment using membrane filtration over conventional technology, Malays. J. Anal. Sci 21 (2017) 643-658.

[4] G. Daufin, J.-P. Escudier, H. Carrère, S. Bérot, L. Fillaudeau, M. Decloux, Recent and emerging applications of membrane processes in the food and dairy industry, Food and Bioproducts Processing 79(2) (2001) 89-102.

[5] D.F. Stamatialis, B.J. Papenburg, M. Gironés, S. Saiful, S.N. Bettahalli, S. Schmitmeier, M. Wessling, Medical applications of membranes: Drug delivery, artificial organs and tissue engineering, Journal of Membrane Science 308(1-2) (2008) 1-34.

[6] H. Strathmann, Introduction to membrane science and technology, John Wiley & Sons2011.

[7] A. Lee, J.W. Elam, S.B. Darling, Membrane materials for water purification: design, development, and application, Environmental Science: Water Research & Technology 2(1) (2016) 17-42.

[8] A.I. Cirillo, G. Tomaiuolo, S. Guido, Membrane fouling phenomena in microfluidic systems: from technical challenges to scientific opportunities, Micromachines 12(7) (2021) 820.

[9] M.R. Singh, A.T. Bell, Design of an artificial photosynthetic system for production of alcohols in high concentration from CO 2, Energy & Environmental Science 9(1) (2016) 193-199.

[10] D.J. Miller, F.A. Houle, Membranes for Solar Fuels Devices, (2018).

[11] J.M. Kim, Y.-H. Lin, P.P. Aravindhan, B.S. Beckingham, Impact of hydrophobic pendant phenyl groups on transport and co-transport of methanol and acetate in PEGDA-SPMAK cation exchange membranes, Chemical Engineering Research and Design 185 (2022) 418-429.

[12] W. Li, K. Chu, L. Liu, Multipurpose zwitterionic polymer-coated glass fiber filter for effective separation of oil–water mixtures and emulsions and removal of heavy metals, ACS Applied Polymer Materials 3(3) (2021) 1276-1284.

[13] F. Xuan, J. Liu, Preparation, characterization and application of zwitterionic polymers and membranes: current developments and perspective, Polymer international 58(12) (2009) 1350-1361.

[14] M.S. Wrighton, Photoelectrochemical conversion of optical energy to electricity and fuels, Accounts of Chemical Research 12(9) (1979) 303-310.

[15] Y. Liu, L. Guo, On factors limiting the performance of photoelectrochemical CO2 reduction, The Journal of Chemical Physics 152(10) (2020).

[16] S. Chen, Y. Qi, C. Li, K. Domen, F. Zhang, Surface strategies for particulate photocatalysts toward artificial photosynthesis, Joule 2(11) (2018) 2260-2288.

[17] L. Guo, Y. Chen, J. Su, M. Liu, Y. Liu, Obstacles of solar-powered photocatalytic water splitting for hydrogen production: a perspective from energy flow and mass flow, Energy 172 (2019) 1079-1086.

[18] J.M. Kim, Y.-h. Lin, S.M. Bannon, G.M. Geise, B.S. Beckingham, Improved Structural Stability of Charged Hydrogels under Organic CO2 Reduction Products: Effect of Acrylate and Methacrylate Backbone Linkages, The Journal of Physical Chemistry C 127(22) (2023) 10826-10832.

[19] J.M. Kim, Y.-h. Lin, B. Hunter, B.S. Beckingham, Transport and co-transport of carboxylate ions and ethanol in anion exchange membranes, Polymers 13(17) (2021) 2885.

[20] R. Lan, S. Tao, J.T. Irvine, A direct urea fuel cell–power from fertiliser and waste, Energy & Environmental Science 3(4) (2010) 438-441.

[21] E.T. Sayed, T. Eisa, H.O. Mohamed, M.A. Abdelkareem, A. Allagui, H. Alawadhi, K.-J. Chae, Direct urea fuel cells: Challenges and opportunities, Journal of Power Sources 417 (2019) 159-175.

[22] J.M. Kim, Y. Wang, Y.-h. Lin, J. Yoon, T. Huang, D.-J. Kim, M.L. Auad, B.S. Beckingham, Fabrication and Characterization of Cross-Linked Phenyl-Acrylate-Based Ion Exchange Membranes and Performance in a Direct Urea Fuel Cell, Industrial & Engineering Chemistry Research 60(41) (2021) 14856-14867.

[23] L. Wang, M.S. Boutilier, P.R. Kidambi, D. Jang, N.G. Hadjiconstantinou, R. Karnik, Fundamental transport mechanisms, fabrication and potential applications of nanoporous atomically thin membranes, Nature nanotechnology 12(6) (2017) 509-522.

[24] A.J. Jose, J. Kappen, M. Alagar, Polymeric membranes: Classification, preparation, structure physiochemical, and transport mechanisms, Fundamental biomaterials: polymers, Elsevier2018, pp. 21-35.

[25] T. Luo, S. Abdu, M. Wessling, Selectivity of ion exchange membranes: A review, Journal of membrane science 555 (2018) 429-454.

[26] V.P. Swapna, V.S. Abhisha, R. Stephen, Polymer/polyhedral oligomeric silsesquioxane nanocomposite membranes for pervaporation, Polymer nanocomposite membranes for pervaporation, Elsevier2020, pp. 201-229.

[27] F. Peng, F. Pan, D. Li, Z. Jiang, Pervaporation properties of PDMS membranes for removal of benzene from aqueous solution: Experimental and modeling, Chemical Engineering Journal 114(1-3) (2005) 123-129.

[28] P. Das, S. Ray, Analysis of sorption and permeation of acetic acid–water mixtures through unfilled and filled blend membranes, Separation and Purification Technology 116 (2013) 433-447.

[29] T.-H. Yang, S.J. Lue, Coupled concentration-dependent diffusivities of ethanol/water mixtures through a polymeric membrane: Effect on pervaporative flux and diffusivity profiles, Journal of membrane science 443 (2013) 1-9.

[30] P.N. Patil, D. Roilo, R.S. Brusa, A. Miotello, S. Aghion, R. Ferragut, R. Checchetto, Free volumes and gas transport in polymers: amine-modified epoxy resins as a case study, Physical Chemistry Chemical Physics 18(5) (2016) 3817-3824.

[31] R.P. White, J.E. Lipson, Polymer free volume and its connection to the glass transition, Macromolecules 49(11) (2016) 3987-4007.

[32] C. Li, A. Strachan, Free volume evolution in the process of epoxy curing and its effect on mechanical properties, Polymer 97 (2016) 456-464.

[33] L. Tao, J. He, T. Arbaugh, J.R. McCutcheon, Y. Li, Machine learning prediction on the fractional free volume of polymer membranes, Journal of Membrane Science 665 (2023) 121131.

[34] A. Thran, G. Kroll, F. Faupel, Correlation between fractional free volume and diffusivity of gas molecules in glassy polymers, Journal of Polymer Science Part B: Polymer Physics 37(23) (1999) 3344-3358.

[35] A.S. Gupta, Direct Measurement of Free Volume Properties in Polymeric Materials, Advances in Physicochemical Properties of Biopolymers (Part 1) (2017) 295.

[36] E. Abdel-Hady, H.F. Mohamed, Microstructure changes of poly (vinyl chloride) investigated by positron annihilation techniques, Polymer degradation and stability 77(3) (2002) 449-456.

[37] P. Utpalla, S.K. Sharma, K. Sudarshan, S.K. Deshpande, M. Sahu, P.K. Pujari, Investigating the correlation of segmental dynamics, free volume characteristics, and ionic conductivity in poly (ethylene oxide)-based electrolyte: a broadband dielectric and positron annihilation spectroscopy study, The Journal of Physical Chemistry C 124(8) (2020) 4489-4501.

[38] J. Kruse, J. Kanzow, K. Rätzke, F. Faupel, M. Heuchel, J. Frahn, D. Hofmann, Free volume in polyimides: positron annihilation experiments and molecular modeling, Macromolecules 38(23) (2005) 9638-9643.

[39] H.F. Mohamed, Y. Kobayashi, S. Kuroda, A. Ohira, Positron trapping and possible presence of SO3H clusters in dry fluorinated polymer electrolyte membranes, Chemical Physics Letters 544 (2012) 49-52.

[40] D.R. Paul, Reformulation of the solution-diffusion theory of reverse osmosis, Journal of membrane science 241(2) (2004) 371-386.

[41] J.G. Wijmans, R.W. Baker, The solution-diffusion model: a review, Journal of membrane science 107(1-2) (1995) 1-21.

[42] H. Yasuda, C. Lamaze, L. Ikenberry, Permeability of solutes through hydrated polymer membranes. Part I. Diffusion of sodium chloride, Die Makromolekulare Chemie: Macromolecular Chemistry and Physics 118(1) (1968) 19-35.

[43] G.M. Geise, H.S. Lee, D.J. Miller, B.D. Freeman, J.E. McGrath, D.R. Paul, Water purification by membranes: the role of polymer science, Journal of Polymer Science Part B: Polymer Physics 48(15) (2010) 1685-1718.

[44] B.M. Carter, B.M. Dobyns, B.S. Beckingham, D.J. Miller, Multicomponent transport of alcohols in an anion exchange membrane measured by in-situ ATR FTIR spectroscopy, Polymer 123 (2017) 144-152.

[45] J.R. Werber, C.O. Osuji, M. Elimelech, Materials for next-generation desalination and water purification membranes, Nature Reviews Materials 1(5) (2016) 1-15.

[46] J. Kamcev, B.D. Freeman, Charged polymer membranes for environmental/energy applications, Annual review of chemical and biomolecular engineering 7(1) (2016) 111-133.

[47] F.G. Donnan, The theory of membrane equilibria, Chemical reviews 1(1) (1924) 73-90.

[48] P. Aydogan Gokturk, R. Sujanani, J. Qian, Y. Wang, L.E. Katz, B.D. Freeman, E.J. Crumlin, The Donnan potential revealed, Nature communications 13(1) (2022) 5880.

[49] J. Mackie, P. Meares, The diffusion of electrolytes in a cation-exchange resin membrane I. Theoretical, Proceedings of the Royal Society of London. Series A. Mathematical and Physical Sciences 232(1191) (1955) 498-509.

[50] G.S. Manning, Limiting laws and counterion condensation in polyelectrolyte solutions II. Self-diffusion of the small ions, The Journal of Chemical Physics 51(3) (1969) 934-938.

[51] G.S. Manning, Limiting laws and counterion condensation in polyelectrolyte solutions I. Colligative properties, The journal of chemical Physics 51(3) (1969) 924-933.

[52] G.S. Manning, Polyelectrolytes, Annual review of physical chemistry 23(1) (1972) 117-140.

[53] G.S. Manning, The molecular theory of polyelectrolyte solutions with applications to the electrostatic properties of polynucleotides, Quarterly reviews of biophysics 11(2) (1978) 179-246.

[54] F.G. Helfferich, Ion exchange, Courier Corporation1995.

[55] Y. Ji, H. Luo, G.M. Geise, Specific co-ion sorption and diffusion properties influence membrane permselectivity, Journal of membrane science 563 (2018) 492-504.

[56] J. Kamcev, M. Galizia, F.M. Benedetti, E.-S. Jang, D.R. Paul, B.D. Freeman, G.S. Manning, Partitioning of mobile ions between ion exchange polymers and aqueous salt solutions: importance of counter-ion condensation, Physical Chemistry Chemical Physics 18(8) (2016) 6021-6031.

[57] G.S. Manning, The critical onset of counterion condensation: A survey of its experimental and theoretical basis, Berichte der Bunsengesellschaft für physikalische Chemie 100(6) (1996) 909-922.

[58] B.M. Carter, L. Keller, M. Wessling, D.J. Miller, Preparation and characterization of crosslinked poly (vinylimidazolium) anion exchange membranes for artificial photosynthesis, Journal of Materials Chemistry A 7(41) (2019) 23818-23829.

[59] L.M. Robeson, H.H. Hwu, J.E. McGrath, Upper bound relationship for proton exchange membranes: Empirical relationship and relevance of phase separated blends, Journal of Membrane Science 302(1-2) (2007) 70-77.

[60] G.M. Geise, D.R. Paul, B.D. Freeman, Fundamental water and salt transport properties of polymeric materials, Progress in Polymer Science 39(1) (2014) 1-42.

[61] H. Ju, A.C. Sagle, B.D. Freeman, J.I. Mardel, A.J. Hill, Characterization of sodium chloride and water transport in crosslinked poly (ethylene oxide) hydrogels, Journal of Membrane Science 358(1-2) (2010) 131-141.

[62] Y.-h. Lin, J.M. Kim, B.S. Beckingham, Salt Transport in Crosslinked Hydrogel Membranes Containing Zwitterionic Sulfobetaine Methacrylate and Hydrophobic Phenyl Acrylate, Polymers 15(6) (2023) 1387.

[63] J.M. Kim, B.S. Beckingham, Transport and co-transport of carboxylate ions and alcohols in cation exchange membranes, Journal of Polymer Science 59(21) (2021) 2545-2558.

[64] S.M. Dischinger, S. Gupta, B.M. Carter, D.J. Miller, Transport of neutral and charged solutes in imidazolium-functionalized poly (phenylene oxide) membranes for artificial photosynthesis, Industrial & Engineering Chemistry Research 59(12) (2019) 5257-5266.

[65] D.F. Sanders, Z.P. Smith, R. Guo, L.M. Robeson, J.E. McGrath, D.R. Paul, B.D. Freeman, Energy-efficient polymeric gas separation membranes for a sustainable future: A review, Polymer 54(18) (2013) 4729-4761.

[66] H. Ju, B.D. McCloskey, A.C. Sagle, V.A. Kusuma, B.D. Freeman, Preparation and characterization of crosslinked poly (ethylene glycol) diacrylate hydrogels as fouling-resistant membrane coating materials, Journal of Membrane Science 330(1-2) (2009) 180-188.

[67] M. Paul, H.B. Park, B.D. Freeman, A. Roy, J.E. McGrath, J. Riffle, Synthesis and crosslinking of partially disulfonated poly (arylene ether sulfone) random copolymers as candidates for chlorine resistant reverse osmosis membranes, Polymer 49(9) (2008) 2243-2252.

[68] W. Xie, G.M. Geise, B.D. Freeman, C.H. Lee, J.E. McGrath, Influence of processing history on water and salt transport properties of disulfonated polysulfone random copolymers, Polymer 53(7) (2012) 1581-1592.

[69] G. Geise, B. Freeman, D. Paul, Characterization of a sulfonated pentablock copolymer for desalination applications, Polymer 51(24) (2010) 5815-5822.

[70] H. Miyoshi, M. Chubachi, M. Yamagami, T. Kataoka, Characteristic coefficients for equilibrium between solution and Neosepta or Selemion cation exchange membranes, Journal of Chemical and Engineering Data 37(1) (1992) 120-124.

[71] J. Bontha, P.N. Pintauro, Water orientation and ion solvation effects during multicomponent salt partitioning in a Nafion cation exchange membrane, Chemical engineering science 49(23) (1994) 3835-3851.

[72] G.M. Geise, B.D. Freeman, D.R. Paul, Sodium chloride diffusion in sulfonated polymers for membrane applications, Journal of membrane science 427 (2013) 186-196.

[73] A.R. Khare, N.A. Peppas, Swelling/deswelling of anionic copolymer gels, Biomaterials 16(7) (1995) 559-567.

[74] P.J. Flory, Thermodynamics of high polymer solutions, The Journal of chemical physics 10(1) (1942) 51-61.

Chapter 3: Materials and Experimental Methods

The following sections detail the materials and experimental methods utilized in performing the research in this dissertation. Additional background details for the experimental methods used are also included to provide motivation, context, and scientific understanding of the methods.

3.1. Materials

Sodium chloride (NaCl), lithium chloride (LiCl), potassium chloride (KCl), magnesium chloride ($MgCl_2$), ammonium chloride (NH_4Cl, ≥ 99.5%), and calcium chloride ($CaCl_2$) were obtained from VWR (Radnor, PA, USA). Sodium hydroxide beads (NaOH), potassium acetate (KOAc, ≥ 99.0%), potassium chromate (K_2CrO_4, 5% w/v), and silver nitrate ($AgNO_3$, 1 M) were procured from British Drug Houses (Poole, UK). Selemion® AMVN membranes were purchased from AGC Engineering Co. (Tokyo, Japan), while Fumasep FAA-3-50 (FAA) membranes were sourced from FuMA-Tech (St. Ingbert, Germany). Methanol (MeOH, ≥ 99.9%), ethanol (EtOH, ≥ 99%), poly(ethylene glycol) diacrylate (PEGDA, n = 13 and n = 10), 2-acrylamido-2-methyl-1-propanesulfonic acid (AMPS, 99%), (3-acrylamidopropyl)trimethylammonium chloride solution (APTA, 75 wt.% in water), phenoxyethyl acrylate (PEA, n = 1), poly(ethylene glycol) phenyl ether acrylate (PEGPEA, n = 3), [2-(Acryloyloxy)ethyl]trimethylammonium chloride (AETAC, ~80% in water), 3-sulfopropyl acrylate potassium salt (SPAK), 3-sulfopropyl methacrylate potassium

salt (SPMAK), hydrochloric acid (HCl), potassium hydroxide (KOH), sulfobetaine methacrylate (SBMA), 2-methyl-2-propene-1-sulfonic acid sodium salt (MPS), and 2,2′-azobis(2-methylpropionitrile) (AIBN, 98%) were supplied by Sigma-Aldrich Chemicals (St. Louis, MO, USA). Dimethyl sulfoxide (DMSO, ≥ 99.9%) was obtained from Macron Fine Chemicals (Radnor, PA). Sodium formate (NaOFm, ≥ 99%) was purchased from Alfa Aesar (Haverhill, MA), and phenyl acrylate (PA, 97%) was sourced from Ambeed (Arlington Heights, IL). Phenyl methacrylate (PMA, > 97%), nickel chloride ($NiCl_2$), methacroylcholine chloride (MACC, ~80% in water), N,N'-methylenebisacrylamide (MBAA, > 98%), 2-(Methacryloyloxy)ethyl trimethylammonium chloride (MAETAC, ~80% in water), and 1-hydroxycyclohexyl phenyl ketone (HCPK) were procured from TCI (Tokyo, Japan). Sodium acetate (NaOAc, ≥ 99%) was obtained from ACS Chemical Inc. (Point Pleasant, NJ), while potassium formate (KOFm, ≥ 98%) was purchased from BeanTown Chemical (Hudson, NH). Potassium bicarbonate ($KHCO_3$, ≥ 98%) was sourced from Ward's Science. Type-1 deionized water (18.2 MΩ·cm at 25 °C, 1.2 ppb TOC) was produced using a Waterpro BT Purification System from Labconco® (Kansas City, MO). Feeler gauges (205 μm spacers) and glass plates (5" × 5" × 0.25") were obtained from McMaster-Carr (Elmhurst, IL).

3.2. Synthesis of Polymer Membranes

Membranes can be manufactured using various techniques, such as phase inversion and radical polymerization, each offering distinct advantages and limitations. A common approach to synthesizing IEMs involves a two-step process, where a hydrophobic cross-linked polymer is first synthesized, followed by the introduction of fixed charge groups onto the polymer backbone [1].

However, this method complicates the independent adjustment of membrane properties like water content and fixed charge concentration because the addition of charged groups generally increases the hydrophilicity and water uptake of the membrane [2-4], driven by the favorable interactions between charged groups and polar water molecules [5]. And high degree of functionalization can result in excessive swelling and water uptake, ultimately reducing the polymer's mechanical strength [4-7]. Using a one-step synthesis procedure can address this issue. However, a key challenge in one-step synthesis is achieving compatibility between the charged monomer and the crosslinker. Charged monomers are typically highly hydrophilic, while crosslinkers are often more hydrophobic, leading to heterogeneous pre-polymerization solutions and, during polymerization, may cause phase separation. Additionally, the choice of solvent, crosslinker, and charged monomer plays a critical role in determining the membrane's physiochemical properties. For instance, higher solvent content in the pre-polymerization solution tends to create void spaces in the membrane structure [8, 9]. Increasing crosslinker content increases the crosslink density, which reduces water uptake and limits swelling [9-12]. Thus, optimizing these parameters is essential for achieving the desired balance of membrane properties. All the membranes in this dissertation were synthesized using a one-step synthesis procedure.

3.2.1. UV Photopolymerization

In this dissertation, the membranes discussed in Chapters 4 and 5 were synthesized using free radical UV photocrosslinking, using HCPK at 0.1 wt% relative to the total amount of crosslinker and monomer as the photoinitiator. Figure 3.1 shows the membrane synthesis process. The pre-polymerization mixtures were sonicated for 30 minutes to ensure a homogeneous solution

and then sandwiched between two quartz plates (5 × 5 × 1/4") separated by spacers with a thickness of 305 μm. This assembly was placed inside a UV crosslinking oven (Spectrolinker™ XL-1500, Spectroline, Westbury, NY) and exposed to 254 nm UV light for 3 minutes at an intensity of 3.0 mW/cm². After crosslinking, the resulting films, matching the thickness of the spacers, were carefully removed and immersed in 1 liter of deionized (DI) water for 2 days. The DI water was replaced daily to ensure equilibrium was attained. This step was performed to exchange the solvent and remove any residual monomers before further use.

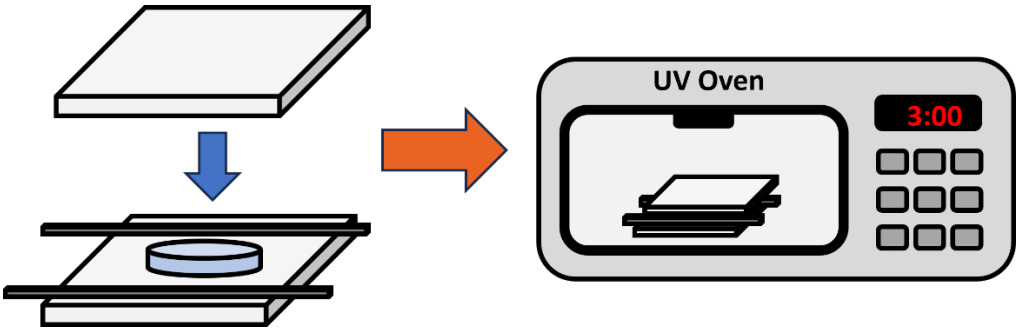

Figure 3.1. Schematic depiction of the membrane synthesis process.

In Chapter 4, we synthesize one neutral membrane and two AEMs through UV copolymerization, as detailed in Table 3.1.

Table 3.1. Membrane properties from pre-polymerization mixtures in Chapter 4.

	APTA[1] (mol%)	PEGDA (g)	APTA (g)	Water (g)	HCPK (g)
A0	0	8.00	0.00	2.00	0.008
A8	8	7.80	0.20	2.00	0.008
A12	12	7.69	0.31	2.00	0.008

[1] APTA = mol of APTA/(mol of PEGDA + mol of APTA) × 100 %

In Chapter 5, we synthesized five neutral membranes and seven CEMs using UV copolymerization, as detailed in Table 3.2.

Table 3.2. Membrane characteristics from pre-polymerization mixtures in Chapter 5.

	SPMAK[a] (mol %)	E or G[b] (mol %)	PEGDA (g)	SPMAK (g)	E or G[b] (g)	Water (g)	HCPK (g)
1. P	-	-	8.00	-	-	2.00	0.008
2. P-S16	16	-	7.50	0.50	-	2.00	0.008
3. P-S24	24	-	7.20	0.80	-	2.00	0.008
4. P-S32	32	-	6.86	1.14	-	2.00	0.008
5. P-E16	-	16	7.60	-	0.40	2.00	0.008
6. P-E32	-	32	7.08	-	0.92	2.00	0.008
7. P-G16	-	16	7.35	-	0.65	2.00	0.008
8. P-G32	-	32	6.57	-	1.43	2.00	0.008
9. P-S16/E16	16	16	6.97	0.58	0.45	2.00	0.008
10. P-S24/E8	24	8	6.92	0.86	0.22	2.00	0.008
11. P-S16/G16	16	16	6.71	0.56	0.73	2.00	0.008
12. P-S24/G8	24	8	6.79	0.84	0.37	2.00	0.008

[a]SPMAK = mol of SPMAK/(mol of PEGDA + mol of SPMAK + mol of E or G) × 100 %
[b]E or G = mol of E or G/(mol of PEGDA + mol of SPMAK + mol of E or G) × 100 %

3.2.2. Thermal Polymerization

In this dissertation, the membranes described in Chapters 6 through 11 were synthesized via thermal copolymerization, using AIBN at 0.1 wt% relative to the total amount of crosslinker and monomer as the thermal initiator. The monomer, crosslinker, and charge monomer were combined and sonicated for approximately 30 minutes to achieve homogeneous mixtures. The pre-polymerization solution was then sandwiched between two glass plates separated by spacers with a thickness of 205 μm and placed in an oven at 65 °C for 24 hours to facilitate the polymerization of the monomer and crosslinker. After polymerization, the glass plates were carefully separated, and the resulting polymer films were immersed in 1 liter of DI water for at least 48 hours before any subsequent characterization. The DI water was replaced daily to ensure equilibrium was

reached. This process was essential for solvent exchange and the removal of any residual monomers before further use.

In Chapter 6, we synthesize two AEMs using either AETAC or MAETAC and two CEMs using SPAK and SPMAK through thermal copolymerization, as detailed in Table 3.3

Table 3.3. Pre-polymerization mixture compositions in Chapter 6.

Name	PA (mol%)	MBAA (mol%)	Charge monomer (mol%)
PA/A	49	30	21
PA/MA	49	30	21
PA/S	49	30	21
PA/SM	49	30	21

In Chapter 7, we prepared six zwitterionic membranes through thermal copolymerization, as detailed in Table 3.4.

Table 3.4. Pre-polymerization mixture compositions in Chapter 7.

Membrane	PA (mol%)	SBMA (mol%)	MBAA [1] (mol%)
S20-10	80	20	10
S20-20	80	20	20
S30-10	70	30	10
S30-20	70	30	20
S40-10	60	40	10
S40-20	60	40	20

[1] MBAA = mol of MBAA/ (mol of PA + mol of SBMA) × 100%

In Chapter 8, we synthesized three PEGDA-crosslinked membranes and three MBAA-crosslinked membranes through thermal copolymerization, as detailed in Table 3.5

Table 3.5. Pre-polymerization mixtures compositions in Chapter 8.

	APTA (mol%)	PEGDA (mol%)	PA (mol%)
A0/P20	0	20	80
A8/P12	8	12	80
A12/P8	12	8	80
	APTA (mol%)	**MBAA (mol%)**	**PA (mol%)**
A0/M20	0	20	80
A8/M12	8	12	80
A12/M8	12	8	80

In Chapter 9, we synthesized one neutral membrane and eight CEMs through thermal copolymerization, as detailed in Table 3.6.

Table 3.6. Pre-polymerization mixtures compositions in Chapter 9.

Name	PA (mol%)	PEGDA (mol%)	SPMAK (mol%)
PA80P10S10	80	10	10
PA80P15S5	80	15	5
PA90P5S5	90	5	5
PA85P10S5	85	10	5
Name	**PA (mol%)**	**PEGDA (mol%)**	**MPS (mol%)**
PA80P10M10	80	10	10
PA80P15M5	80	15	5
PA90P5M5	90	5	5
PA85P10M5	85	10	5
PA80P20	80	20	0

In Chapter 10, we synthesized one neutral membrane and six AEMs through thermal copolymerization, as detailed in Table 3.7.

Table 3.7. Composition of Pre-polymerization mixtures in Chapter 10.

Name	PA (mol%)	MBAA (mol%)	APTA (mol%)	DMSO (wt%)
P55M20AP25	55	20	25	42
P65M15AP20	65	15	20	45
P80M10AP10	80	10	10	60
Name	**PA (mol%)**	**MBAA (mol%)**	**AETAC (mol%)**	**DMSO (wt%)**
P55M20AE25	55	20	25	50
P65M15AE20	65	15	20	59
P80M10AE10	80	10	10	62
P80M20	80	20	0	69

Table 3.8. Membrane characteristics from pre-polymerization mixtures in Chapter 11.

Cation Exchange Membranes

Name	MBAA[a] (mol%)	AMPS[b] (mol%)	PA or PMA (g)	AMPS (g)	AIBN (g)	MBAA (g)	DMSO (g)
PA/A-5	5	30	1.492	0.894	0.003	0.111	2.500
PA/A-10	10	30	1.428	0.856	0.003	0.212	2.500
PA/A-20	20	30	1.317	0.789	0.003	0.391	2.500
PA/A-30	30	30	1.221	0.732	0.002	0.545	2.500
PMA/A-5	5	30	1.541	0.844	0.003	0.112	2.500
PMA/A-10	10	30	1.475	0.808	0.003	0.214	2.500
PMA/A-20	20	30	1.359	0.744	0.003	0.394	2.500
PMA/A-30	30	30	1.260	0.690	0.002	0.547	2.500

Anion Exchange Membranes

Name	MBAA[a] (mol%)	MACC[c] (mol%)	PA or PMA (g)	MACC (g)	AIBN (g)	MBAA (g)	DMSO (g)	Water[d] (g)
PA/M-5	5	30	1.491	0.896	0.003	0.111	2.276	0.224
PA/M-10	10	30	1.427	0.858	0.003	0.212	2.286	0.214
PA/M-20	20	30	1.316	0.790	0.003	0.391	2.302	0.198
PA/M-30	30	30	1.220	0.733	0.002	0.544	2.317	0.183
PMA/M-5	5	30	1.540	0.845	0.003	0.112	2.289	0.211
PMA/M-10	10	30	1.474	0.809	0.003	0.214	2.298	0.202
PMA/M-20	20	30	1.358	0.745	0.003	0.394	2.314	0.186

[a]MBAA = mol of MBAA/(mol of PA or PMA + mol of AMPS or MACC) × 100 %
[b]AMPS = mol of AMPS/(mol of PA or PMA + mol of AMPS) × 100 %
[c]MACC = mol of MACC/(mol of PA or PMA + mol of MACC) × 100 %
[d]Water, from the MACC solution as 20 % of the solution is water.

3.3. Membrane Characterization

Membrane characterization is essential for understanding and optimizing membrane performance in various applications. By analyzing key properties such as water content, ion exchange capacity, mechanical strength, thermal stability, permeability, and solubility, we can evaluate how well a membrane meets the requirements of a specific process. Moreover, characterization provides insights into the relationship between the membrane's structure, physiochemical, and transport behavior, enabling the fine-tuning of parameters like water content, crosslink density, fixed charge concentration, and hydrophilicity to achieve desired outcomes. Through comprehensive characterization, membranes can be tailored to enhance efficiency, durability, and compatibility with their intended operational environments, ensuring reliable and sustainable solutions for separation, filtration, or electrochemical applications.

3.3.1. Water Content and Polymer Density

Water uptake, represented as ω_w, is a critical parameter for evaluating the transport capacity of a membrane [13, 14]. It is largely influenced by the free volume within the membrane, which consists of the voids between polymer chains. These voids result from the inefficient packing of polymer chains in amorphous, non-crystalline structures, enabling water absorption and solute transport. Water uptake is defined as the amount of water absorbed per gram of dry membrane and was measured using a gravimetric method. A hole punch with a 0.75-inch diameter was used to cut the hydrated films.

$$\omega_w = \frac{W_s - W_d}{W_d} \times 100\% \quad (3.1)$$

Where W_s represents the mass of the hydrated membrane, measured after briefly blotting it with tissue paper, while W_d denotes the mass of the dry membrane, taken after the membrane was dried under a vacuum at 50°C for 24 hours [15, 16]. The masses of the hydrated and dried membranes are used to calculate both water uptake and water volume fraction. However, water uptake cannot accurately explain transport behavior, as it fails to consider the role of polymer density. The water volume fraction addresses this limitation by incorporating the membrane's density into the calculation. For example, two membranes with the same water uptake but the membrane with higher density will exhibit greater transport ability than the membrane with lower density because it has a higher water uptake per unit volume. Similarly, for hydrated membranes with identical volumes, a reduction in polymer density, caused by disruptions in chain packing, can lead to a corresponding decrease in the water volume fraction [17, 18]. The water volume fraction, which represents the ratio of water volume to the total volume of the hydrated polymer, is a widely used metric for evaluating a membrane's transport capacity. This parameter provides a clear indication of the free volume available within a hydrated membrane. Its calculation, denoted as $\emptyset_w$, incorporates the volumes of both water and polymer, taking into account the membrane's water uptake and density properties.

$$\emptyset_w = \frac{(W_s - W_d)/\rho_w}{(W_s - W_d)/\rho_w + W_d/\rho_p} \tag{3.2}$$

Where ρ_w represents the density of water, and ρ_p represents the density of the dry polymer. The dry polymer density was determined using the buoyancy method with a density kit (ML-DNY-43, Mettler Toledo) coupled with a scale (ML204T, Mettler Toledo) [12, 16, 19]

$$\rho_p = (\rho_w - \rho_0)\left(\frac{W_0}{W_0 - W_L}\right) + \rho_0 \tag{3.3}$$

The symbol W_A represents the mass of the sample measured in the auxiliary liquid, with W_A denoting the density of the auxiliary liquid at the measurement temperature, and ρ_0 indicating the density of air (1.225 kg/m³) [15, 16].

3.3.2. Dimensional Swelling

The volume ratio between hydrated and dry films was calculated using the photograph-caliper method at 25 °C. Circular samples, 19 mm in diameter, were prepared for the measurements. The surface area of each film was determined from digital photographs analyzed with ImageJ software, while the thickness was measured with a digital caliper, averaging readings taken at three random points. The membranes were then dried in a vacuum oven at 50 °C for 24 hours, after which their surface area and thickness were re-measured in the dry state. Dimensional swelling was subsequently calculated based on these measurements.

$$\frac{V_H}{V_D} \tag{3.4}$$

Where V_H represents the volume of hydrated membrane, and V_D represents the volume of dry membrane. Moreover, the membrane deswelling ratio (volume of the membrane after immersion in the target solution/volume of the hydrated membrane) between the hydrated membrane and the membrane after the solubility experiment was determined at 25 °C. Circular samples with a diameter of 19 mm were prepared for the solubility experiment. The surface area of each sample was measured using digital photographs analyzed with ImageJ software, while the thickness was recorded using a digital caliper, averaging measurements from three random points. Following the

solubility experiment, the membranes' surface area and thickness were re-measured, and dimensional swelling was calculated.

3.3.3. Ion Exchange Capacity

Ion exchange capacity (IEC), commonly expressed in milliequivalents (meq) of fixed charge per gram of dry polymer [1, 6, 12, 16], can represent the degrees of functionalization and the concentration of fixed charge groups, serving as a measure of charge monomer content per unit mass. For CEMs, IEC is typically determined using titration methods [20-22], whereas the Mohr method [23, 24] is employed for AEMs.

For CEMs, the membranes were first dried in a vacuum oven at 50°C for 24 hours until a stable dry weight (W_d) was obtained. The dried membranes were then immersed in a 1M hydrochloric acid (HCl) solution for at least 48 hours to allow counterions to exchange with protons (H^+). Afterward, any excess HCl and counterions were removed by rinsing the membranes with DI water until the pH of the rinse water stabilized. The membranes were then submerged in a 1M sodium chloride solution for two days to facilitate the exchange of H^+ with Na^+ in the desorption solution. Subsequently, 3–5 drops of phenolphthalein indicator were added to the desorption solution, followed by dropwise titration with 0.1M NaOH until a stable pink endpoint was observed. The IEC was calculated as:

$$IEC = \frac{V_{NaOH} \times C_{NaOH}}{W_d} \tag{3.5}$$

where V_{NaOH} represents the volume of the NaOH solution added, and C_{NaOH} denotes its concentration.

For AEMs, the hydrated membranes were first dried in a vacuum oven at 50 °C for 24 hours, and the dry weight (W_d) of the films (~1.5 g) was recorded. The membranes in chloride form were then converted to the hydroxyl form by immersing them in a 1M NaOH solution for two days. The chloride ions released during this process were quantified through titration with a 0.1M $AgNO_3$ solution, using K_2CrO_4 (~5 mL) as an indicator. The $AgNO_3$ solution was added gradually until the solution exhibited a stable red-brown color. The IEC values were determined based on the amount of chloride ions released and were expressed in mmol per gram of dry membrane.

$$IEC = \frac{V_{AgNO_3} \times C_{AgNO_3}}{W_d} \tag{3.6}$$

where V_{AgNO_3} is the volume of $AgNO_3$ solution added, and C_{AgNO_3} is the concentration of the $AgNO_3$ solution.

3.3.4. Fixed Charge Concentration and Density

The fixed charge concentration, $C_A^{m,w}$ (mol of fixed charge per liter of water), and fixed charge density, $C_A^{m,p}$ (mol of fixed charge per liter of hydrated membrane), are key volumetric parameters used to evaluate the charge content in ion exchange membranes. The fixed charge concentration measures the charge content in relation to the volume of absorbed water, while the fixed charge density relates to the charge content relative to the total volume of the hydrated membrane. These parameters are calculated as below using the experimentally determined IEC, WU, and water volume fractions [25, 26]:

$$C_A^{m,w} = \frac{IEC \times \rho_w}{W_u} \tag{3.7}$$

$$C_A^{m,p} = C_A^{m,w} \times \emptyset_w \tag{3.8}$$

3.3.5. Ionic Conductivity

The conductivity of IEMs determines their ability to transport ions under an electric field. In electrochemical cells, such as fuel cells, IEMs conductivity is crucial for current flow, as ions must move between electrodes to maintain charge neutrality while electrons transfer. In-plane conductivity is measured using a four-point conductivity cell (BekkTech BT-110) at 25 ℃ coupled with a Gamry Interface 1000 potentiostat [27]. A rectangular piece of the membrane (1 x 0.5 cm) was cut and inserted into the conductivity cell, which was then immersed in 500 mL of DI water. Electrochemical impedance spectroscopy (EIS) was conducted after the open circuit potential stabilized (frequency: 10 Hz–1 MHz, AC voltage: 10 mV) [6, 12, 27, 28]. The EIS data was processed using Gamry Echem Analyst software, and the resistance, R, was determined from the Nyquist plot. The ionic conductivity, denoted as σ, was calculated as follows:

$$\sigma = \frac{L}{RWT} \tag{3.9}$$

where L, W, and T are the distance between two electrodes (0.5 cm), width, and thickness of the film, respectively.

3.3.6. Mechanical Properties

For most applications, membranes must possess strong mechanical stability to function effectively. The mechanical properties of the hydrated polymer films were evaluated at room temperature (~25 °C) using a commercial tensile testing device (DMA, TA Instruments RSA III).

The films, with a thickness of 0.2 mm, were cut into rectangular strips measuring 10 mm × 40 mm. The samples were mounted lengthwise between the clamps of the tensile testing machine, maintaining an initial gauge length of 10 mm. During testing, the upper clamp was moved upward at a constant deformation rate of 0.05 mm/s [15, 28]. Each composition was tested three times, and Young's modulus was determined from the initial slope of the stress-strain curves.

3.3.7. Crosslink Density

Crosslink density refers to the number of chemical bonds that link polymer chains together within a polymer network. It is commonly quantified in terms of moles of crosslinks per unit volume (mmol/cm³). Crosslink density is a key factor influencing the mechanical and thermal properties of the material, such as stiffness, elasticity, and resistance to deformation. Higher crosslink density typically results in a more rigid and less flexible material, while lower crosslink density leads to greater flexibility. The storage moduli (E') of the membrane were measured to estimate their crosslink densities [29, 30]. Membranes were prepared using 1 mm spacers. The films were first hydrated in DI water for at least 5 days and then freeze-dried for 24 hours. After drying, the films were cut into rectangular shapes (10×20 mm). The storage modulus of each film was measured using dynamic mechanical analysis (DMA, TA Instruments RSA III) at a heating rate of 1 °C/min, from 23 to 30 °C (the rubbery plateau), with a test frequency of 1 Hz. The crosslink density was calculated using Flory's rubber elasticity theory [31]:

$$V_e = \frac{E'}{3RT} \tag{3.10}$$

where E' is the storage modulus (Pa), R is the gas constant (8314 $cm^3 \cdot Pa/K \cdot mmol$), and T is the temperature (298.15 K).

3.3.8. Thermal Properties

The glass transition temperature (T_g) for a membrane refers to the temperature at which the polymer material transitions from a rigid, glassy state to a more flexible, rubbery state. It is a critical property that influences the membrane's mechanical, thermal, and transport behavior. Below the T_g, the membrane is typically brittle and less permeable, while above the T_g, it becomes more flexible, allowing for greater ion or molecule mobility. Thermal transitions were analyzed using a TA Instruments Q20 differential scanning calorimeter (DSC). Approximately 10 mg of each dried sample was weighed and placed in an aluminum pan. To eliminate any potential relaxation enthalpy, the sample was first heated to 180 °C (above the expected transition temperature) and then cooled to -70 °C. The samples were subsequently heated at a rate of 10 °C/min from -70 °C to 180 °C under a nitrogen flow of 50 mL/min. The T_g was identified as the midpoint of the step change in heat capacity.

3.3.9. Contact Angle

The static water contact angle is a key parameter for evaluating the hydrophilicity of material surfaces, offering insights into polymer solubility, partitioning behavior, and aggregation properties [32]. For this analysis, hydrated membrane samples were secured to glass plates using adhesive tape. A water droplet was carefully placed on each membrane surface, and images were captured for analysis. The contact angles were then measured using ImageJ software (National

Institutes of Health, Bethesda, MD, USA). A contact angle of 90 degrees or higher indicates a hydrophobic surface, while angles below 90 degrees signify a hydrophilic surface [33]. These measurements are crucial for understanding the interactions between membranes and water.

3.4. Counterion Exchange

In Chapter 4, the chloride (Cl^-) counterion in AEMs was exchanged for bicarbonate (HCO_3^-). Circular membranes were prepared using 0.75-inch and 1-inch hole punches (General Tools 1271 Arch Punches), with the smaller membrane designated for sorption-desorption experiments and the permeability experiments. The membranes were immersed in 1 M sodium bicarbonate ($NaHCO_3$) solution for two days, with the solution replaced daily to ensure sufficient driving force for ion exchange. The setup was gently stirred throughout the process [23]. Following ion exchange, the films were thoroughly rinsed with DI water and soaked in fresh DI water for another two days to remove residual Cl^- and $NaHCO_3$. The DI water was replaced daily, and a conductivity meter confirmed that the final solution's conductivity matched that of pure DI water ($\leq$18.2 mΩ·cm at 25 °C). The extent of ion exchange from Cl^- to HCO_3^- was determined using elemental analysis performed with a Zeiss EVO 50 scanning electron microscope (SEM) equipped with INCA energy-dispersive spectroscopy (EDS). Likewise, in Chapter 11, the chloride (Cl^-) counterion in PA/MACC-30 membranes and the bromide (Br^-) counterion in Fumasep® FAA-3-50 membranes were replaced with hydroxide (OH^-) through ion exchange using a 1 M KOH solution.

3.5. Transport Properties

3.5.1. Permeability

Salt permeability coefficients were determined using custom-built glass diffusion cells, as described in Section 2.3.3 and illustrated in Figure 2.7. A membrane sample was clamped between two glass diffusion cells. The feed cell contained 25 mL of single or binary target solute solution and concentration, while the downstream cell was filled with 25 mL of DI water. Magnetic stir bars ensured consistent mixing of the solutions throughout the experiment, and the temperature was maintained at 25 °C using a bath circulator. The solute concentration in the downstream cell was monitored over time using either an in-situ conductivity probe (PC820 Precision Benchtop, Apera Instruments, Schaumburg, IL, USA) for single-solute systems or an in-situ Attenuated Total Reflectance-Fourier Transform Infrared (ATR-FTIR) probe (Mettler-Toledo ReactIR™ 15 with a shallow-tip 9.5 mm DSun AgX DiComp probe) for alcohols and two-solute systems. The average salt permeability coefficient was calculated using Yasuda's model.

$$P_i = ln\left[1 - 2\frac{c_{il}(t)}{c_{io}(0)}\right]\left(\frac{-lV}{2At}\right) \tag{3.11}$$

where $c_{il}(t)$ represents the time-dependent concentration of solute i in the receiver cell, l is the membrane thickness measured post-experiment, $c_{io}(0)$ is the initial solute concentration in the feed cell, V denotes the volume of the half-cell (25 mL), A is the orifice area of the half-cell (1.1423 cm^2), and t refers to time. A calibration curve was constructed by measuring the conductivities of solutions with known salt concentrations, enabling the estimation of the downstream salt concentration from conductivity readings.

To calibrate the ATR-FTIR probe, specific wavenumbers (λ, cm^{-1}) were chosen for each solute, MeOH (1018 cm^{-1}), EtOH (1044 cm^{-1}), OFm^- (1350 cm^{-1}), and OAc^- (1414 cm^{-1}), based on their absorbance spectra to ensure optimal peak separation and sensitivity to concentration changes. Solutions with varying concentrations of each solute were prepared, and their absorbance values at the specified wavenumbers were measured, as illustrated in Figure 3.2 [34]. To correct for any interference caused by co-solutes, absorbance values for the co-solutes at the corresponding wavenumbers were also recorded, as shown in Figure 3.3 [34]. Finally, the molar absorptivity ($\varepsilon_{i,\lambda}$) for each solute at its specific wavenumber was calculated using the Beer-Lambert law[35].

$$A_\lambda = \sum_{i=1}^{n} \varepsilon_{i,\lambda} c_i \tag{3.12}$$

where A_λ denotes the absorbance intensity at a specific wavenumber, $\varepsilon_{i,\lambda}$ represents the molar absorptivity of solute i at that wavenumber, and c_i is the concentration of solute i. Thus, the solute's absorptivity (slop) is determined from the plot of absorbance versus concentration.

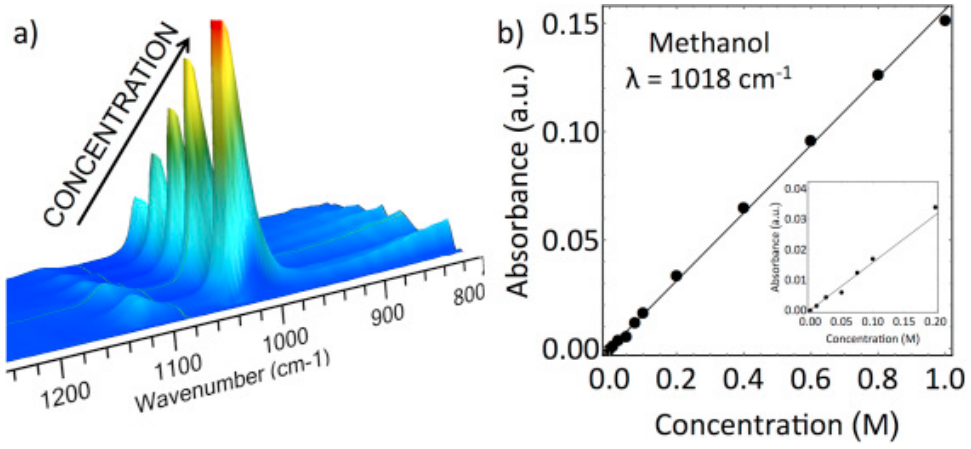

Figure 3.2. a) ATR-FTIR spectra of methanol at varying concentrations, and b) the linear least-squares regression of absorbance against concentration at 1018 cm^{-1}. The error bars in the figure are smaller than the symbols representing the data points[34].

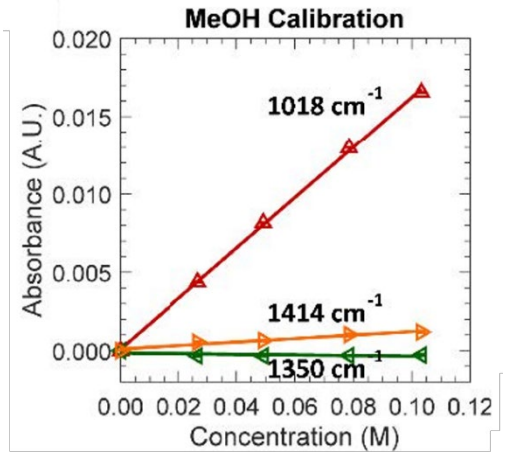

Figure 3.3. An example of ATR-FTIR absorbance as a function of MeOH concentration at wavenumbers 1018 cm^{-1} (△, red), 1044 cm^{-1} (▽, blue), 1350 cm^{-1} (◁, green), and 1414 cm^{-1} (▷, yellow).

To determine the concentration of the solution measured by ATR-FTIR, the time-resolved absorbances were obtained from the receiver cell solution and converted to concentration using the molar absorptivities. Additionally, for binary solute transport, both solutes' absorbances must be considered at the selected wavenumber. Here we use methanol and sodium acetate as an example.

$$A_{1018} = \varepsilon_{1018,m} c_m + \varepsilon_{1018,a} c_a \tag{3.13}$$

$$A_{1414} = \varepsilon_{1414,m} c_m + \varepsilon_{1414,a} c_a \tag{3.14}$$

where A_{1018} and A_{1414} represent the measured absorbance at the wavelengths 1018 cm^{-1} and 1414 cm^{-1} for MeOH and NaOAc, $\varepsilon_{1018,m}$ and $\varepsilon_{1018,a}$ are the effective molar absorptivities for MeOH and NaOAc at the wavelength 1018 cm^{-1}, $\varepsilon_{1414,a}$ and $\varepsilon_{1414,m}$ are the effective molar absorptivities for NaOAc and MeOH at the wavelength 1414 cm^{-1}, and c_m and c_a are the

concentrations of MeOH and NaOAc, respectively. Therefore, the concentrations of MeOH and NaOAc are calculated as follows:

$$c_m = \frac{A_{1018} - \frac{\varepsilon_{1018,a} A_{1414}}{\varepsilon_{1414,a}}}{\varepsilon_{1018,m} - \frac{\varepsilon_{1018,a} \varepsilon_{1414,m}}{\varepsilon_{1414,a}}} \tag{3.15}$$

$$c_m = \frac{A_{1414} - \frac{\varepsilon_{1414,m} A_{1018}}{\varepsilon_{1018,m}}}{\varepsilon_{1414,a} - \frac{\varepsilon_{1414,m} \varepsilon_{1018,a}}{\varepsilon_{1018,m}}} \tag{3.16}$$

3.5.2. Solubility

To evaluate the solubility of various salts in membranes, a previously described sorption-desorption method was employed [6, 15, 19]. Membrane films were prepared by cutting them into discs using a 19 mm diameter hole punch, followed by quick blotting with tissue paper. As shown in Figure 3.4, the prepared films were immersed in a single or binary solute solution of the target salt at a known concentration for at least three days. Each solution was prepared in triplicate, with the solution being replaced daily. The thickness of the films was measured at three random points on the film surface using a digital caliper, while their area was determined using ImageJ software from captured photographs. After immersion, the membranes were wiped dry and transferred to a desorption solution (10 mL of deionized water) for at least three days. The salt concentration in the desorption solution was determined using conductivity measurements or high-performance liquid chromatography (HPLC) equipped with a refractive index detector and an Aminex HPX-87H column (Bio-Rad, CA). The solubility (K_i) was then calculated based on these measurements.

$$K_i = \frac{C_i^m}{C_i^s} \tag{3.17}$$

The solute concentration in the sorption solution is denoted by C_i^s, while the solute concentration within the film (C_i^m) is calculated based on the solute concentration in the desorption solution and the volume of the film.

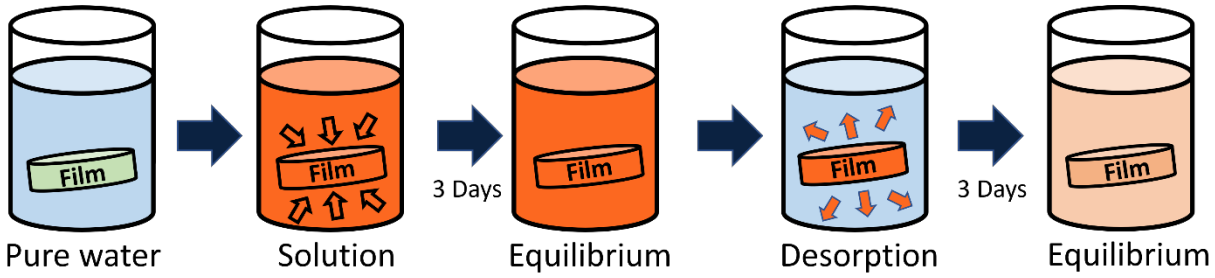

Figure 3.4. Schematic diagram of sorption-desorption experiment.

3.6. References

[1] F.G. Helfferich, Ion exchange, Courier Corporation1995.

[2] W. Xie, J. Cook, H.B. Park, B.D. Freeman, C.H. Lee, J.E. McGrath, Fundamental salt and water transport properties in directly copolymerized disulfonated poly (arylene ether sulfone) random copolymers, Polymer 52(9) (2011) 2032-2043.

[3] G. Geise, B. Freeman, D. Paul, Characterization of a sulfonated pentablock copolymer for desalination applications, Polymer 51(24) (2010) 5815-5822.

[4] R. Weiss, A. Sen, L. Pottick, C. Willis, Block copolymer ionomers: 2. Viscoelastic and mechanical properties of sulphonated poly (styrene-ethylene/butylene-styrene), Polymer 32(15) (1991) 2785-2792.

[5] G.M. Geise, D.R. Paul, B.D. Freeman, Fundamental water and salt transport properties of polymeric materials, Progress in Polymer Science 39(1) (2014) 1-42.

[6] J.M. Kim, Y.-H. Lin, P.P. Aravindhan, B.S. Beckingham, Impact of hydrophobic pendant phenyl groups on transport and co-transport of methanol and acetate in PEGDA-SPMAK cation exchange membranes, Chemical Engineering Research and Design 185 (2022) 418-429.

[7] M. Paul, H.B. Park, B.D. Freeman, A. Roy, J.E. McGrath, J. Riffle, Synthesis and crosslinking of partially disulfonated poly (arylene ether sulfone) random copolymers as candidates for chlorine resistant reverse osmosis membranes, Polymer 49(9) (2008) 2243-2252.

[8] H. Ju, A.C. Sagle, B.D. Freeman, J.I. Mardel, A.J. Hill, Characterization of sodium chloride and water transport in crosslinked poly (ethylene oxide) hydrogels, Journal of Membrane Science 358(1-2) (2010) 131-141.

[9] H. Ju, B.D. McCloskey, A.C. Sagle, V.A. Kusuma, B.D. Freeman, Preparation and characterization of crosslinked poly (ethylene glycol) diacrylate hydrogels as fouling-resistant membrane coating materials, Journal of Membrane Science 330(1-2) (2009) 180-188.

[10] S.K. Bajpai, S. Singh, Analysis of swelling behavior of poly (methacrylamide-co-methacrylic acid) hydrogels and effect of synthesis conditions on water uptake, Reactive and Functional Polymers 66(4) (2006) 431-440.

[11] L.M. Robeson, The upper bound revisited, Journal of membrane science 320(1-2) (2008) 390-400.

[12] J.M. Kim, Y. Wang, Y.-h. Lin, J. Yoon, T. Huang, D.-J. Kim, M.L. Auad, B.S. Beckingham, Fabrication and Characterization of Cross-Linked Phenyl-Acrylate-Based Ion Exchange

Membranes and Performance in a Direct Urea Fuel Cell, Industrial & Engineering Chemistry Research 60(41) (2021) 14856-14867.

[13] G.M. Geise, H.S. Lee, D.J. Miller, B.D. Freeman, J.E. McGrath, D.R. Paul, Water purification by membranes: the role of polymer science, Journal of Polymer Science Part B: Polymer Physics 48(15) (2010) 1685-1718.

[14] H. Yasuda, C. Lamaze, L. Ikenberry, Permeability of solutes through hydrated polymer membranes. Part I. Diffusion of sodium chloride, Die Makromolekulare Chemie: Macromolecular Chemistry and Physics 118(1) (1968) 19-35.

[15] Y.-h. Lin, J.M. Kim, B.S. Beckingham, Salt Transport in Crosslinked Hydrogel Membranes Containing Zwitterionic Sulfobetaine Methacrylate and Hydrophobic Phenyl Acrylate, Polymers 15(6) (2023) 1387.

[16] J.M. Kim, Y.-h. Lin, B. Hunter, B.S. Beckingham, Transport and co-transport of carboxylate ions and ethanol in anion exchange membranes, Polymers 13(17) (2021) 2885.

[17] H. Luo, J. Aboki, Y. Ji, R. Guo, G.M. Geise, Water and salt transport properties of triptycene-containing sulfonated polysulfone materials for desalination membrane applications, ACS applied materials & interfaces 10(4) (2018) 4102-4112.

[18] K. Chang, H. Luo, S.M. Bannon, S.Y. Lin, W.-A.S. Agata, G.M. Geise, Methoxy groups increase water and decrease salt permeability properties of sulfonated polysulfone desalination membranes, Journal of Membrane Science 630 (2021) 119298.

[19] B.M. Dobyns, J.M. Kim, B.S. Beckingham, Multicomponent transport of methanol and sodium acetate in poly (ethylene glycol) diacrylate membranes of varied fractional free volume, European Polymer Journal 134 (2020) 109809.

[20] X.C. Chen, J.B. Kortright, N.P. Balsara, Water uptake and proton conductivity in porous block copolymer electrolyte membranes, Macromolecules 48(16) (2015) 5648-5655.

[21] C. Menictas, M. Skyllas-Kazacos, T.M. Lim, Advances in batteries for medium and large-scale energy storage: types and applications, Elsevier2014.

[22] T.M. Lim, M. Ulaganathan, Q. Yan, Advances in membrane and stack design of redox flow batteries (RFBs) for medium-and large-scale energy storage, Advances in Batteries for Medium and Large-Scale Energy Storage, Elsevier2015, pp. 477-507.

[23] T. Xua, Z. Liub, W. Yanga, Fundamental studies of a new series of anion exchange membranes: membrane prepared from poly (2, 6-dimethyl-1, 4-phenylene oxide)(PPO) and triethylamine, Journal of Membrane Science 249(1-2) (2005) 183-191.

[24] F. Karas, J. Hnát, M. Paidar, J. Schauer, K. Bouzek, Determination of the ion-exchange capacity of anion-selective membranes, International journal of hydrogen energy 39(10) (2014) 5054-5062.

[25] D. Kitto, J. Kamcev, The need for ion-exchange membranes with high charge densities, Journal of Membrane Science 677 (2023) 121608.

[26] J.C. Díaz, J. Park, A. Shapiro, H. Patel, L. Santiago-Pagán, D. Kitto, J. Kamcev, Understanding Monovalent Cation Diffusion in Negatively Charged Membranes and the Role of Membrane Water Content, Macromolecules 57(5) (2024) 2468-2481.

[27] J.M. Kim, B.M. Dobyns, R. Zhao, B.S. Beckingham, Multicomponent transport of methanol and acetate in a series of crosslinked PEGDA-AMPS cation exchange membranes, Journal of Membrane Science 614 (2020) 118486.

[28] J.M. Kim, Y.-h. Lin, S.M. Bannon, G.M. Geise, B.S. Beckingham, Improved Structural Stability of Charged Hydrogels under Organic CO2 Reduction Products: Effect of Acrylate and Methacrylate Backbone Linkages, The Journal of Physical Chemistry C 127(22) (2023) 10826-10832.

[29] E.-S. Jang, J. Kamcev, K. Kobayashi, N. Yan, R. Sujanani, T.J. Dilenschneider, H.B. Park, D.R. Paul, B.D. Freeman, Influence of water content on alkali metal chloride transport in cross-linked Poly (ethylene glycol) Diacrylate. 1. Ion sorption, Polymer 178 (2019) 121554.

[30] S. Kalakkunnath, D.S. Kalika, H. Lin, B.D. Freeman, Segmental relaxation characteristics of cross-linked poly (ethylene oxide) copolymer networks, Macromolecules 38(23) (2005) 9679-9687.

[31] P.J. Flory, Principles of polymer chemistry, Cornell university press1953.

[32] J.C. Foster, I. Akar, M.C. Grocott, A.K. Pearce, R.T. Mathers, R.K. O'Reilly, 100th anniversary of macromolecular science viewpoint: The role of hydrophobicity in polymer phenomena, ACS Macro Letters 9(11) (2020) 1700-1707.

[33] A.W. Adamson, A.P. Gast, Physical chemistry of surfaces, Interscience publishers New York1967.

[34] B.S. Beckingham, N.A. Lynd, D.J. Miller, Monitoring multicomponent transport using in situ ATR FTIR spectroscopy, Journal of Membrane Science 550 (2018) 348-356.

[35] Beer, Bestimmung der Absorption des rothen Lichts in farbigen Flüssigkeiten, Annalen der Physik 162(5) (1852) 78-88.

Chapter 4: Single and Co-transport of Ethanol and Carboxylate in AEMs

---

Reproduced from: J.M. Kim, Y. Lin, B. Hunter, B.S. Beckingham, Transport and Co-Transport of Carboxylate Ions and Ethanol in Anion Exchange Membranes, Polymers. 13 (2021) 2885. https://doi.org/10.3390/polym13172885.

4.1. Introduction

Anion exchange membranes (AEM [1, 2]) are a crucial component of devices for various applications, including direct ethanol fuel cells [3], direct urea fuel cells [4], water purification devices [5], water electrolyzers [6], CO_2 electrolyzers [7] and photoelectrochemical CO_2 reduction cells (PEC-CRC) [8-12]. Of particular interest here are PEC-CRCs, which utilize solar power to reduce CO_2 to various chemicals [13, 14], such as methanol (MeOH), ethanol (EtOH), formate (OFm^-), and acetate (OAc^-). Major roles of the AEM in such devices are to provide preferential ion transport (i.e., hydroxide (OH^- and anionic electrolytes (bicarbonates, $HCO3^-$) [15, 16]) with membrane-bound, charged functional groups (i.e., quaternary ammonium (QA^+) for AEMs) and to minimize the permeation of CO_2 reduction products to the anode chamber, as they readily oxidize back to CO_2 and by-products [11, 12]. While the majority of ion exchange membranes (IEM [17-20]) designed for PEC-CRCs have focused on AEMs, one of the major drawbacks of AEMs for such devices is their high diffusibility for negatively charged CO_2 reduction products (OFm^- and OAc^-). To avoid this issue, our group has performed a series of investigations to gain a

fundamental understanding of cation exchange membranes (CEM [21-24]) for PEC-CRCs, such as how the presence of a series of charge-neutral comonomers (acrylic acid, hydroxyethyl methacrylate and poly(ethylene glycol) methacrylate (PEGMA) [25, 26]) or how the presence of co-diffusing neutral CO_2 reduction products (alcohols) can act to impact and, in some cases, mitigate the permeation of CO_2 reduction products (carboxylates) [27-32]); see Figure 4.1 A, D. In the case of Nafion® 117 (a commercial CEM) and PEGDA-AMPS (a crosslinked CEM that we prepared by incorporating 2-acrylamido-2- methyl-1-propanesulfonic acid (AMPS, sulfonate-containing ionomer) with a crosslinker, poly(ethylene glycol) diacrylate (PEGDA)), both OFm^- and OAc^- diffusivities were increased in co-diffusion with either MeOH or EtOH, where we conjectured a potential charge screening by co-diffusing alcohol [32]. In the case of PEGDA-AMPS CEMs, which also incorporated a charge-neutral comonomer (PEGDA-AMPS/AA/HEMA, and/PEGMA) into the structure, the OAc^- diffusivities in PEGDA-AMPS/PEGMA and/HEMA were increased (as in comonomer-free PEGDA-AMPS films) [28]. However, those of PEGDA-AMPS/ PEGMA were the same [28] or slightly decreased in co-diffusion with MeOH, where we conjectured a potential charge screening by long pendant chains.

Here, to further investigate multicomponent transport behavior [33] in IEMs, we perform an analogous investigation on a series of AEMs, Selemion® AMVN (AMVN) and PEGDA-APTA (A8 and A12). AMVN is a commercial AEM and PEGDA-APTA is a crosslinked AEM that we prepare by incorporating (3-acrylamidopropyl) trimethylammonium chloride (APTA, QA+-containing ionomer) with a crosslinker, PEGDA [28, 30, 34, 35]; see Figure 4.2.

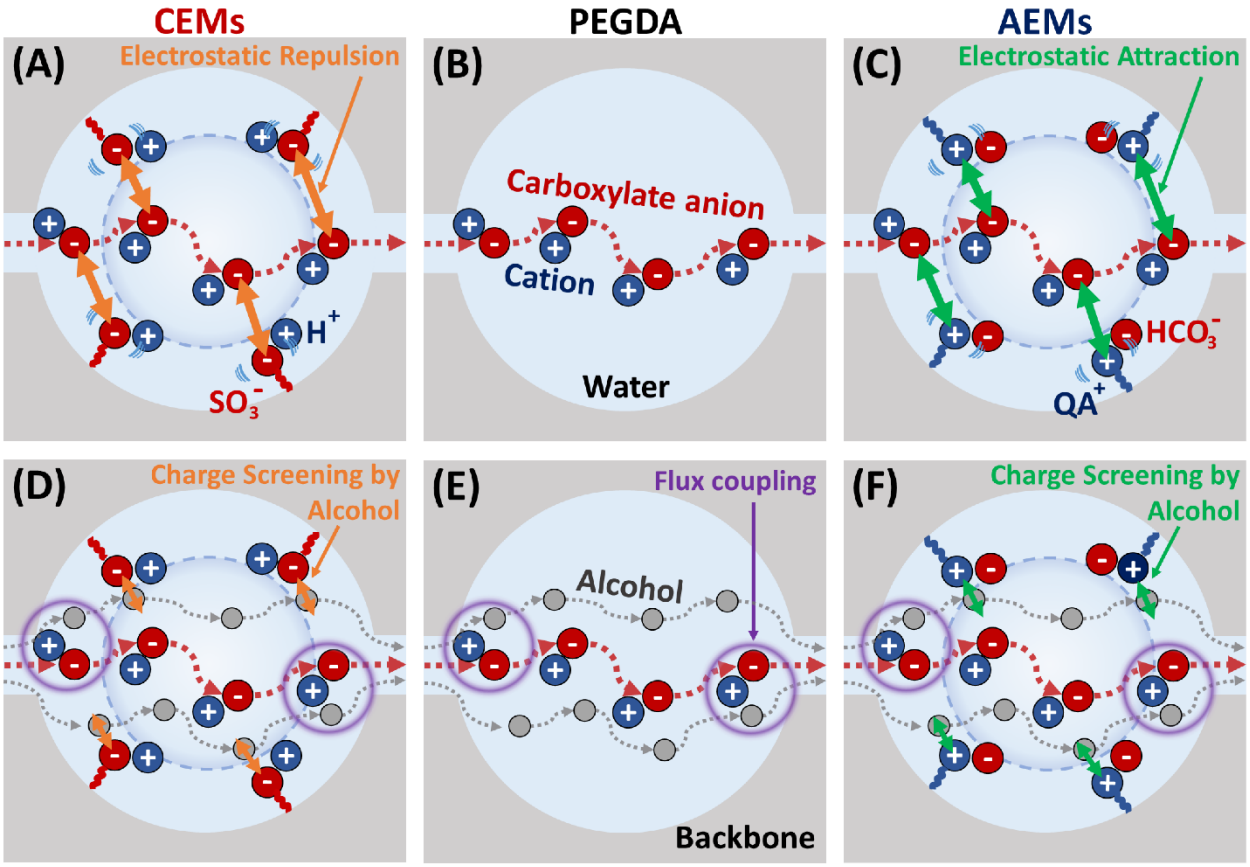

Figure 4.1. Schematic depiction of a carboxylate salt diffusion in (A,D) cation exchange membranes (i.e. PEGDA-AMPS and Nafion® 117), (B,E) crosslinked PEGDA (i.e. A0) and (C,F) anion exchange membranes (i.e. P8, P12, and AMVN) in (A-C) single and (D-F) co-diffusion with an alcohol (MeOH or EtOH). Figures are reprinted from [28, 30, 32] with permission from Elsevier, Wiley, and MDPI.

Moreover, we prepare and characterize a crosslinked PEGDA (A0) as an uncharged analog to exclude the effect of QA^+ from A8 and A12 for comparison. The aim of this work is to examine how the presence of co-permeating EtOH impacts the transport behavior and whether this behavior is consistent with our prior findings for similar systems. Previously, Carter et al. investigated the co-transport of alcohols (MeOH, EtOH and n-PrOH) in Selemion AMV, where they observed a competitive sorption and flux coupling behavior in co-transport [8]. Based on our prior work

described above on the co-transport of carboxylates and alcohols in CEMs, a pictorial description of how the presence of copermeating alcohols could be interfering with the electrostatic interactions (repulsion for CEMs and attraction for AEMs [18, 36, 37]) between membrane-bound charge groups (sulfonates for CEMs or QA^+ for AEMs) and a mobile carboxylate anion is shown in Figure 4.1. In Figure 4.1 A-C, the diffusion of the carboxylate anion by itself is depicted, where the mobile carboxylate anion experiences electrostatic repulsion from bound sulfonate in CEMs (Figure 4.1 A) and electrostatic attraction from bound QA^+ in AEMs (Figure 4.1 C) (ion-polymer interaction). In Figure 4.1 D-F, the diffusion of carboxylates is assisted by co-diffusing alcohols (flux coupling; [38]) (ion–alcohol interaction), where the electrostatic interaction between bound charge groups and the mobile carboxylate anion is screened by the co-permeating alcohol (alcohol–polymer interaction, charge screening; [27, 29-31]; Figure 4.1 D, F).

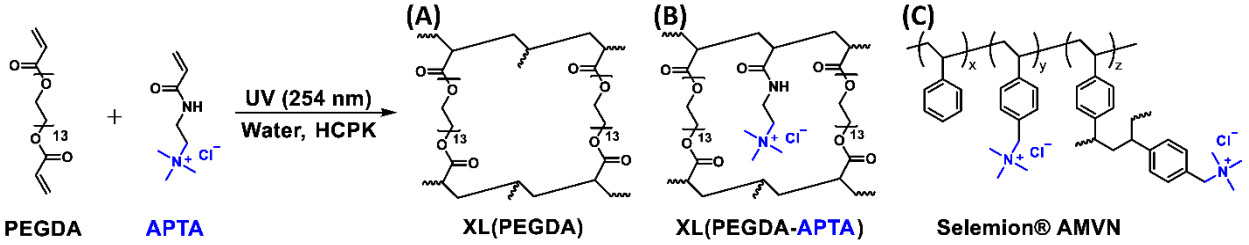

Figure 4.2. (A, B) Synthetic scheme of (A) crosslinked PEGDA, A0, and (B) crosslinked PEGDA-APTA, A8 and A12. (C) Schematic of Selemion AMVN, functionalized polystyrene-divinylbenzene (PS-DVB)-based film.

To probe this behavior in the AEMs of interest here, for each AEM, we measure their permeability (P_i) and solubility (K_i) to both K^+ and Na^+ forms of formate (OFm^-) and acetate (OAc^-). Permeabilities are measured by diffusion cell experiments coupled with in situ attenuated total reflectance–Fourier transform infrared (ATR–FTIR) spectroscopy [29]; solubilities are

measured by sorption–desorption experiments coupled with high-performance liquid chromatography (HPLC) [22]. Additionally, we measure carboxylate permeability (in co-diffusion) and solubility (from a mixture) with ethanol (EtOH). We then calculate diffusivities (D_i) to OFm^- and OAc^- in both K^+ and Na^+ forms (KOFm, KOAc, NaOFm, and NaOAc) using the solution-diffusion model (Equation (4.1)) [39], which describes the overall solute permeation, which is dependent on solute sorption [22, 40-43] into the membrane and diffusion [18, 42, 44, 45]through the fractional free volume [46-49] within the polymer matrix,

$$P_i = D_i K_i \tag{4.1}$$

where P_i is the permeability to solute i, D_i is the diffusivity to solute i, and K_i is the solubility to solute i, for EtOH [8, 50] or a carboxylate anion (OFm^- or OAc^- [51, 52]) in single and co-transport between EtOH and a carboxylate (EtOH-KOFm, EtOH-KOAc, EtOH-NaOFm and EtOH-NaOAc. The multi-solute permeability measurement was enabled by our in situ ATR–FTIR probe approach, which we recently devised [29]. This method is particularly useful upon measuring the alcohol permeabilities and multi-solute permeabilities as the alternative methods typically involve aliquots, where the loss of the solution in either the feed or receiver cell is inevitable and characterization of the multicomponent aliquots ex-situ can be a challenge (especially for volatile species). Ultimately, we analyze and discuss the observed multi-solute transport behavior in these AEMs, which will allow more target-specific design of membranes for CO_2 reduction cells.

4.2. Results and Discussion

The materials, membrane synthesis methods, and experimental procedures are detailed in Chapter 3. A PEGDA membrane and two PEGDA-APTA anion exchange membranes (AEMs) were prepared by UV photopolymerization of pre-polymerization mixtures, as shown in Figure 4.2 A, B and Table 4.1. In the film name (A#), A represents APTA and # represents the mol% of the APTA content. For example, A12 denotes the film prepared with PEGDA (88 mol%) and APTA (12 mol%). Each pre-polymerization mixture was prepared with 20 wt.% of water content and HCPK (0.1 wt.% of the polymer) (Table 4.1).

Table 4.1. Membrane properties from pre-polymerization mixtures.

	APTA[1] (mol%)	PEGDA (g)	APTA (g)	Water (g)	HCPK (g)
A0	0	8.00	0.00	2.00	0.008
A8	8	7.80	0.20	2.00	0.008
A12	12	7.69	0.31	2.00	0.008

[1] APTA = mol of APTA/(mol of PEGDA + mol of APTA) × 100 %.

A charge-neutral film (A0) and three positively charged AEMs (A8, A12, and AMVN) were prepared to investigate the effect of polymer-bound quaternary ammonium cations (QA^+) on OFm^--containing salts (KOFm and NaOFm) and OAc^--containing salts (KOAc and NaOAc) in single and co-transport with EtOH. To further understand this behavior, the EtOH transport of all films in single and co-transport with each salt was also analyzed. The permeabilities, solubilities, and diffusivities of each solute in all films were measured. These values were then analyzed based on three parameters: (1) the charge densities of cations, Na^+ (0.14mC/cm^2) > K^+ (0.07mC/cm^2) [53], (2) the hydrated diameters of cations, K^+ (6.6 Å [54]) < Na^+ (7.2 Å [54]) and anions, OFm^- (5.9 Å [51]) < OAc^- (7.4 Å [51]), and the kinetic diameter of EtOH (4.5 Å [54]) (Figure 4.3), and

(3) the in-water diffusivities of cations, K^+ (2.0 x 10^5 cm^2/s [55]) > Na^+ (1.3 x 10^5 cm^2/s [55]), anions, OFm^- (1.5 x 10^5 cm^2/s [56]) > OAc^- (1.1 x 10^5 cm^2/s [55, 56]) and EtOH (1.23 x 10^5 cm^2/s [57]). The relative kinetic diameters and hydrated diameters are shown in Figure 4.3.

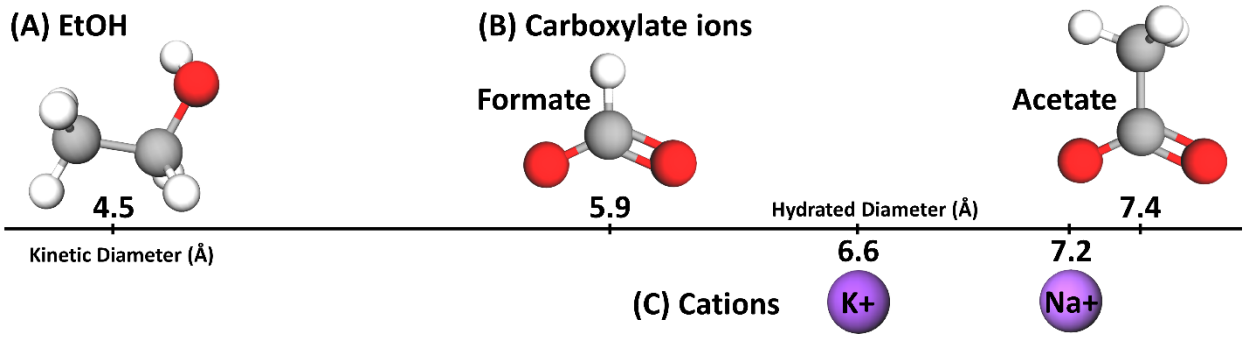

Figure 4.3. Molecular structure of (A) EtOH (4.5 Å), (B) carboxylate ions, OFm^- (5.9 Å) and OAc^- (7.4 Å) and (C) cations, K^+ (6.6 Å) and Na^+ (7.2 Å), where kinetic diameters are stated for EtOH and hydrated diameters are stated for ions. Carbons are shown in grey, oxygens are shown in red, hydrogens are shown in white, K^+ is shown in a darker purple, and Na^+ is shown in a lighter purple.

4.2.1. Water Uptake, Density, and Water Volume Fraction

Water uptakes, dry polymer densities and water volume fractions of films were measured gravimetrically, with results shown in Table 4.2. Generally, the water uptakes of PEGDA-based films (A0, A8 and A12) were higher than that of the PS-DVB-based film (AMVN, see Figure 4.2 for structure) by four times, on average. This is due to differences in the polymer backbones, where PEGDA-based films consist of a hydrophilic backbone (PEG) and AMVN consists of a hydrophobic backbone (PS-DVB). Water uptakes of A8 and A12 were higher than A0 by 3 and 6%, respectively, for those in Cl^- form and by 13 and 22%, respectively, for those in HCO_3^- form. This is likely due to the increase in the free volume in films with decreasing crosslink density (PEGDA content) and increasing charged quaternary ammonium (QA+) content (APTA content)

[35]. Generally, water uptakes of AEMs (A8, A12 and AMVN) in HCO_3^- form were higher than those in Cl^- form by 15%, on average, analogous to prior results for QA^+-poly(sulfone)-based AEMs reported elsewhere [15]. Here, the hydration number plays a role as the hydration number of HCO_3^- (7-8 [58]) is higher than that of Cl^- (5.1-8.4 [59, 60]) and, therefore, the films in HCO_3^- form are more likely to hold more water molecules compared to the films in Cl^- form.

Table 4.2. Water uptake, dry polymer density, and water volume fraction of all films.

	Water uptake, ω_w (water g/dry polymer g·100%)		**Dry polymer density, ρ_p (g/mL)**		**Water volume fraction, ϕ_w**	
	Cl^-	HCO_3^-	Cl^-	HCO_3^-	Cl^-	HCO_3^-
A0	68 ± 1		1.22 ± 0.01		0.45	
A8	70 ± 0	77 ± 0	1.24 ± 0.02	1.25 ± 0.05	0.46	0.49
A12	72 ± 2	83 ± 1	1.21 ± 0.00	1.22 ± 0.01	0.46	0.50
AMVN	18 ± 1	27 ± 0	1.01 ± 0.00	1.02 ± 0.01	0.15	0.22

The dry polymer density of A0 (1.22 g/mL) is consistent with previously reported values [35, 41, 48]. Generally, the densities of the PEGDA-based films are higher than those of PS-DVB-based AMVN, in part due to the difference in atomic compositions, as shown in Table 4.3. For instance, PEGDA-based films contain ~35% of oxygen (16 g/mol) and ~65% of carbon (12 g/mol), whereas AMVN contains only ~5% of oxygen and ~94% of carbon. Moreover, the densities of AEMs in HCO_3^- form are slightly higher than those in Cl^--form, which is attributed to the higher density of HCO_3^- compared to Cl^- (i.e., the densities of $KHCO_3$ and KCl are 2.17 and 1.98 g/mL, respectively).

The diffusivity of a solute in a hydrated, dense membrane is often described by free volume theory, in which solute diffusion occurs through the vacant and transient space between repeating polymer chains[61, 62]. To describe this behavior, Yasuda et al. assumed that all the fractional

free volume (FFV) within a hydrated film would be filled with water and proposed the following equation:

$$D_i = D_{0,i} exp\left[-\beta\left(\frac{1}{\emptyset_w} - 1\right)\right] \quad (4.2)$$

where D_i is the diffusivity of a membrane to a solute i, $D_{0,i}$ is the solute diffusivity in pure water, β is the empirical constant for each polymeric material, and $\emptyset_w$ is the water volume fraction. Therefore, Equation 4.2 predicts solute diffusivity to rapidly increase with the water volume fraction and gradually equilibrate toward the solute diffusivity in pure water ($\emptyset_w$ = 1). Assuming that the empirical constants do not differ drastically, the solute diffusivities of PEGDA-based films (A0, A8 and A12) will be higher than those of AMVN due to the differences in water volume fraction; see Table 4.2. We will return to this point in our discussion of solute diffusivities calculated using the solution-diffusion equation below.

4.2.2. Counterion Conversion, Ionic Conductivity, and IEC

The weight compositions of carbon, oxygen, and chloride were measured from EDS elemental analysis on A8, A12, and AMVN before and after the counterion conversion; see Table 4.3 for values. Generally, the carbon and oxygen compositions of both A8 and A12 were closely matched with the theoretical compositions from the pre-polymerization mixture. However, chlorine compositions were lower than the theoretical values by three times, on average. Complete counterion conversion (Cl^- to HCO_3^-) is presumed in all AEMs (A8, A12, and AMVN) as Cl^- was not detected in EDS elemental analysis on any film after the conversion [16].

The ionic conductivity (σ) and ion exchange capacity (IEC) of each AEM (A8, A12, and AMVN) were determined, yielding the results shown in Table 4.4. Generally, the measured IECs for both A8 and A12 are close to that of the theoretical IEC (calculated from the composition of the pre-polymerization mixture). This indicates that essentially complete conversion from monomers (PEGDA and APTA) to a crosslinked film has been achieved. The IEC of AMVN (1.5 meq/g) was significantly higher than those of PEGDA-based films by an order of magnitude, such that considerably more interactions between bound quaternary ammonium groups (QA^+) and mobile species (K^+, Na^+, OFm^-, OAc^-, and EtOH) are expected for AMVN. Consequently, the ionic conductivity of AMVN is also greater than A8 and A12, by six times, on average.

Table 4.3. Weight percent (wt.%) of AEMs (A8, A12, and AMVN) in Cl^- and HCO_3^- forms.

	Name	**Measured**			**Theoretical***		
		C	**O**	**Cl**	**C**	**O**	**Cl**
Cl-form	A8	57.8 ± 0.7	41.6 ± 0.6	0.6 ± 0.1	59.9	37.8	2.3
	A12	57.7 ± 0.3	41.1 ± 0.3	1.2 ± 0.1	59.8	36.8	3.4
	AMVN	89.6 ± 0.4	6.2 ± 0.3	4.1 ± 0.1	-	-	-
HCO3-form	A8	59.5 ± 0.2	40.5 ± 0.2	-	59.7	40.3	-
	A12	58.9 ± 0.5	41.1 ± 0.5	-	59.6	40.4	-
	AMVN	91.3 ± 0.3	8.7 ± 0.3	-	-	-	-

*Theoretical values of A8 and A12 were calculated based on the compositions in prepolymerization mixtures.

Table 4.4. Water uptake, dry polymer density, and water volume fraction of all films.

Name	**Ionic conductivity (σ, mS/cm)**		**IEC (meq/g dry polymer)**	
	Cl^-	HCO_3^-	Cl^-	HCO_3^-
A8	1.0 ± 0.0	0.9 ± 0.0	0.121	0.125 ± 0.004
A12	1.2 ± 0.0	0.8 ± 0.0	0.187	0.190 ± 0.001
AMVN	7.0 ± 0.0	4.1 ± 0.0	1.5[1]	-

[1] Reported by the manufacturer

The ionic conductivities of the AEMs in HCO_3^- form were lower than those in Cl^- form by 1.4 times, on average [16]. The ionic conductivities of films in both Cl^- and HCO_3^- form are plotted in a function of inverse water volume in Figure 4.4 along with the upper bound regression line for a series of Selemion® AMV and ImPPO-χ AEMs [16]. While the conductivities of AMVN are within the range of other AEMs (Selemion® AMV and ImPPO-χ[16]), the conductivities of both A8 and A12 are lower than their expected conductivity for their respective water volume fractions. This indicates that the transport behavior in A8 and A12 is expected to be closer to that of hydrated, dense membranes (i.e., A0) over the state-of-the-art AEMs (i.e., AMVN, Selemion® AMV and ImPPO-χ).

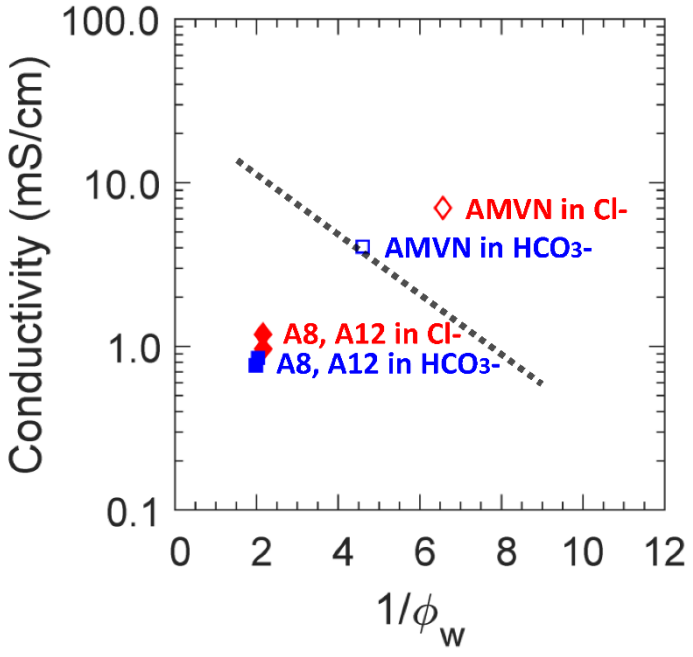

Figure 4.4. Ionic conductivity as a function of inverse water volume fraction for A8, A12 (filled markers), and AMVN (empty markers) in Cl^- (diamonds, ◇) and in HCO_3^- (squares, □). The line is a regression on a series of ImPPO-χ AEMs and Selemion® AMV from the literature [16].

4.2.3. Permeation

One-component permeabilities to EtOH and carboxylate salts (KOFm, NaOFm, KOAc, and NaOAc) of a charge-neutral A0 and positively charged A8, A12 and AMVN films in HCO_3^- form are shown in Figure 4.5, where (A) and (B) are scaled differently. Generally, the thickness of AMVN films after permeation was essentially the same (all within 5%) and those of PEGDA-based films were slightly decreased (7–17%) with increasing APTA content; see Table 4.5. Permeabilities across all films were increased with increasing water volume fraction, showing similar results to those reported elsewhere [16, 30, 42, 48]. This is primarily due to increased diffusion, where solute diffusivities tend to increase with increasing water volume fraction (i.e., free volume theory [61, 62]); for values. For all films, salt permeabilities are in the order of KOFm > NaOFm > KOAc > NaOAc, indicating that the primary discrimination is the size difference between the two carboxylate anions, OFm^- (5.9 Å) < OAc^- (7.4 Å), followed by the difference between the two cations, K^+ (6.6 Å) < Na^+ (7.2 Å); see Figure 4.3.

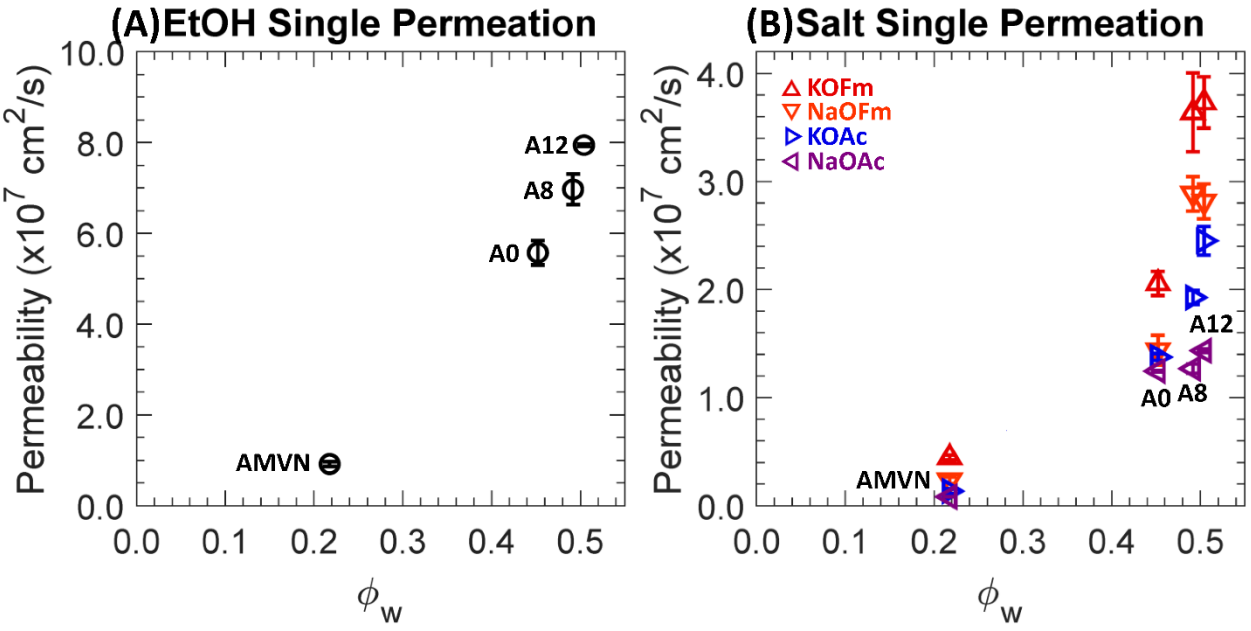

Figure 4.5. (A) Permeabilities to EtOH, ○, in single permeation. (B) Permeabilities to KOFm (△, red), NaOFm (▽, orange), KOAc (▷, blue) and NaOAc (◁, purple) in single permeation. Each data point is the average of 3 experiments with error bars corresponding to the standard deviation.

Two-component permeabilities to EtOH and carboxylate salts (KOFm, NaOFm, KOAc, and NaOAc) of a charge-neutral A0 and positively charged A8, A12, and AMVN films in HCO_3^- form are shown in Figure 4.6, where (A) and (B) are scaled differently; see Table 4.5.

Table 4.5. Normalized film thickness to hydrated membrane after permeability measurements.

	AMVN	A0	A8	A12
Hydrated	1.00	1.00	1.00	1.00
1. EtOH	1.05	0.93	0.91	0.85
2. KOFm	0.99	0.93	0.90	0.83
3. NaOFm	0.95	0.92	0.88	0.85
4. KOAc	1.02	0.91	0.90	0.83
5. NaOAc	1.05	0.93	0.89	0.83
6. EtOH/KOFm	1.01	0.92	0.91	0.87
7. EtOH/NaOFm	1.03	0.93	0.90	0.85
8. EtOH/KOAc	1.03	0.93	0.90	0.84
9. EtOH/NaOAc	1.03	0.93	0.90	0.84

In co-permeation, the permeabilities of AMVN to EtOH are increased by 1.7 times, while those of PEGDA-based films are essentially the same. This is largely due to the differences in sorption, which are described below; see Figures 4.7 and 4.8. Interestingly, QA^+-free A0 permeabilities to NaOAc and KOFm are decreased by 1.1 times, on average, in co-permeation, while those to NaOFm and KOAc are increased by 1.2 and 1.1 times, respectively, on average. However, QA^+-containing A8 and A12 permeabilities to NaOAc, KOFm, NaOFm, and KOAc all decrease, by 2.2, 1.4, 1.3, and 1.1 times, respectively, on average. To rationalize this behavior, we conjecture the permeation of carboxylate salts to be dependent on the polyatomic carboxylate anions over the cations. Consequently, electrostatic attraction (i.e., counterion condensation [18]) between the bound quaternary ammonium (QA^+) and mobile carboxylate anions (OFm^- and OAc^-) can be suppressed by co-permeation with EtOH (i.e., charge screening [29, 30, 32]); see Figure 4.1. As a result, the overall salt permeabilities of QA^+-containing A8 and A12 are decreased in co-permeation with EtOH. Similarly, AMVN permeabilities to OFm^--containing salts (KOFm and NaOFm) are decreased by three times, while those to OAc^--containing salts (KOAc and NaOAc) are similar. More details of this behavior will be discussed below in the section 4.2.5.

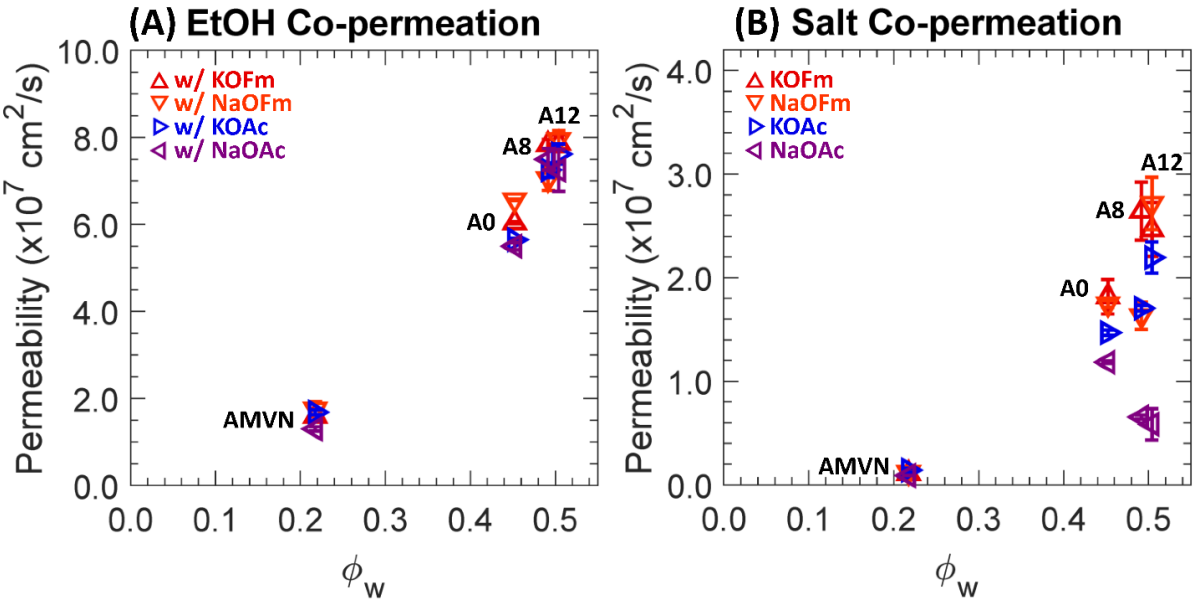

Figure 4.6. (A) Permeabilities to EtOH in co-permeation with KOFm (△, red), NaOFm (▽, orange), KOAc (▷, blue), and NaOAc (◁, purple). (B) Permeabilities to KOFm (△, red), NaOFm (▽, orange), KOAc (▷, blue), and NaOAc (◁, purple) in co-permeation with EtOH. Each data point is the average of 3 experiments with error bars corresponding to the standard deviation.

4.2.4. Sorption

One-component solubilities to EtOH and carboxylate salts (KOFm, KOAc, NaOFm and NaOAc) of a charge-neutral A0 and positively charged A8, A12 and AMVN films in HCO_3^- form are shown in Figure 4.7, where (A) and (B) are scaled differently. Generally, the volumes of AMVN films after sorption in all external solutions were slightly increased (6–9%), and the volumes of PEGDA-based films were essentially the same (within 3%) or slightly increased (up to 9%) after sorption; see Table 4.6.

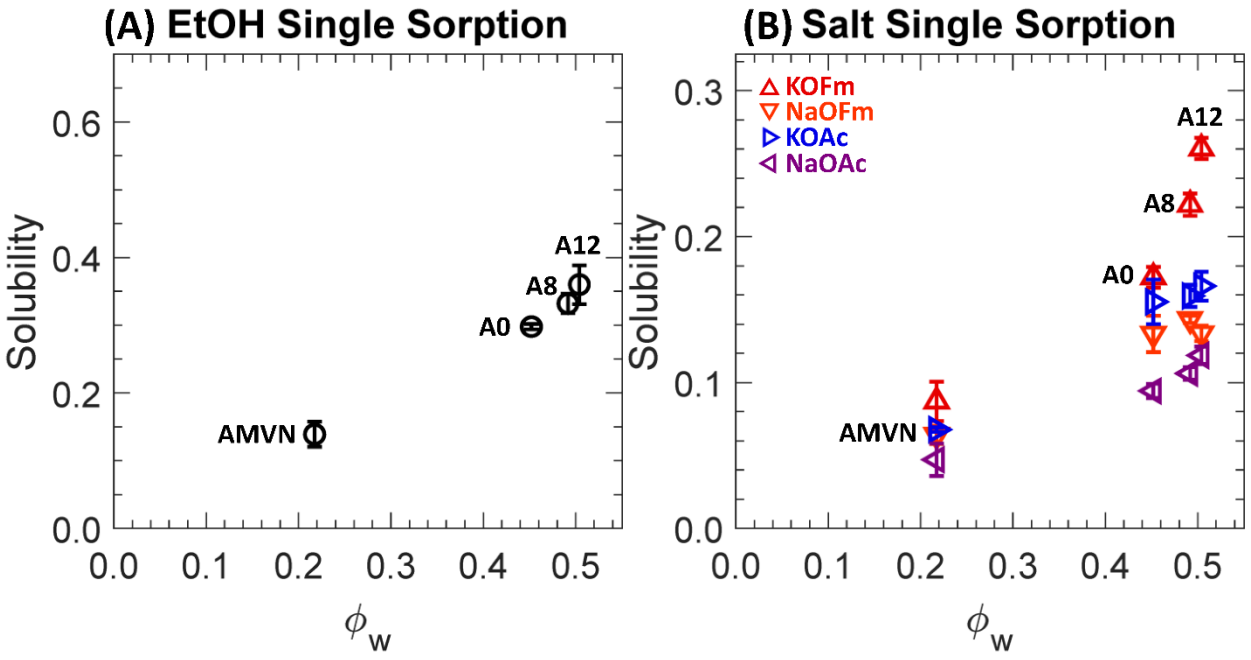

Figure 4.7. (A) Solubilities to EtOH, ○, in single sorption. (B) Solubilities to KOFm (△, red), NaOFm (▽, orange), KOAc (▷, blue) and NaOAc (◁, purple) in single sorption. Each data point is the average of 3 experiments with error bars corresponding to the standard deviation.

Table 4.6. Volume of hydrated films and volume of swollen films (mm^3) after sorption experiments were measured from photographs and a digital caliper. Normalized to the volume of the hydrated films.

	A0	A8	A12	AMVN
Hydrated	1.000	1.000	1.000	1.000
1. EtOH	0.988	0.904	0.899	1.085
2. KOFm	0.976	0.926	0.926	1.081
3. NaOFm	0.994	0.885	0.959	1.078
4. KOAc	0.968	0.885	0.880	1.068
5. NaOAc	0.946	0.899	0.876	1.084
6. EtOH/KOFm	1.090	1.016	0.993	1.070
7. EtOH/NaOFm	1.074	0.975	0.975	1.082
8. EtOH/KOAc	1.022	0.980	1.005	1.093
9. EtOH/NaOAc	1.002	0.969	0.984	1.078

Generally, EtOH solubilities are higher than those of salt solubilities by 1.7 times, on average, indicating that EtOH uptake is preferred in these films ($\emptyset_w$: 0.2–0.5) over the uptake of carboxylate salts. We observed similar behavior in a previous investigation of cation exchange membranes (CEM) [29, 32, 50], where the alcohol (MeOH and EtOH) solubilities were higher than the carboxylate (NaOFm and NaOAc) solubilities. However, contrary to our previous investigations of CEMs, the EtOH concentrations in the AEMs here (A8, A12, and AMVN) after sorption in the external solution (1 M EtOH) were less than those of the external solution, such that EtOH is less preferred in these films over the external solution; see Table 4.7.

Table 4.7. Volume fraction among the solution, EtOH ($\emptyset_e$)-carboxylate salt ($\emptyset_c$), inside the membranes after sorption experiments, where the remaining is the volume fraction of water ($\emptyset_w$) from the solution.

	External, 1 M		**AMVN**		**A0**		**A8**		**A12**	
	ϕ_e	ϕ_c	ϕ_e	ϕ_c	ϕ_e	ϕ_c	ϕ_e	ϕ_c	ϕ_e	ϕ_c
1. EtOH	0.058	-	0.038	-	0.033	-	0.051	-	0.047	-
2. KOFm	-	0.044	-	0.017	-	0.016	-	0.025	-	0.025
3. NaOFm	-	0.035	-	0.010	-	0.009	-	0.014	-	0.010
4. KOAc	-	0.063	-	0.022	-	0.018	-	0.027	-	0.024
5. NaOAc	-	0.054	-	0.012	-	0.010	-	0.015	-	0.015
6. EtOH/KOFm	0.058	0.044	0.044	0.015	0.076	0.014	0.051	0.019	0.046	0.017
7. EtOH/NaOFm	0.058	0.035	0.045	0.008	0.081	0.010	0.053	0.011	0.047	0.010
8. EtOH/KOAc	0.058	0.063	0.051	0.019	0.070	0.012	0.053	0.024	0.046	0.019
9. EtOH/NaOAc	0.058	0.054	0.052	0.011	0.087	0.013	0.056	0.014	0.047	0.013

For PEGDA-based films (A0, A8, and A12), the carboxylate salt solubilities were in the order of KOFm > KOAc > NaOFm > NaOAc. This result indicates that the salts with K^+(KOFm and KOAc) are preferred over the salts with Na+ (NaOFm and NaOAc). A similar result was observed by Jang et al. [41], where the potassium chloride (KCl) solubilities of crosslinked PEGDA films were higher than their sodium chloride (NaCl) solubilities. They proposed that it is easier for K^+ ions to bind with PEG as they can directly interact with the dipole moment of the

ether oxygen group in the absence of a strongly bound hydration layer due to the relatively low surface charge density (0.072 mC/cm^2), while it is more difficult for Na+ ions to interact with the dipole moment with a strongly bound hydration layer due to the relatively high surface charge density (0.142 mC/cm^2) [41]. Similarly, Sartori et al. reported the binding constant of K^+ to ethylene oxide to be higher than that of Na^+ to ethylene oxide [63]. This result also suggests that the salts with OFm^- (KOFm and NaOFm) are preferred over the salts with OAc^- (KOAc and NaOAc). A possible cause of this difference between the solubilities of OFm^- and OAc^- is the effect of molecular size, where the larger OAc^- (7.4 Å) would experience more steric hindrance from the polymer structure than smaller OFm^- (5.9 Å) (Figure 4.3) [32, 41, 51, 64]. For AMVN, the salt solubilities are in the order of KOFm > NaOFm > KOAc > NaOAc; the order between NaOFm and KOAc is changed. This indicates that the effect of carboxylates ($OFm^- > OAc^-$) is more apparent than the effect of cations ($K^+ > Na^+$). This is likely due to the fact that the polystyrene-divinylbenzene (PS-DVB) backbone in AMVN does not contain functional groups with a strong dipole moment as ether oxygen groups in PEG; see Figure 4.2.

Two-component solubilities to EtOH and carboxylate salts (KOFm, NaOFm, KOAc, and NaOAc) of a charge-neutral A0 and positively charged A8, A12 and AMVN films in HCO_3^- form are shown in Figure 4.8, where (A) and (B) are scaled differently.

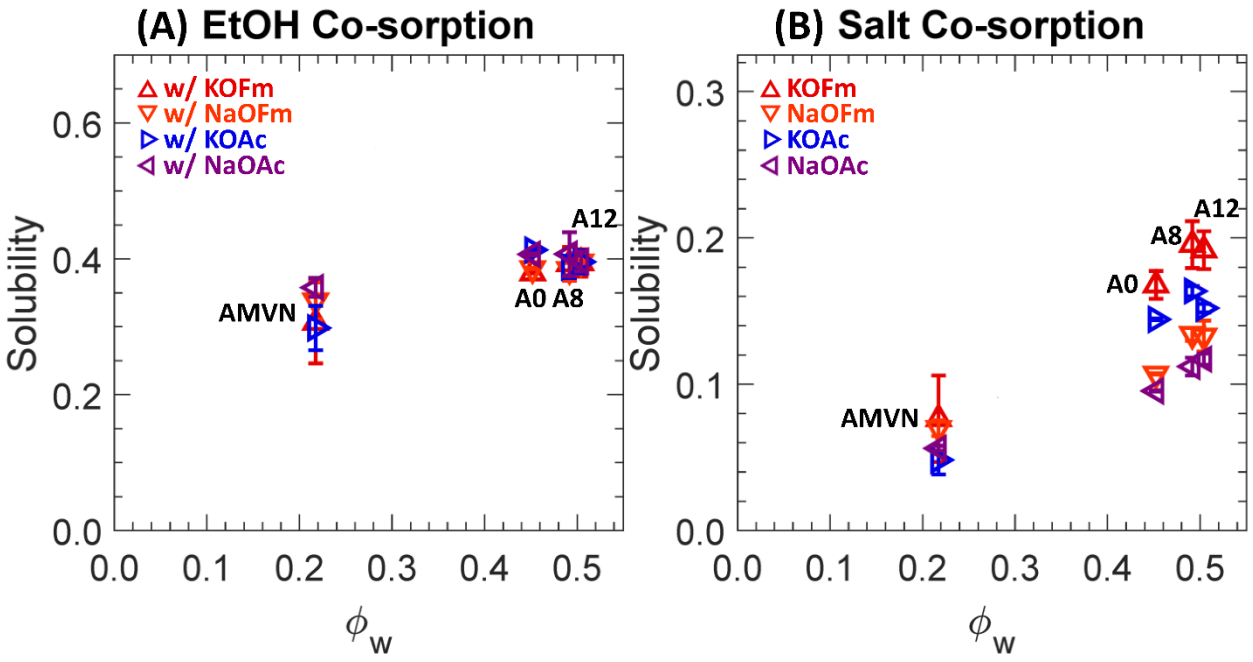

Figure 4.8. (A) Solubilities to EtOH in co-sorption with KOFm (△, red), NaOFm (▽, orange), KOAc (▷, blue) and NaOAc (◁, purple). (B) Solubilities to KOFm (△, red), NaOFm (▽, orange), KOAc (▷, blue) and NaOAc (◁, purple) in co-sorption with EtOH. Each data point is the average of 3 experiments with error bars corresponding to the standard deviation.

In co-sorption, PEGDA-based films' (A0, A8, and A12) solubilities to EtOH are increased by 1.3, 1.2, and 1.1 times, on average, respectively, while those to salts are decreased by 1.1 times, on average. Again, EtOH is preferentially sorbed into PEGDA-based films over carboxylate salts in co-sorption. Our group reported similar behavior [32] for a series of crosslinked PEGDA (same as A0) and sulfonate-bearing PEGDA-based CEMs (similar to A8 and A12, but a CEM with negatively charged sulfonate groups). For those CEMs, solubilities to alcohols in co-sorption with a carboxylate salt were increased by 1.2 and 1.1 times, on average, respectively, while those to salts in co-sorption were essentially the same. A possible cause of this behavior is the difference in hydrophobicity [65]. While both EtOH and carboxylate salts are hydrophilic, as they bear an

alcohol group (-OH) and charged groups (i.e., a carboxylate$^-$ and either K^+ or Na^+), respectively, the carboxylate salts are relatively more hydrophilic due to the hydration of the charge groups and, therefore, their interaction might be less preferred with a polymer structure (relatively hydrophobic).

In co-sorption, AMVN solubilities to EtOH are increased by 2.1 times, on average, while those to salts are essentially the same. This is contrary to behavior reported for CEMs [32], where the solubilities of a commercial perfluorosulfonic acid (PFSA) CEM, Nafion® 117, to alcohols in co-sorption with a carboxylate salt were decreased by 1.1 times, on average. As current state-of-the-art IEMs, AMVN and Nafion® 117 share some common characteristics, such as a hydrophobic backbone (i.e., PS-DVB and PF), similar IEC (i.e., 1.5 and 0.9 meq/g) and similar water volume fraction (i.e., 0.22 and 0.25 [30]). To rationalize this difference in transport be[16]havior between AEM and CEM, we conjecture a potential repulsive interaction between bound QA^+ and mobile EtOH in single sorption (i.e., AEM direct ethanol fuel cells, DEFC [3]), which might be interfered with by mobile carboxylate anions as they are attracted to the bound QA^+ and screen the interaction between the QA^+ and EtOH. Nevertheless, the increase in EtOH sorption in AEM is a concerning behavior for CO_2 reduction cells [8-10, 12, 16] and, therefore, it would be appropriate to make efforts to suppress this behavior in the design of AEMs for CO_2 reduction [7, 28].

4.2.5. Diffusion

One-component diffusivities to EtOH and carboxylate salts (KOFm, KOAc, NaOFm and NaOAc) of a charge-neutral A0 and positively charged A8, A12, and AMVN films in HCO_3^- form were calculated using the solution-diffusion relationship (Equation (4.1)) and the results are shown

in Figure 4.9. The Mackie–Meares model was used to correlate the diffusivities with the water volume fraction of each membrane (Equation (4.3)).

$$D_i = D_{0,i}\left(\frac{\emptyset_w}{2-\emptyset_w}\right)^2 \tag{4.3}$$

where D_i is the diffusivity of a membrane to a solute i, $D_{0,i}$ is the solute diffusivity in pure water. Table 4.8 presents the diffusivities of the targeted solute in water.

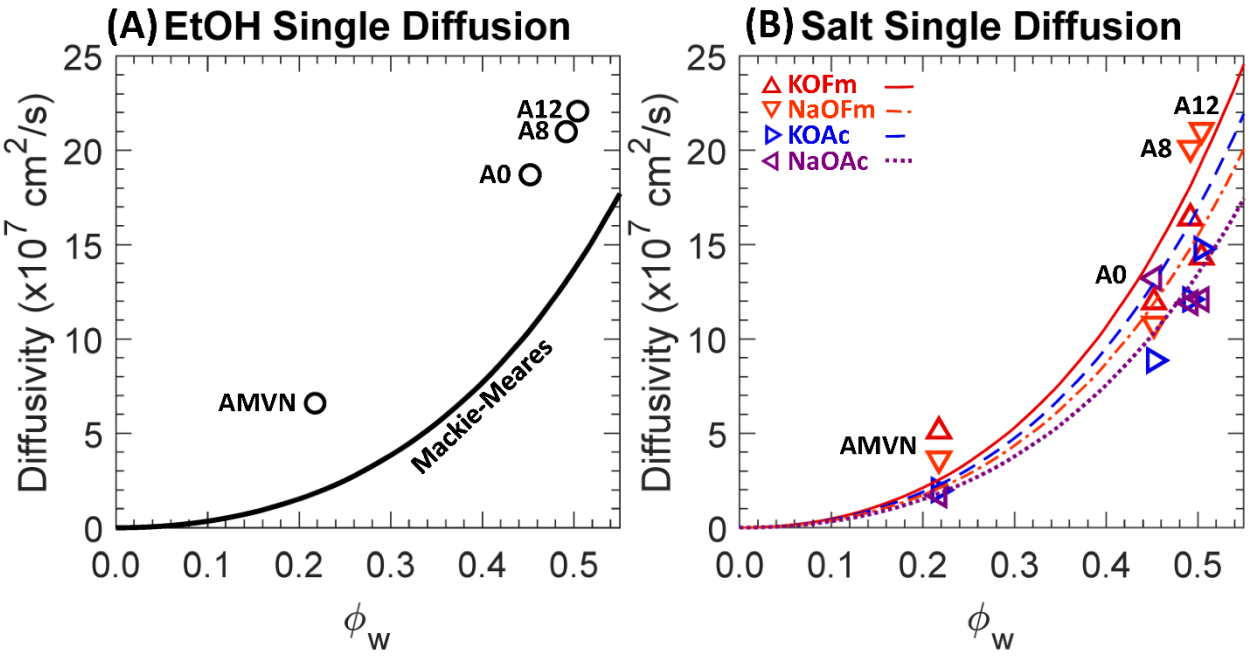

Figure 4.9. (A) Diffusivities to EtOH, ○, in single diffusion. The solid line is the Mackie-Meares' fit. (B) Diffusivities to KOFm (△, red), NaOFm (▽, orange), KOAc (▷, blue) and NaOAc (◁, purple) in single diffusion. The lines are the Mackie-Meares' fits, KOFm (solid line, red), NaOFm (dot-dashed, orange), KOAc (dashed, blue), and NaOAc (dotted, purple).

Table 4.8. Solute diffusivities of select species in water (× 10^5 cm^2/s) at 25 ºC in the dilute condition.

Solute	Diffusivity in water
Water	2.45 [66]
EtOH	1.23 [57]
OFm^-	1.454 [56]
OAc^-	1.089 [55, 56]
K^+	1.957 [55]
Na^+	1.334 [55]

The calculated EtOH diffusivities are higher than those estimated by the Mackie– Meares model by 2.1 times, on average, showing a similar result to MeOH diffusivities reported elsewhere [42]. This under-prediction of alcohol diffusivity has been observed previously and attributed to the Mackie–Meares model being initially devised for ionic species [67]. The relative difference in the calculated and the estimated diffusivities was larger in AMVN. For instance, the calculated EtOH diffusivity of AMVN was 3.6 times higher than the estimated value from the Mackie–Meares model, while those of PEGDA-based films were 1.7 times higher. A contribution to the significantly low estimation for AMVN is made by the inherent weakness of the model at low water volume fraction. For instance, the model implies that the solutes become immobile at zero water volume fraction, which is not true as they can diffuse through the backbone structure [18, 67]. Another contribution is the increase in the volume fraction of solution, $\emptyset_s$ [42]:

$$\emptyset_s = \frac{V_s - (W_d/\rho_p)}{V_s} \tag{4.4}$$

where W_d is the mass of the dried film, ρ_L is the density of dry polymer, and V_s is the volume of the swollen film after sorption. To determine V_s, the film surface area was extracted from digital photographs and the thickness was measured using a digital caliper; see Table 4.9 for values. As the solution volume fraction was higher than the water volume fraction by 1.1 times, the AMVN

diffusivities can be closer to the Mackie–Meares' fit as this would constitute a rightward shift in the values in Figure 4.9 A.

Table 4.9. Water volume fractions ($\emptyset_w$) and solution volume fractions ($\emptyset_s$) of films after sorption experiments, where the remaining is the polymer volume fraction ($\emptyset_p$) from the dry polymer density.

	AMVN, ϕ_s	**A0, ϕ_s**	**A8, ϕ_s**	**A12, ϕ_s**
Water volume fractions, ϕ_w	0.217	0.452	0.492	0.504
1. EtOH	0.245	0.452	0.382	0.446
2. KOFm	0.242	0.445	0.397	0.462
3. NaOFm	0.240	0.455	0.369	0.481
4. KOAc	0.233	0.441	0.369	0.434
5. NaOAc	0.244	0.428	0.380	0.432
6. EtOH/KOFm	0.235	0.503	0.451	0.499
7. EtOH/NaOFm	0.243	0.496	0.427	0.489
8. EtOH/KOAc	0.250	0.470	0.430	0.505
9. EtOH/NaOAc	0.240	0.460	0.424	0.494

The salt diffusivities are closer to the Mackie–Meares' fits; see Figure 4.9 B. To calculate the diffusivities of salts in water ($D_{0,i}$), we assume the diffusivities of a salt consisting of monovalent ions (i.e., Na^+ and Cl^- for NaCl) and that the salt diffusivity is close to the average diffusivities of the two ions (mobility-weighted average diffusivity [68]). For instance, using the reported diffusivities of Na^+, K^+, Cs^+, and Cl^- in water (1.33×10^{-5}, 1.96×10^{-5}, 2.06×10^{-5} and 2.03×10^{-5} cm^2/s, respectively [55]), the estimated diffusivities of NaCl, KCl, and CsCl in water are 1.68×10^{-5}, 2.00×10^{-5} and 2.04×10^{-5} cm^2/s, respectively, and these are close to the reported diffusivities for these salts: 1.61×10^{-5} [69], 1.99×10^{-5} and 2.04×10^{-5} cm^2/s, respectively. Here, using the reported diffusivities of K^+, Na^+, OFm^-, and OAc^- in water, 1.96×10^{-5}, 1.33×10^{-5}, 1.45×10^{-5} and 1.09×10^{-5} cm^2/s [55, 56], respectively, we estimate the diffusivities of EtOH, KOFm,

KOAc, NaOFm, and NaOAc in water as 1.23×10^{-5}, 1.71×10^{-5}, 1.52×10^{-5}, 1.39×10^{-5} and 1.21×10^{-5} cm^2/s, respectively.

Generally, salt diffusivities to AMVN are higher than the estimated diffusivities by 1.4 times, on average, while those to PEGDA-based films are essentially the same. Again, a contribution to the low estimation for AMVN is presumably made by the inherent weakness of the model at low water volume fraction. For AMVN, the calculated diffusivities to K^+- containing salts (KOFm and KOAc) are higher than the estimated diffusivities by 1.5 times, on average, while those to Na+-containing salts (NaOFm and NaOAc) are higher than the estimated diffusivities by 1.4 times, on average. The calculated diffusivities of PEGDA-based films to Na+-containing salts are higher than the estimated diffusivities by 1.1 times, on average, while those to K+-containing salts are lower than the estimated diffusivities by 1.3 times, on average

Two-component diffusivities to EtOH and carboxylate salts (KOFm, NaOFm, KOAc, and NaOAc) of a charge-neutral A0 and positively charged A8, A12 and AMVN films in HCO_3^- form are shown in Figure 4.10 along with predicted diffusivities using the Mackie–Meares model.

In co-diffusion, the EtOH diffusivities are decreased by 1.2 times, on average. Our group reported a similar result for CEMs (PEGDA-AMPS and Nafion® 117) [32], where both MeOH and EtOH diffusivities were decreased in co-diffusion with a carboxylate salt (either NaOFm or NaOAc). To rationalize this behavior, we conjectured there to be competitive diffusion between the co-solutes [32], and that the diffusional path of a fast-diffusing diffusant can be interfered with by a slow-diffusing co-diffusant. A similar diffusant– diffusant interaction is likely of consequence for the EtOH diffusion with these carboxylate salts in the AEMs studied here. For PEGDA-based films (A0, A8 and A12), the decrease in EtOH diffusivities was more apparent in co-diffusion with

OAc^--containing salts (KOAc and NaOAc). While EtOH diffusivities in co-diffusion with OFm^--containing salts (KOFm and NaOFm) were decreased by 1.11 times, on average, those with OAc^--containing salts were decreased by 1.23 times, on average. The impact of the difference in carboxylate anion (as stated above) was more apparent than the impact from the difference in cation, where EtOH diffusivities in co-diffusion with K^+-containing salts (KOFm and KOAc) and Na^+-containing salts (NaOFm and NaOAc) were decreased by 1.15 and 1.18 times, on average, respectively. A possible cause is the hydrated diameter of OFm^- (5.9 Å) being significantly less than that of OAc^- (7.4 Å) and, therefore, the larger-diameter anion correlates to a larger impediment to the fast-diffusing EtOH, while the differences in the hydrated diameters of K^+ (6.6 Å) and Na^+ (7.2 Å) are relatively small (Figure 4.3). For AMVN, the impact of the difference in cation was more apparent than the impact of the difference in anion. While EtOH diffusivities in co-diffusion with K^+-containing salts were decreased by 1.39 times, on average, those with Na^+-containing salts were increased by 1.07 times, on average. EtOH diffusivities in co-diffusion with OFm^--containing salts and OAc^--containing salts were decreased by 1.13 and 1.10 times, on average, respectively. To rationalize the increase in EtOH diffusivity in co-diffusion with Na^+-containing salts, we conjecture that the diffusional path of EtOH is less interfered with by the salts with Na^+. As the surface charge density of Na^+ is higher than that of K^+, the electrostatic repulsion from bound QA^+ to Na^+ can be higher than that to K^+. Consequently, more salts with Na^+ might diffuse away from the bound water region and, therefore, more EtOH can diffuse near the bound water region, which will have a lesser effect on the fast-diffusing EtOH. On the other hand, the diffusional path of EtOH and the salts with K+ might be overlapping and, therefore, more salts can impede the EtOH diffusion.

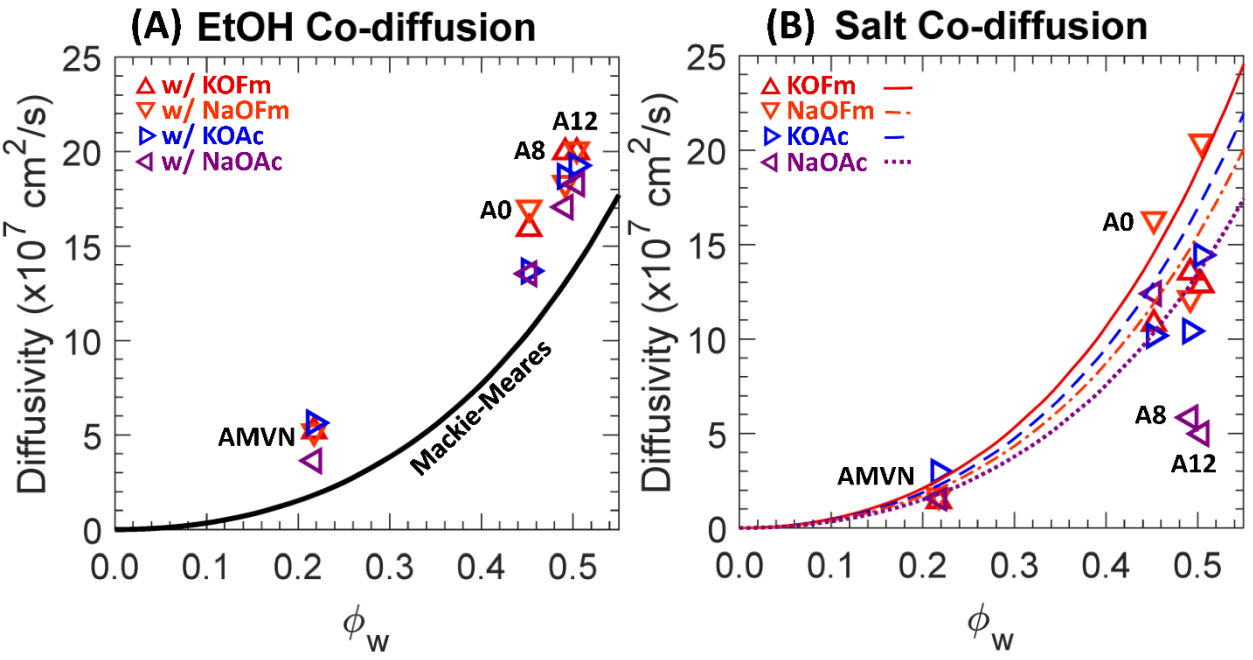

Figure 4.10. (A) Diffusivities to EtOH, ○, in co-diffusion with KOFm (△, red), NaOFm (▽, orange), KOAc (▷, blue) and NaOAc (◁, purple). The solid line is the Mackie-Meares' fit. (B) Diffusivities to KOFm (△, red), NaOFm (▽, orange), KOAc (▷, blue) and NaOAc (◁, purple) in co-diffusion with EtOH. The lines are the Mackie-Meares' fits, KOFm (solid line, red), NaOFm (dot-dashed, orange), KOAc (dashed, blue), and NaOAc (dotted, purple).

In co-diffusion with EtOH, QA^+-free A0 (crosslinked PEGDA) diffusivities to carboxylate salts were slightly increased by 1.1 times, on average, and a similar result was reported elsewhere [32]. This behavior is partially due to flux coupling [12, 38] between fast-diffusing EtOH and slow-diffusing carboxylate salts. The diffusivities of QA^+-containing AEMs (A8, A12 and AMVN) to carboxylate salts were decreased by 1.3 times, on average, in co-diffusion with EtOH.We observed the opposite behavior in sulfonate (SO_3^-)-containing CEMs [32], where the diffusivities of SO_3^--containing PEGDA-AMPS (equivalent to A8 and A12, but with SO_3^- group) and Nafion® 117 were increased by 1.4 times, on average. To rationalize this behavior, we conjectured a partial charge screening [27, 31] by a co-diffusing alcohol [29, 30] such that the electrostatic repulsion

(Donnan exclusion; [36]) between bound SO_3^- and mobile carboxylate anions (co-ions in CEM) is diminished and, therefore, the overall salt diffusivity is increased. Typically, the salt diffusion in an IEM (while maintaining the charge neutrality) is often limited by the co-ion (electrostatic repulsion) [18] and, therefore, the charge screening between the bound charge and the co-ion was in line with the traditional understanding of salt diffusion in IEM. If the co-ion (either K^+ or Na^+) of these carboxylate salts shows a significant impact on the diffusion through AEMs, then the charge screening by alcohol might be assisting the overall salt diffusion (rather than suppressing, as seen in this investigation). This leads to a conjecture that the impact of K^+ or Na^+ is not apparent and a possible contribution is the difference in the kinetic diameters of cations and carboxylate anions. As polyatomic anions, the kinetic diameters of carboxylate anions are significantly larger than those of K^+ and Na^+. These differences may impact the hydration shells of the cations (unlike those with a smaller monovalent anion, Cl^-; [44]). Taken together, the electrostatic attraction (counterion condensation theory; [18, 20, 37]) between bound QA^+ and mobile carboxylate anions (counterions in AEM) can be dominant over cations and can be diminished through a partial charge screening by the co-diffusing EtOH and, therefore, the overall salt diffusivity is decreased as the diffusivity of the condensed counterion [18] is diminished; see Figure 4.1. Overall, these changes in interactions suggest that differences in diffusion behavior from the above-described interactions are a primary driver of changes in membrane diffusivities to carboxylate salts in single and co-diffusion with alcohols and perhaps for understanding the co-diffusion of other complex mixtures through IEMs.

4.3. Conclusions

A QA^+-free PEGDA (A0), two QA^+-containing PEGDA-APTA (A8 and A12), and Selemion® AMVN (AMVN) were investigated for their transport and co-transport behavior when challenged with carboxylate ions, EtOH and mixtures of carboxylate ions and EtOH. Permeabilities and solubilities to EtOH or carboxylate salt (either KOFm, KOAc, NaOFm, or NaOAc) were measured both by themselves and in co-transport. Solute diffusivities for each case were then calculated using the solution-diffusion model, where, generally, EtOH exhibited higher solubility and diffusivity than the carboxylate salts in all films. A charge screening behavior is conjectured based on the assumption that the diffusion of a carboxylate salt is dependent on the polyatomic carboxylate anion over the cation. The carboxylate salt diffusivities of AEMs (A8, A12, and AMVN) are decreased in codiffusion with EtOH, which we ascribe to the screening of the electrostatic attraction by the co-diffusing EtOH (charge screening), as shown in Figure 4.11. Overall, multi-component transport in ion exchange membranes is a highly complex system as various mobile components (i.e., cation, uncondensed carboxylate anions, condensed carboxylate anions, EtOH, and bulk water) are permeating in various fixed components (i.e., QA^+, polymer backbone, and bound water) and the array of interactions between solutes and between solutes and the membrane are dynamic and complicated. Therefore, while this investigation extends our understanding of the transport and co-transport behavior of select solutes (carboxylate ions and EtOH), more fundamental investigations are needed to further develop our understanding of the transport behavior of complex mixtures in polymer membranes.

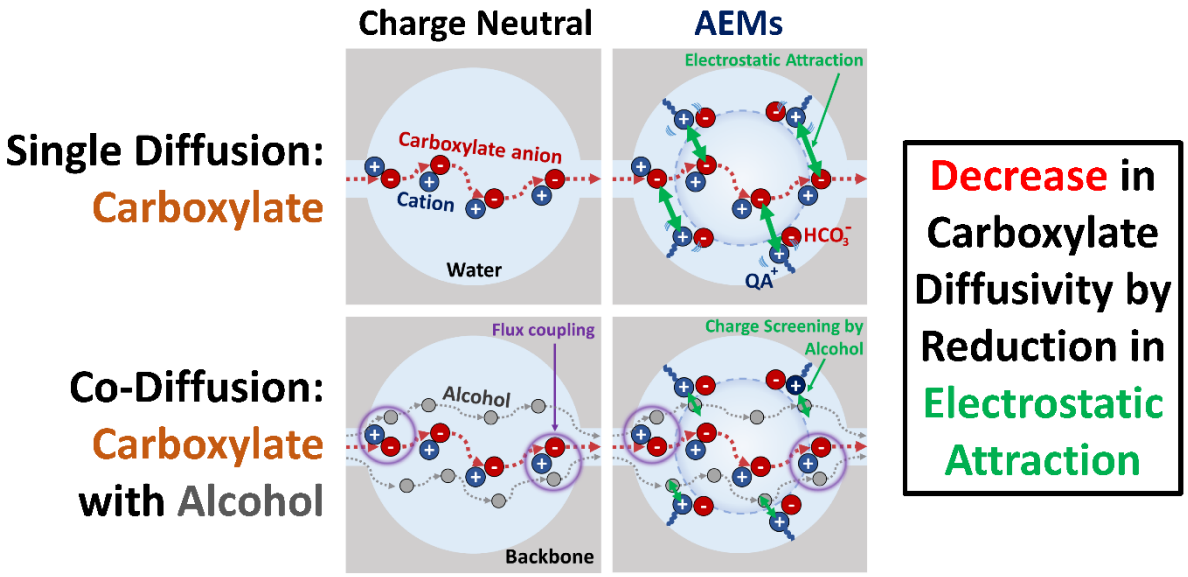

Figure 4.11. Schematic depiction of a carboxylate salt diffusion in charge neutral crosslinked PEGDA and anion exchange membranes in single and co-diffusion with alcohol.

4.4. References

[1] M.A. Hickner, A.M. Herring, E.B. Coughlin, Anion exchange membranes: Current status and moving forward, Journal of Polymer Science Part B: Polymer Physics 51(24) (2013) 1727-1735.

[2] G.M. Geise, M.A. Hickner, B.E. Logan, Ionic resistance and permselectivity tradeoffs in anion exchange membranes, ACS applied materials & interfaces 5(20) (2013) 10294-10301.

[3] N. Fujiwara, Z. Siroma, S.-i. Yamazaki, T. Ioroi, H. Senoh, K. Yasuda, Direct ethanol fuel cells using an anion exchange membrane, Journal of Power Sources 185(2) (2008) 621-626.

[4] J. Yoon, D. Lee, Y.N. Lee, Y.S. Yoon, D.-J. Kim, Solid solution palladium-nickel bimetallic anode catalysts by co-sputtering for direct urea fuel cells (DUFC), Journal of Power Sources 431 (2019) 259-264.

[5] G. Chen, K. Wei, A. Hassanvand, B. Freeman, S. Kentish, Single and binary ion sorption equilibria of monovalent and divalent ions in commercial ion exchange membranes [Erratum: May 2021, v. 196, p. 117110], (2020).

[6] D. Li, E.J. Park, W. Zhu, Q. Shi, Y. Zhou, H. Tian, Y. Lin, A. Serov, B. Zulevi, E.D. Baca, Highly quaternized polystyrene ionomers for high performance anion exchange membrane water electrolysers, Nature Energy 5(5) (2020) 378-385.

[7] D.A. Salvatore, C.M. Gabardo, A. Reyes, C.P. O'Brien, S. Holdcroft, P. Pintauro, B. Bahar, M. Hickner, C. Bae, D. Sinton, Designing anion exchange membranes for CO2 electrolysers, Nature Energy 6(4) (2021) 339-348.

[8] B.M. Carter, B.M. Dobyns, B.S. Beckingham, D.J. Miller, Multicomponent transport of alcohols in an anion exchange membrane measured by in-situ ATR FTIR spectroscopy, Polymer 123 (2017) 144-152.

[9] B.M. Carter, L. Keller, M. Wessling, D.J. Miller, Preparation and characterization of crosslinked poly (vinylimidazolium) anion exchange membranes for artificial photosynthesis, Journal of Materials Chemistry A 7(41) (2019) 23818-23829.

[10] M. Krödel, B.M. Carter, D. Rall, J. Lohaus, M. Wessling, D.J. Miller, Rational design of ion exchange membrane material properties limits the crossover of CO2 reduction products in artificial photosynthesis devices, ACS applied materials & interfaces 12(10) (2020) 12030-12042.

[11] M.R. Singh, A.T. Bell, Design of an artificial photosynthetic system for production of alcohols in high concentration from CO 2, Energy & Environmental Science 9(1) (2016) 193-199.

[12] D.J. Miller, F.A. Houle, Membranes for Solar Fuels Devices, (2018).

[13] A.J. Garza, A.T. Bell, M. Head-Gordon, Mechanism of CO2 reduction at copper surfaces: pathways to C2 products, Acs Catalysis 8(2) (2018) 1490-1499.

[14] L.-C. Weng, A.T. Bell, A.Z. Weber, Towards membrane-electrode assembly systems for CO 2 reduction: a modeling study, Energy & Environmental Science 12(6) (2019) 1950-1968.

[15] A. Amel, N. Gavish, L. Zhu, D.R. Dekel, M.A. Hickner, Y. Ein-Eli, Bicarbonate and chloride anion transport in anion exchange membranes, Journal of Membrane Science 514 (2016) 125-134.

[16] S.M. Dischinger, S. Gupta, B.M. Carter, D.J. Miller, Transport of neutral and charged solutes in imidazolium-functionalized poly (phenylene oxide) membranes for artificial photosynthesis, Industrial & Engineering Chemistry Research 59(12) (2019) 5257-5266.

[17] J. Kamcev, D.R. Paul, B.D. Freeman, Effect of fixed charge group concentration on equilibrium ion sorption in ion exchange membranes, Journal of Materials Chemistry A 5(9) (2017) 4638-4650.

[18] J. Kamcev, D.R. Paul, G.S. Manning, B.D. Freeman, Ion diffusion coefficients in ion exchange membranes: significance of counterion condensation, Macromolecules 51(15) (2018) 5519-5529.

[19] J. Kamcev, M. Galizia, F.M. Benedetti, E.-S. Jang, D.R. Paul, B.D. Freeman, G.S. Manning, Partitioning of mobile ions between ion exchange polymers and aqueous salt solutions: importance of counter-ion condensation, Physical Chemistry Chemical Physics 18(8) (2016) 6021-6031.

[20] J. Kamcev, D.R. Paul, B.D. Freeman, Ion activity coefficients in ion exchange polymers: applicability of Manning's counterion condensation theory, Macromolecules 48(21) (2015) 8011-8024.

[21] A. Kusoglu, A.Z. Weber, New insights into perfluorinated sulfonic-acid ionomers, Chemical reviews 117(3) (2017) 987-1104.

[22] G.M. Geise, L.P. Falcon, B.D. Freeman, D.R. Paul, Sodium chloride sorption in sulfonated polymers for membrane applications, Journal of Membrane Science 423 (2012) 195-208.

[23] G.M. Geise, B.D. Freeman, D.R. Paul, Sodium chloride diffusion in sulfonated polymers for membrane applications, Journal of membrane science 427 (2013) 186-196.

[24] G.M. Geise, C.M. Doherty, A.J. Hill, B.D. Freeman, D.R. Paul, Free volume characterization of sulfonated styrenic pentablock copolymers using positron annihilation lifetime spectroscopy, Journal of membrane science 453 (2014) 425-434.

[25] S. Kalakkunnath, D.S. Kalika, H. Lin, B.D. Freeman, Segmental relaxation characteristics of cross-linked poly (ethylene oxide) copolymer networks, Macromolecules 38(23) (2005) 9679-9687.

[26] A.C. Sagle, H. Ju, B.D. Freeman, M.M. Sharma, PEG-based hydrogel membrane coatings, Polymer 50(3) (2009) 756-766.

[27] G.M. Geise, D.R. Paul, B.D. Freeman, Fundamental water and salt transport properties of polymeric materials, Progress in Polymer Science 39(1) (2014) 1-42.

[28] J.M. Kim, B.S. Beckingham, Comonomer effects on co-permeation of methanol and acetate in cation exchange membranes, European Polymer Journal 147 (2021) 110307.

[29] B.S. Beckingham, N.A. Lynd, D.J. Miller, Monitoring multicomponent transport using in situ ATR FTIR spectroscopy, Journal of Membrane Science 550 (2018) 348-356.

[30] J.M. Kim, B.M. Dobyns, R. Zhao, B.S. Beckingham, Multicomponent transport of methanol and acetate in a series of crosslinked PEGDA-AMPS cation exchange membranes, Journal of Membrane Science 614 (2020) 118486.

[31] A. Allegrezza Jr, B. Parekh, P. Parise, E. Swiniarski, J. White, Chlorine resistant polysulfone reverse osmosis modules, Desalination 64 (1987) 285-304.

[32] J.M. Kim, B.S. Beckingham, Transport and co-transport of carboxylate ions and alcohols in cation exchange membranes, Journal of Polymer Science 59(21) (2021) 2545-2558.

[33] M. Soltanieh, S. Sahebdelfar, Interaction effects in multicomponent separation by reverse osmosis, Journal of Membrane Science 183(1) (2001) 15-27.

[34] Y. Yu, N. Yan, B.D. Freeman, C.-C. Chen, Mobile ion partitioning in ion exchange membranes immersed in saline solutions, Journal of Membrane Science 620 (2021) 118760.

[35] N. Yan, D.R. Paul, B.D. Freeman, Water and ion sorption in a series of cross-linked AMPS/PEGDA hydrogel membranes, Polymer 146 (2018) 196-208.

[36] F.G. Helfferich, Ion exchange, Courier Corporation1995.

[37] G.S. Manning, Limiting laws and counterion condensation in polyelectrolyte solutions I. Colligative properties, The journal of chemical Physics 51(3) (1969) 924-933.

[38] K.A. Thompson, R. Mathias, D. Kim, J. Kim, N. Rangnekar, J. Johnson, S.J. Hoy, I. Bechis, A. Tarzia, K.E. Jelfs, N-Aryl–linked spirocyclic polymers for membrane separations of complex hydrocarbon mixtures, Science 369(6501) (2020) 310-315.

[39] R.W. Baker, Membrane technology and applications, John Wiley & Sons2023.

[40] G. Geise, B. Freeman, D. Paul, Characterization of a sulfonated pentablock copolymer for desalination applications, Polymer 51(24) (2010) 5815-5822.

[41] E.-S. Jang, J. Kamcev, K. Kobayashi, N. Yan, R. Sujanani, T.J. Dilenschneider, H.B. Park, D.R. Paul, B.D. Freeman, Influence of water content on alkali metal chloride transport in cross-linked Poly (ethylene glycol) Diacrylate. 1. Ion sorption, Polymer 178 (2019) 121554.

[42] M. Galizia, D.R. Paul, B.D. Freeman, Liquid methanol sorption, diffusion and permeation in charged and uncharged polymers, Polymer 102 (2016) 281-291.

[43] K. Chang, H. Luo, G.M. Geise, Water content, relative permittivity, and ion sorption properties of polymers for membrane desalination, Journal of membrane science 574 (2019) 24-32.

[44] E.-S. Jang, J. Kamcev, K. Kobayashi, N. Yan, R. Sujanani, T.J. Dilenschneider, H.B. Park, D.R. Paul, B.D. Freeman, Influence of water content on alkali metal chloride transport in cross-linked Poly (ethylene glycol) diacrylate. 2. Ion diffusion, Polymer 192 (2020) 122316.

[45] G.S. Manning, Limiting laws and counterion condensation in polyelectrolyte solutions II. Self-diffusion of the small ions, The Journal of Chemical Physics 51(3) (1969) 934-938.

[46] H. Ju, A.C. Sagle, B.D. Freeman, J.I. Mardel, A.J. Hill, Characterization of sodium chloride and water transport in crosslinked poly (ethylene oxide) hydrogels, Journal of Membrane Science 358(1-2) (2010) 131-141.

[47] W.J. Horne, M.S. Shannon, J.E. Bara, Correlating fractional free volume to CO2 selectivity in [Rmim][Tf2N] ionic liquids, The Journal of Chemical Thermodynamics 77 (2014) 190-196.

[48] B.M. Dobyns, J.M. Kim, B.S. Beckingham, Multicomponent transport of methanol and sodium acetate in poly (ethylene glycol) diacrylate membranes of varied fractional free volume, European Polymer Journal 134 (2020) 109809.

[49] H. Lin, B.D. Freeman, S. Kalakkunnath, D.S. Kalika, Effect of copolymer composition, temperature, and carbon dioxide fugacity on pure-and mixed-gas permeability in poly (ethylene glycol)-based materials: Free volume interpretation, Journal of membrane science 291(1-2) (2007) 131-139.

[50] B.M. Dobyns, J.M. Kim, J. Li, Z. Jiang, B.S. Beckingham, Multicomponent transport of alcohols in Nafion 117 measured by in situ ATR FTIR spectroscopy, Polymer 209 (2020) 123046.

[51] R. Caminiti, P. Cucca, M. Monduzzi, G. Saba, G. Crisponi, Divalent metal–acetate complexes in concentrated aqueous solutions. An x-ray diffraction and NMR spectroscopy study, The Journal of chemical physics 81(1) (1984) 543-551.

[52] H.M. Rahman, G. Hefter, R. Buchner, Hydration of formate and acetate ions by dielectric relaxation spectroscopy, The Journal of Physical Chemistry B 116(1) (2012) 314-323.

[53] R.A. Robinson, R.H. Stokes, Electrolyte solutions, Courier Corporation2002.

[54] E. Nightingale Jr, Phenomenological theory of ion solvation. Effective radii of hydrated ions, The Journal of Physical Chemistry 63(9) (1959) 1381-1387.

[55] E.E. Hills, M.H. Abraham, A. Hersey, C.D. Bevan, Diffusion coefficients in ethanol and in water at 298 K: Linear free energy relationships, Fluid Phase Equilibria 303(1) (2011) 45-55.

[56] P. Vanýsek, Ionic conductivity and diffusion at infinite dilution, CRC handbook of chemistry and physics 94 (1993).

[57] L. Hao, D.G. Leaist, Binary mutual diffusion coefficients of aqueous alcohols. Methanol to 1-heptanol, Journal of Chemical & Engineering Data 41(2) (1996) 210-213.

[58] J.R. Rustad, S.L. Nelmes, V.E. Jackson, D.A. Dixon, Quantum-chemical calculations of carbon-isotope fractionation in CO2 (g), aqueous carbonate species, and carbonate minerals, The Journal of Physical Chemistry A 112(3) (2008) 542-555.

[59] A. Tongraar, B.M. Rode, The hydration structures of F− and Cl− investigated by ab initio QM/MM molecular dynamics simulations, Physical Chemistry Chemical Physics 5(2) (2003) 357-362.

[60] A. Tongraar, T. Jiraroj, S. Rujirawat, S. Limpijumnong, Structure of the hydrated Ca2+ and Cl−: Combined X-ray absorption measurements and QM/MM MD simulations study, Physical Chemistry Chemical Physics 12(36) (2010) 10876-10887.

[61] H. Yasuda, C. Lamaze, L. Ikenberry, Permeability of solutes through hydrated polymer membranes. Part I. Diffusion of sodium chloride, Die Makromolekulare Chemie: Macromolecular Chemistry and Physics 118(1) (1968) 19-35.

[62] H. Yasuda, A. Peterlin, C. Colton, K. Smith, E. Merrill, Permeability of solutes through hydrated polymer membranes. Part III. Theoretical background for the selectivity of dialysis membranes, Die Makromolekulare Chemie: Macromolecular Chemistry and Physics 126(1) (1969) 177-186.

[63] R. Sartori, L. Sepulveda, F. Quina, E. Lissi, E. Abuin, Binding of electrolytes to poly (ethylene oxide) in aqueous solutions, Macromolecules 23(17) (1990) 3878-3881.

[64] P.J. Flory, Principles of polymer chemistry, Cornell university press1953.

[65] C.M. Hansen, The three dimensional solubility parameter, Danish Technical: Copenhagen 14 (1967).

[66] W. Hayduk, H. Laudie, Prediction of diffusion coefficients for nonelectrolytes in dilute aqueous solutions, AIChE Journal 20(3) (1974) 611-615.

[67] J. Mackie, P. Meares, The diffusion of electrolytes in a cation-exchange resin membrane I. Theoretical, Proceedings of the Royal Society of London. Series A. Mathematical and Physical Sciences 232(1191) (1955) 498-509.

[68] D. Hallinan, N. Balsara, Annual Review of Materials Research, Annual Reviews, Palo Alto2013.

[69] H.S. Harned, C.L. Hildreth Jr, The differential diffusion coefficients of lithium and sodium chlorides in dilute aqueous solution at 25, Journal of the American Chemical Society 73(2) (1951) 650-652.

Chapter 5: Single and Co-transport of Methanol and Acetate in CEMs

---

Reproduced from: Kim, J. M.; Lin, Y.-H.; Aravindhan, P. P.; Beckingham, B. S. Impact of Hydrophobic Pendant Phenyl Groups on Transport and Co-Transport of Methanol and Acetate in PEGDA-SPMAK Cation Exchange Membranes. Chemical Engineering Research and Design 2022, 185, 418–429. DOI:10.1016/j.cherd.2022.07.017.

5.1. Introduction

Artificial photosynthetic applications such as photoelectrochemical CO_2 reduction cells (PEC-CRCs [1]) are a promising approach for reducing atmospheric CO_2, which is a primary greenhouse gas of concern for climate change. Due to a lack of catalyst specificity, CO_2 is often being reduced to a variety of chemicals within a device [2], including carbon monoxide (CO), methane (CH_4), ethylene (C_2H_4), formate (OFm^-), acetate (OAc^-), methanol (MeOH), and ethanol (EtOH) [3]. PEC-CRCs incorporate either a CEM [4, 5] or anion exchange membrane (AEM) [6-11] to provide ion-selective transport and an electrolyte (i.e. potassium bicarbonate ($KHCO_3$) [9, 12]to facilitate the CO_2 reduction process. Recently, Singh and Bell devised an advanced PEC-CRC [1], which targets maximizing the recovery of alcohols (MeOH and EtOH) to utilize as carbon neutral fuels. One of the major challenges of this approach is the current lack of ion exchange membranes that sufficiently minimize the crossover of electrolyte-dissolved CO_2 reduction products [13-18] and OAc^- [8, 18, 19], which results in their subsequent oxidation back

to CO_2 and other by-products. In this context, understanding the transport behavior of CO_2 reduction products is important to design a target-specific membrane.

Single permeant transport behavior in hydrated ion exchange membranes has been investigated to understand the interactions between membrane bound ions and mobile permeants (e.g., Donnan exclusion [20], counterion condensation [21, 22], volume expansion [16], and charge screening [23-25]). However, relatively few efforts have been made to analyze and understand multi-solute transport behavior [8, 11, 13, 17, 18, 26]. Previously, our group observed increased permeabilities, P_i, of CEMs (Nafion® 117 [18] and PEGDA-AMPS [19]) to carboxylates (OFm^- and OAc^-) in the presence of an alcohol (either MeOH or EtOH) [26]. It was found that this behavior is mainly due to a change in diffusivities, D_i, as opposed to solubilities, K_i (solution-diffusion model, $P_i = K_i \times D_i$ [26-28]. As this type of transport behavior is concerning [29], we examined a series of comonomers with pendant groups with varied number of ethylene oxide groups (*n*) in the side chain: carboxyl (n = 0), ethylene oxide (n = 1), and PEG (n = 5)) by incorporating the comonomer (acrylic acid (AA), hydroxyethyl methacrylate (HEMA), and poly(ethylene glycol) methacrylate (PEGMA), respectively) in a model CEM, which we prepared with a crosslinker, (PEGDA, n = 13 [30-32], and a comonomer with a terminal negatively- charged sulfonate, 2-acrylamido-2-methylpropanesulfonic acid (AMPS [33-35]), namely PEGDA-AMPS/AA, PEGDA-AMPS/HEMA, PEGDA-AMPS/PEGMA [8]. While OAc^- permeabilities of PEGDA-AMPS/HEMA and PEGDAAMPS/ AA increased in co-permeation with an alcohol (MeOH), those of PEGDA-AMPS/PEGMA in co-permeation were consistent with OAc^- permeabilities by itself [8]. We then focused on PEGDA-AMPS/ PEGMA films to examine how pendant PEO chains impact behavior, where we reported (1) the change in permeabilities is due to

the change in diffusivities and (2) electrostatic interactions between polymer-bound sulfonate and mobile acetate anions may be suppressed by the long PEO pendant chains (n = 5) and, therefore, the electrostatic repulsion may already be suppressed even in single diffusion [36].

Here, we investigate two additional pendant chains, phenoxyethyl acrylate (PEA, n = 1) and poly(ethylene glycol) phenyl ether acrylate (PEGPEA, n = 3) on OAc^- diffusion in transport and co-transport with MeOH through a model crosslinked CEM that is prepared with PEGDA (*n* = 13) and a negative-charged comonomer, 3-sulfopropyl methacrylate potassium (SPMAK). As in PEGDA-AMPS, and discussed below, we observe OAc^- diffusivities of PEGDA-SPMAK increase in co-diffusion with MeOH. This is presumably due to charge screening by the co-transporting alcohol as shown schematically in Figure 5.1 (A, D).

Conversely, we observe distinct behavior in PEGPEA-containing films, namely PEGDA-PEGPEA and PEGDA-SPMAK/ PEGPEA. OAc^- diffusivities of sulfonate-free PEGDA-PEGPEA films increase in co-diffusion. We postulate that this distinct difference is, at least in part, due to changes (increased) in segmental dynamics of the network from the interactions of MeOH with the relatively long (n = 3) and bulky (with phenyl group) PEGPE chains; see Figure 5.1 (C, F). On the other hand, OAc^- diffusivities of PEGDA-SPMAK/PEGPEA films decrease in co-diffusion, which conversely could be linked to decreased segmental dynamics as SPMAK-PEGPEA sidechain interactions induce steric effects; see Figure 5.1 (B, E). These empirical-based conjectures are further discussed in the context of our physiochemical and transport results.

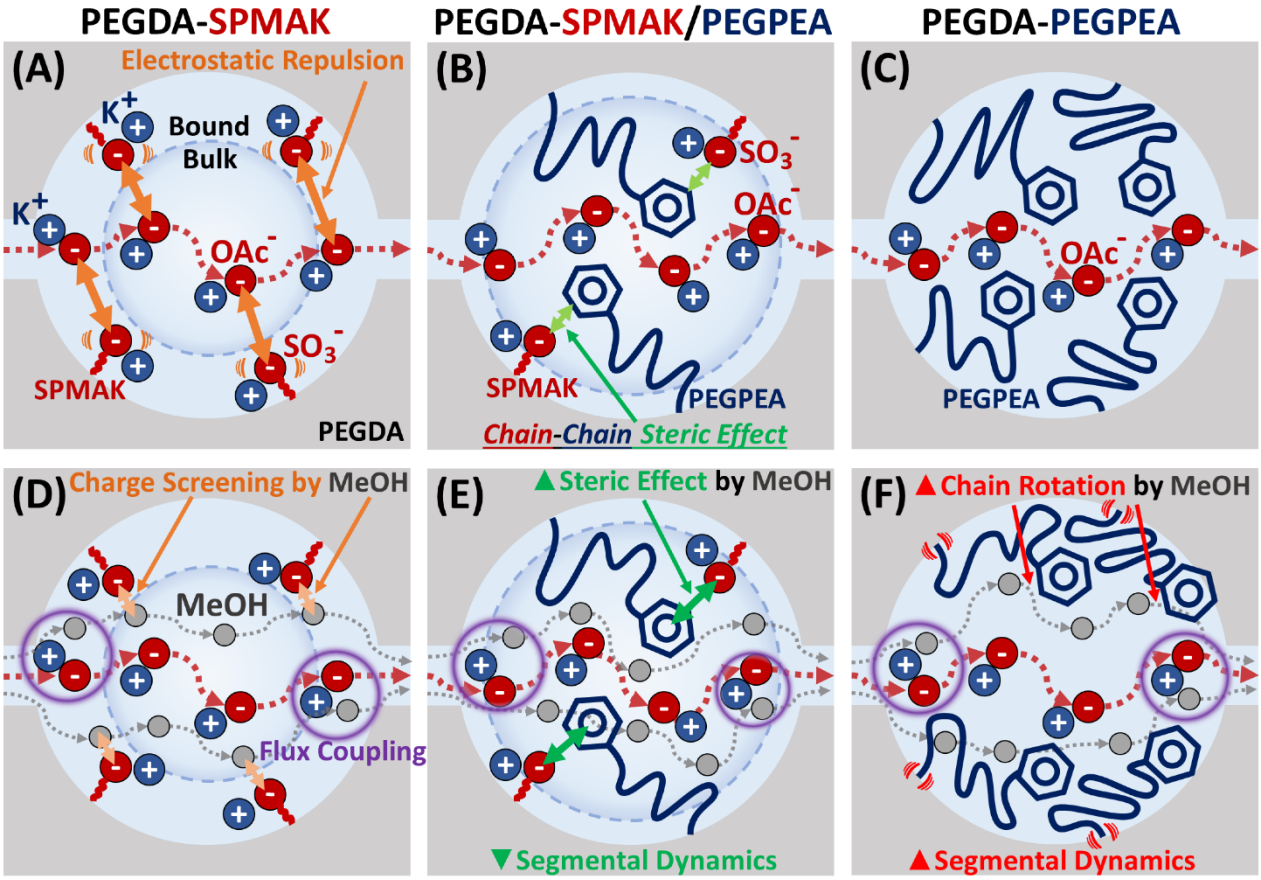

Figure. 5.1. Illustration of KOAc diffusion in (A-C) single and (D-F) co-diffusion with MeOH. (A,D) PEGDA-SPMAK, (B,E) PEGDASPMAK/PEGPEA, and (C,F) PEGDA-PEGPEA.

5.2. Results and Discussion

The materials, membrane synthesis methods, and experimental procedures are detailed in Chapter 3. A series of binary films were prepared, as shown in Table 5.1 and Figure 5.2, PEGDA-SPMAK (P-S), PEGDA-PEA (P-E), and PEGDA-PEGPEA (P-G), and ternary films, PEGDA-SPMAK/PEA (P-S/E) and PEGDA-SPMAK/PEGPEA (P-S/G), to investigate the impact of varied sidechain length, PEA (n = 1) and PEGPEA (n = 3), on the multi-solute transport of MeOH and KOAc in CEMs. Moreover, the impact of interactions between (1) mobile MeOH (partially

hydrophobic) and PEGPEA (hydrophobic) chains and (2) SPMAK (hydrophilic) and PEGPEA on the observed transport behavior are conjectured.

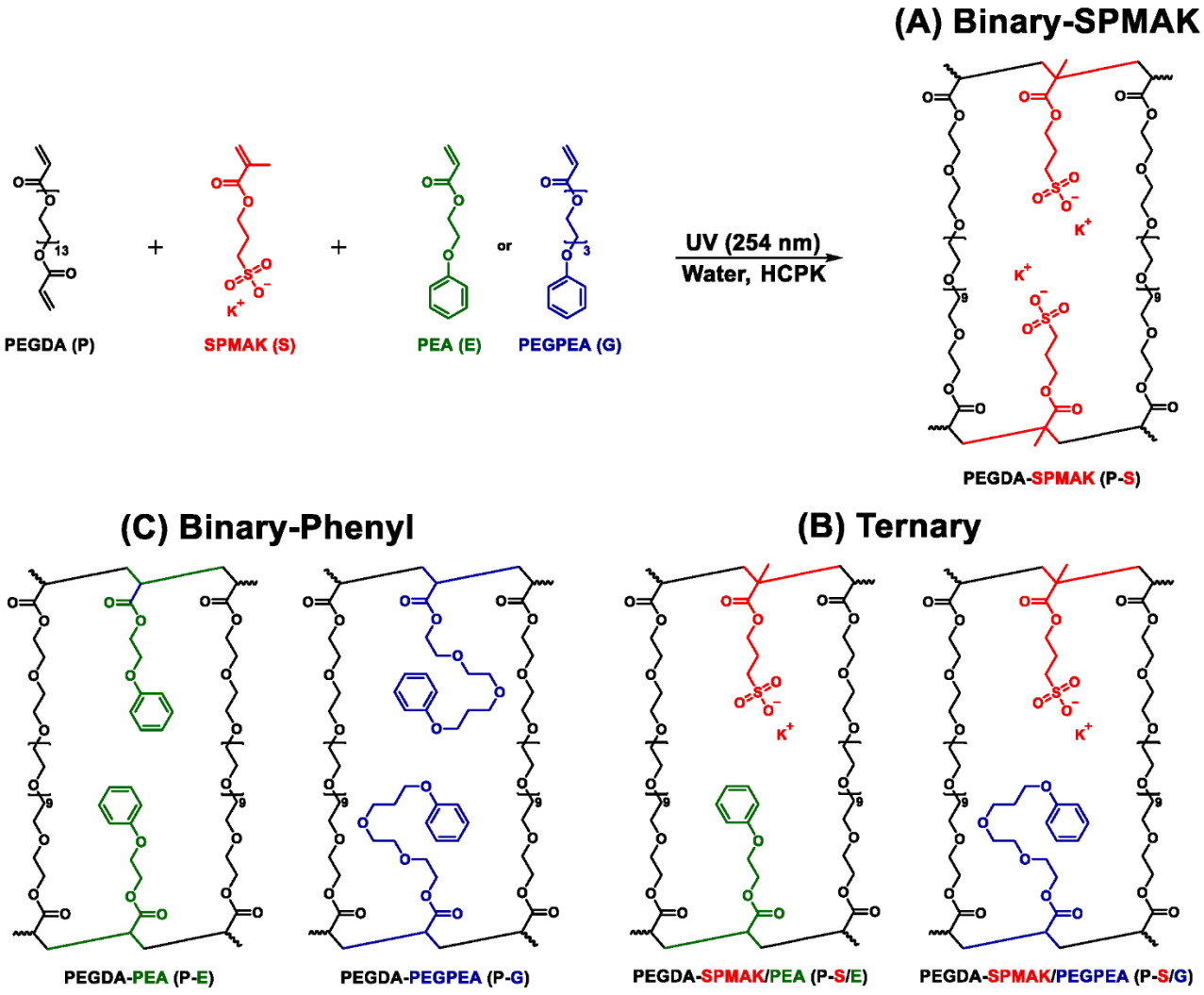

Figure 5.2. Scheme of prepared (A) binary-SPMAK films, P-S, (B) binary-phenyl films, P-E and P-G, and (C) ternary films, P-S/E and P-S/G.

Table 5.1. Membrane characteristics from pre-polymerization mixtures.

	SPMAK[a] (mol %)	E or G[b] (mol %)	PEGDA (g)	SPMAK (g)	E or G[b] (g)	Water (g)	HCPK (g)
1. P	-	-	8.00	-	-	2.00	0.008
2. P-S16	16	-	7.50	0.50	-	2.00	0.008
3. P-S24	24	-	7.20	0.80	-	2.00	0.008
4. P-S32	32	-	6.86	1.14	-	2.00	0.008
5. P-E16	-	16	7.60	-	0.40	2.00	0.008
6. P-E32	-	32	7.08	-	0.92	2.00	0.008
7. P-G16	-	16	7.35	-	0.65	2.00	0.008
8. P-G32	-	32	6.57	-	1.43	2.00	0.008
9. P-S16/E16	16	16	6.97	0.58	0.45	2.00	0.008
10. P-S24/E8	24	8	6.92	0.86	0.22	2.00	0.008
11. P-S16/G16	16	16	6.71	0.56	0.73	2.00	0.008
12. P-S24/G8	24	8	6.79	0.84	0.37	2.00	0.008

[a]SPMAK = mol of SPMAK/(mol of PEGDA + mol of SPMAK + mol of E or G) × 100 %
[b]E or G = mol of E or G/(mol of PEGDA + mol of SPMAK + mol of E or G) × 100 %

5.2.1. Ionic Conductivity and IEC of Membranes

Measured ionic conductivity of SPMAK-containing films (P-S, P-S/E, and P-S/G) are shown in Figure 5.3 and Table 5.2. SPMAK-free membranes (P, P-E, and P-G) were not measured as they do not contain charged moieties [8]. As expected, ionic conductivities of SPMAK-containing films increase with increasing SPMAK content and are otherwise consistent across the membrane chemistries examined here [8, 36]. Likewise, the IEC of each membrane increases as SPMAK content increases due to the increase in sulfonate content and thereby counterion content. Notably, the average difference between theoretical and measured IEC values are in good agreement (2 %), as shown in Table 5.2.

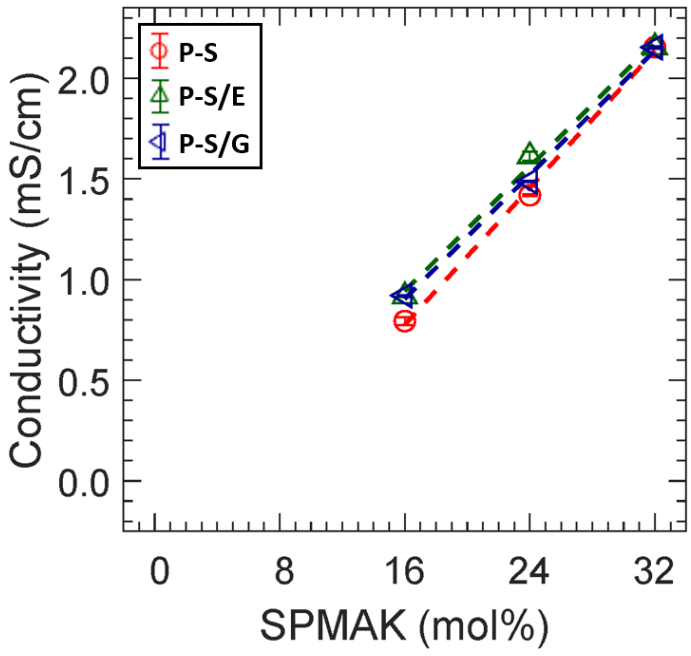

Figure 5.3. Ionic conductivity of P-S, ○, P-S/E, △, and P-S/G, ◁. Standard deviations are denoted by error bars and lines provided as a guide.

Table 5.2. Measured Conductivities and IECs

	PEGDA (mol%)	SPMAK (mol%)	Conductivity (σ, mS/cm)	Theoretical IEC (meq/g dry polymer)[a]	Measured IEC (meq/g dry polymer)
P-S	100	0	-	-	-
	84	16	0.79 ± 0.02	0.26	0.27 ± 0.01
	76	24	1.42 ± 0.00	0.41	0.40 ± 0.01
	68	32[b]	2.15 ± 0.01	0.58	0.57 ± 0.01
P-S/E	68	0	-	-	-
	68	16	0.92 ± 0.00	0.29	0.29 ± 0.00
	68	24	1.61 ± 0.02	0.44	0.43 ± 0.01
	68	32[b]	2.15 ± 0.01	0.58	0.57 ± 0.01
P-S/G	68	0	-	-	-
	68	16	0.92 ± 0.00	0.28	0.28 ± 0.00
	68	24	1.49 ± 0.00	0.43	0.42 ± 0.01
	68	32[b]	2.15 ± 0.01	0.58	0.57 ± 0.01

[a]Theoretical IEC = mmol SPMAK/(PEGDA mass + SPMAK mass + Comonomer mass (E or G)
[b]These are the same film.

5.2.2. Membrane Water Volume Fraction

Measured water uptakes and dry polymer densities (see Table 5.3) were used to calculate membrane water volume fractions (Figure 5.4 and Table 5.3). Generally, water volume fractions of P-S films increase with SPMAK content (decreased with PEGDA content); see Figure 5.4 (A). This is likely due to (1) bound sulfonate anions being hydrophilic and holding more water molecules than PEGDA [4] and (2) crosslink densities of the films decrease as PEGDA content decreases [31]. In the case of P-E and P-G films, water volume fractions are essentially the same; see Figure 5.4 (B, C). This is likely due to the decrease in crosslinking (and consequently increase in water volume fraction) being offset by inclusion of the more hydrophobic phenyl-containing pendant groups (PEA and PEGPEA). In ternary films (PS/E, and P-S/G), water volume fractions increase with SPMAK content (decrease with phenyl content); see Figure 5.4 (D, E). This is due to the increase in sulfonate group content (hydrophilic) and a decrease in the phenyl group content (hydrophobic).

Table 5.3. Water uptake, dry polymer density, water volume fraction, crosslink density, and glass transition temperature of all membranes.

	SPMAK (mol%)	Water uptake (ω_w, g H_2O/g dry membrane ·100%)	Dry polymer density (g/mL)	Water volume fraction	Storage modulus (MPa)	Glass transition (°C)
1. P	-	62 ± 3	1.20 ± 0.00	0.428 ± 0.011	25.6 ± 0.8	-43 ± 1
2. P-S16	16	75 ± 0	1.22 ± 0.00	0.478 ± 0.001	28.2 ± 1.3	-33 ± 3
3. P-S24	24	79 ± 3	1.24 ± 0.01	0.495 ± 0.010	28.3 ± 0.3	-33 ± 2
4. P-S32	32	84 ± 0	1.25 ± 0.01	0.514 ± 0.001	29.1 ± 2.5	-29 ± 2
5. P-E16	-	65 ± 0	1.22 ± 0.01	0.441 ± 0.002	25.8 ± 1.8	-36 ± 2
6. P-E32	-	63 ± 0	1.21 ± 0.00	0.433 ± 0.001	25.4 ± 3.3	-33 ± 2
7. P-G16	-	58 ± 0	1.20 ± 0.00	0.412 ± 0.001	24.3 ± 1.5	-38 ± 1
8. P-G32	-	56 ± 1	1.19 ± 0.01	0.403 ± 0.003	24.9 ± 1.4	-38 ± 0
9. P-S16/E16	16	70 ± 0	1.22 ± 0.00	0.460 ± 0.000	23.2 ± 1.4	-30 ± 2
10. P-S24/E8	24	74 ± 1	1.23 ± 0.00	0.477 ± 0.003	24.2 ± 3.6	-32 ± 2
11. P-S16/G16	16	68 ± 0	1.21 ± 0.00	0.454 ± 0.000	24.3 ± 2.8	-28 ± 3
12. P-S24/G8	24	76 ± 1	1.24 ± 0.01	0.485 ± 0.002	26.8 ± 5.7	-31 ± 2

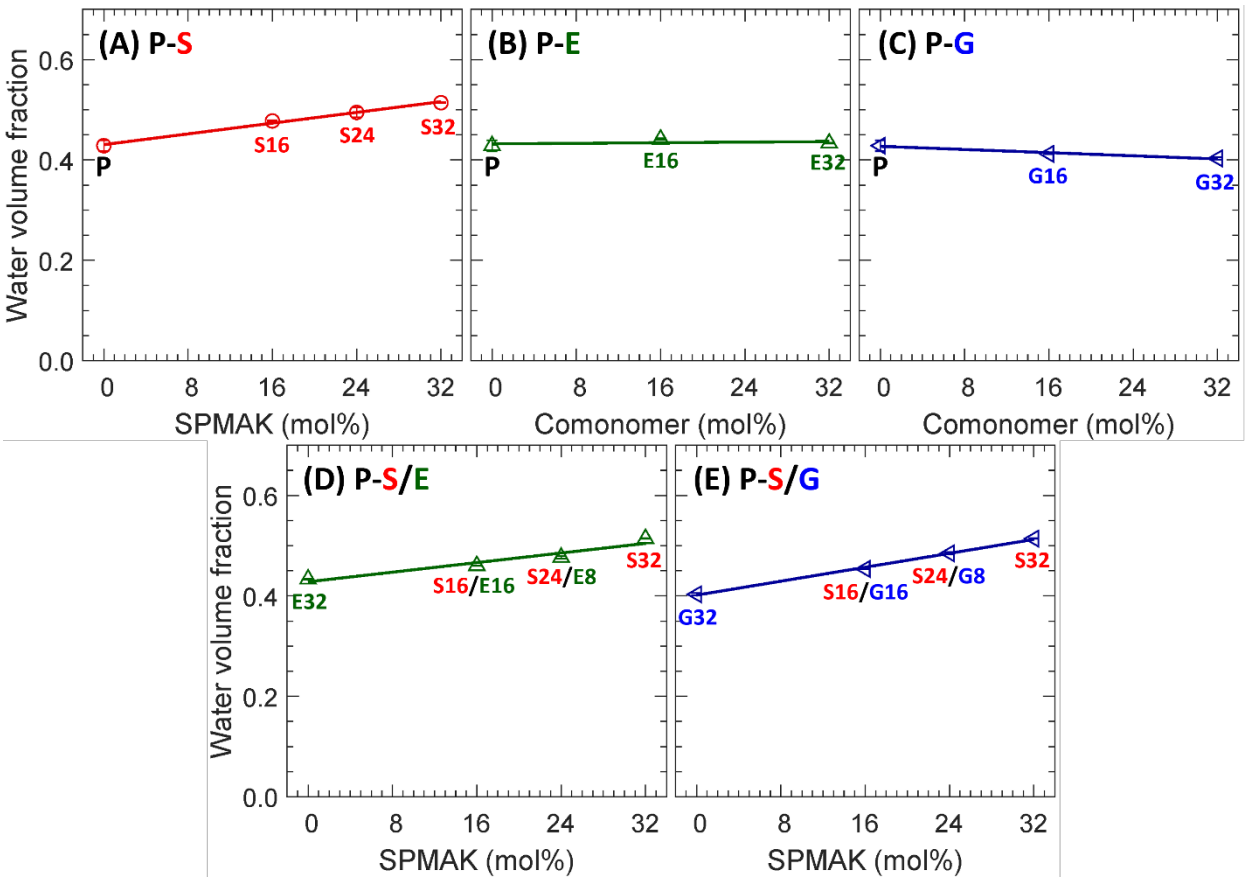

Figure 5.4. Water volume fraction of (A) P-S, ○, (B) P-E, △, (C) P-G, ◁, (D) P-S/E, △, and (E) P-S/G, ◁. The error bars show the standard deviation and all lines are a guide to the eye.

5.2.3. Storage Modulus

Measured storage moduli are shown in Figure 5.5 and Table 5.3. Generally, storage moduli increase as the water volume fraction increases and for P-S films as SPMAK content increases (Figure 5.5 (A)). This behavior is partially due to the presence of the methyl group in the methacrylate (as opposed to acrylates) of SPMAK, which increases polymer backbone rigidity (a steric effect [37]) and, therefore, allows for storage of more mechanical energy. Yan et al.

conducted similar experiments on analogous films (PEGDA-AMPS, where AMPS is an acrylate (no additional methyl group)) and reported the storage moduli of PEGDA-AMPS films decrease as AMPS content increases, due to the reduced crosslink density as PEGDA is replaced by the pendent comonomer (AMPS) [33]. The difference in these, and many other, studies suggest various factors impact the storage modulus of copolymeric hydrogels (itself a field of intense interest across a wide range of applications) [38]. The storage modulus of both P-E (n = 1) and P-G (n = 3) films was essentially the same with increasing phenyl content; see Figure 5.5 (B, C). This indicates the presence of the two additional ethylene oxide repeat units on the PEGPEA sidechain have a negligible impact on the storage modulus. In the case of ternary films, the storage modulus generally increases with increasing SPMAK content; see Figure 5.5 (D, E). This is presumably due to the interactions between hydrophilic SPMAK and hydrophobic PEA or PEGPEA chains leading to decreased polymer segmental dynamics (reduction in storage modulus).

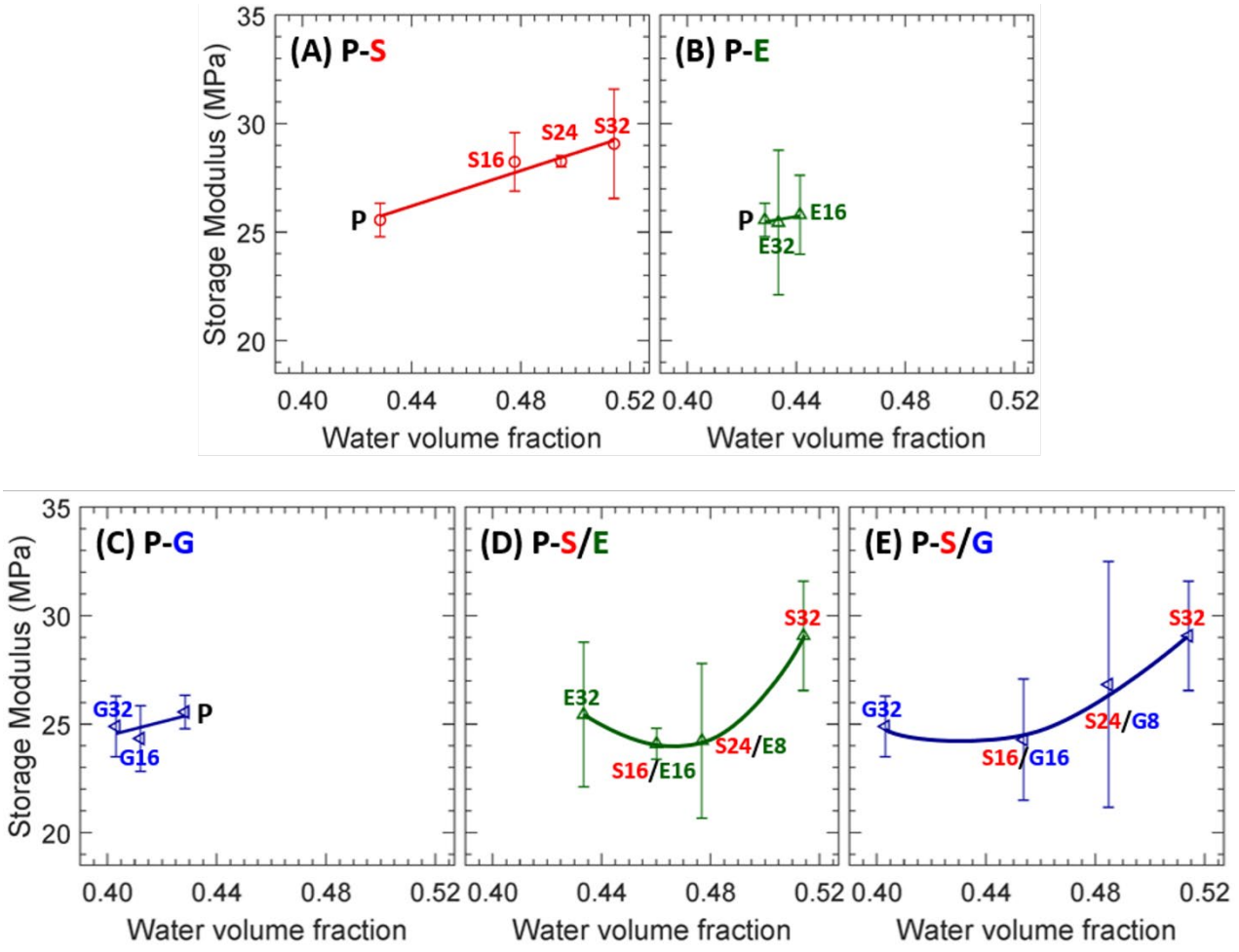

Figure 5.5. Storage modulus of (A) P-S, ○, (B) P-E, △, (C) P-G, ◁, (D) P-S/E, △, and P-S/G, ◁. The error bars show the standard deviation and all lines are a guide to the eye.

5.2.4. Membrane Permeability

Membrane permeabilities were measured by diffusion cell experiments, as shown in Figure 5.6. Additionally, the volume expansion of each membrane was estimated from the film thickness before (hydrated) and after permeation, as measured by a digital caliper to get the average of 5 random locations; see Table 5.4 for normalized values. Generally, the thickness of all films

did not change significantly. For instance, the thickness of the film after single MeOH permeation was essentially the same (increased by 0.2 %), on average, and those of the film after single KOAc permeation and co-permeation (1 M of each in feed) were slightly decreased by 1.4 % and 1.6 %, respectively, on average. A contribution to the observed slight deswelling in KOAc permeation experiments is the difference in osmotic pressure as the water concentration in the hydrated film is higher than that of the salt solution in the feed cell [18, 39].

Generally, MeOH permeabilities increase as SPMAK content increases (Figure 5.6 (A, D, E)) and slightly decrease with increasing phenyl-containing comonomer content (Figure 5.6 (B-E)). These trends are somewhat consistent with those observed in the water volume fraction (Figure 5.4), which increase with increasing SPMAK content (Figure 5.6 (A, D, E)) and slightly decrease with increasing phenyl-containing comonomer content (Figure 5.4 (D, E)). In co-permeation with KOAc, MeOH permeabilities decrease slightly. We observed similar behaviors elsewhere [8, 14, 18, 19, 26]. As the permeability, P, is a product of solubility, K, and diffusivity, D (solution-diffusion model), this co-transport behavior will be examined in terms of sorption and diffusion in the following sections. Nevertheless, a reduction in membrane permeability to MeOH is favorable for typical CO_2 reduction cells (minimization of product crossover).

In the case of binary films (P-S, P-E, and P-G), KOAc permeabilities in single permeation decrease with increasing comonomer content (both sulfonate and phenyl contents); see solid lines in Figure 5.6 (A-C). A contribution to the decrease of P-S permeabilities to KOAc is electrostatic repulsion (Donnan exclusion [20]), where repulsive interactions between mobile OAc^- and bound sulfonate anions increase with IEC (Table 5.2). A possible contribution to the decrease in KOAc permeabilities in P-E and P-G is the hydrophobicity of the bound phenyl groups and hydrophilicity

of the mobile KOAc which together lead to a repulsive interaction. In the case of ternary films (P-S/E and P-S/G), KOAc permeabilities in single permeation increase with increasing SPMAK content; see solid lines in Figure 5.6 (D, E). This is consistent with the behavior in binary films as the permeabilities decrease more rapidly with increasing phenyl content than with increasing SPMAK content.

In the case of co-permeation with MeOH, KOAc permeabilities of P-S films increase. We observed similar behavior in other CEMs (Nafion® 117 [18, 26] and PEGDA-AMPS [19, 26], where we conjectured the electrostatic interaction between polymer-bound sulfonate anions and mobile carboxylate anions is suppressed by mobile alcohols (charge screening [18, 19, 23, 25, 26]; see Fig. 5.1(A,D). KOAc permeabilities in co-permeation with MeOH for P-E and P-G films are similar and higher, respectively, compared to those measured by itself. To rationalize these differences in co-permeation, we conjecture potential changes in polymer segmental dynamics in the presence of MeOH. As MeOH is more hydrophobic than ionized K^+ and OAc^- in water, MeOH has more associations with and may permeate closer to the hydrophobic phenyl groups leading to increased segmental dynamics by facilitating mobility (chain rotation) of the sidechains [40]. Due to the longer sidechain for P-G (n = 3) compared to P-E (n = 1) films, the impact of this type of interaction would be greater for P-G films. Discussion on this type of behavior conjectures is continued in the diffusivity section below. For P-S/E films, KOAc permeabilities gradually increase with increasing SPMAK content. This is also likely a result of the screening of electrostatic repulsion between bound sulfonates and mobile carboxylates by mobile MeOH and, therefore, easier to permeate in co-diffusion [26]. While KOAc permeabilities of P-S and P-G films increase in co-transport with MeOH, those of P-S/G films (P-S16/G16 and P-S24/G8) are

essentially the same; see Figure 5.6 (E). A possible cause is the internal structure of P-S/G films being different from P-S and P-G films. To further correlate this transport behavior with the polymer network behavior, we measured the glass transition temperature (T_g) of all films; see Figure 5.7. The T_g generally increased with SPMAK content. Generally, more permeation (and diffusion) is expected for polymer films with a lower T_g due to higher segmental dynamics at a consistent operating temperature [41]. Once again, the S16/G16 permeability to KOAc in single permeation (1.2 ×10-7 cm^2/s) is similar to that in G32 (1.2 ×10-7 cm^2/s) but the S16/G16 permeability to KOAc in co-permeation (1.2 ×10-7 cm^2/s) is lower than that in G32 (1.6 ×10-7 cm^2/s). We conjecture this unexpected behavior is due to the impact of co-permeating MeOH on the internal structure of the polymer (S16/G16), consisting of both SPMAK (hydrophilic sulfonate) and PEGPEA (hydrophobic phenyl with a longer ethylene glycol chain, n = 3). More discussion on these conjectures will be continued in the following section.

Table 5.4. Normalized film thickness to hydrated membrane after permeability measurements.

	SPMAK (mol%)	Water	1 M MeOH	1 M KOAc	1 M MeOH and KOAc
1. P	-	1.00 ± 0.00	0.99 ± 0.01	0.99 ± 0.01	0.99 ± 0.01
2. P-S16	16	1.00 ± 0.01	1.00 ± 0.01	1.00 ± 0.01	0.98 ± 0.01
3. P-S24	24	1.00 ± 0.00	1.02 ± 0.01	0.99 ± 0.01	1.00 ± 0.01
4. P-S32	32	1.00 ± 0.00	1.01 ± 0.00	0.98 ± 0.00	0.99 ± 0.01
5. P-A16	-	1.00 ± 0.00	1.00 ± 0.01	0.98 ± 0.01	0.98 ± 0.00
6. P-A32	-	1.00 ± 0.02	0.99 ± 0.01	0.98 ± 0.00	0.98 ± 0.01
7. P-G16	-	1.00 ± 0.01	1.00 ± 0.00	0.99 ± 0.00	1.00 ± 0.01
8. P-G32	-	1.00 ± 0.02	1.01 ± 0.00	0.99 ± 0.01	0.99 ± 0.01
9. P-S16/E16	16	1.00 ± 0.00	1.01 ± 0.00	1.00 ± 0.00	1.00 ± 0.01
10. P-S24/E8	24	1.00 ± 0.00	1.01 ± 0.01	0.99 ± 0.01	0.99 ± 0.01
11. P-S16/G16	16	1.00 ± 0.02	0.98 ± 0.00	0.96 ± 0.01	0.97 ± 0.00
12. P-S24/G8	24	1.00 ± 0.00	1.00 ± 0.00	0.98 ± 0.01	0.97 ± 0.00
Average		**1.000**	**1.002**	**0.986**	**0.984**

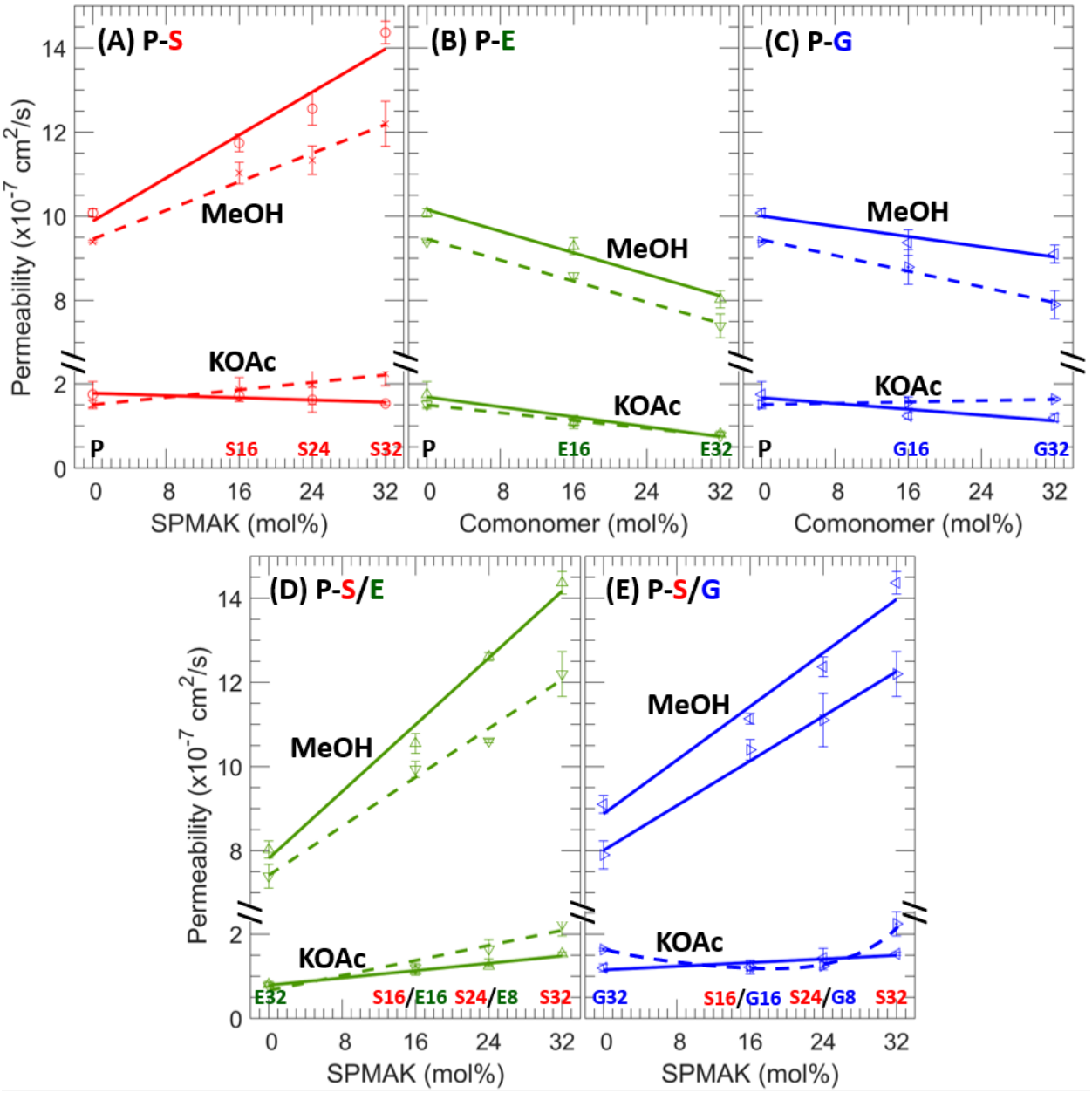

Figure 5.6. Permeabilities of all films to (A-E) MeOH and KOAc measured in one-component (solid line) and two-component (dashed), which consist of (A) P-S (red, one: ○ and two: ×), (B) P-E (green, one: △ and two: ▽), (C) P-G (blue, one: ◁ and two: ▷), (D) P-S/E (green, one: △ and two: ▽), and (E) P-S/G (blue, one: ◁ and two: ▷) films. The error bars show the standard deviation and all lines are a guide to the eye.

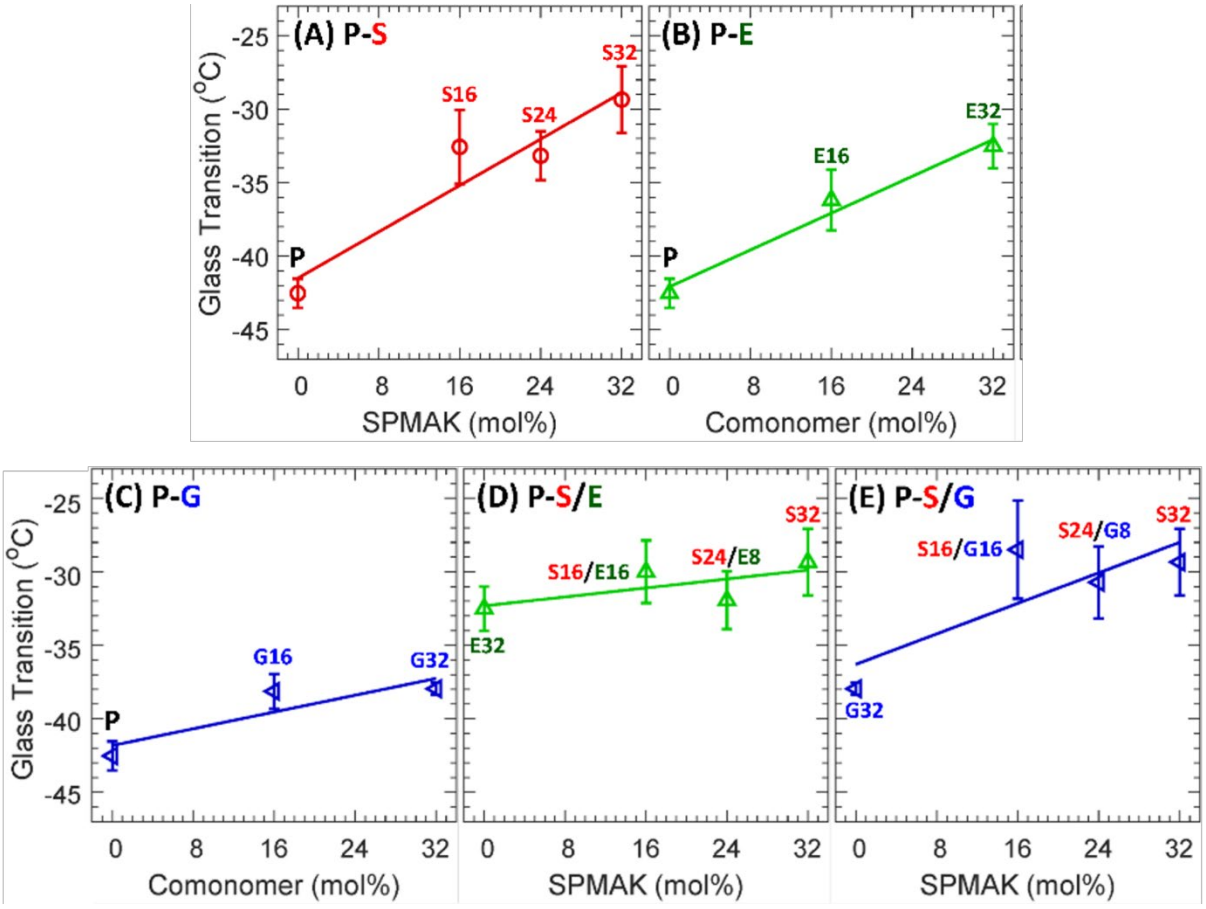

Figure 5.7. Glass transition temperature (T_g, °C) of (A-C) binary films (P-S, P-E, and P-G) and (D,E) ternary films (P-S/E and P-S/G).

5.2.5. Membrane Solubility

Solubilities to MeOH and KOAc were determined by sorption-desorption experiments and values are shown in Figure 5.8. Additionally, the volume expansion of each membrane was calculated from the volumes of the film before (hydrated) and after sorption (solvated) in each solution (1 M MeOH, 1 M KOAc, or 1 M of each); Table 5.5. Generally, the volumes of all films did not change significantly. For instance, the volume of the film after sorption in 1 M MeOH was

essentially the same and those of the film after sorption in KOAc-containing solutions (1 M KOAc and 1 M of each) were slightly deswelled by 1.07 times, on average. A contribution to this deswelling is the difference in osmotic pressure, where the concentration of water within the film is higher than that in the external solution [18, 39].

For single sorption, as the SPMAK content increases so does the MeOH solubilities of P-S films; see solid line in Figure 5.8 (A). This is presumably linked to free volume increases (as indicated by the water volume fraction, Fig. 5.4 (A)), which introduces more regions for the polymer network to interact with the solution (1 M MeOH). Moreover, due to their relative hydrophobicity MeOH is somewhat more preferred by the polymer film over water [40]; see solid lines in Figure 5.8 (B). MeOH solubilities of P-E and P-G films were also increased with increasing comonomer content. It is likely this is due to the increasing hydrophobicity of the polymer with the introduction of phenyl groups and, therefore, more MeOH is expected to interact with the film. For ternary film (P-S/E and P-S/G), MeOH solubilities slightly increase with increasing SPMAK content; see solid lines in Figure 5.8 (D, E). This is consistent with binary films (P-S, P-E, and P-G), as the MeOH solubility increases more rapidly in P-S films than in other films.

In the case of single sorption, KOAc solubilities in P-S films decrease with increasing SPMAK content; see the solid line in Figure 5.8 (A). This is partly a result of electrostatic repulsion (Donnan exclusion [20]) between polymer-bound sulfonate anions and mobile OAc^-. Similarly, KOAc solubilities of P-E and P-G films slightly decrease with increasing comonomer content due to the increased film hydrophobicity with increasing phenyl content; see solid lines in Figure 5.8 (B, C). For ternary films, KOAc solubilities slightly decrease with increasing SPMAK content;

see solid lines in Figure 5.8 (D, E). Again, this is consistent with the binary films, as the decrease in KOAc solubilities is more rapid in P-S films than in other films.

In the case of co-sorption (1 M each solute), both MeOH and KOAc solubilities increase; see dashed lines in Figure 5.8. One contribution to this behavior is the larger difference in osmotic pressure inside the film and the external solution in co-sorption (less water in the external solution). As a result, more water in the film will be replaced by solutes (MeOH or KOAc) from the external solution. While MeOH solubilities of P-S films increase to a similar degree with increasing comonomer content (Figure 5.8 (A)), the gap between those of P-E and P-G films in single and co-permeation becomes narrower with increasing comonomer content (Figure 5.8 (B, C)). For example, MeOH solubilities of P-E and P-G films increase by 1.4, 1.2, and 1.1 times, respectively, on average, with increasing comonomer content (0, 16, and 32 mol%). This type of behavior was also observed in ternary films, where the gap between single and co-permeation becomes narrower with increasing phenyl content (decreasing SPMAK content); see Figure 5.8 (D, E). This behavior may be rationalized somewhat by the relative hydrophobicity of KOAc, MeOH, and the film-bound phenyl groups, where the overall polymer segmental dynamics can be suppressed in the presence of hydrophilic KOAc and can be increased in the presence of partially hydrophobic MeOH as these solutes interact with the film-bound phenyl groups (described above) [42]. However, we note this remains a conjecture as the underlying solute-solute-polymer interactions that lead to this type of behavior are complex.

In the case of co-sorption, KOAc solubilities of P-S films increase uniformly; see Figure 5.8 (A). Again, this is partially due to an increase in osmotic pressure (larger water concentration difference in binary mixture, 1 M each). In the case of phenyl-containing films (P-E, P-G, P-S/E,

and P-S/G), KOAc solubilities slightly increase in co-sorption; see Figure 5.8 (B-D). Nonetheless, the differences between those solubilities measured in single and co-sorption are very close to one another. This indicates the apparent differences in KOAc permeabilities in single and co-permeation are weakly associated with sorption.

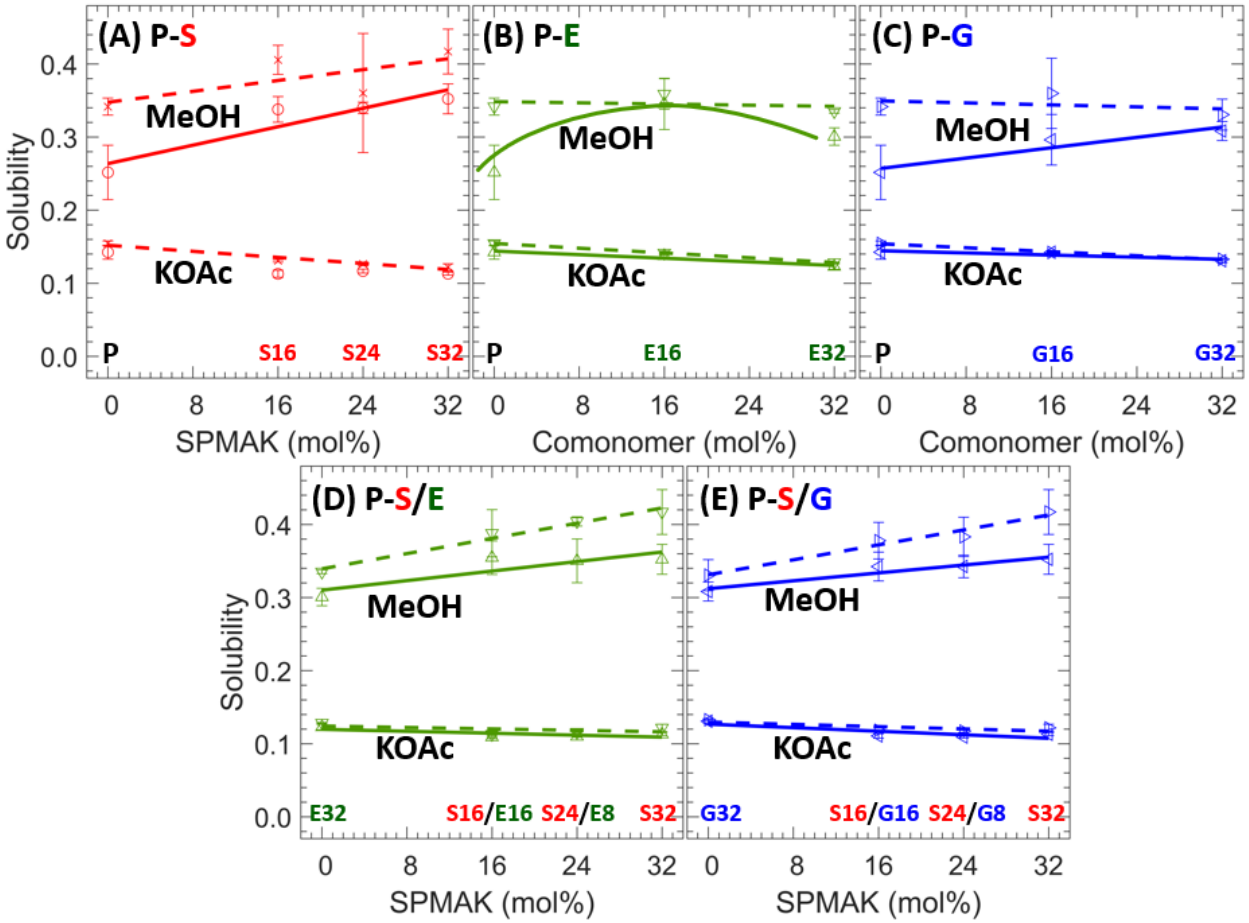

Figure 5.8. Solubilities of all films to (A-E) MeOH and KOAc measured in one-component (solid line) and two-component (dashed), which consist of (A) P-S (red, one: ○ and two: ×), (B) P-E (green, one: △ and two: ▽), (C) P-G (blue, one: ◁ and two: ▷), (D) P-S/E (green, one: △ and two: ▽), and (E) P-S/G (blue, one: ◁ and two: ▷) films. The error bars show the standard deviation and all lines are a guide to the eye.

Table 5.5. Volume of swollen membranes.

	SPMAK (mol%)	Water (mm^3)	1 M MeOH (mm^3)	1 M KOAc (mm^3)	1 M MeOH and KOAc (mm^3)
1. P	-	95 ± 0	99 ± 1	94 ± 2	93 ± 1
2. P-S16	16	99 ± 5	101 ± 4	91 ± 4	90 ± 3
3. P-S24	24	95 ± 1	96 ± 1	88 ± 1	87 ± 1
4. P-S32	32	98 ± 0	99 ± 4	88 ± 1	87 ± 3
5. P-E16	-	91 ± 0	94 ± 1	87 ± 1	88 ± 1
6. P-E32	-	92 ± 0	94 ± 2	87 ± 1	89 ± 0
7. P-G16	-	92 ± 0	95 ± 3	86 ± 1	87 ± 1
8. P-G32	-	93 ± 0	95 ± 1	86 ± 1	87 ± 2
9. P-S16/E16	16	95 ± 2	98 ± 1	87 ± 2	87 ± 1
10. P-S24/E8	24	95 ± 0	98 ± 2	88 ± 1	86 ± 1
11. P-S16/G16	16	94 ± 3	95 ± 4	85 ± 2	87 ± 2
12. P-S24/G8	24	98 ± 1	99 ± 2	85 ± 3	86 ± 2
Average		**94 ± 1**	**97 ± 2**	**87 ± 2**	**88 ± 2**

5.2.6. Membrane Diffusivity

Membrane diffusivity, Di, are calculated using the solution-diffusion relationship (Di = Pi/Ki) and are shown in Figure 5.9. Additionally, the Mackie- Meares model [43] was used to approximate MeOH and KOAc diffusivities in these films (solid lines in Figure 5.9), which states:

$$D_i = D_{0,i}\left(\frac{\emptyset_w}{2-\emptyset_w}\right)^2 \quad (5.1)$$

where D_i is the film diffusivity to solute i, $\emptyset_w$ is the water volume fraction, and $D_{0,i}$ is the solute diffusivity in water (1.49 × 10-5 cm^2/s for MeOH [44] and 1.52 × 10-5 cm^2/s for KOAc [26, 45, 46]. Generally, the Mackie-Meares model is better at approximating the behavior of salts over other molecules as this was the goal when the model was first conceived [43]. Therefore, KOAc diffusivities are closer to the model (Figure 5.9 (D-F)), than MeOH diffusivities (Figure 5.9 (A-C)), where similar behavior is reported elsewhere [16, 26, 47, 48].

Generally, MeOH diffusivities in both binary and ternary films increase with increasing SPMAK content; see red markers in Figure 5.9 (A-C). This is consistent with our previous report on comonomer-free crosslinked PEGDA films, where we observed MeOH permeabilities decrease in co-permeation with sodium acetate (NaOAc) and the relative difference in copermeation compared to single permeation was greater for more hydrated films (higher water volume fraction) [14]. MeOH diffusivities decreased in co-diffusion; see Figure 5.9 (A-C). This is presumably due to competitive diffusion, where the presence of the slow-diffusing KOAc interferes with diffusional path to the faster-diffusing MeOH [26].

In the case of P-S films, KOAc diffusivities increase in the presence of MeOH; see Figure 5.9 (D). We observed similar behavior in various CEMs (i.e. Nafion® 117 and PEGDA-AMPS) [18, 19, 26, 36], where the diffusivities of carboxylate salts (OFm^- and OAc^-) were found to increase in the presence of alcohol. In that prior work we speculated that a charge screening behavior [23, 25, 26], between the polymer-bound sulfonate anions and the diffusing carboxylate anions is suppressed by the interactions with the alcohol; see Fig. 5.1(A,D).

In the case of the KOAc diffusivities of P-E films in codiffusion, essentially no change is observed, while those of PG films increase; see Figure 5.9 (D). To rationalize this behavior, we conjecture (1) more MeOH may interact with phenyl end groups on PEGPEA ($n = 3$) than PEA ($n = 1$) due to the longer PEGPEA sidechain length, (2) more segmental motion is thereby induced in P-G by co-diffusing MeOH, and (3) the increased segmental dynamics increases the overall solute diffusivity; see Figure 1 (C, F). Nonetheless, more investigation on segmental dynamics in these and related materials must be conducted to validate these conjectures (an important but

experimentally complex undertaking) as other factors (relative permittivity [49-51], hydration number [52, 53], pH, etc.) are likely also a factor this complex behavior.

In the case of P-S/G films, both P-S24/G8 and P-S16/G16 diffusivities to KOAc in co-diffusion are slightly lower than those in single diffusion; see Figure 5.9 (F). This behavior is different than that observed in P-G films, as KOAc diffusivities of P-G32 in co-diffusion with MeOH are higher than those in single diffusion by 1.3 times; see Figure 5.9 (F). As we briefly discussed in Section 5.2.5, a probable cause is the influence of co-diffusing MeOH (partially hydrophobic) on the polymer network (partially hydrophobic) such that due to the partial hydrophobicity of MeOH, its presence is likely to increase the polymer segmental dynamics of hydrophobic phenyl-containing films (P-E and P-G). Additionally, compared to PEA (n = 1), PEGPEA (n = 3) has a longer sidechain and, therefore, generally more mobility. Overall, these differences may result in the higher KOAc diffusivity of P-G32 in co-diffusion than that in single diffusion and the comparable KOAc diffusivity of P-E32 in co-diffusion compared to that in single diffusion; see Figure 5.9 (E, F). This increase in chain mobility of PEGPEA in co-diffusion can be suppressed in the presence of the sulfonate group (P-S/G) due to a steric effect between sulfonate (hydrophilic) and phenyl (hydrophobic) groups. In the absence of MeOH, this steric effect may have a negligible effect. However, MeOH has both hydrophilic and hydrophobic end groups and, therefore, may act as a bridge between sulfonate and phenyl groups. The resulting increased interactions between dissimilar functional groups (sulfonate and phenyl) may thereby result in lower P-S/G diffusivities to KOAc in co-diffusion than those in single diffusion due to the co-diffusing MeOH; see Figure 5.1 (B, E) for a pictorial description of our conjecture.

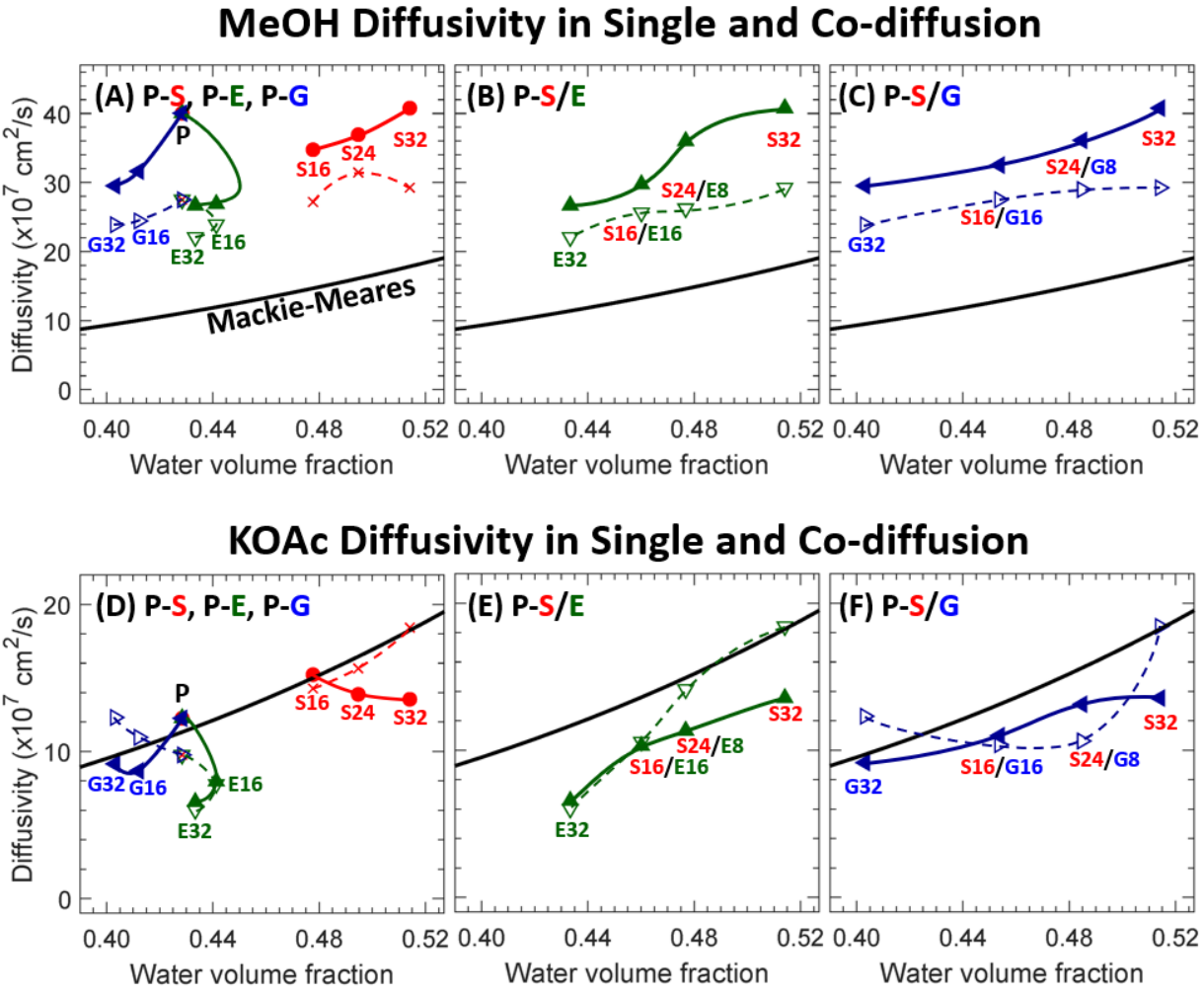

Figure 5.9. (A-C) MeOH and (D-F) KOAc diffusivities of (A,D) binary films (P-S, P-E, and P-G), (B,E) P-S/E films, and (C,F) P-S/G films. Single diffusivities are shown in solid lines with filled markers (E: ▲, G: ◀, and S: ●) and co-diffusivities are shown in dashed lines with empty markers(E: ▽, G: ▷, and S: ×). The error bars show the standard deviation and all lines are a guide to the eye.

This potential chain-chain interaction between these comonomers might provide helpful insight to the conjectured charge screening behavior; see Figure 5.1 (A, D) [26]. Since KOAc diffusivities do not increase in P-S/G films in co-permeation with MeOH, the charge screening behavior can be suppressed by reducing the overall segmental dynamics. Nonetheless, more

investigations are needed to provide additional insights into this complex behavior and to assess the validity of our hypotheses described above. However, the physiochemical or transport roots of this behavior aside, the strategic inclusion of PEGPEA in CEMs targeting CO_2 reduction cells may be beneficial as they suppress the crossover of negatively-charged CO_2 reduction products.

5.3. Conclusions

A series of binary films (PEGDA-SPMAK (P-S), PEGDA-PEA (PE), and PEGDA-PEGPEA (P-G)) and ternary films (P-S/E and PS/G) films were prepared at a constant pre-polymerization water content (20 wt%). Ionic conductivities and ion exchange capacities (IEC) of cation exchange membranes (P-S, P-S/E, and P-S/G) were measured to understand the impact of bound sulfonate anions on both binary and ternary films. Water volume fractions, storage moduli, and glass transition temperatures of all films were measured to fully understand the transport behavior within these films. Permeabilities and solubilities to methanol and potassium acetate (KOAc) were measured in single and co-transport, and diffusivities calculated using solution-diffusion. An interesting co-diffusive behavior was observed in P-S/G films, where KOAc diffusivities did not increase in the presence of MeOH, when those of P-S and P-G films increased by 1.35 times, on average. We conjecture this behavior to be related to a steric effect between sulfonated chains and PEGPEA chains in co-diffusion with MeOH which reduces the overall segmental dynamics. Overall, while further investigations are needed to investigate the emergent transport behavior observed in these and other dense, polymeric membranes, the incorporation of comonomers such as PEGPEA may be a viable strategy for reducing undesirable solute crossover in CO2 reduction cells.

5.4. References

[1] M.R. Singh, A.T. Bell, Design of an artificial photosynthetic system for production of alcohols in high concentration from CO 2, Energy & Environmental Science 9(1) (2016) 193-199.

[2] A.J. Garza, A.T. Bell, M. Head-Gordon, Mechanism of CO2 reduction at copper surfaces: pathways to C2 products, Acs Catalysis 8(2) (2018) 1490-1499.

[3] D.J. Miller, F.A. Houle, Membranes for Solar Fuels Devices, (2018).

[4] A. Kusoglu, A.Z. Weber, New insights into perfluorinated sulfonic-acid ionomers, Chemical reviews 117(3) (2017) 987-1104.

[5] L.M. Robeson, H.H. Hwu, J.E. McGrath, Upper bound relationship for proton exchange membranes: Empirical relationship and relevance of phase separated blends, Journal of Membrane Science 302(1-2) (2007) 70-77.

[6] G.M. Geise, M.A. Hickner, B.E. Logan, Ionic resistance and permselectivity tradeoffs in anion exchange membranes, ACS applied materials & interfaces 5(20) (2013) 10294-10301.

[7] B.M. Carter, L. Keller, M. Wessling, D.J. Miller, Preparation and characterization of crosslinked poly (vinylimidazolium) anion exchange membranes for artificial photosynthesis, Journal of Materials Chemistry A 7(41) (2019) 23818-23829.

[8] J.M. Kim, B.S. Beckingham, Comonomer effects on co-permeation of methanol and acetate in cation exchange membranes, European Polymer Journal 147 (2021) 110307.

[9] S.M. Dischinger, S. Gupta, B.M. Carter, D.J. Miller, Transport of neutral and charged solutes in imidazolium-functionalized poly (phenylene oxide) membranes for artificial photosynthesis, Industrial & Engineering Chemistry Research 59(12) (2019) 5257-5266.

[10] R. Kingsbury, M. Hegde, J. Wang, A. Kusoglu, W. You, O. Coronell, Tunable anion exchange membrane conductivity and permselectivity via non-covalent, hydrogen bond cross-linking, ACS applied materials & interfaces 13(44) (2021) 52647-52658.

[11] J.M. Kim, Y.-h. Lin, B. Hunter, B.S. Beckingham, Transport and co-transport of carboxylate ions and ethanol in anion exchange membranes, Polymers 13(17) (2021) 2885.

[12] M. Krödel, B.M. Carter, D. Rall, J. Lohaus, M. Wessling, D.J. Miller, Rational design of ion exchange membrane material properties limits the crossover of CO2 reduction products in artificial photosynthesis devices, ACS applied materials & interfaces 12(10) (2020) 12030-12042.

[13] B.M. Dobyns, J.M. Kim, J. Li, Z. Jiang, B.S. Beckingham, Multicomponent transport of alcohols in Nafion 117 measured by in situ ATR FTIR spectroscopy, Polymer 209 (2020) 123046.

[14] B.M. Dobyns, J.M. Kim, B.S. Beckingham, Multicomponent transport of methanol and sodium acetate in poly (ethylene glycol) diacrylate membranes of varied fractional free volume, European Polymer Journal 134 (2020) 109809.

[15] M. Soniat, S.M. Dischinger, L.C. Weng, H. Martinez Beltran, A.Z. Weber, D.J. Miller, F.A. Houle, Toward predictive permeabilities: Experimental measurements and multiscale simulation of methanol transport in Nafion, Journal of Polymer Science 59(7) (2021) 594-613.

[16] M. Galizia, D.R. Paul, B.D. Freeman, Liquid methanol sorption, diffusion and permeation in charged and uncharged polymers, Polymer 102 (2016) 281-291.

[17] B.M. Carter, B.M. Dobyns, B.S. Beckingham, D.J. Miller, Multicomponent transport of alcohols in an anion exchange membrane measured by in-situ ATR FTIR spectroscopy, Polymer 123 (2017) 144-152.

[18] B.S. Beckingham, N.A. Lynd, D.J. Miller, Monitoring multicomponent transport using in situ ATR FTIR spectroscopy, Journal of Membrane Science 550 (2018) 348-356.

[19] J.M. Kim, B.M. Dobyns, R. Zhao, B.S. Beckingham, Multicomponent transport of methanol and acetate in a series of crosslinked PEGDA-AMPS cation exchange membranes, Journal of Membrane Science 614 (2020) 118486.

[20] F.G. Helfferich, Ion exchange, Courier Corporation1995.

[21] G.S. Manning, Limiting laws and counterion condensation in polyelectrolyte solutions I. Colligative properties, The journal of chemical Physics 51(3) (1969) 924-933.

[22] J. Kamcev, D.R. Paul, B.D. Freeman, Ion activity coefficients in ion exchange polymers: applicability of Manning's counterion condensation theory, Macromolecules 48(21) (2015) 8011-8024.

[23] A. Allegrezza Jr, B. Parekh, P. Parise, E. Swiniarski, J. White, Chlorine resistant polysulfone reverse osmosis modules, Desalination 64 (1987) 285-304.

[24] P. Parise, A. Allegrezza Jr, B. Parekh, Reverse osmosis: chlorine-resistant polysulfone reverse osmosis membrane and module, Ultrapure Water 4(7) (1987) 54-65.

[25] G.M. Geise, D.R. Paul, B.D. Freeman, Fundamental water and salt transport properties of polymeric materials, Progress in Polymer Science 39(1) (2014) 1-42.

[26] J.M. Kim, B.S. Beckingham, Transport and co-transport of carboxylate ions and alcohols in cation exchange membranes, Journal of Polymer Science 59(21) (2021) 2545-2558.

[27] J.G. Wijmans, R.W. Baker, The solution-diffusion model: a review, Journal of membrane science 107(1-2) (1995) 1-21.

[28] R.W. Baker, Membrane technology and applications, John Wiley & Sons2023.

[29] D.A. Salvatore, C.M. Gabardo, A. Reyes, C.P. O'Brien, S. Holdcroft, P. Pintauro, B. Bahar, M. Hickner, C. Bae, D. Sinton, Designing anion exchange membranes for CO2 electrolysers, Nature Energy 6(4) (2021) 339-348.

[30] H. Lin, E. Van Wagner, J.S. Swinnea, B.D. Freeman, S.J. Pas, A.J. Hill, S. Kalakkunnath, D.S. Kalika, Transport and structural characteristics of crosslinked poly (ethylene oxide) rubbers, Journal of Membrane Science 276(1-2) (2006) 145-161.

[31] H. Ju, B.D. McCloskey, A.C. Sagle, V.A. Kusuma, B.D. Freeman, Preparation and characterization of crosslinked poly (ethylene glycol) diacrylate hydrogels as fouling-resistant membrane coating materials, Journal of Membrane Science 330(1-2) (2009) 180-188.

[32] H. Ju, A.C. Sagle, B.D. Freeman, J.I. Mardel, A.J. Hill, Characterization of sodium chloride and water transport in crosslinked poly (ethylene oxide) hydrogels, Journal of Membrane Science 358(1-2) (2010) 131-141.

[33] N. Yan, D.R. Paul, B.D. Freeman, Water and ion sorption in a series of cross-linked AMPS/PEGDA hydrogel membranes, Polymer 146 (2018) 196-208.

[34] Y. Yu, N. Yan, B.D. Freeman, C.-C. Chen, Mobile ion partitioning in ion exchange membranes immersed in saline solutions, Journal of Membrane Science 620 (2021) 118760.

[35] N. Yan, R. Sujanani, J. Kamcev, M. Galizia, E.-S. Jang, D.R. Paul, B.D. Freeman, Influence of fixed charge concentration and water uptake on ion sorption in AMPS/PEGDA membranes, Journal of Membrane Science 644 (2022) 120171.

[36] J.M. Kim, A. Mazumder, J. Li, Z. Jiang, B.S. Beckingham, Impact of PEGMA on transport and co-transport of methanol and acetate in PEGDA-AMPS cation exchange membranes, Journal of Membrane Science 642 (2022) 119950.

[37] K. Chang, T. Xue, G.M. Geise, Increasing salt size selectivity in low water content polymers via polymer backbone dynamics, Journal of Membrane Science 552 (2018) 43-50.

[38] E.M. Ahmed, Hydrogel: Preparation, characterization, and applications: A review, Journal of advanced research 6(2) (2015) 105-121.

[39] G.M. Geise, L.P. Falcon, B.D. Freeman, D.R. Paul, Sodium chloride sorption in sulfonated polymers for membrane applications, Journal of Membrane Science 423 (2012) 195-208.

[40] J.I. Monroe, S. Jiao, R.J. Davis, D. Robinson Brown, L.E. Katz, M.S. Shell, Affinity of small-molecule solutes to hydrophobic, hydrophilic, and chemically patterned interfaces in aqueous solution, Proceedings of the National Academy of Sciences 118(1) (2021) e2020205118.

[41] L. Kwisnek, J. Goetz, K.P. Meyers, S.R. Heinz, J.S. Wiggins, S. Nazarenko, PEG containing thiol–ene network membranes for CO2 separation: effect of cross-linking on thermal, mechanical, and gas transport properties, Macromolecules 47(10) (2014) 3243-3253.

[42] A. Katzenberg, A. Angulo, A. Kusoglu, M.A. Modestino, Impacts of organic sorbates on the ionic conductivity and nanostructure of perfluorinated sulfonic-acid ionomers, Macromolecules 54(11) (2021) 5187-5195.

[43] J. Mackie, P. Meares, The diffusion of electrolytes in a cation-exchange resin membrane I. Theoretical, Proceedings of the Royal Society of London. Series A. Mathematical and Physical Sciences 232(1191) (1955) 498-509.

[44] L. Hao, D.G. Leaist, Binary mutual diffusion coefficients of aqueous alcohols. Methanol to 1-heptanol, Journal of Chemical & Engineering Data 41(2) (1996) 210-213.

[45] E.E. Hills, M.H. Abraham, A. Hersey, C.D. Bevan, Diffusion coefficients in ethanol and in water at 298 K: Linear free energy relationships, Fluid Phase Equilibria 303(1) (2011) 45-55.

[46] P. Vanýsek, Ionic conductivity and diffusion at infinite dilution, CRC handbook of chemistry and physics 94 (1993).

[47] J.M. Kim, Y. Wang, Y.-h. Lin, J. Yoon, T. Huang, D.-J. Kim, M.L. Auad, B.S. Beckingham, Fabrication and Characterization of Cross-Linked Phenyl-Acrylate-Based Ion Exchange Membranes and Performance in a Direct Urea Fuel Cell, Industrial & Engineering Chemistry Research 60(41) (2021) 14856-14867.

[48] E.-S. Jang, J. Kamcev, K. Kobayashi, N. Yan, R. Sujanani, T.J. Dilenschneider, H.B. Park, D.R. Paul, B.D. Freeman, Influence of water content on alkali metal chloride transport in cross-linked Poly (ethylene glycol) diacrylate. 2. Ion diffusion, Polymer 192 (2020) 122316.

[49] K. Chang, G.M. Geise, Dielectric permittivity properties of hydrated polymers: measurement and connection to ion transport properties, Industrial & Engineering Chemistry Research 59(12) (2019) 5205-5217.

[50] K. Chang, H. Luo, G.M. Geise, Water content, relative permittivity, and ion sorption properties of polymers for membrane desalination, Journal of membrane science 574 (2019) 24-32.

[51] K. Chang, H. Luo, G.M. Geise, Influence of salt concentration on hydrated polymer relative permittivity and state of water properties, Macromolecules 54(2) (2021) 637-646.

[52] E.-S. Jang, J. Kamcev, K. Kobayashi, N. Yan, R. Sujanani, T.J. Dilenschneider, H.B. Park, D.R. Paul, B.D. Freeman, Influence of water content on alkali metal chloride transport in cross-linked Poly (ethylene glycol) Diacrylate. 1. Ion sorption, Polymer 178 (2019) 121554.

[53] M. Galizia, F.M. Benedetti, D.R. Paul, B.D. Freeman, Monovalent and divalent ion sorption in a cation exchange membrane based on cross-linked poly (p-styrene sulfonate-co-divinylbenzene), Journal of Membrane Science 535 (2017) 132-142.

Chapter 6: Effect of Acrylate and Methacrylate Backbone Linkages in IEMs

---

Reproduced from: Kim, J. M., Lin, Y., Bannon, S. M., Geise, G. M., & Beckingham, B. S. (2023a). Improved structural stability of charged hydrogels under organic CO2 reduction products: Effect of acrylate and methacrylate backbone linkages. The Journal of Physical Chemistry C, 127(22), 10826–10832. https://doi.org/10.1021/acs.jpcc.3c01854

6.1. Introduction

Greenhouse gases (e.g., CO_2 and CH_4) are major contributors to climate change, and there have been significant efforts toward their capture, utilization, and storage [1]. CO_2 reduction cells (CO_2RCs) are one promising technology to convert captured atmospheric CO_2 to valuable fuel sources (e.g., alcohols) and chemicals (e.g., carboxylates), enabling their utilization while simultaneously replacing fine chemicals traditionally sourced from petroleum [2]. A CO_2RC often consists of three components: (1) cathode cell, (2) anode cell, and (3) ion exchange membrane (IEM).

A linear polymer-based anion exchange membrane (AEM) is often selected as the IEM to facilitate electrolyte (e.g., bicarbonate, HCO_3^-) and hydroxide (OH^-, from water oxidization) transport. Unfortunately, linear polymers often swell in the presence of alcohols such as methanol (MeOH[3, 4]), a polar organic sorbate and CO2 reduction product, and isopropanol [5]. Moreover, AEMs typically permit the crossover of carboxylates (CO_2 reduction products, e.g., formate (OFm^-), a charged organic sorbate) [6]. Linear polymer-based cation exchange membranes (CEMs)

have also been used, though less frequently, in CO_2RCs [7-9] to facilitate the transport of electrolytes (e.g., potassium, K^+) and protons (H^+, from water reduction). While linear polymer-based CEMs (e.g., Nafion 117 [3]) are advantageous in suppressing the crossover of carboxylate anions, they still suffer from swelling in the presence of polar organic sorbates [3].

Cross-linked polymer-based IEMs are one promising alternative to linear polymer-based IEMs (cross-linked sulfonated polysulfone [10]), as cross-links within the polymer network support the structural stability of the films and limit their swelling [10, 11]. However, several cross-linked films (e.g., cross-linked PEGDA-based IEMs [6, 12-14]) tend to have low toughness, which has limited their application. Recently, we developed a series of phenyl-based cross-linked IEMs by employing phenyl acrylate (PA) and phenyl methacrylate. We reported that the PA-based films had more favorable monomer solubility in solvent (i.e., DMSO) and Young's modulus than the phenyl methacrylate-based films [11]. This manuscript thereby focuses in on the use of PA as the neutral comonomer and investigates the role of methacrylate vs acrylate backbone linkages for the ion exchange comonomers for both AEMs and CEMs.

Solute transport in polymeric membranes can often be explained by the solution-diffusion model [15], where the membrane permeability (P_i), a thickness and driving force normalized flux, can be expressed as a product of a sorption coefficient (K_i, which is sensitive to polymer−solute interactions [16]) and a diffusion coefficient (Di, which is representative of the kinetic factors that contribute to the permeability [15]): $P_i = K_i \times D_i$. By measuring MeOH and KOFm diffusive permeabilities (P_m and P_f) via permeation cell experiments using both single and multisolute solutions, we aim to infer the efficacy of PA-based XL-IEMs (both AEMs and CEMs) in CO_2RC. Moreover, we performed sorption−desorption experiments to measure the sorption coefficients,

and we characterized the relative dielectric permittivity properties to investigate the polymer−solute−water interactions. Additionally, we evaluated the impact of polymer steric hindrance by replacing the acrylate with methacrylate on the backbone of the charged comonomer (Figure 6.1). We prepared four different films with two quaternary ammonium (QA^+)-containing monomers [2-(acryloyloxy)ethyl trimethylammonium chloride (AETAC, A) and 2-(methacryloyloxy)ethyl trimethylammonium chloride (MAETAC, MA)] and two sulfonates (SO_3^-)-containing monomers [3-sulfopropyl acrylate potassium (SPAK, S) and 3-sulfopropyl methacrylate potassium (SPMAK, SM)], namely PA/A, PA/MA, PA/S, and PA/SM. Among these charged monomers, AETAC (A) and SPAK (S) have acrylates in the backbone, and MAETAC (MA) and SPMAK (SM) have methacrylates in the backbone. In terms of the polymer chains, the methacrylate-containing films are more sterically constrained than the acrylate-containing films [17]. In the case of poly(methyl methacrylate) (PMMA) and poly-(methyl acrylate) (PMA), where the only difference is the presence of the methyl group on PMMA, the glass transition temperatures (T_g) differ by approximately 100 °C (105 °C for PMMA and 9 °C for PMA).18 Therefore, the chains are more rigid and less able to relax in response to changing solvent conditions. Here, the difference in T_g is less pronounced (6−7 °C) in the final membranes (see Table 6.1 for T_g values) but follows a similar behavior with the methacrylate-containing films exhibiting higher T_g than the analogous acrylate-containing films.

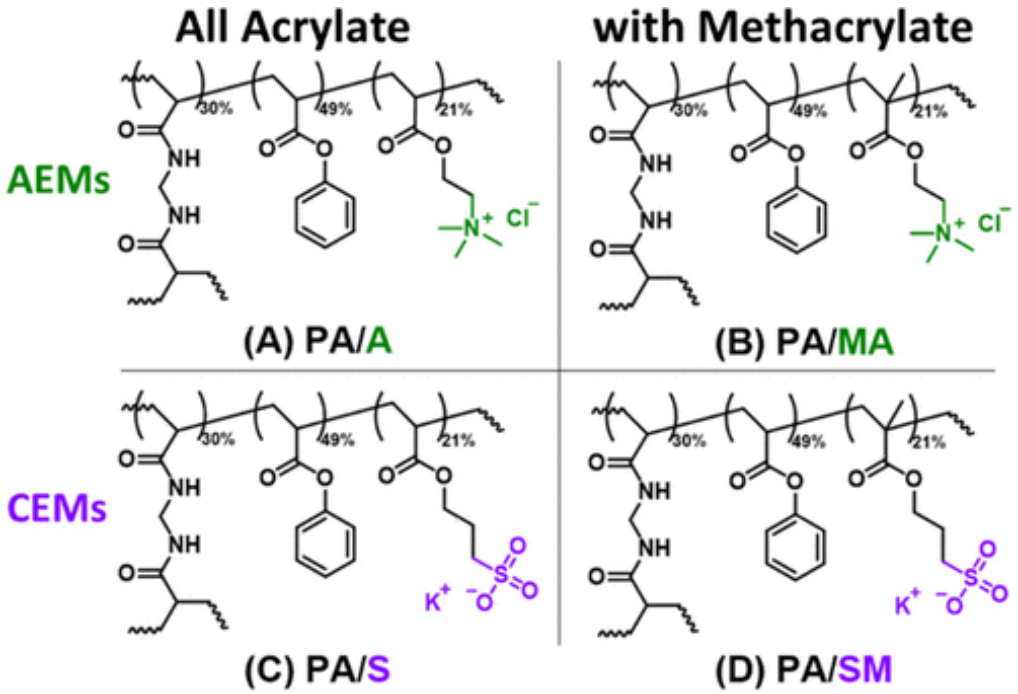

Figure 6.1. Scheme of prepared PA/A, PA/MA, PA/S, and PA/SM hydrogels.

Table 6.1. Glass transition temperature (T_g) values of dry polymer films.

	T_g (°C)
PA/A	179.8
PA/MA	185.7
PA/S	185.1
PA/SM	195.8

6.2. Results and Discussion

The materials, membrane synthesis methods, and experimental procedures are detailed in Chapter 3. Briefly, four transparent prepolymerization solutions were prepared by dissolving 30 mol % MBAA, 49 mol % PA, 21 mol % of a charged monomer (A, MA, S, or SM), and 0.1 wt %

AIBN in DMSO (50 wt %). Solutions were placed on a glass plate, and two feeler gauges (205μm) were placed on two sides, carefully covered with an identical glass plate, and placed inside an oven at 60 °C for 8 hours. Each film was placed in about 500 mL of DI water for 2 days to exchange DMSO to water.

6.2.1. Water Volume Fraction

The water volume fraction ($\emptyset_w$) of all films was measured in triplicate (Table 6.2). Generally, $\emptyset_w$ of sulfonate (SO_3^-) containing films (PA/S and PA/SM) was higher than that of quaternary ammonium (QA^+) containing films (PA/A and PA/MA). This result is likely due to the hydration number of sulfonate ($R{-}SO_3^-$ [18]) being higher than that of ammonium (NH_4^+ [19]). Next, the methacrylate-containing films (PA/MA and PA/SM) had greater $\emptyset_w$ than the methacrylate-free films (PA/A and PA/S). Similarly, the hydrated film thicknesses of PA/MA and PA/SM were 150 and 153 μm, respectively, and those of PA/A and PA/S were 130 and 137 μm, respectively. Methacrylate-containing films are expected to experience less osmotic deswelling because of greater steric hindrance due to the quaternary (4°) carbons on the polymer backbone.

Table 6.2. Water Volume Fractions, Ionic Conductivities (Cl^- Conductivity for PA/A and PA/MA and K^+ Conductivity for PA/S and PA/SM), and Young's Moduli of All Films.

	Water volume fraction, $\emptyset_w$	**Ionic conductivity (mS/cm)**	**Young's modulus (MPa)**
PA/A	0.39 ± 0.01	6.1 ± 0.1	0.87 ± 0.01
PA/MA	0.43 ± 0.00	6.0 ± 0.0	0.75 ± 0.03
PA/S	0.47 ± 0.00	10.6 ± 0.0	0.66 ± 0.01
PA/SM	0.50 ± 0.01	11.8 ± 0.0	0.62 ± 0.01

6.2.2. Ionic Conductivity

Chloride (Cl^-) conductivities of QA^+ containing AEMs (PA/A and PA/MA) and potassium (K^+) conductivities of SO_3^- containing CEMs (PA/S and PA/SM) were measured (Table 6.2). For CEMs, we assumed the ionic conduction is occurring primarily by K^+. The conductivities of methacrylate-free and methacrylate-containing films were essentially unchanged for the AEMs and slightly elevated for the methacrylate-containing CEMs; 6.1 ≈ 6.0 mS/cm and 10.6 ≈ 11.8 mS/cm, respectively. These results indicate the methacrylates have a negligible to very small impact on the electromigration of both K^+ and Cl^-. Notably, these conductivity values might be affected if CO_2 reduction products (MeOH and KOFm) are included in the measurement. For instance, the inclusion of formate ion ($K_b = 5.55 \times 10^{-11}$) in solution will alter the pH of the potassium formate/ water solutions (8.9 for 1 M KOFm and 9.2 for 4 M KOFm). The K^+ conductivities of CEMs were higher than Cl^- conductivities of AEMs. This result is unexpected as the ionic mobilities of K^+ and Cl^- are close (K^+: $7.62 \times 10^{-4} \approx Cl^-$: 7.91×10^{-4} $cm^2\ s^{-1}\ V^{-1}$). A possible contribution to this behavior is the $\emptyset_w$ of CEMs being higher and, therefore, easier for K^+ to migrate through the polymer network. Another possible contribution is the binding affinity of K^+ to SO_3^- might be less than that of Cl^- to QA^+.

6.2.3. Young's Modulus

Young's moduli of all films were measured in triplicate (Table 6.2); see Figure 6.2 for strain-stress curves. All films showed comparable Young's moduli to a commercial AEM (FAA, 2.0 MPa) and a commercial CEM (Nafion 117, 1.0 MPa), which we previously measured [11].

Generally, Young's moduli values decrease as $\emptyset_w$ increases. A similar trend was observed in our previous investigation for analogous PA-based AEMs (PA/MA) and CEMs (PA/2-acrylamido-2-methylpropane sulfonic acid (PA/AMPS))[11]. These trends indicate PA-based crosslinked films (prepared under similar conditions) with a lower $\emptyset_w$ likely undergo more deswelling during solvent exchange from DMSO to water which provides additional capacity for subsequent chain stretching.

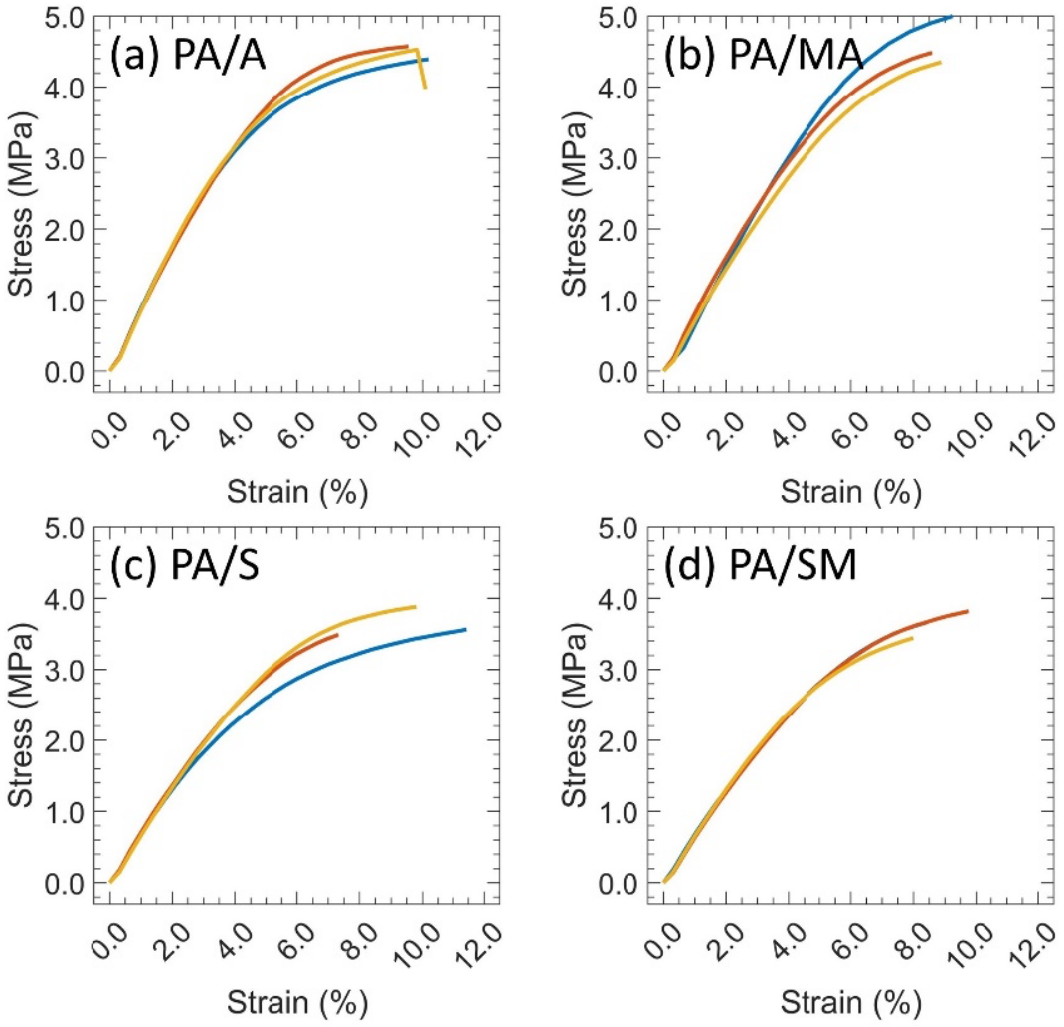

Figure 6.2. Stress-strain curves for (a) PA/A, (b) PA/MA, (c) PA/S, and (d) PA/SM.

6.2.4. MeOH and KOFm Permeability

MeOH permeabilities (P_m) and KOFm permeabilities (P_f) of all films were measured in single solute permeation ($P_{i,1}$) and mixed solute permeation ($P_{i,2}$) experiments (Figure 6.3). Generally, solute permeabilities were higher for the films with a larger $\emptyset_w$ and when the smaller solute (MeOH) was considered. The kinetic diameter of MeOH (3.6 A [20]) is smaller than the hydrated diameters of K^+ (6.6 Å [21]) and OFm^- (HCO_2^-, > 5.9 Å [22, 23]). Continued discussion on the relative impacts of diffusion and sorption can be found in the next section.

The KOFm permeability values for all films were essentially unaffected by the presence or absence of MeOH in the measurement (Figure 6.3 (b)). This result indicates that copermeating MeOH did not alter the overall KOFm permeabilities. In contrast, MeOH permeabilities in mixed solute permeation with KOFm ($P_{m,2}$) are different from those by itself ($P_{m,1}$), where $P_{m,2}$ of PA/A, PA/MA, PA/S, and PA/SM are different from $P_{m,1}$ of these films by +21, + 9, 0, and −7%, respectively. These results indicate that copermeating KOFm alters the overall MeOH permeation. To explain these differences, we conjecture a potential relationship between the $\emptyset_w$ and the flux coupling [24] (MeOH−KOFm). Assuming the average chain spacing within each film is proportional to $\emptyset_w$, the solute−solute interaction may be more likely as the chain spacing decreases (lower $\emptyset_w$); therefore, the flux coupling is more likely to occur (more MeOH diffusion along with KOFm). However, the solute−solute interaction is less likely as the chain spacing increases (higher $\emptyset_w$); therefore, the flux coupling is less likely to occur (less MeOH diffusion).

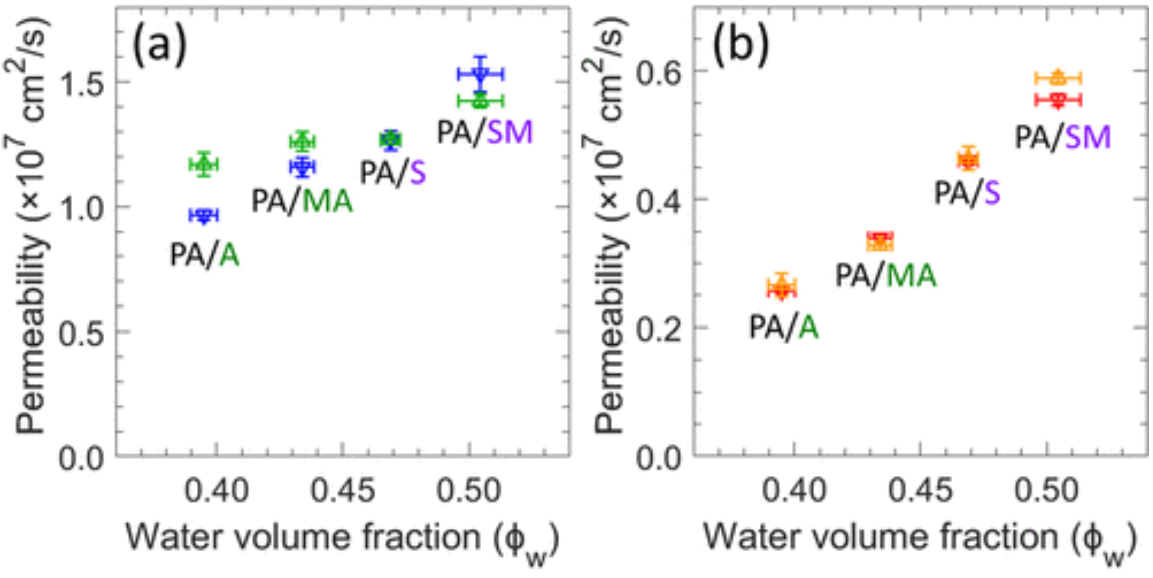

Figure 6.3. (a) MeOH permeabilities in single (blue) in mixed solute permeation with KOFm (green) and (b) KOFm permeabilities in single (red) in mixed solute permeation with MeOH (orange) as a function of water volume fraction.

6.2.5. MeOH and KOFm Sorption Coefficients

MeOH sorption coefficients (K_m) and KOFm sorption coefficients (K_f) of all films were measured in single sorption ($K_{i,1}$) and mixed solute sorption ($K_{i,2}$) experiments (Figure 6.4). Generally, MeOH sorption coefficients in single sorption ($K_{m,1}$) and mixed solute sorption with KOFm ($K_{m,2}$) were similar (Figure 6.4 (a)). Based on the volume fraction of MeOH−KOFm−water−polymer within the swollen films, we observed more rigid films (PA/MA and PA/SM) had a higher MeOH fraction in cosorption with KOFm (17% and 14%, respectively) when less rigid films (PA/A and PA/S) had the same MeOH fraction in cosorption. This result indicates MeOH is more favorable in rigid structures.

On the other hand, KOFm sorption coefficients were affected by the presence of MeOH. KOFm sorption coefficients in cosorption with MeOH were less than those measured by itself; $K_{f,2} < K_{f,1}$ (Figure 6.4 (b)). Based on the volume fractions of MeOH−KOFm−water−polymer within the swollen films, we observed the KOFm fraction decrease by 25%, on average (Table 6.3).

In addition, we also noticed the gaps between $K_{f,1}$ and $K_{f,2}$ were larger for QA^+-containing films (PA/A, 22%, and PA/MA, 20%) than those of SO_3^--containing films (PA/S, 17%, and PA/SM, 13%). As a conjecture, mobile formate anions (OFm^-) may be more favorable in QA^+-containing films (counterion condensation [25, 26]). In mixed solute sorption, OFm^- mobility can be reduced in these films as MeOH softens the fixed charge interface and interferes with the counterion condensation [3, 6].

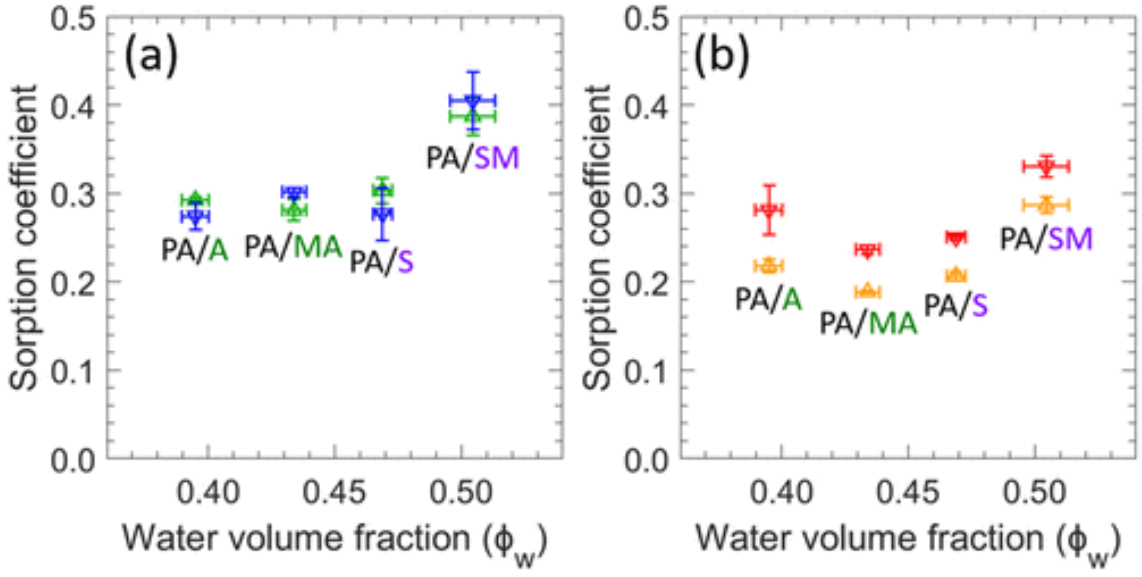

Figure 6.4. (a) MeOH sorption coefficients in single (blue) in mixed solute sorption with KOFm (green) and (b) KOFm sorption coefficients in single (red) in mixed solute sorption with MeOH (orange) as a function of water volume fraction.

Table 6.3. The volume fraction of solutes (MeOH and/or KOFm), water, and polymer after equilibration with single solute solutions (1 M MeOH or 1 M KOFm) or a mixed solute solution (1 M MeOH and 1 M KOFm). The polymer volume fraction is the remaining volume fraction in these swollen materials. All measurements were made at room temperature, and all values were measured in triplicate (standard deviations are reported).

	MeOH		**KOFm**		**Mix**		
	MeOH ($\emptyset_m$)	**Water ($\emptyset_w$)**	**KOFm ($\emptyset_f$)**	**Water ($\emptyset_w$)**	**MeOH ($\emptyset_m$)**	**KOFm ($\emptyset_f$)**	**Water ($\emptyset_w$)**
PA/A	0.012 ± 0.000	0.447 ± 0.012	0.012 ± 0.001	0.426 ± 0.035	0.012 ± 0.001	0.009 ± 0.000	0.477 ± 0.011
PA/MA	0.011 ± 0.000	0.387 ± 0.018	0.010 ± 0.000	0.281 ± 0.027	0.013 ± 0.000	0.008 ± 0.000	0.237 ± 0.084
PA/S	0.012 ± 0.001	0.508 ± 0.017	0.011 ± 0.000	0.414 ± 0.018	0.012 ± 0.001	0.008 ± 0.000	0.410 ± 0.015
PA/SM	0.016 ± 0.001	0.506 ± 0.009	0.015 ± 0.001	0.0431 ± 0.025	0.018 ± 0.001	0.012 ± 0.000	0.389 ± 0.005

6.2.6. Relative Permittivity

Relative permittivity (ϵ') values of hydrated films were measured before and after sorption in 1 M MeOH, 1 M KOFm, or 1 M of each mix thereof (Figure 6.5). It is useful to frame the analysis within the context of the bulk solution relative permittivity values; the relative permittivity of pure water is the highest (78 [27]), followed by 1 M MeOH (76 [27]), 1 M KOFm (~68, based on 0.96 M NaOFm [28]), and 1 M of each mix thereof (~66, estimated based on both 1 M MeOH and 1 M KOFm). We expect the external solution relative permittivity properties to affect the relative permittivity properties of the membrane [29]. For instance, the films equilibrated with KOFm-containing solutions (i.e., 1 M KOFm and 1 M MeOH/1 M KOFm) may have lower relative permittivity values than those films equilibrated with KOFm-free solutions (i.e., pure water and 1M MeOH).

For all films, the relative permittivity values for films equilibrated in water and 1 M MeOH were close to one another (within 10% on average), and this result may be consistent with the fact that the relative permittivity properties of water and 1 M MeOH are similar (Figure 6.5 (a)). In contrast, the relative permittivity values of certain films were much more affected by equilibration with KOFm-containing solutions (i.e., 1 M KOFm or a solution containing 1 M MeOH and 1 M KOFm). For the acrylate films (PA/A and PA/S, without methacrylate backbone linkages), relative permittivity values after equilibration with 1 M KOFm were less than those before equilibration by 40% on average (Table 6.4, cyan and red in Figure 6.5 (b)). This result is expected, as the relative permittivity properties of KOFm-containing solutions are lower than KOFm-free solutions. Alternatively, the relative permittivity values of methacrylate-based films (PA/MA and PA/SM)

before sorption were close to those after equilibration with KOFm (Table 6.4). This result is unexpected, as the KOFm sorption coefficients of PA/MA and PA/SM were close to those of PA/A and PA/S. These observations may be consistent with a physical picture where methyl group incorporation influences polymer/solvent interactions so that KOFm does not interfere with the hydrogen bonding between the polymer and water, which leads to maintaining the relative permittivity [29].

In the acrylate films (PA/A and PA/S), the relative permittivity values, after equilibration with the external solution containing 1 M MeOH and 1 M KOFm, were close to those before equilibration, within 12% on average (Table 6.4). In contrast, the relative permittivity values of the methacrylate films (PA/MA and PA/SM) after equilibration with the external solution containing 1 M MeOH and 1 M KOFm were less than those before equilibration by 28% on average (Table 6.4). This result may be due to the impact of reduced water content within the methacrylate films after sorption in the mixed solute solution. We observed that the water volume fractions within PA/MA and PA/SM, after equilibration with the mixed solute solution, were lower, by 5%, than those values after equilibration with the single solute solutions (either 1 M MeOH or 1 M KOFm). At the same time, the volume fraction for PA/A and PA/S decreased by only 2% when comparing equilibration with the mixed solute solution and the single solute solutions (Table 6.4).

These results suggest that polymer rigidity (i.e., methyl group incorporation) may impact the relative permittivity properties of the swollen polymers, especially in the mixed organic solute solution. Moreover, these results suggest that relative permittivity values of hydrated films can be a valuable tool to investigate the influence of sorbed organic solutes on material properties.

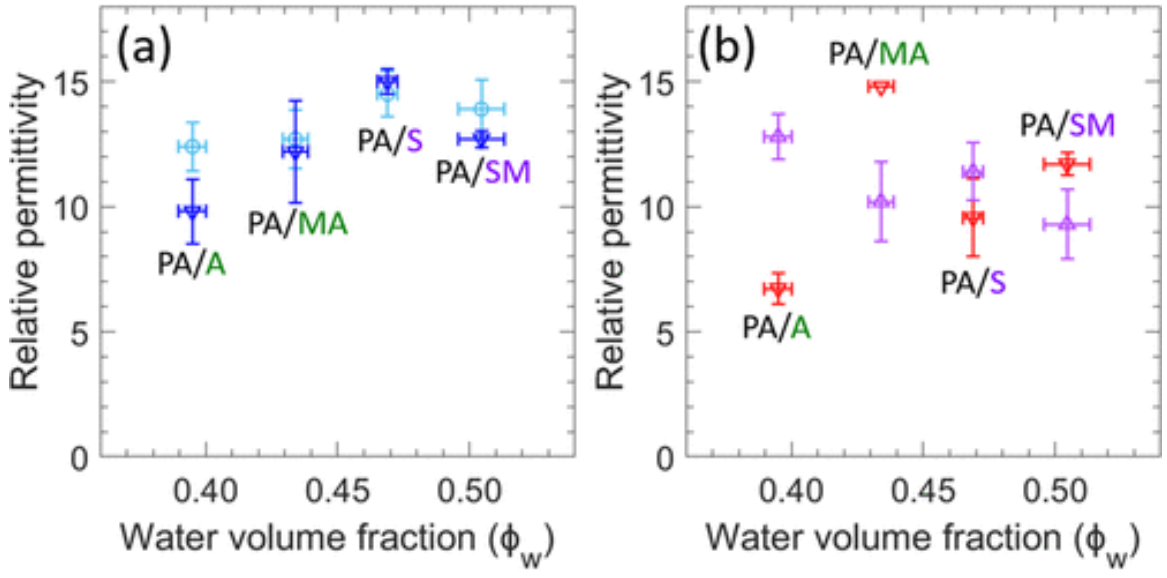

Figure 6.5. (a) Relative permittivity values (at 45 MHz) of all films in water (cyan) and after equilibration with 1 M MeOH (blue). (b) Relative permittivity values of all films after equilibration with 1 M KOFm (red) and a mixed solute solution containing 1 M MeOH and 1 M KOFm (purple).

Table 6.4. Relative permittivity values at 45 MHz of hydrated films before and after equilibration with either 1 M MeOH, 1 M KOFm, or a mixed solute solution containing 1 M MeOH and 1 M KOFm. All measurements were made at room temperature, and all values were measured in triplicate (standard deviations are reported).

	Water Volume Fraction, $\emptyset_w$	**Water**	**1 M MeOH**	**1 M KOFm**	**1M MeOH & 1 M KOFm**
PA/A	0.39 ± 0.01	12.4 ± 1.0	9.8 ± 1.3	6.7 ± 0.6	12.8 ± 0.9
PA/MA	0.43 ± 0.00	12.7 ± 1.2	12.2 ± 2.0	14.8 ± 0.0	10.2 ± 1.6
PA/S	0.47 ± 0.00	14.5 ± 0.9	15.0 ± 0.5	9.6 ± 1.6	11.4 ± 1.2
PA/SM	0.50 ± 0.01	13.9 ± 1.2	12.7 ± 0.3	11.7 ± 0.5	9.3 ± 1.4

6.3. Conclusions

The single and mixed solute transport of two CO_2 reduction products, methanol (MeOH) and formate (OFm^-), were investigated in four different phenyl acrylate (PA)-based crosslinked ion exchange membranes (PA/A, PA/MA, PA/S, and PA/SM). Briefly, PA/A and PA/MA are anion exchange membranes with QA^+ functional groups and PA/S and PA/SM are cation exchange

membranes with SO_3^- functional groups, where PA/A and PA/S are methacrylate-free films, while PA/ MA and PA/SM are methacrylate-containing films. In mixed solute permeation experiments, we observed MeOH tends to permeate more rapidly than KOFm at a lower water volume fraction, presumably due to the flux coupling. In mixed solute sorption experiments, we note that PA/MA had the lowest MeOH and KOFm sorption coefficients, which is encouraging in terms of preventing the crossover of these CO_2 reduction products. Finally, we hypothesized that methacrylate backbone linkages, which provide greater polymer rigidity in PA/MA and PA/SM compared to PA/A and PA/S, may influence polymer−water interactions such that KOFm does not interfere significantly with the hydrogen bond network within the material; as shown in Figure 6.6. We observed lower relative permittivity values when MeOH was present in the equilibration solution likely due to lower water content within swollen films. Based on these findings, enhancing anion exchange membranes by incorporating methacrylate monomers to increase steric hindrance (via the quaternary carbons) may be useful for engineering membranes for CO_2 reduction cells.

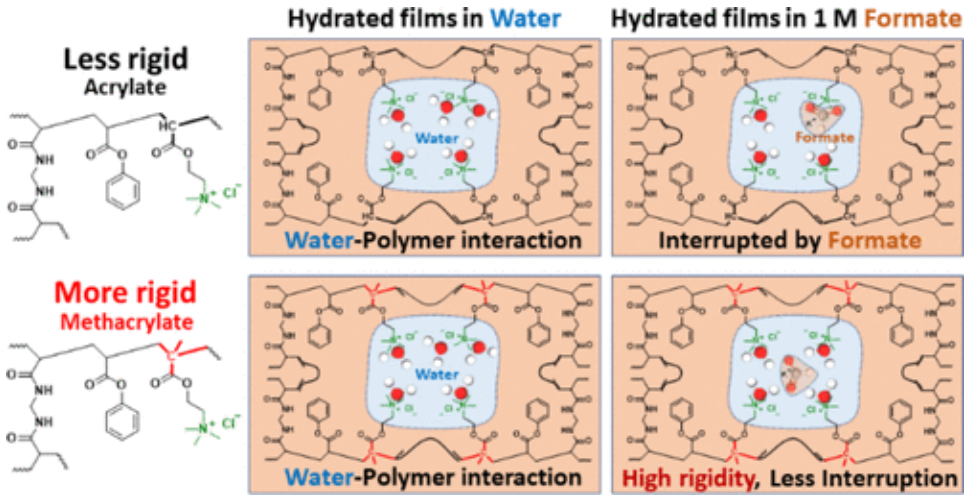

Figure 6.6. Schematic depiction of different rigidity hydrated film interaction with water and formate.

6.4. References

[1] M. Anwar, A. Fayyaz, N. Sohail, M. Khokhar, M. Baqar, W. Khan, K. Rasool, M. Rehan, A. Nizami, CO2 capture and storage: a way forward for sustainable environment, Journal of environmental management 226 (2018) 131-144.

[2] J. Resasco, A.T. Bell, Electrocatalytic CO2 reduction to fuels: progress and opportunities, Trends in Chemistry 2(9) (2020) 825-836.

[3] A. Katzenberg, A. Angulo, A. Kusoglu, M.A. Modestino, Impacts of organic sorbates on the ionic conductivity and nanostructure of perfluorinated sulfonic-acid ionomers, Macromolecules 54(11) (2021) 5187-5195.

[4] J. Baessler, T. Oliveira, R. Keller, M. Wessling, Paired electrosynthesis of formic acid from CO2 and formaldehyde from methanol, ACS Sustainable Chemistry & Engineering 11(18) (2023) 6822-6828.

[5] Z. Wang, J. Parrondo, V. Ramani, Anion exchange membranes based on polystyrene-block-poly (ethylene-ran-butylene)-block-polystyrene triblock copolymers: cation stability and fuel cell performance, Journal of The Electrochemical Society 164(12) (2017) F1216.

[6] J.M. Kim, Y.-h. Lin, B. Hunter, B.S. Beckingham, Transport and co-transport of carboxylate ions and ethanol in anion exchange membranes, Polymers 13(17) (2021) 2885.

[7] J. Park, Y.-j. Ko, C. Lim, H. Kim, B.K. Min, K.-Y. Lee, J.H. Koh, H.-S. Oh, W.H. Lee, Strategies for CO2 electroreduction in cation exchange membrane electrode assembly, Chemical Engineering Journal 453 (2023) 139826.

[8] N. Wang, R.K. Miao, G. Lee, A. Vomiero, D. Sinton, A.H. Ip, H. Liang, E.H. Sargent, Suppressing the liquid product crossover in electrochemical CO2 reduction, SmartMat 2(1) (2021) 12-16.

[9] M. Ramdin, A.R. Morrison, M. de Groen, R. van Haperen, R. De Kler, L.J. Van Den Broeke, J.M. Trusler, W. De Jong, T.J. Vlugt, High pressure electrochemical reduction of CO2 to formic acid/formate: a comparison between bipolar membranes and cation exchange membranes, Industrial & engineering chemistry research 58(5) (2019) 1834-1847.

[10] M. Paul, H.B. Park, B.D. Freeman, A. Roy, J.E. McGrath, J. Riffle, Synthesis and crosslinking of partially disulfonated poly (arylene ether sulfone) random copolymers as candidates for chlorine resistant reverse osmosis membranes, Polymer 49(9) (2008) 2243-2252.

[11] J.M. Kim, Y. Wang, Y.-h. Lin, J. Yoon, T. Huang, D.-J. Kim, M.L. Auad, B.S. Beckingham, Fabrication and Characterization of Cross-Linked Phenyl-Acrylate-Based Ion Exchange

Membranes and Performance in a Direct Urea Fuel Cell, Industrial & Engineering Chemistry Research 60(41) (2021) 14856-14867.

[12] J.M. Kim, A. Mazumder, J. Li, Z. Jiang, B.S. Beckingham, Impact of PEGMA on transport and co-transport of methanol and acetate in PEGDA-AMPS cation exchange membranes, Journal of Membrane Science 642 (2022) 119950.

[13] J.M. Kim, Y.-H. Lin, P.P. Aravindhan, B.S. Beckingham, Impact of hydrophobic pendant phenyl groups on transport and co-transport of methanol and acetate in PEGDA-SPMAK cation exchange membranes, Chemical Engineering Research and Design 185 (2022) 418-429.

[14] J.M. Kim, B.S. Beckingham, Transport and co-transport of carboxylate ions and alcohols in cation exchange membranes, Journal of Polymer Science 59(21) (2021) 2545-2558.

[15] J.G. Wijmans, R.W. Baker, The solution-diffusion model: a review, Journal of membrane science 107(1-2) (1995) 1-21.

[16] G. Geise, B. Freeman, D. Paul, Characterization of a sulfonated pentablock copolymer for desalination applications, Polymer 51(24) (2010) 5815-5822.

[17] K. Chang, T. Xue, G.M. Geise, Increasing salt size selectivity in low water content polymers via polymer backbone dynamics, Journal of Membrane Science 552 (2018) 43-50.

[18] A. Kusoglu, A.Z. Weber, New insights into perfluorinated sulfonic-acid ionomers, Chemical reviews 117(3) (2017) 987-1104.

[19] S.-T. Pei, S. Jiang, Y.-R. Liu, T. Huang, K.-M. Xu, H. Wen, Y.-P. Zhu, W. Huang, Properties of ammonium ion–water clusters: analyses of structure evolution, noncovalent interactions, and temperature and humidity effects, The Journal of Physical Chemistry A 119(12) (2015) 3035-3047.

[20] H. Wu, Q. Gong, D.H. Olson, J. Li, Commensurate adsorption of hydrocarbons and alcohols in microporous metal organic frameworks, Chemical Reviews 112(2) (2012) 836-868.

[21] E. Nightingale Jr, Phenomenological theory of ion solvation. Effective radii of hydrated ions, The Journal of Physical Chemistry 63(9) (1959) 1381-1387.

[22] R. Caminiti, P. Cucca, M. Monduzzi, G. Saba, G. Crisponi, Divalent metal–acetate complexes in concentrated aqueous solutions. An x-ray diffraction and NMR spectroscopy study, The Journal of chemical physics 81(1) (1984) 543-551.

[23] M. Ito, P. Kostyuk, T. Oshima, Further study on anion permeability of inhibitory post-synaptic membrane of cat motoneurones, The Journal of Physiology 164(1) (1962) 150.

[24] W.J. Koros, R. Chern, V. Stannett, H. Hopfenberg, A model for permeation of mixed gases and vapors in glassy polymers, Journal of polymer Science: polymer physics edition 19(10) (1981) 1513-1530.

[25] J. Kamcev, D.R. Paul, B.D. Freeman, Ion activity coefficients in ion exchange polymers: applicability of Manning's counterion condensation theory, Macromolecules 48(21) (2015) 8011-8024.

[26] G.S. Manning, J. Ray, Counterion condensation revisited, Journal of Biomolecular Structure and Dynamics 16(2) (1998) 461-476.

[27] P.S. Albright, L.J. Gosting, Dielectric constants of the methanol-water system from 5 to 55, Journal of the American Chemical Society 68(6) (1946) 1061-1063.

[28] H.M. Rahman, G. Hefter, R. Buchner, Hydration of formate and acetate ions by dielectric relaxation spectroscopy, The Journal of Physical Chemistry B 116(1) (2012) 314-323.

[29] K. Chang, G.M. Geise, Dielectric permittivity properties of hydrated polymers: measurement and connection to ion transport properties, Industrial & Engineering Chemistry Research 59(12) (2019) 5205-5217.

Chapter 7: Salt Transport in Zwitterionic Membranes

Reproduced from: Lin, Y.; Kim, J. M.; Beckingham, B. S. Salt Transport in Crosslinked Hydrogel Membranes Containing Zwitterionic Sulfobetaine Methacrylate and Hydrophobic Phenyl Acrylate. Polymers 2023, 15 (6), 1387. DOI:10.3390/polym15061387.

7.1. Introduction

Wastewater containing metal ions is produced from a wide variety of commercial activities, including oil extraction, metal plating, mining, battery production, paint manufacturing, etc [1]. The metals in these streams must be removed prior to discharge as they are hazardous to the environment and human health where they have the propensity to accumulate in the human body and induce disease [2]. Wastewater treatment is difficult; however, methods such as chemical precipitation, oxidation, ion exchange, filtration, biological treatment, and adsorption have been used to remove metal ions from aqueous solutions [3, 4]. Membrane separation processes are promising unit operations for the removal of these species due to the potential for high selectivity and low energy consumption, which has led to the adoption of membrane separation technologies for the remediation of wastewater [5]. However, the long-standing issue of colloidal, organic, and other membrane fouling substantially impairs membrane functionality, limiting membrane performance and lifetime [6]. Numerous attempts have been made to modify and optimize the membrane surface to improve membrane performance, as the chemical and physical characteristics

of the membrane surface play a significant role in membrane performance. Relatedly, zwitterionic polymers, which bear both positive and negative charges while being charge neutral overall, have received a great deal of attention as hydrophilic, ultra-low fouling materials that can withstand the adsorption by bacteria, cells, and protein [7]. The significant surface hydration caused by electrostatically induced hydrogen bonding in these zwitterionic polymer films is thought to be the source of the antifouling characteristics [8]. The presence of the zwitterions and thereby firmly bonded hydration layers at the surface act as physical and energetic barriers to foulant surface adhesion [9]. Zwitterions have been incorporated into polymers in various ways including as surface layers, grafted into or polymerized within the pores of filtration membranes as transport-controlling materials, and within unsupported dense polymer membranes [10-20]. For instance, Ni et al. investigated zwitterionic polymer films fabricated using sulfobetaine methacrylate (SBMA) or carboxybetaine methacrylate (CBMA) as the zwitterionic comonomer with poly(ethylene glycol) diacrylate (PEGDA) as the crosslinker where water uptake and permeability increased with zwitterion content, but salt permeability increased for SBMA-containing and decreased for CBMA-containing films as salt concentration increased [19]. Relatedly, Chiao et al. found the coating of porous polyvinylidene difluoride (PVDF) membranes coated with zwitterionic poly(SBMA) led to higher water flux, increased bovine serum albumin rejection, and improved antifouling performance [20].

Herein, we combine phenyl acrylate (PA), a monomer previously found to improve mechanical properties [21, 22], and the commercially available zwitterionic monomer, sulfobetaine methacrylate (SBMA), within crosslinked polymer films using N,N'-methylenebisacrylamide (MBAA). The physiochemical properties of a series of fabricated

polymer membranes at varied PA/SBMA content—including water content, dry polymer density, and transport behavior including permeability and solubility—are characterized and discussed.

7.2. Results and Discussion

A total of 6 membrane chemistries denoted SX-Y where X represents the mol% SBMA with the remaining PA, and Y represents the mol% MBAA of total monomer (PA and SBMA) S20-10, S20-20, S30-10, S30-20, S40-10, and S40-20 were prepared by thermal copolymerization of pre-polymerization mixtures, as shown in Figure 7.1. The composition of the pre-polymerization mixtures is provided in Table 7.1. Each mixture contained 70 wt.% DMSO and 0.1 wt.% AIBN. The materials, membrane synthesis methods, and experimental procedures are detailed in Chapter 3.

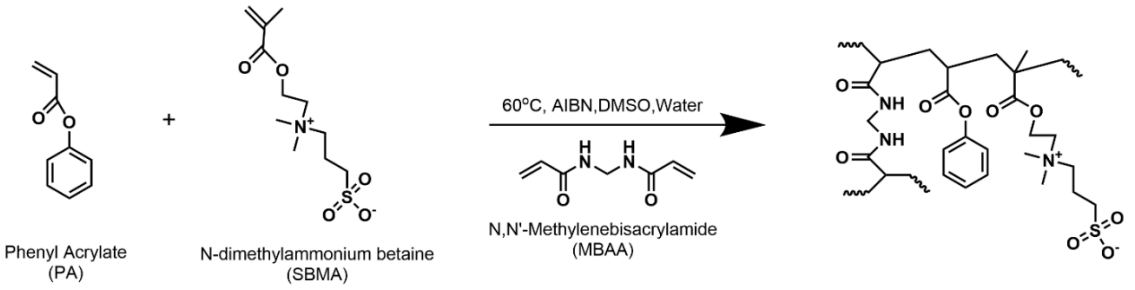

Figure 7.1. Synthetic scheme of PA-SBMA membrane.

Table 7.1. Pre-polymerization mixture compositions.

Membrane	PA (mol%)	SBMA (mol%)	MBAA [1] (mol%)
S20-10	80	20	10
S20-20	80	20	20
S30-10	70	30	10
S30-20	70	30	20
S40-10	60	40	10
S40-20	60	40	20

[1] MBAA = mol of MBAA/ (mol of PA + mol of SBMA) × 100%

7.2.1. Membrane Characterization

ATR-FTIR was utilized to analyze the zwitterionic polymer films and determine the degree of conversion of their acrylate groups. The spectra of all films are presented in Figure 7.2, wherein the absorption at 1640 cm^{-1} is attributed to the C=C group. Notably, this band was absent in the crosslinked film spectra, suggesting the complete conversion of acrylate groups and the breakage of the double bond during polymerization.

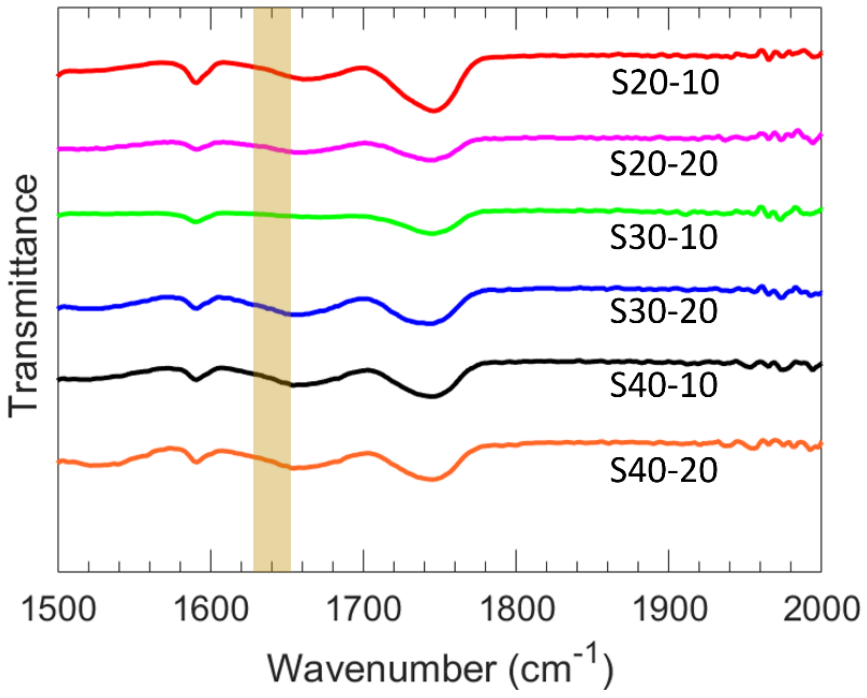

Figure 7.2. Representative FTIR spectra for each membrane composition.

The characterized water uptake, dry polymer density, ionic conductivity, and Young's modulus for each of the six investigated polymer film chemistries are shown in Table 7.2, and the membrane water volume fraction is shown in Figure 7.3. With increased MBAA content, water

uptake decreases for both S20-Y and S30-Y, which is attributed to the corresponding increase in crosslinking density [23, 24]. For S40-Y, a decrease was observed as well, but it is within the experimental error (~1%). Water uptake also decreases with increasing SBMA content, which may be due in part to structural differences within the films. Increasing the SBMA content results in a more compact structure due to its linear shape whereas the comparably bulky phenyl ring on PA likely results in more fractional free volume, even though, structurally, PA is a more hydrophobic comonomer. In addition, we conjecture that higher SBMA content films have more ionic interactions between the ammonium and sulfonate moieties, which serve as dynamic crosslinks resulting in decreased water uptake and water volume fraction. These differences in water uptake and the polymer network structure also manifest as differences in the water volume fraction (Figure 7.3). For the lower MBAA content series (SX-10), the water volume fraction decreases somewhat as the SBMA content increases from 0.613 for S20-10 to 0.573 for S40-10. A similar general trend is observed for the SX-20 series. However, S30-20 showed both the lowest water uptake and water volume fraction of the membranes characterized. Relatedly, membrane ionic conductivities increase with increasing SBMA content due to the increase in ion content, which is consistent with the generally observed properties of ionic polymers [25, 26]. Interestingly, the highest ionic conductivity is observed for S40-20 (1.56 mS/cm) and is significantly higher (22%) than the next highest ionic conductivity (1.28 mS/cm for S40-10). The primary difference between these two films is the increased MBAA content for S40-20; correspondingly, S40-20 has slightly lower PA and SBMA contents. The resulting structural difference is a tighter network due to the higher crosslink density for S40-20, which may be the cause of this increased conductivity. Regardless, this behavior will be investigated in a subsequent study.

Table 7.2. Water uptake, dry polymer density, and ionic conductivity of all films.

	ω_w (g water/ g dry polymer)	ρ_p (g/mL)	Ionic Conductivity (mS/cm)	Young's Modulus (MPa)
S20-10	125 ± 2	1.26 ± 0.04	1.20 ± 0.01	0.93 ± 0.03
S20-20	116 ± 4	1.30 ± 0.04	1.22 ± 0.04	1.00 ± 0.00
S30-10	108 ± 0	1.29 ± 0.00	1.26 ± 0.03	0.52 ± 0.02
S30-20	100 ± 1	1.29 ± 0.01	1.27 ± 0.02	0.78 ± 0.05
S40-10	104 ± 1	1.29 ± 0.01	1.28 ± 0.03	0.26 ± 0.01
S40-20	103 ± 1	1.31 ± 0.01	1.56 ± 0.03	0.27 ± 0.02

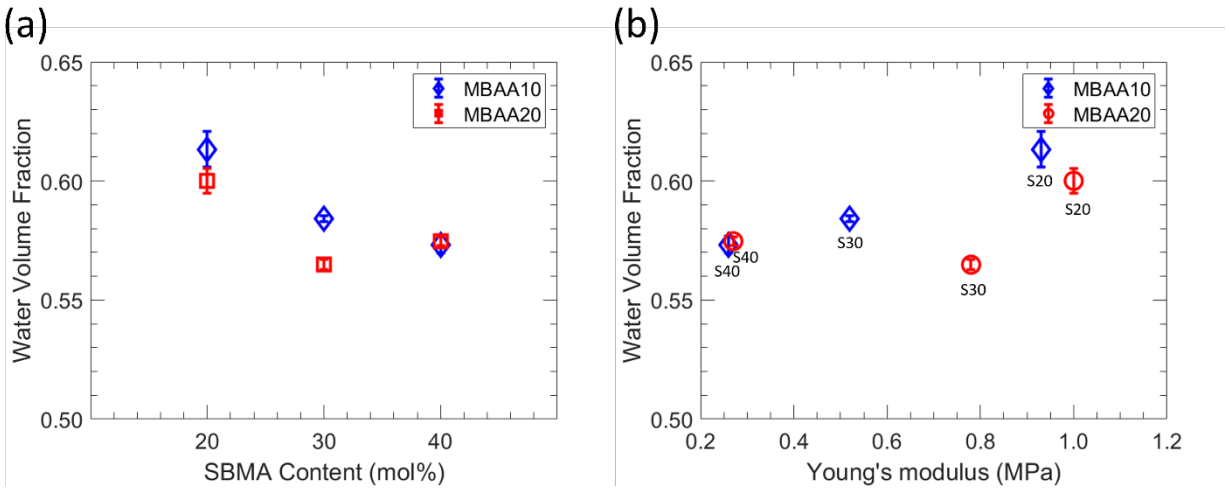

Figure 7.3. (a) Water volume fraction as functions of SBMA content. (b) Water volume fraction as function of Young's modulus.

7.2.2. Mechanical Characterization

Tensile tests were performed in triplicate to evaluate the mechanical properties of all membranes, and exemplary stress-strain curves are shown in Figure 7.4. The average Young's modulus (Table 7.2) increases with increasing PA and/or MBAA content. The higher Young's modulus with increasing PA content is attributed primarily to its hydrophobicity and the rigid benzene ring, which impact the inner structure and strength of the hydrated films. However, this

increase in Young's modulus comes with a corresponding decrease in the strain at break. Notably, these SBMA-containing hydrogel membranes have a relatively high Young's modulus compared to some other reported SBMA-containing membranes [27-29]. For instance, Shen et al. reported crosslinked poly(SBMA) hydrogel membranes, using MBAA as the crosslinker analogous to our work here, to have a Young's modulus of 0.002 MPa, and crosslinked copolymer hydrogels of SBMA with acrylic acid all had Young's moduli under 0.4 MPa [27].

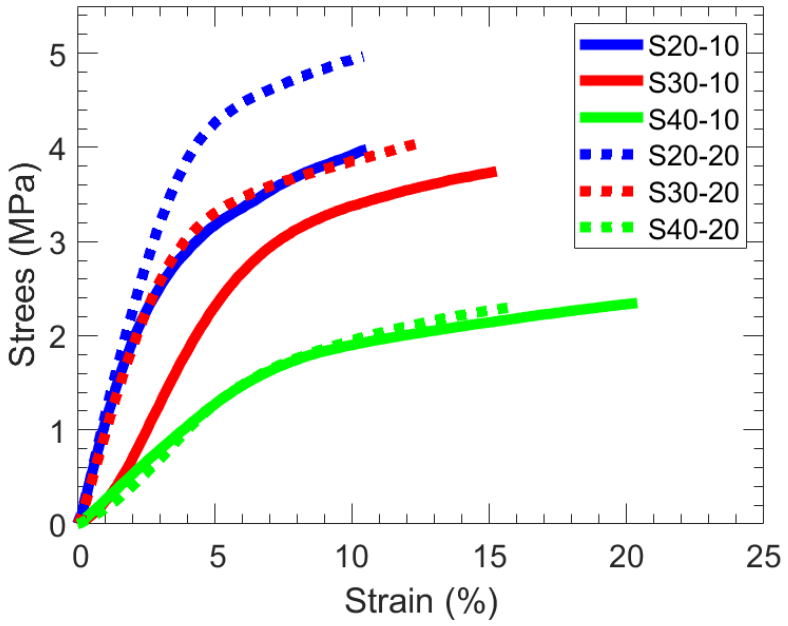

Figure 7.4. Representative stress–strain curves for (solid) SX-10 and (dotted) SX-20 films.

7.2.3. Salt Permeability

Permeabilities to NaCl, LiCl, KCl, $NiCl_2$, $CaCl_2$, and $MgCl_2$ of all six films were measured by in situ conductivity diffusion cell with the results shown in Figure 7.5. Generally, permeability to metal ions increases with an increasing water volume fraction value or decreasing MBAA content. This behavior is expected as the water volume fraction increases as solute diffusivities

tend to rise with increasing water volume fraction within a membrane (free volume theory [30, 31]).

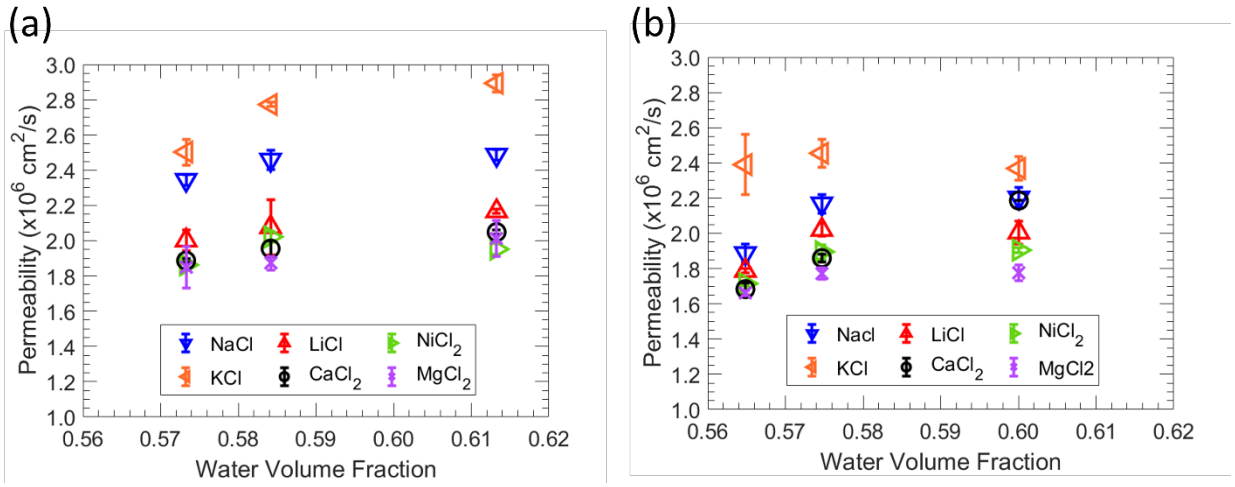

Figure 7.5. (a) Correlation between permeability and water volume fraction in MBAA 10 zwitterionic polymer. (b) Correlation between permeability and water volume fraction in MBAA 20 zwitterionic polymers. The average of three experiments is shown by each data point, and the error bars represent the standard deviation**.**

Salt permeabilities for all films generally follow the order of KCl > NaCl > LiCl > $NiCl_2$ > $CaCl_2$ > $MgCl_2$, suggesting that the size difference between cation serves as the main criterion for differentiation since the alkali metal chloride solutions share a common anion (Cl^-). The reported hydration radius of the metal ions [32] are in the order of K^+ (3.31 Å) < Na^+ (3.58 Å) < Li^+ (3.82 Å) < Ni^{2+} (4.04 Å) < Ca^{2+} (4.12 Å) < Mg^{2+} (4.28 Å) such that we find that the observed variations in permeability between these solutions may be ascribed primarily to the identity of the cation [33]. The salt permeability of the films is consistent with water sorption behavior, where a higher water volume fraction leads to a higher permeability. The relationship between water content and salt permeability for these zwitterionic polymer membranes is generally consistent with Yasuda's model, where high water sorption corresponds with high salt permeability.

7.2.4. Salt Solubility

The relationship between the salt sorption and the membrane zwitterion content is shown in Figure 7.6. Salt solubility was determined through a kinetic desorption experiment using 0.1 M solutions of the salt of interest (NaCl, LiCl, KCl, $NiCl_2$, $CaCl_2$, or $MgCl_2$) [30, 34]. Interestingly, the order of the salt sorption changes as the content of the zwitterionic monomer changes such that the salt sorption cannot be explained simply by correlating the size of the hydrated cation and surface charge density to the magnitude of salt sorption. Yasuda et al. hypothesized that the capacity of a polymer to sorb salt is severely constrained in the absence of water by assuming the water in the membrane phase dissolves all salt [30]. Since water molecules cluster at or near polymer chains in membranes with greater water absorption, direct interactions between polymer chains and ions are restricted [35]. However, as the membrane water content declines, increasing the interactions between polymer and ions, as well as the interactions between the polymer and water, may cause the ions in the membrane to behave in a highly non-ideal manner, which would then influence ion sorption. Because the water content decreases with increasing SBMA content, interactions between the polymer and the ion and the polymer and the water are thought to have an impact on how different salts interact with them within the film. In other words, the main determinants of alkali metal chloride sorption in polymers are the polymer water content and the interactions between ions and polymer segments. In addition, ion charge density, which affects an ion's propensity for hydration and interactions with the polymer, has been shown in several investigations to affect the precise interactions between various ions and polymer segments [36, 37]. The sorption of alkali chlorides is significantly impacted by the cations since NaCl, LiCl, KCl,

$NiCl_2$, $CaCl_2$, and $MgCl_2$ all share Cl^-, a large, low-charge density ion that weakly binds water molecules. Moreover, ion charge density increases as the ion crystal radius decrease in the alkali metal ion series, where the order of the crystal's radius is K (1.33 Å) > Ca (0.99 Å) > Na (0.95 Å) > Ni (0.70 Å) > Mg (0.65 Å) > Li (0.60 Å) [32]. The amount of water absorbed by the polymer varies depending on the salt solution because ions with various charge densities carry different amounts of water molecules into the polymer matrix. For example, Li^+ ions carry more water molecules than K^+ ions into the polymer matrix. Since salt sorption in charged polymers is strongly correlated with properties related to the charged groups on the polymer [38-40], increasing the zwitterionic monomer content generally increases the sorption such that charged groups in these zwitterionic polymer membranes may enhance salt sorption, though in different degrees as observed here [8, 41].

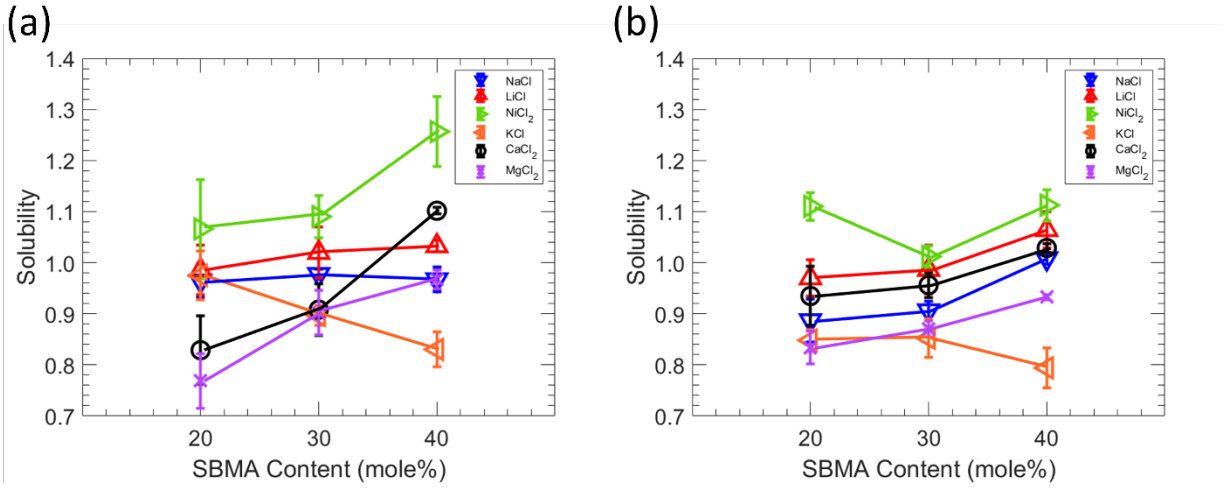

Figure 7.6. (a) Effect of SBMA content on the salt solubility to MBAA 10 films. (b) Effect of SBMA content on the salt solubility to MBAA 20 films. The average of three experiments is shown by each data point, and the error bars represent the standard deviation. Lines are guides to the eye.

7.2.5. Salt Diffusivity

Salt sorption and permeability parameters were assessed and utilized to determine the effective diffusivity using Equation 7.1. Figure 7.7 presents the correlation between diffusivity and the water volume fraction. The diffusivity, D_i, of solute i in a membrane is closely related to the fractional free volume of membranes by

$$D_i = \alpha_i \exp\left(\frac{-b_i}{v_f}\right) \tag{7.1}$$

where α_i and b_i are empirical parameters; α_i is related to a geometric factor and the velocity of solute i, and b_i is linked to the Lennard–Jones diameter of solute i [42, 43]

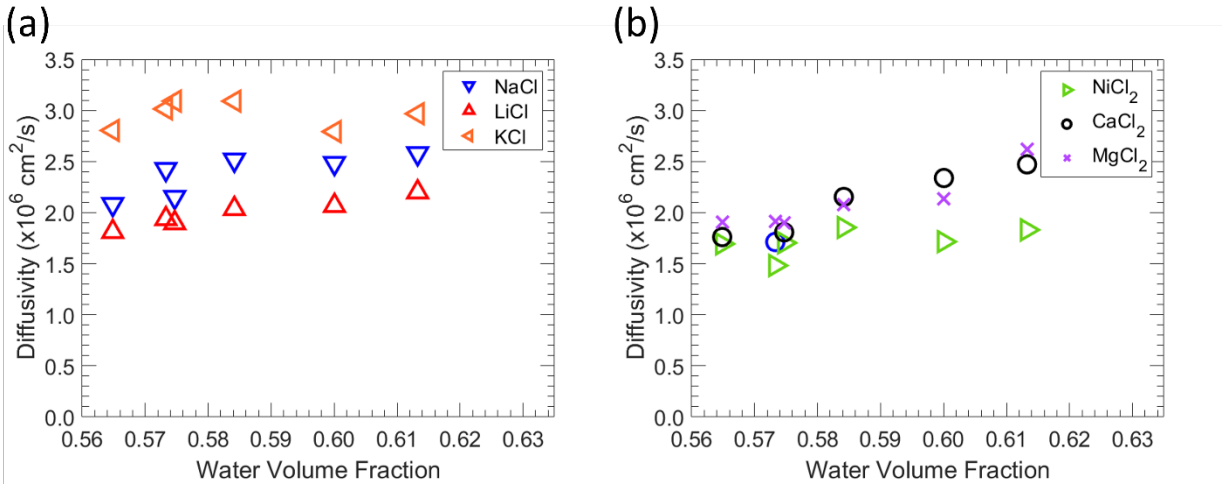

Figure 7.7. Correlation of diffusivity and water volume fraction in zwitterionic polymers. (a) Effect of water volume fraction on the monovalent salt diffusivity. (b) Effect of water volume fraction on the divalent salt diffusivity.

According to eq 7.1, the diffusivity of a solute of a specific size rises with v_f. Because the water volume fraction is directly connected to the fractional free volume available in the hydrated

polymers for diffusion, raising the water volume fraction values generally results in higher salt diffusivity [44, 45]. For a wide range of polymers, this result is consistent with a connection between salt diffusivity and water absorption. The order varies with polymer water content, indicating that ion hydration and particular interactions between polymer and ions affect alkali metal chloride diffusion behavior in polymers. Ions with lower hydrated radii diffuse in aqueous solutions more quickly than ions with higher hydrated radii [46].

7.3. Conclusions

This study investigates the fundamental transport properties of small molecules including NaCl, LiCl, KCl, $NiCl_2$, $CaCl_2$, and $MgCl_2$ in a series of zwitterionic polymers prepared via thermal free-radical polymerization from SBMA and PA, which were crosslinked at two different MBAA contents. The properties of zwitterionic polymer films were investigated through various analytical techniques, including ATR-FTIR spectroscopy, water volume fraction measurements, ionic conductivity, Young's modulus, and salt permeability. The results show that the degree of conversion of acrylate groups was high in crosslinked films and increasing the SBMA content led to a decreased water volume fraction and increased ionic conductivity due to corresponding increases in polymer density, dynamic crosslinks, and increased ion content; as shown in Figure 7.8. The higher Young's modulus with increasing PA content was attributed to its hydrophobicity and rigid benzene ring. Interestingly, while permeabilities are generally linked to the water content within the membrane, the order of the preference for salt sorption changes as the content of the zwitterionic monomer changes. Salt permeability was primarily affected by the size of the cation, and the relationship between water content and salt permeability was consistent with Yasuda's

model. The salt sorption capacity of the polymer films could not be solely explained by the size of the hydrated cation and surface charge density but is indicative of more complex interactions between the membrane and the solutes, which requires further investigation to both understand and exploit the design of polymer membranes for emerging applications.

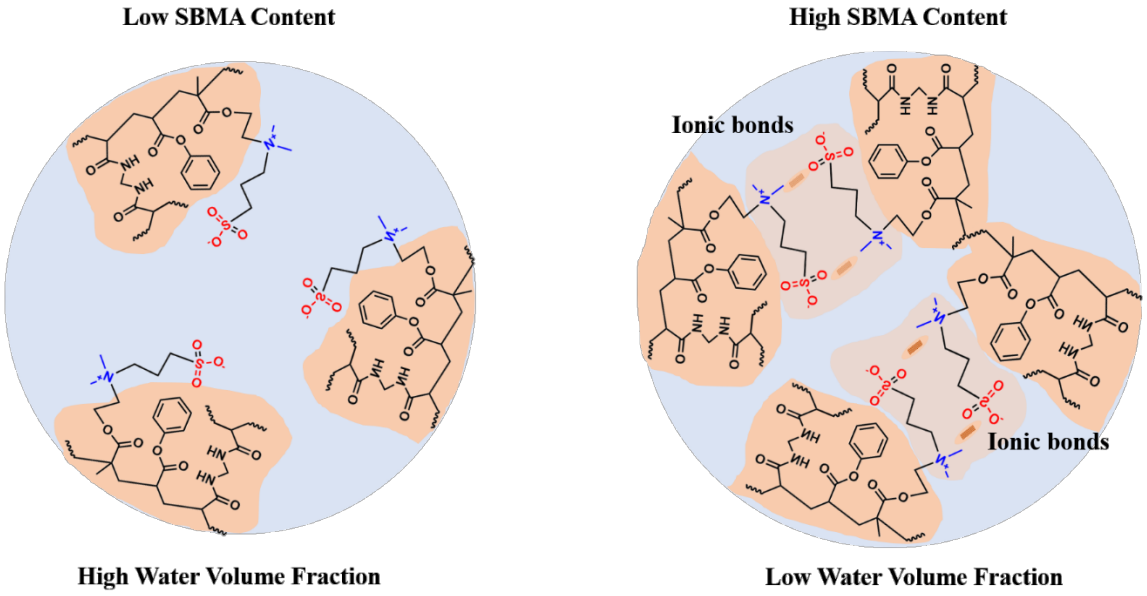

Figure 7.8. Schematic depiction of ionic interactions between the ammonium and sulfonate groups in both low and high SBMA content.

7.4. References

[1] F. Fu, Q. Wang, Removal of heavy metal ions from wastewaters: a review, Journal of environmental management 92(3) (2011) 407-418.

[2] G.P. Kumar, P.A. Kumar, S. Chakraborty, M. Ray, Uptake and desorption of copper ion using functionalized polymer coated silica gel in aqueous environment, Separation and Purification Technology 57(1) (2007) 47-56.

[3] E.A. Deliyanni, G.Z. Kyzas, K.A. Matis, Various flotation techniques for metal ions removal, Journal of Molecular Liquids 225 (2017) 260-264.

[4] L.P. Lingamdinne, J.R. Koduru, R.R. Karri, A comprehensive review of applications of magnetic graphene oxide based nanocomposites for sustainable water purification, Journal of environmental management 231 (2019) 622-634.

[5] K.V. Plakas, A.J. Karabelas, Removal of pesticides from water by NF and RO membranes—A review, Desalination 287 (2012) 255-265.

[6] A. Widjaya, T. Hoang, G.W. Stevens, S.E. Kentish, A comparison of commercial reverse osmosis membrane characteristics and performance under alginate fouling conditions, Separation and purification technology 89 (2012) 270-281.

[7] W. Li, K. Chu, L. Liu, Multipurpose zwitterionic polymer-coated glass fiber filter for effective separation of oil–water mixtures and emulsions and removal of heavy metals, ACS Applied Polymer Materials 3(3) (2021) 1276-1284.

[8] S. Shah, J. Liu, S. Ng, S. Luo, R. Guo, C. Cheng, H. Lin, Transport properties of small molecules in zwitterionic polymers, Journal of Polymer Science Part B: Polymer Physics 54(19) (2016) 1924-1934.

[9] S. Chen, L. Li, C. Zhao, J. Zheng, Surface hydration: Principles and applications toward low-fouling/nonfouling biomaterials, Polymer 51(23) (2010) 5283-5293.

[10] P. Salimi, A. Aroujalian, D. Iranshahi, Graft copolymerization of zwitterionic monomer on the polyethersulfone membrane surface by corona air plasma for separation of oily wastewater, Separation and Purification Technology 258 (2021) 117939.

[11] P. Bengani, Y. Kou, A. Asatekin, Zwitterionic copolymer self-assembly for fouling resistant, high flux membranes with size-based small molecule selectivity, Journal of Membrane Science 493 (2015) 755-765.

[12] P. Bengani-Lutz, I. Sadeghi, S.J. Lounder, M.J. Panzer, A. Asatekin, High flux membranes with ultrathin zwitterionic copolymer selective layers with~ 1 nm pores using an ionic liquid cosolvent, ACS Applied Polymer Materials 1(8) (2019) 1954-1959.

[13] S.J. Lounder, A. Asatekin, Zwitterionic ion-selective membranes with tunable subnanometer pores and excellent fouling resistance, Chemistry of Materials 33(12) (2021) 4408-4416.

[14] J. Xu, J. Xu, H. Moon, H.O. Sintim, H. Lee, Zwitterionic porous conjugated polymers as a versatile platform for antibiofouling implantable bioelectronics, ACS applied polymer materials 2(2) (2020) 528-536.

[15] S.K. Lau, W.F. Yong, Recent progress of zwitterionic materials as antifouling membranes for ultrafiltration, nanofiltration, and reverse osmosis, ACS Applied Polymer Materials 3(9) (2021) 4390-4412.

[16] M.-C. Sin, S.-H. Chen, Y. Chang, Hemocompatibility of zwitterionic interfaces and membranes, Polymer journal 46(8) (2014) 436-443.

[17] S. Buyukdagli, R. Podgornik, Interactions between zwitterionic membranes in complex electrolytes, Physical Review E 102(1) (2020) 012806.

[18] S.J. Lounder, A. Asatekin, Interaction-based ion selectivity exhibited by self-assembled, cross-linked zwitterionic copolymer membranes, Proceedings of the National Academy of Sciences 118(37) (2021) e2022198118.

[19] L. Ni, J. Meng, G.M. Geise, Y. Zhang, J. Zhou, Water and salt transport properties of zwitterionic polymers film, Journal of membrane science 491 (2015) 73-81.

[20] Y.-H. Chiao, S.-T. Chen, M. Sivakumar, M.B.M.Y. Ang, T. Patra, J. Almodovar, S.R. Wickramasinghe, W.-S. Hung, J.-Y. Lai, Zwitterionic polymer brush grafted on polyvinylidene difluoride membrane promoting enhanced ultrafiltration performance with augmented antifouling property, Polymers 12(6) (2020) 1303.

[21] J.M. Kim, Y. Wang, Y.-h. Lin, J. Yoon, T. Huang, D.-J. Kim, M.L. Auad, B.S. Beckingham, Fabrication and Characterization of Cross-Linked Phenyl-Acrylate-Based Ion Exchange Membranes and Performance in a Direct Urea Fuel Cell, Industrial & Engineering Chemistry Research 60(41) (2021) 14856-14867.

[22] M.T.I. Mredha, S.K. Pathak, J. Cui, I. Jeon, Hydrogels with superior mechanical properties from the synergistic effect in hydrophobic–hydrophilic copolymers, Chemical Engineering Journal 362 (2019) 325-338.

[23] A. Jastram, T. Lindner, C. Luebbert, G. Sadowski, U. Kragl, Swelling and diffusion in polymerized ionic liquids-based hydrogels, Polymers 13(11) (2021) 1834.

[24] H. Lin, T. Kai, B.D. Freeman, S. Kalakkunnath, D.S. Kalika, The effect of cross-linking on gas permeability in cross-linked poly (ethylene glycol diacrylate), Macromolecules 38(20) (2005) 8381-8393.

[25] C.G. Cho, H.Y. Jang, Y.G. You, G.H. Li, S.G. An, Preparation of Poly (phenylene oxide-gstyrenesulfonic acid) and their Characterization for DMFC Membrane, High Performance Polymers 18(5) (2006) 579-591.

[26] Y. Li, J. Sniekers, J.C. Malaquias, C. Van Goethem, K. Binnemans, J. Fransaer, I.F. Vankelecom, Crosslinked anion exchange membranes prepared from poly (phenylene oxide)(PPO) for non-aqueous redox flow batteries, Journal of Power Sources 378 (2018) 338-344.

[27] J. Shen, M. Du, Z. Wu, Y. Song, Q. Zheng, Strategy to construct polyzwitterionic hydrogel coating with antifouling, drag-reducing and weak swelling performance, RSC advances 9(4) (2019) 2081-2091.

[28] O. Hu, J. Lu, S. Weng, L. Hou, X. Zhang, X. Jiang, An adhesive, anti-freezing, and environment stable zwitterionic organohydrogel for flexible all-solid-state supercapacitor, Polymer 254 (2022) 125109.

[29] M. He, L. Chen, L. Zhang, L. Shen, H. Zhen, L. Wang, P. Xu, J. Bao, A zwitterion-based hydrogel with high-strength, high transparency, anti-adhesion and degradability, Journal of Materials Science 57(35) (2022) 16830-16841.

[30] H. Yasuda, C. Lamaze, L. Ikenberry, Permeability of solutes through hydrated polymer membranes. Part I. Diffusion of sodium chloride, Die Makromolekulare Chemie: Macromolecular Chemistry and Physics 118(1) (1968) 19-35.

[31] H. Yasuda, A. Peterlin, C. Colton, K. Smith, E. Merrill, Permeability of solutes through hydrated polymer membranes. Part III. Theoretical background for the selectivity of dialysis membranes, Die Makromolekulare Chemie: Macromolecular Chemistry and Physics 126(1) (1969) 177-186.

[32] E. Nightingale Jr, Phenomenological theory of ion solvation. Effective radii of hydrated ions, The Journal of Physical Chemistry 63(9) (1959) 1381-1387.

[33] U.G. Wegst, H. Bai, E. Saiz, A.P. Tomsia, R.O. Ritchie, Bioinspired structural materials, Nature materials 14(1) (2015) 23-36.

[34] K. Nagaia, S. Tanakaa, Y. Hirataa, T. Nakagawaa, M.E. Arnoldb, B.D. Freemanb, D. Lerouxc, D.E. Bettsc, J.M. DeSimonec, F.A. DiGianod, Solubility and diffusivity of sodium chloride in phase-separated block copolymers of poly 2-dimethylaminoethyl methacrylate), poly 1, 1 0-dihydroperfluorooctyl methacrylate) and poly 1, 1, 2, 2-tetrahydroperfluorooctyl acrylate), Polymer 42(9941) (2001) 9948.

[35] E.-S. Jang, J. Kamcev, K. Kobayashi, N. Yan, R. Sujanani, T.J. Dilenschneider, H.B. Park, D.R. Paul, B.D. Freeman, Influence of water content on alkali metal chloride transport in cross-linked Poly (ethylene glycol) Diacrylate. 1. Ion sorption, Polymer 178 (2019) 121554.

[36] B. Tansel, J. Sager, T. Rector, J. Garland, R.F. Strayer, L. Levine, M. Roberts, M. Hummerick, J. Bauer, Significance of hydrated radius and hydration shells on ionic permeability during nanofiltration in dead end and cross flow modes, Separation and Purification Technology 51(1) (2006) 40-47.

[37] M. Takano, K. Ogata, S. Kawauchi, M. Satoh, J. Komiyama, Ion-specific swelling behavior of poly (N-vinyl-2-pyrrolidone) gel: Correlations with water hydrogen bond and non-freezable water, Polymer Gels and Networks 6(3-4) (1998) 217-232.

[38] J. Kamcev, B.D. Freeman, Charged polymer membranes for environmental/energy applications, Annual review of chemical and biomolecular engineering 7(1) (2016) 111-133.

[39] H. Zhang, G.M. Geise, Modeling the water permeability and water/salt selectivity tradeoff in polymer membranes, Journal of Membrane Science 520 (2016) 790-800.

[40] J. Kamcev, D.R. Paul, G.S. Manning, B.D. Freeman, Predicting salt permeability coefficients in highly swollen, highly charged ion exchange membranes, ACS applied materials & interfaces 9(4) (2017) 4044-4056.

[41] J.B. Schlenoff, Zwitteration: coating surfaces with zwitterionic functionality to reduce nonspecific adsorption, Langmuir 30(32) (2014) 9625-9636.

[42] G.M. Geise, D.R. Paul, B.D. Freeman, Fundamental water and salt transport properties of polymeric materials, Progress in Polymer Science 39(1) (2014) 1-42.

[43] M.H. Cohen, D. Turnbull, Molecular transport in liquids and glasses, The Journal of Chemical Physics 31(5) (1959) 1164-1169.

[44] S. Zhao, K. Huang, H. Lin, Impregnated membranes for water purification using forward osmosis, Industrial & Engineering Chemistry Research 54(49) (2015) 12354-12366.

[45] H. Ju, A.C. Sagle, B.D. Freeman, J.I. Mardel, A.J. Hill, Characterization of sodium chloride and water transport in crosslinked poly (ethylene oxide) hydrogels, Journal of Membrane Science 358(1-2) (2010) 131-141.

[46] E.-S. Jang, J. Kamcev, K. Kobayashi, N. Yan, R. Sujanani, T.J. Dilenschneider, H.B. Park, D.R. Paul, B.D. Freeman, Influence of water content on alkali metal chloride transport in cross-linked Poly (ethylene glycol) diacrylate. 2. Ion diffusion, Polymer 192 (2020) 122316.

Chapter 8: Impact of Crosslinker on Physicochemical Properties and Transport Behavior in AEMs

8.1. Introduction

The use of solar energy in converting CO_2 through photo electrochemistry, also known as artificial photosynthesis, has attracted considerable attention [1-3]. This process aims to generate fuel and valuable chemicals like formate (OFm^-) and acetate (OAc^-) by reducing CO_2. [4] Typically, photoelectrochemical CO_2 reduction cells (PEC-CRC) consist of an anode and a cathode separated by an ion exchange membrane and liquid electrolyte [3, 5, 6]. Within these devices, the cathode facilitates the reduction of carbon dioxide into alcohol or other products, while the anode oxidizes water to generate oxygen. Membranes in these devices serve a dual role: First, facilitating the movement of electrolyte charge carriers between the electrodes to enable the flow of electric current and second, reducing the crossover of CO_2 reduction products from the cathode to the anode. When the reduction products reach the anode and undergo oxidation, it leads to the loss of products and wasted energy [1, 5, 7]. Therefore, anion exchange membranes (AEMs) play a crucial role in artificial photosynthesis devices due to their ability to selectively transport anions using charged functional groups within the membrane, such as quaternary ammonium (QA^+). In prior

research, our group has conducted a series of experiments using PEGDA-based membranes to enhance our understanding of PEGDA-based cation exchange membranes (CEMs) and AEMs for PEC-CRC applications [4, 8-12]. For CEMs synthesized using PEGDA, with 20 wt.% prepolymerization solvent content, and 2-acrylamido-2-methyl-1-propanesulfonic acid (AMPS) or sulfopropyl methacrylate potassium (SPMAK), the water volume fraction was approximately 50% and 45% respectively and permeability to CO_2 reduction products (methanol, sodium acetate) on the order of 10^{-7} cm²/s.[8, 10] Furthermore, for AEMs composed of PEGDA/APTA with 20 wt.% prepolymerization solvent content, the water volume fraction in the membranes is about 46%, the permeability to CO_2 reduction products (ethanol, sodium acetate, sodium formate, potassium acetate, and potassium formate) were also on the order of 10^{-7} cm²/s [4]. For both cases, it would be desirable to reduce the water volume fraction, improve the mechanical properties, and reduce the permeability to the CO_2 reduction products. In order to vary the water content in the membranes, there are several strategies that can be applied including variation of the solvent content of the prepolymerization mixture and/or variation of the polymer membrane chemistry to incorporate more hydrophobic moieties. For instance, in prior work varying the prepolymerization solvent content (water) in PEGDA membranes the water uptake could be varied by a factor of 3 in going from no water to 60 wt.% water in the prepolymerization mixture [9]. We also previously introduced different hydrophobic comonomers that featured hydrophobic phenyl groups at the end of their side chain— phenoxyethyl acrylate (PEA), and poly(ethylene glycol) phenyl ether acrylates (PEGPEA)—into crosslinked membranes and prepared neutral and AEMs [8]. For example, for PEGDA-SPMAK-PEGPEA, and PEGDA-SPMAK-PEA membranes, where the PEGDA content was constant but the ratio of SPMAK to either PEA or PEGPEA was varied, the

water content decreases with increasing phenyl-bearing comonomer content [8]. Mredha et al., reported hydrogels with notable mechanical attributes (modulus and strength) and relatively low water content through the incorporation of the even shorter chain and more hydrophobic phenyl acrylate (PA) [13]. This inspired some of our other prior work incorporating phenyl acrylate as a hydrophobic comonomer. For instance, we synthesized PA-based crosslinked membranes for direct urea fuel cells that incorporated either the anion exchange comonomer methacroylcholine chloride (MACC) or the cation exchange comonomer AMPS, as an ion exchange comonomer, and were crosslinked using N, N'-methylenebisacrylamide (MBAA) where increasing the crosslinker content, at a constant PA/ionic comonomer ratio, led to decreasing water volume fraction and increasing Youngs Modulus [14]. Importantly, the PA-MACC membrane with the highest crosslinking (and lowest water content) showed permeabilities to urea on the order of 10^{-6} cm^2/s and better performance, with respect to power density, in a direct urea fuel cell compared to Fumasep FAA-3-50, a commercially available membrane used in this application [14]. Here, we extend these studies to further investigate the role of crosslinker and relative crosslinker-ionic comonomer content in phenyl acrylate-based membranes by synthesizing and characterizing a new series of anion exchange membranes that incorporate a high content of phenyl acrylate (80 mol%), and varied relative amounts of APTA as the anion exchange comonomer, and either PEGDA or MBAA as the crosslinker.

8.2. Results and Discussion

The materials, membrane synthesis methods, and experimental procedures are detailed in Chapter 3. In this study, six membranes were produced from pre-polymerization mixtures

through thermal copolymerization, as illustrated in Figure 8.1. Each pre-polymerization mixture consisted of 50 wt.% DMSO and AIBN (0.1 wt.% of total monomer). The polymer composition information is summarized in Table 8.1. The membrane nomenclature is as follows: A for APTA, P for PEGDA, M for MBAA, and # for mol% of APTA, PEGDA, or MBAA. For instance, A8/P12 refers to a membrane prepared with APTA (8 mol%), PEGDA (12 mol%), and PA (80 mol%).

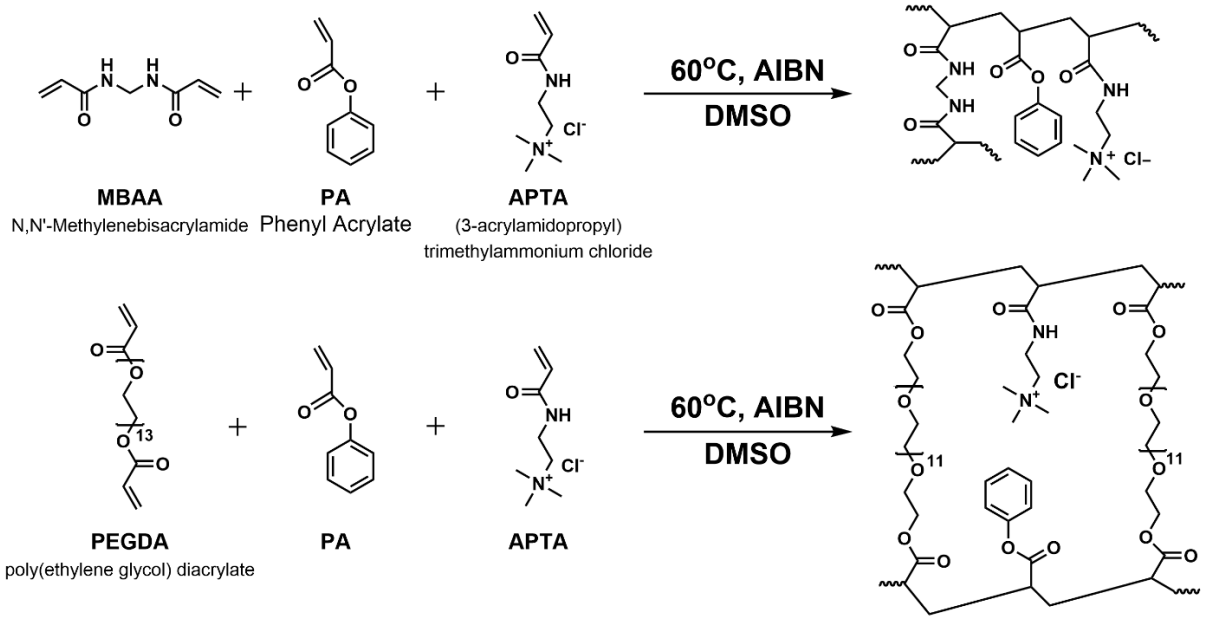

Figure 8.1. Synthetic scheme of crosslinked MBAA-PA-APTA and PEGDA-PA-APTA membranes.

Table 8.1. Pre-polymerization mixtures compositions.

	APTA (mol%)	PEGDA (mol%)	PA (mol%)
A0/P20	0	20	80
A8/P12	8	12	80
A12/P8	12	8	80
	APTA (mol%)	**MBAA (mol%)**	**PA (mol%)**
A0/M20	0	20	80
A8/M12	8	12	80
A12/M8	12	8	80

8.2.1. Membrane Physiochemical Properties

Water volume fractions of the membranes were calculated from measured water uptakes and dry polymer densities, as presented in Figure 8.2 and Table 8.2. In general, water volume fractions of the membranes increase as APTA content increases. This trend may be attributed to the decreasing crosslink densities (number of crosslinks per volume) of the membranes with decreasing PEGDA or MBAA content [15-17], as well as the increasing content of charged quaternary ammonium (QA^+) groups (APTA content) [18]. This is consistent with prior research where decreased crosslink density has been found to increase water uptake by giving the polymer network more polymer chain mobility and ability to swell [19], and membranes with fixed charge groups increase hydrophilicity and thereby water uptake due to favorable interactions between charged groups and polar water molecules [20-22]. Correspondingly, PEGDA-containing membranes have higher water volume fractions than MBAA-containing membranes which we attribute to the more hydrophilic backbone (PEG) and longer crosslinker chain length. Interestingly, A0/P20 and A0/M20 exhibit comparable water volume fractions (0.19 and 0.18 respectively) where the membrane chemistry only differs by the crosslinker. Previously, we prepared PEGDA/APTA membranes utilizing 20 wt.% water as the prepolymerization solvent and PEGDA/APTA mole ratios of 100:0 (A0), 92:8 (A8), and 88:12 (A12), respectively where higher water volume fractions were observed (45%, 46%, and 46% respectively) [4]. This is notable as a large increase in prepolymerization solvent typically results in correspondingly large increases in water content [15, 23]. For example, Ju et al. measured water uptakes of crosslinked PEGDA (n=13) where water volume fractions (calculated using a dry polymer density of 1.19 g/cm^3 [23, 24]

increased from 0.43 to 0.57 for 20 wt.% and 50 wt.% prepolymerization water content respectively [15, 23, 24]. Here, in lieu of water the solvent is DMSO in order to achieve dissolution of the high phenyl acrylate content such that increasing the prepolymerization solvent content does not necessarily lead to an increase in water volume fraction upon solvent exchange. The above comparison of A0 from our prior work (100% crosslinked PEGDA) compared to A0/P20 here shows a significant reduction in water volume fraction when PA is incorporated instead of PEGDA, as desired, even though the crosslink density is reduced, and more solvent was used in preparing A0/P20.

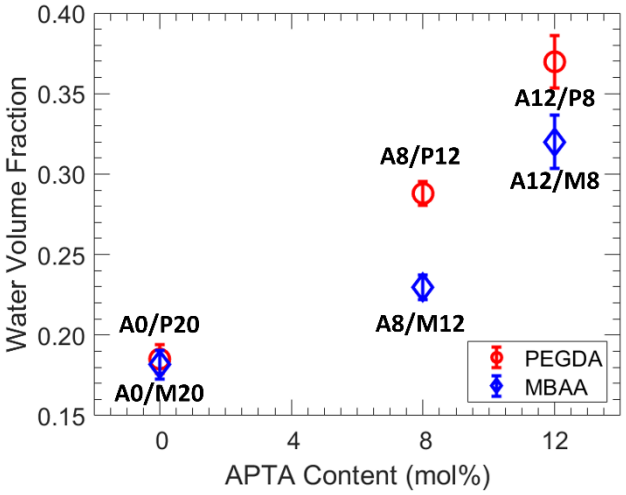

Figure 8.2. Water volume fraction as functions of APTA content.

Table 8.2. Water uptake, dry polymer density, and water volume fraction of all membranes.

Name	ω_w (water g/dry polymer g·100%)	ρ_p (g/mL)	$\emptyset_w$	V_H/V_D	Contact Angle
A0/P20	18.5 ± 1.1	1.22 ± 0.00	0.19 ± 0.01	1.65 ± 0.03	69.8 ± 1.4
A8/P12	33.5 ± 1.3	1.21 ± 0.01	0.29 ± 0.01	1.68 ± 0.02	73.6 ± 0.9
A12/P8	47.9 ± 3.4	1.22 ± 0.00	0.37 ± 0.02	2.22 ± 0.03	74.9 ± 0.7
A0/M20	17.6 ± 0.7	1.26 ± 0.01	0.18 ± 0.01	1.37 ± 0.03	65.1 ±0.0
A8/M12	24.0 ± 0.6	1.24 ± 0.00	0.23 ± 0.01	1.39 ± 0.06	69.7 ± 0.9
A12/M8	37.6 ± 1.9	1.25 ± 0.00	0.32 ± 0.02	1.46 ± 0.02	71.5 ± 0.4

Next, when then examining the impact of introducing APTA (and reducing crosslinker content) it is clear for the membranes here that the water volume fraction is significantly influenced by increasing APTA content and corresponding decreasing crosslinker content for both PEGDA and APTA. Whereas the water volume fractions for the APTA-free membranes are essentially the same, PEGDA-crosslinked membranes show a more pronounced increase in water volume fraction with increasing APTA content compared to MBAA. This trend of increasing water volume fraction is interesting for these high PA content membranes our prior work on PEGDA-APTA membranes with analogous APTA contents (8 and 12 mol%) found the water volume fraction of the membrane to be unaffected by the probed variation in crosslinker content [4, 8]. However, those prior membranes had much higher crosslinker contents, whereas the membranes herein with lower crosslinker content are more impacted by variation in crosslinker content. Related to the water volume fraction is the degree of dimensional swelling; shown in Table 8.2. Dimensional swelling of both PEGDA and MBAA-crosslinked membranes increases with decreasing crosslinker content as one might expect for a more open network structure. In comparison to PEGDA-crosslinked membranes, MBAA-crosslinked membranes display lower dimensional swelling, which can be

attributed to the shorter MBAA chain length and its mechanical properties, which will be discussed in the following section.

The water contact angle values for the membranes are presented in Figure 8.3 and Table 8.2. In order to assess the membranes' hydrophilicity, water contact angle is a widely applied technique to gain insight for polymer solubility, partitioning behavior, and aggregation [25]. Here water contact angle and hydration capacity are characterized, where a contact angle at or above 90 degrees indicates a hydrophobic surface and a contact angles less than 90 degrees indicates a hydrophilic [26]. A hydrophilic membrane surface could potentially improve the fouling resistance of the hydrogel when used as a surface coating for the separation of oily wastewater, organic compounds, and proteins [27-30]. As shown in Figure 3, PEGDA-containing membranes display an increase in contact angle with APTA content, more hydrophobic, as one might expect based on the chemical structures of PEGDA and APTA; PEGDA being more hydrophilic due to the presence of the 13 ethylene oxide repeat units. Comparing PEGDA-crosslinked to MBAA-crosslinked membranes, the PEGDA membranes exhibit slightly higher water contact angles than MBAA-crosslinked membranes at analogous compositions (3-5 degrees). This was unintuitive as one might expect MBAA-crosslinked membranes to be more hydrophobic based on their relative chemical structure and the water solubility of PEGDA and MBAA (PEGDA 700 is water soluble whereas MBAA water solubility is reported to be only 0.01-0.1 g/100 mL at 18 ºC). This difference is likely due to differences in the crosslinked network structure from the different chain lengths (PEGDA vs MBAA); as the difference in contact angle decreases slightly with decreasing crosslinker content. The rigid network formed with MBAA may retain a more hydrophilic surface due to its shorter crosslinks, which allow greater surface exposure of polar amide groups, reflected

in the higher polymer density of the membrane. In contrast, although PEGDA contains a hydrophilic PEG backbone and longer chain length, its lower polymer density likely reduces the surface exposure of polar groups, resulting in a less hydrophilic surface.

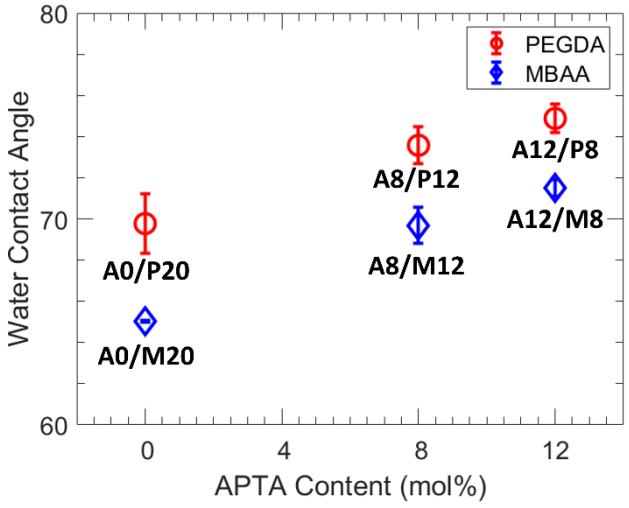

Figure 8.3. Effect of copolymer composition on water contact angle for all membranes.

Table 8.3. Young's Modulus and ion exchange capacity of all membranes.

Name	T_g (°C)	Name	T_g (°C)	IEC (mmol/g)	Ionic conductivity (mS/cm)	Youngs Modulus (MPa)
		A0/P20	0.7	N/A	N/A	0.036 ± 0.000
poly(APTA)	49	**A8/P12**	20.5	0.36	1.303 ±0.008	0.028 ± 0.001
poly(PEGDA)	-41	**A12/P8**	36.1	0.57	3.003 ±0.009	0.026 ± 0.001
poly(PA)	33	**A0/M20**	111.2	N/A	N/A	2.120 ± 0.070
poly(MBAA)	150	**A8/M12**	63.9	0.48	2.127 ±0.003	1.863 ± 0.078
		A12/M8	39.5	0.73	3.931 ±0.026	1.600 ± 0.025

The glass transition temperature (T_g) for dry copolymer membranes was characterized using differential scanning calorimetry; Figure 8.4 and Table 8.3. Each copolymer displayed a single T_g, implying that these copolymer membranes behave like homogeneous materials [31]. Poly(APTA), poly(PEGDA), poly (PA), and poly(MBAA) membranes were also synthesized

using 50 wt.% of solutions of the monomer of interest in DMSO (50 wt.%) with AIBN as the initiator (0.1 wt.% of total monomer). The T_gs for poly(APTA), poly(PEGDA), poly(PA), and poly(MBAA) were characterized and found to be 49 ℃, -41 ℃, 33 ℃, and 150 ℃ respectively. As expected, decreasing the PEGDA content increases T_g as PEGDA has the lowest T_g of any of these constituents. Conversely, the T_g of MBAA-crosslinked membranes decrease with decreasing MBAA-content as MBAA has the highest T_g of any of the constituents. This variation in T_g has implications for the transport behavior, as polymers with lower T_gs will have more chain mobility.

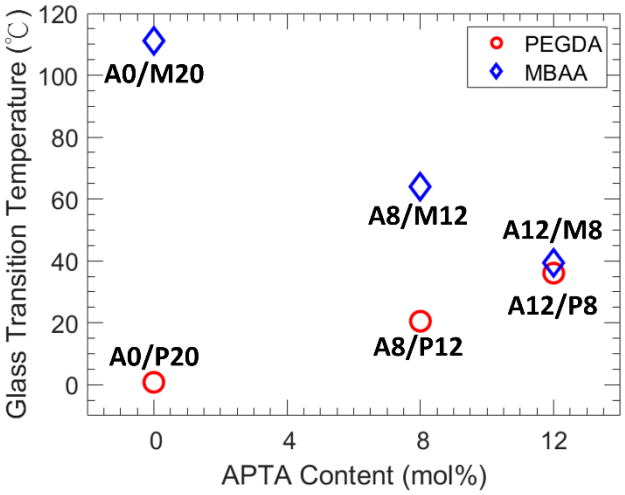

Figure 8.4. Glass transition temperature as a function of APTA content for all membranes.

Table 8.3 presents the results of the membrane ion exchange capacities (IECs). APTA-free membranes (P20 and M20) were not characterized since they don't have membrane-bound charged moieties [11]. The IECs of membranes decreased with increasing content of crosslinkers (PEGDA and MBAA), which can be attributed to the corresponding reduction in the number of quaternary ammonium groups (QA^+) as the APTA content decreased. In an electrochemical cell, the AEMs or CEMs are commonly employed because they allow ions to migrate between electrodes, ensuring

charge neutrality is maintained while electrons traverse from one electrode to another. Figure 8.5 presents the results of measuring the ionic conductivities of all membranes at 25 °C. As expected, the ionic conductivities of membranes demonstrated an increase with higher APTA content. The counterion is the mobile ion responsible for contributing to the conductivity, and its concentration is proportional to the fixed charge density of the membrane, determined by electroneutrality. Additionally, the ionic conductivity of ion exchange membranes increases as the water volume fraction increases [1, 32]. As the water volume fraction increases, the fixed charge concentration decreases, and the solute diffusion coefficient increases [33]. The ionic conductivity of MBAA-crosslinked membranes was higher than those of PEGDA-crosslinked membranes, resulting in more interactions between bound quaternary ammonium groups (QA^+) and mobile species due to higher QA^+ content in the same weight of membranes(IEC). Consequently, the ionic conductivity of A8/M12 and A12/M8 exceeded A8/P12 and A12/P8, respectively.

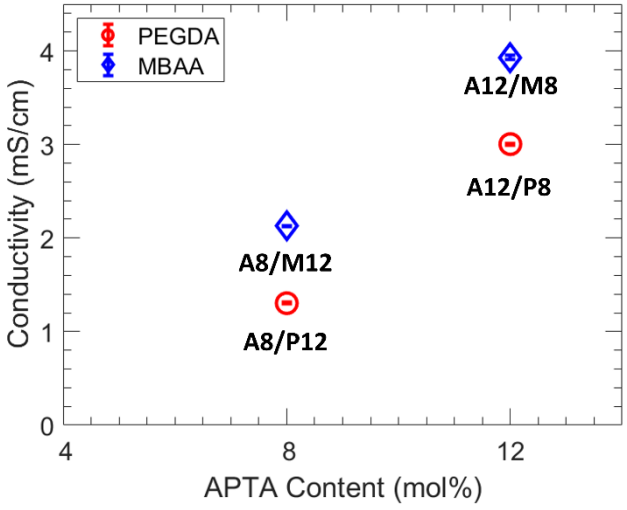

Figure 8.5. Ionic conductivity as a function of APTA content of A12/P8, A8/P12, A12/M8, and A8/M12 membranes.

Mechanical properties were probed using tensile testing in triplicate for all membranes, and illustrative stress-strain curves are shown in Figure 8.6 (where A and B are scaled differently); extracted Young's moduli are presented in Table 8.3. Generally, membranes with lower PEGDA and MBAA (crosslinker) content were found to be more ductile than those with higher crosslinker content because of the lower crosslink density, allowing the membrane to stretch. However, A12/P8 and A12/M8 demonstrated less strain at break than A8/P12 and A8/M12, potentially because of the limited ability of the membranes to withstand deformation before fracture, which is a common tradeoff. Therefore, A8/P12 and A8/M12 represent the optimal composition for achieving the highest strain at break. Young's modulus of the membranes increased with increasing PEGDA and MBAA (crosslinker) content, as expected owing to the increase in crosslink density and decrease in water volume fraction [18, 34]. Additionally, it should be noted that MBAA-crosslinked membranes exhibit a higher Young's modulus and lower strain at break in comparison to analogous PEGDA-crosslinked membranes. The variation in crosslinker structure accounts for this phenomenon, and MBAA-crosslinked membranes are in a glassy state at 25 ℃, which has been supported by the measured glass transition temperatures. Concerning dimensional swelling, PEGDA-crosslinked membranes tend to shrink more during the drying process, not only due to their higher water volume fraction but also because of their higher strain and lower Young’s modulus. For example, A0/P20 and A0/M20 have comparable water volume fractions but distinctly different dimensional swelling values.

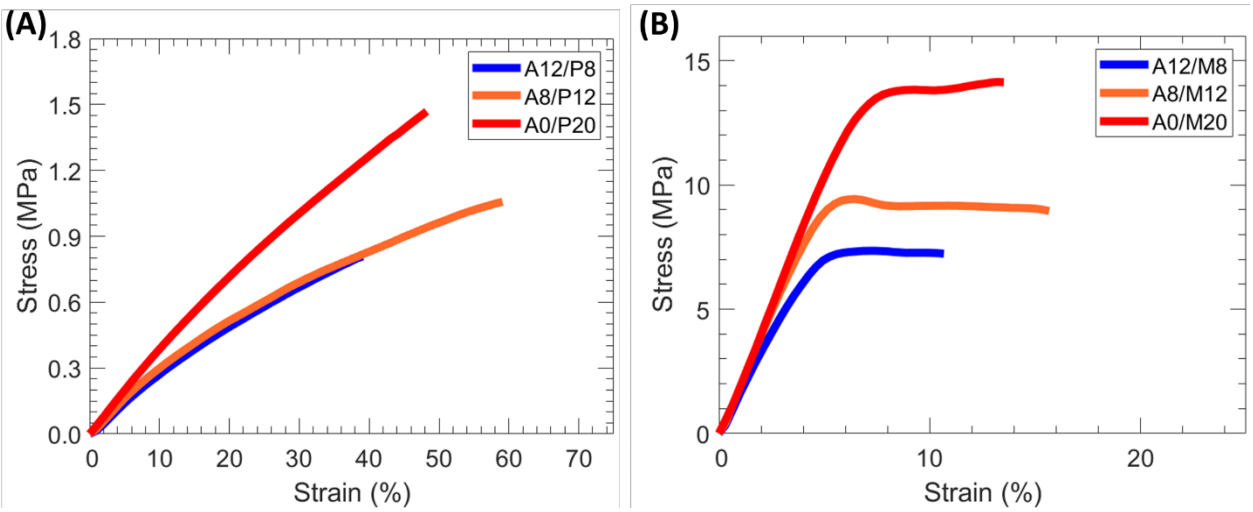

Figure 8.6. Representative stress–strain curves for (A) PEGDA-contained membranes and (B) MBAA-contained membranes.

8.2.2. Salt Permeability

As noted in the introduction, desirable attributes for anion exchange membranes (AEMs) for artificial photosynthesis are high charge carrier conductivity while exhibiting low permeability to reduction products. To evaluate these characteristics, the diffusive permeability to various solutes, including KOAc, KOFm, NaOAc, NaOFm, KCl, and NH_4Cl, were characterized using a diffusion cell experiment, as illustrated in Figure 8.7. Formate and acetate are particularly appealing as target products for CO_2 reduction, as they can be used as deicers or as raw materials for chemical synthesis [35]. Potassium chloride and ammonium chloride are important and common electrolytes [36]. Across all membranes, it was observed that the permeability to these salts increased with higher APTA content (lower crosslinker content). This trend is correlated with the fractional free volume (FFV) where the free volume is the available space between polymer

chains for solute transport as characterized here through the relative water volume fractions [37, 38]. The reason for this is mainly attributed to enhanced diffusion, as the diffusivity of solutes typically rises with a higher fraction of water volume [37, 38]. Previous studies by Yasuda et al. have demonstrated that changes in the polymer's water volume fraction can significantly affect solute permeation by altering solute diffusivity [37, 38]. Consequently, permeability often exhibits a significant dependence on the polymer's water volume fraction. Interestingly, although A0/P20 and a0/M20 have similar water volume fractions, A0/P20 exhibits an average permeability that is 82 times higher than A0/M20. This indicates that water volume fraction alone does not dominate solute permeability. Moreover, prior studies on membranes using PEGDA/APTA with mole ratios of 100:0 (A0), 92:8 (A8), and 88:12 (A12) exhibit higher water volume fractions (45%, 46%, and 46%, respectively) compared to the membranes in this study, yet they display comparable permeability (1 to 3.5×10^{-7} cm/s) to A8/P12, A12/P8, and A12/M8 [4]. This observation suggests that PA can substantially decrease water volume fraction, but polymer structure plays a crucial role in permeability as well, such that water volume fraction does not solely determine relative permeability. Similar findings have been reported in other research, indicating that microstructural disparities among membranes could significantly influence permeability [39]. In general, the relative permeabilities of the solutes tend to correspond to the order of their hydrated diameters (diameters of cations $NH_4^+ = K^+$ (6.6 Å) < Na^+ (7.2 Å) and diameter of anion OFm^- (5.9 Å) < Cl^- (6.6 Å)< OAc^- (7.4 Å).[40, 41] Moreover, permeabilities to these solutes for A8/P12 and A12/P8 show no significant differences, whereas membranes containing MBAA and A0/P20 each exhibit noticeable variations in permeability to the different solutes.

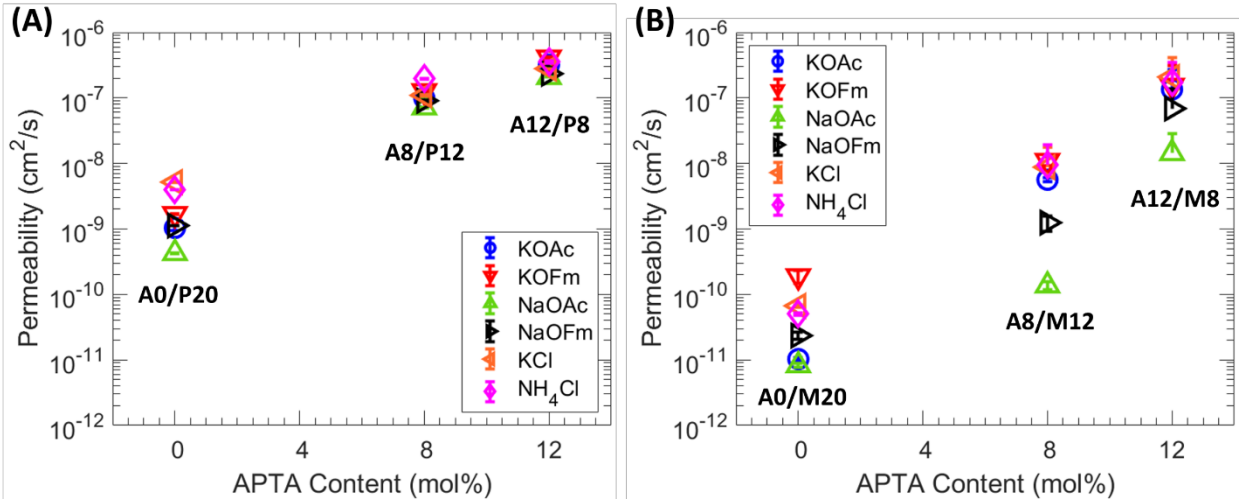

Figure 8.7. (A) The correlation between permeability and APTA content is demonstrated for A0/P20, A8/P12, and A12/P8. (B) The correlation between permeability and APTA content is demonstrated for A0/M20, A8/M12, and A12/M8. The data points reflect the average of three experiments, and the standard deviation is depicted by the error bars.

8.2.3. Salt Solubility

The relationship between the characterized salt sorption behavior and the membrane APTA content is shown in Figure 8.8. Salt solubility was characterized through a kinetic desorption experiment using 1 M solutions of the salt of interest (NH_4Cl, KCl, KOFm, KOAc, NaOFm, and NaOAc) [38]. We have observed a clear relationship in all membranes between the increase in APTA content and the corresponding increase in solubility. This connection is likely due to the higher water volume fraction, which provides more opportunities for the polymer network to interact with the solution. Similar patterns have been noted in previous studies on hydrated polymers, where a greater water content generally facilitates the distribution of salt within the polymer membrane [22]. MBAA-crosslinked membranes usually have a lower water volume

fraction compared to PEGDA-crosslinked membranes with the same charge monomer content, but the former display higher solubility than the latter. Even though A0/P20 and A0/M20 membranes have similar water volume fractions, A0/M20 exhibits greater solubility than A0/P20. Furthermore, the water content and interactions between ions and polymer segments are vital for understanding ion sorption in polymers. It is essential to explore the relationship between salt solubility and hydrophobicity as well. The behavior of ions within the membrane often deviates significantly from expectations based on their hydrated radius or ion charge density which affects hydration tendency and interaction with the polymer and impacts the specific interactions between different ions and polymer segments [42, 43]. However, the membrane solubilities do not follow the order of hydrated radius and ion charge density. This discrepancy arises due to the intricate interplay between the polymer, ions, and water interactions. These non-ideal behaviors can greatly influence ion sorption and contribute to the complexity of investigating the order of salt sorption.

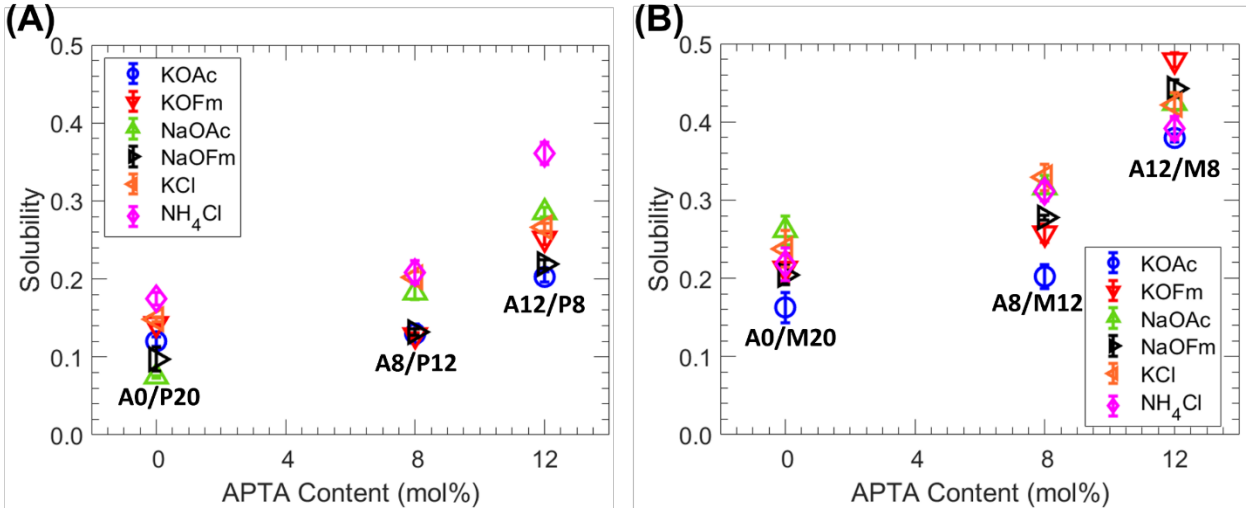

Figure 8.8. (A) The impact of APTA content on salt solubility in A0/P20, A8/P12, and A12/P8. (B) The impact of APTA content on salt solubility in A0/M20, A8/M12, and A12/M8. Each data point represents the average of three experiments, with error bars indicating the standard deviation.

8.2.4. Salt Diffusivity

The membrane diffusivities are determined through the application of the solution diffusion relationship ($D_i = P_i/K_i$), as illustrated in Figure 8.9. The diffusivity relationship follows the principles of the free volume theory, where the amount of water present directly affects the availability of free volume within the hydrated polymers for diffusion [37, 38]. Increasing the water volume generally leads to higher salt diffusivity [44]. Additionally, the order of solute diffusivity correlates with the diffusivity of the solute in water. In terms of water diffusivity, the cation order is: NH_4^+ (2.0×10^5 cm^2/s) = K^+ (2.0×10^5 cm^2/s) > Na^+ (1.3×10^5 cm^2/s), and the anions order is Cl^- (2.0×10^5 cm^2/s) > OFm^- (1.5×10^5 cm^2/s) > OAc^- (1.1×10^5 cm^2/s) [45, 46].

To compute the diffusivities of salts in water, we assume that the diffusivity of a salt composed of monovalent ions is approximately equal to the average diffusivity of the two ions, taking into account their respective mobilities (referred to as mobility-weighted average diffusivity [47]). For instance, based on the provided diffusivity values, the estimated diffusivities for KOAc, KOFm, NaOAc, NaOFm, KCl, and NH_4Cl are $1.52x10^5$, $1.71x10^5$, $1.21x10^5$, $1.39x10^5$, $1.99x10^5$, and $1.99x10^5$ cm^2/s, respectively. The order of diffusivity of the solute in water is NH_4Cl = KCl > KOFm > KOAc > NaOFm > NaOAc. However, the order is not readily observed in PEGDA-contained membranes compared to MBAA-contained membranes. The scatter in diffusivity implies that microstructural factors play a major role [39]. Moreover, the diffusivity is influenced by the flexibility of polymer chains, which is often characterized by the glass transition temperature of the polymer [48]. A lower T_g indicates increased segmental dynamics, resulting in

higher solute diffusivity. Conversely, a higher T_g leads to reduced mobility of the membrane chains. Overall, with the same crosslinker content, PEGDA-contained membranes typically exhibit higher diffusivities when compared to MBAA-contained membranes. This disparity can be attributed to differences in the water volume fraction and the glass transition temperature between the two types of membranes. Because of the comparable water volume fraction, we conclude that the disparity in A0/P20 and A0/M20 primarily stems from the glass transition temperature's influence. However, further investigation into the segmental dynamics of these materials, as well as related factors such as relative permittivity and structure analysis, is necessary to validate this conclusion, as these complex behaviors are likely influenced by multiple factors.

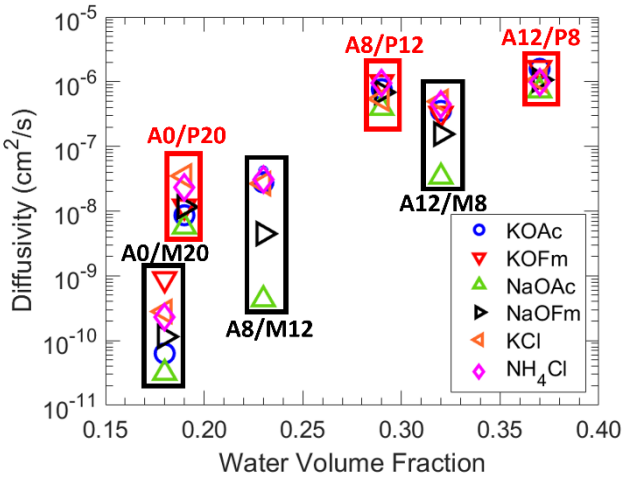

Figure 8.9. The correlation between diffusivity and water volume fraction.

8.3. Conclusions

This study investigated the physicochemical properties and transport behavior of crosslinked AEMs based on PA and APTA, with either PEGDA or MBAA as the crosslinker. The

results highlight the significant influence crosslinker type and content has on membrane properties such as water volume fraction, ionic conductivity, mechanical strength, permeability, and diffusivity. MBAA-crosslinked membranes demonstrated higher glass transition temperatures (T_g), greater stiffness, and lower permeability compared to PEGDA-crosslinked membranes, attributed to reduced chain mobility. However, PEGDA-crosslinked membranes exhibited higher water content and diffusivity, enhancing ionic conductivity at the cost of increased permeability. These findings emphasize the trade-offs between ionic conductivity and selectivity critical for artificial photosynthesis applications. Mechanical testing revealed that increasing crosslinker content boosted Young's modulus and decreased water volume fraction. MBAA-crosslinked membranes demonstrated greater stiffness and lower strain than PEGDA due to their higher T_g. While the overall permeability aligned with the free volume theory, this investigation revealed A0/P20 and A0/M20 with similar water volume fractions but distinct permeabilities. Specifically, A0/M20 exhibited relatively low permeability due to its low diffusivity. Diffusivity depends on polymer chain flexibility indicated by the glass transition temperature (T_g). Lower T_g enhances segmental dynamics, increasing solute diffusivity, while higher T_g restricts membrane chain mobility, reducing solute diffusivity. The distinct behaviors observed in membranes with comparable water content but differing crosslinker chemistry underscore the significant role of polymer segmental mobility and microstructure in determining transport properties.

8.4. References

[1] B.M. Carter, L. Keller, M. Wessling, D.J. Miller, Preparation and characterization of crosslinked poly (vinylimidazolium) anion exchange membranes for artificial photosynthesis, Journal of Materials Chemistry A 7(41) (2019) 23818-23829.

[2] M. Krödel, B.M. Carter, D. Rall, J. Lohaus, M. Wessling, D.J. Miller, Rational design of ion exchange membrane material properties limits the crossover of CO2 reduction products in artificial photosynthesis devices, ACS applied materials & interfaces 12(10) (2020) 12030-12042.

[3] M.R. Singh, E.L. Clark, A.T. Bell, Effects of electrolyte, catalyst, and membrane composition and operating conditions on the performance of solar-driven electrochemical reduction of carbon dioxide, Physical Chemistry Chemical Physics 17(29) (2015) 18924-18936.

[4] J.M. Kim, Y.-h. Lin, B. Hunter, B.S. Beckingham, Transport and co-transport of carboxylate ions and ethanol in anion exchange membranes, Polymers 13(17) (2021) 2885.

[5] M.R. Singh, A.T. Bell, Design of an artificial photosynthetic system for production of alcohols in high concentration from CO 2, Energy & Environmental Science 9(1) (2016) 193-199.

[6] R.B. Kutz, Q. Chen, H. Yang, S.D. Sajjad, Z. Liu, I.R. Masel, Sustainion imidazolium-functionalized polymers for carbon dioxide electrolysis, Energy Technology 5(6) (2017) 929-936.

[7] D.J. Miller, F.A. Houle, Membranes for Solar Fuels Devices, (2018).

[8] J.M. Kim, Y.-H. Lin, P.P. Aravindhan, B.S. Beckingham, Impact of hydrophobic pendant phenyl groups on transport and co-transport of methanol and acetate in PEGDA-SPMAK cation exchange membranes, Chemical Engineering Research and Design 185 (2022) 418-429.

[9] B.M. Dobyns, J.M. Kim, B.S. Beckingham, Multicomponent transport of methanol and sodium acetate in poly (ethylene glycol) diacrylate membranes of varied fractional free volume, European Polymer Journal 134 (2020) 109809.

[10] J.M. Kim, B.M. Dobyns, R. Zhao, B.S. Beckingham, Multicomponent transport of methanol and acetate in a series of crosslinked PEGDA-AMPS cation exchange membranes, Journal of Membrane Science 614 (2020) 118486.

[11] J.M. Kim, B.S. Beckingham, Comonomer effects on co-permeation of methanol and acetate in cation exchange membranes, European Polymer Journal 147 (2021) 110307.

[12] J.M. Kim, B.S. Beckingham, Transport and co-transport of carboxylate ions and alcohols in cation exchange membranes, Journal of Polymer Science 59(21) (2021) 2545-2558.

[13] M.T.I. Mredha, S.K. Pathak, J. Cui, I. Jeon, Hydrogels with superior mechanical properties from the synergistic effect in hydrophobic–hydrophilic copolymers, Chemical Engineering Journal 362 (2019) 325-338.

[14] J.M. Kim, Y. Wang, Y.-h. Lin, J. Yoon, T. Huang, D.-J. Kim, M.L. Auad, B.S. Beckingham, Fabrication and Characterization of Cross-Linked Phenyl-Acrylate-Based Ion Exchange Membranes and Performance in a Direct Urea Fuel Cell, Industrial & Engineering Chemistry Research 60(41) (2021) 14856-14867. 10.1021/acs.iecr.1c02798.

[15] H. Ju, B.D. McCloskey, A.C. Sagle, V.A. Kusuma, B.D. Freeman, Preparation and characterization of crosslinked poly (ethylene glycol) diacrylate hydrogels as fouling-resistant membrane coating materials, Journal of Membrane Science 330(1-2) (2009) 180-188.

[16] A. Jastram, T. Lindner, C. Luebbert, G. Sadowski, U. Kragl, Swelling and diffusion in polymerized ionic liquids-based hydrogels, Polymers 13(11) (2021) 1834.

[17] H. Lin, T. Kai, B.D. Freeman, S. Kalakkunnath, D.S. Kalika, The effect of cross-linking on gas permeability in cross-linked poly (ethylene glycol diacrylate), Macromolecules 38(20) (2005) 8381-8393.

[18] N. Yan, D.R. Paul, B.D. Freeman, Water and ion sorption in a series of cross-linked AMPS/PEGDA hydrogel membranes, Polymer 146 (2018) 196-208.

[19] S.K. Bajpai, S. Singh, Analysis of swelling behavior of poly (methacrylamide-co-methacrylic acid) hydrogels and effect of synthesis conditions on water uptake, Reactive and Functional Polymers 66(4) (2006) 431-440.

[20] W. Xie, J. Cook, H.B. Park, B.D. Freeman, C.H. Lee, J.E. McGrath, Fundamental salt and water transport properties in directly copolymerized disulfonated poly (arylene ether sulfone) random copolymers, Polymer 52(9) (2011) 2032-2043.

[21] G. Geise, B. Freeman, D. Paul, Characterization of a sulfonated pentablock copolymer for desalination applications, Polymer 51(24) (2010) 5815-5822.

[22] G.M. Geise, D.R. Paul, B.D. Freeman, Fundamental water and salt transport properties of polymeric materials, Progress in Polymer Science 39(1) (2014) 1-42.

[23] H. Ju, A.C. Sagle, B.D. Freeman, J.I. Mardel, A.J. Hill, Characterization of sodium chloride and water transport in crosslinked poly (ethylene oxide) hydrogels, Journal of Membrane Science 358(1-2) (2010) 131-141.

[24] A.C. Sagle, E.M. Van Wagner, H. Ju, B.D. McCloskey, B.D. Freeman, M.M. Sharma, PEG-coated reverse osmosis membranes: desalination properties and fouling resistance, Journal of Membrane Science 340(1-2) (2009) 92-108.

[25] J.C. Foster, I. Akar, M.C. Grocott, A.K. Pearce, R.T. Mathers, R.K. O'Reilly, 100th anniversary of macromolecular science viewpoint: The role of hydrophobicity in polymer phenomena, ACS Macro Letters 9(11) (2020) 1700-1707.

[26] A.W. Adamson, A.P. Gast, Physical chemistry of surfaces, Interscience publishers New York1967.

[27] H. Ju, B.D. McCloskey, A.C. Sagle, Y.-H. Wu, V.A. Kusuma, B.D. Freeman, Crosslinked poly (ethylene oxide) fouling resistant coating materials for oil/water separation, Journal of Membrane Science 307(2) (2008) 260-267.

[28] S. Chen, L. Li, C. Zhao, J. Zheng, Surface hydration: Principles and applications toward low-fouling/nonfouling biomaterials, Polymer 51(23) (2010) 5283-5293.

[29] A. Mehta, A.L. Zydney, Permeability and selectivity analysis for ultrafiltration membranes, Journal of membrane science 249(1-2) (2005) 245-249.

[30] G. Belfort, R.H. Davis, A.L. Zydney, The behavior of suspensions and macromolecular solutions in crossflow microfiltration, Journal of membrane science 96(1-2) (1994) 1-58.

[31] N.G. McCrum, C.P. Buckley, C.B. Bucknall, Principles of polymer engineering, Oxford University Press1997.

[32] L.M. Robeson, H.H. Hwu, J.E. McGrath, Upper bound relationship for proton exchange membranes: Empirical relationship and relevance of phase separated blends, Journal of Membrane Science 302(1-2) (2007) 70-77.

[33] S.M. Dischinger, S. Gupta, B.M. Carter, D.J. Miller, Transport of neutral and charged solutes in imidazolium-functionalized poly (phenylene oxide) membranes for artificial photosynthesis, Industrial & Engineering Chemistry Research 59(12) (2019) 5257-5266.

[34] A.C. Sagle, H. Ju, B.D. Freeman, M.M. Sharma, PEG-based hydrogel membrane coatings, Polymer 50(3) (2009) 756-766.

[35] C. Giebson, K. Seyfarth, J. Stark, Influence of acetate and formate-based deicers on ASR in airfield concrete pavements, Cement and Concrete Research 40(4) (2010) 537-545.

[36] X. Zhang, J. Li, Y.-Y. Li, Y. Jung, Y. Kuang, G. Zhu, Y. Liang, H. Dai, Selective and high current CO2 electro-reduction to multicarbon products in near-neutral KCl electrolytes, Journal of the American Chemical Society 143(8) (2021) 3245-3255.

[37] H. Yasuda, L. Ikenberry, C. Lamaze, Permeability of solutes through hydrated polymer membranes. Part II. Permeability of water soluble organic solutes, Die Makromolekulare Chemie: Macromolecular Chemistry and Physics 125(1) (1969) 108-118.

[38] H. Yasuda, C. Lamaze, L. Ikenberry, Permeability of solutes through hydrated polymer membranes. Part I. Diffusion of sodium chloride, Die Makromolekulare Chemie: Macromolecular Chemistry and Physics 118(1) (1968) 19-35.

[39] R. Kingsbury, K. Bruning, S. Zhu, S. Flotron, C. Miller, O. Coronell, Influence of water uptake, charge, manning parameter, and contact angle on water and salt transport in commercial ion exchange membranes, Industrial & Engineering Chemistry Research 58(40) (2019) 18663-18674.

[40] E. Nightingale Jr, Phenomenological theory of ion solvation. Effective radii of hydrated ions, The Journal of Physical Chemistry 63(9) (1959) 1381-1387.

[41] R. Caminiti, P. Cucca, M. Monduzzi, G. Saba, G. Crisponi, Divalent metal–acetate complexes in concentrated aqueous solutions. An x-ray diffraction and NMR spectroscopy study, The Journal of chemical physics 81(1) (1984) 543-551.

[42] E.-S. Jang, J. Kamcev, K. Kobayashi, N. Yan, R. Sujanani, T.J. Dilenschneider, H.B. Park, D.R. Paul, B.D. Freeman, Influence of water content on alkali metal chloride transport in cross-linked Poly (ethylene glycol) Diacrylate. 1. Ion sorption, Polymer 178 (2019) 121554.

[43] B. Tansel, J. Sager, T. Rector, J. Garland, R.F. Strayer, L. Levine, M. Roberts, M. Hummerick, J. Bauer, Significance of hydrated radius and hydration shells on ionic permeability during nanofiltration in dead end and cross flow modes, Separation and Purification Technology 51(1) (2006) 40-47.

[44] Y.-h. Lin, J.M. Kim, B.S. Beckingham, Salt Transport in Crosslinked Hydrogel Membranes Containing Zwitterionic Sulfobetaine Methacrylate and Hydrophobic Phenyl Acrylate, Polymers 15(6) (2023) 1387.

[45] E.E. Hills, M.H. Abraham, A. Hersey, C.D. Bevan, Diffusion coefficients in ethanol and in water at 298 K: Linear free energy relationships, Fluid Phase Equilibria 303(1) (2011) 45-55.

[46] P. Vanýsek, Ionic conductivity and diffusion at infinite dilution, CRC handbook of chemistry and physics 94 (1993).

[47] D.T. Hallinan Jr, N.P. Balsara, Polymer electrolytes, Annual review of materials research 43(1) (2013) 503-525.

[48] S. Matteucci, Y. Yampolskii, B.D. Freeman, I. Pinnau, Transport of gases and vapors in glassy and rubbery polymers, Materials science of membranes for gas and vapor separation (2006) 1-47.

Chapter 9: Transport Behavior Differences between CEMs Containing SPMAK and MPS

9.1. Introduction

Global warming poses a significant threat to humanity. The link between CO_2 and global warming has caught widespread attention through the recognized phenomenon of the greenhouse effect [1]. Because of the extensive burning of fossil fuels like coal and petroleum, coupled with industrial development, the concentration of CO_2 in the atmosphere is steadily rising year by year [2-4]. This exacerbates the greenhouse effect, leading to planetary warming [2-4]. Photoelectrochemical CO_2 reduction cells (PEC-CRC) are considered a promising to convert CO_2 into sustainable chemical fuels such as methanol, and ethanol [5, 6]. Ion exchange membranes (IEMs), featuring ionizable functional groups, play a crucial role in PEC-CRC by facilitating the transport of counter-ions between the anode and cathode, ensuring overall charge balance while chemically isolating the two half-cell reactions and restricting the crossover of oxidation and reduction byproducts generated at the electrode [5, 6]. Although commercial Nafion membranes are distinguished by their sulfonate groups and demonstrate satisfactory ion-conducting, transport, and mechanical properties, their complex morphology poses a challenge for systematically

studying of their structure-property relationships, which are critical to guide the design of optimal membranes [7-9]. Our previous studies have leveraged a tunable membrane design approach, manipulating (meth)acrylate, crosslinking density, and bound ion content as a platform for studying structure-property relationships in IEMs [7, 10-14]. Those studies illustrated that salt permeability to membranes typically conforms to the free volume theory, where a higher water volume fraction leads to increased permeability [7, 10-14]. While salt permeability is predominantly influenced by water volume fraction, it results from the interplay of solubility and diffusivity. Factors such as co-transport, membrane glass transition temperature, and membrane structure can also exert influence. Additionally, various factors, such as crosslink density, counter ion chemistry, and functional groups, can impact water volume fraction [7, 10-14]. Although past studies offer valuable insights for designing innovative membranes, further research is crucial to delve into structure-property relationships as adjusting membrane composition to tailor their physiochemical and transport behavior involves trade-offs, highlighting the need for comprehensive investigation. In this Chapter, a range of CEMs are synthesized incorporating two distinct charge monomers that both incorporate a polymerizable methacrylate moiety and a charge-bearing sulfonate moiety: 3-sulfopropyl methacrylate potassium (SPMAK) or 2-methyl-2-propene-1-sulfonic acid sodium salt (MPS). The ratios of these two charged monomers, poly(ethylene glycol) diacrylate (PEGDA, n = 10), and phenyl acrylate (PA) were varied and compared. The high quantities of PA are included as it has demonstrated in our prior work to enhance membrane mechanical properties and reduce water content [10-12]. This platform of membrane thereby extends upon prior related work where. However, the difference in variation

and comparison in the charged monomers (SPMAK and MPS) allows for the investigating influence of monomer structure and the relationship between each component.

9.2. Results and Discussion

The materials, membrane synthesis methods, and experimental procedures are detailed in Chapter 3. A total of 8 IEMs and 1 charge-neutral membrane were synthesized through thermally initiated free radical copolymerization. The naming used for the membranes is as follows: PA(w)P(x)S(y) and PA(w)P(x)M(z), with w, x, y, and z denoting the molar percentages of phenyl acrylate, PEGDA, and SPMAK or MPS, respectively. The amounts of chemicals used for membrane synthesis are detailed in Table 9.1, and the general synthetic scheme is depicted in Figure 9.1. Each pre-polymerization mixture consisted of 70 wt.% DMSO and 0.1 wt.% AIBN, combining PA, PEGDA, SPMAK, or MPS as specified in Table 9.1.

Table 9.1. Pre-polymerization mixtures compositions.

Name	PA (mol%)	PEGDA (mol%)	SPMAK (mol%)
PA80P10S10	80	10	10
PA80P15S5	80	15	5
PA90P5S5	90	5	5
PA85P10S5	85	10	5
Name	**PA (mol%)**	**PEGDA (mol%)**	**MPS (mol%)**
PA80P10M10	80	10	10
PA80P15M5	80	15	5
PA90P5M5	90	5	5
PA85P10M5	85	10	5
PA80P20	80	20	0

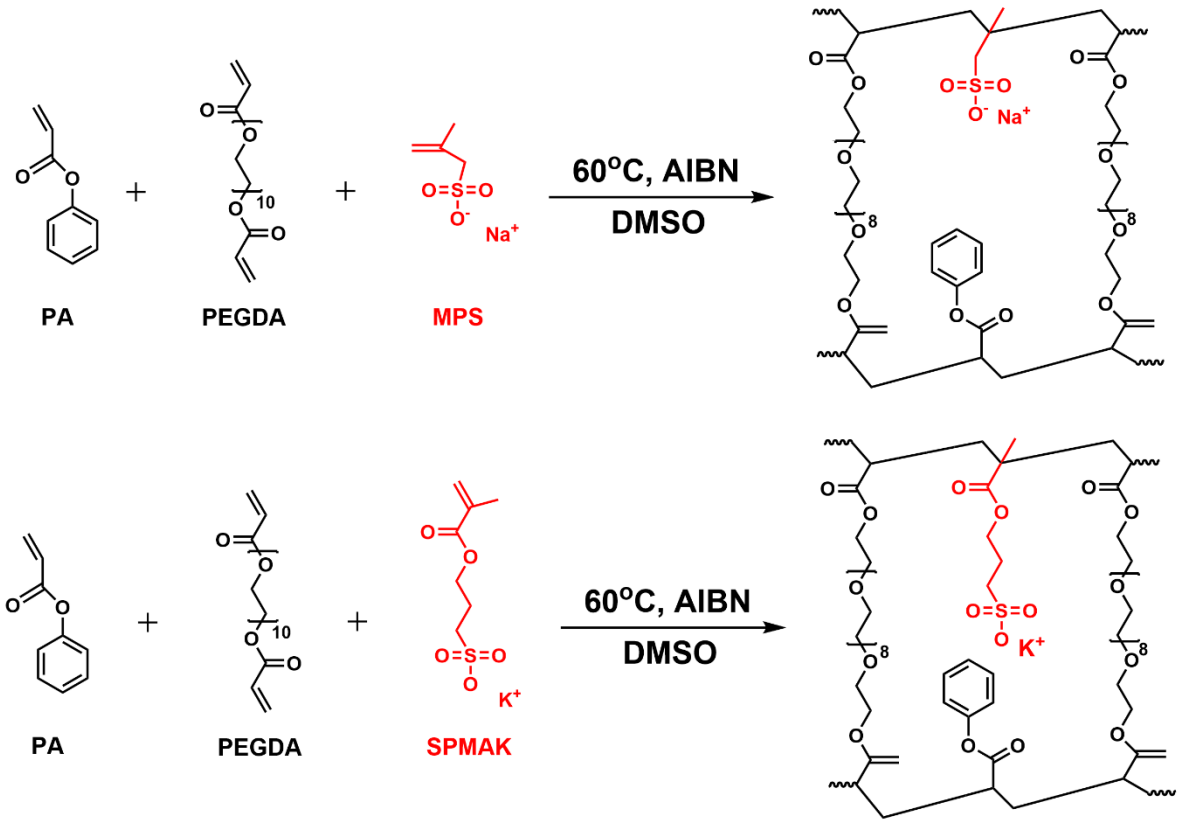

Figure 9.1. Synthetic scheme of PA/PEGDA/SPMAK and PA/PEGDA/MPS.

9.2.1. Membrane Water Content

The water uptake, polymer density, and water volume fraction are shown in Table 9.2. The water volume fraction of the 9 membranes is shown in Figure 9.2. In this study, membranes containing MPS were found to have a higher water volume fraction compared to those containing SPMAK. This disparity can be attributed to the influence of polymer structure on water volume fraction, where membranes containing SPMAK may experience higher steric effects and structural obstacles [15-17] because of their 3-carbon propyl chain and ester group, resulting in lower water content in these membranes. Moreover, the counter-ion also influences the water content [13].

Since sodium has a higher hydration radius than potassium [18, 19], membranes containing MPS will exhibit higher water content than those containing SPMAK. Based on our previous research, we noted a general decrease in water volume fraction with increasing crosslinker content [11, 13, 14]. Interestingly, although crosslinker content significantly influences water volume fraction, the hydrophobic phenyl acrylate monomer also plays a crucial role. Specifically, in the cases of P85P10S5 (WVF 0.17) and P80P15S5 (WVF 0.19), as well as P85P10M5 (WVF 0.2) and P80P15M5 (WVF 0.26), an increase in the amount of PA led to a lower water volume fraction. This may be due to the difference in hydrophobicity between PA and PEGDA, as discussed in the following contact angle section. Additionally, membranes with higher charge monomer content tend to attract water, due to the energetic interactions between the charge groups and polar water molecules [20-22].

Table 9.2. Water uptake, dry polymer density, and water volume fraction.

Name	ω_w (water g/dry polymer g·100%)	ρ_p (g/mL)	$\emptyset_w$
P80P10S10	34.12 ± 1.57	1.254 ± 0.004	0.300 ± 0.009
P80P15S5	18.34 ± 0.03	1.252 ± 0.012	0.187 ± 0.002
P90P5S5	44.98 ± 1.31	1.171 ± 0.003	0.345 ± 0.007
P85P10S5	16.26 ± 0.09	1.245 ± 0.009	0.169 ± 0.001
P80P10M10	66.28 ± 1.31	1.246 ± 0.012	0.453 ± 0.006
P80P15M5	28.33 ± 1.56	1.225 ± 0.004	0.258 ± 0.011
P90P5M5	47.34 ± 1.76	1.237 ± 0.006	0.370 ± 0.008
P85P10M5	20.91 ± 1.05	1.225 ± 0.011	0.204 ± 0.009
P80P20	7.74 ± 1.01	1.368 ± 0.027	0.096 ± 0.010

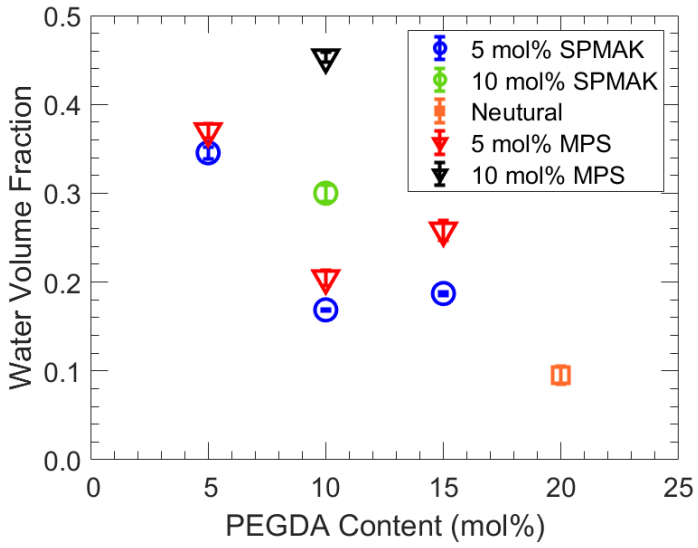

Figure 9.2. Water volume fraction of PA/PEGDA/SPMAK (circle), PA/PEGDA (square) and PA/PEGDA/MPS (triangle). Each data point represents the average of measurements from three separate membranes, while the error bars indicate the extent of the standard deviation.

9.2.2. Membrane Characterization

Table 9.3 presents the data of contact angle, Tg, IEC, ionic conductivity, and Young's modulus. Water contact angle is a straightforward approach to assess membrane surface hydrophilicity, and is also used as an indication of anti-fouling ability and water absorption capacity [23-25]. Typically, contact angles equal to or exceeding 90 degrees signify hydrophobic surfaces, whereas angles below 90 indicate hydrophilic surfaces [26]. Although all the membranes are classified as hydrophilic, no significant correlation between contact angle and water volume fraction was observed. This is consistent with our previous findings and those of other studies [27].

Table 9.3. Membrane Characterization.

Name	Contact Angle	T_g (°C)	IEC (mmol/g)		Ionic conductivity (mS/cm)	Youngs Modulus (MPa)
			Theoretically	Measured		
P80P10S10	71.17 ± 1.8	48.8	0.50	0.49	1.596 ± 0.001	0.243 ± 0.017
P80P15S5	73.96 ± 2.5	27.43	0.23	0.22	0.697 ± 0.011	0.032 ± 0.002
P90P5S5	87.99 ± 1.1	54.55	0.29	0.28	0.981 ± 0.077	1.646 ± 0.097
P85P10S5	82.08 ± 2.2	39.18	0.26	0.25	0.268 ± 0.067	0.303 ± 0.006
P80P10M10	72.29 ± 2.1	36.25	0.52	0.51	1.627 ± 0.008	0.054 ± 0.004
P80P15M5	70.97 ± 3.3	22.07	0.24	0.23	0.263 ± 0.001	0.019 ± 0.002
P90P5M5	80.28 ± 1.7	43.69	0.29	0.27	0.225 ± 0.029	0.993 ± 0.190
P85P10M5	81.97 ± 3.7	32.47	0.26	0.24	0.211 ± 0.001	0.060 ± 0.011
P80P20	83.20 ± 2.6	11.7	N/A	N/A	N/A	0.014 ± 0.001

The IEC of the membranes was measured yielding the results shown in Table 9.3. IEC of the membranes increases with decreasing PEGDA content and increasing SPMAK or MPS content, which is likely due to the combination of difference in molecular weight and the increase in the charge monomer content. The measured IECs of all films were closely matched with the theoretical IECs. This indicates that essentially complete conversion of the monomers into the crosslinked films has been achieved. Moreover, Table 9.3 and Figure 9.3 display the T_g values for dry polymer membranes. Each membrane exhibits a singular T_g, indicating behavior like homogeneous copolymers [28]. In membranes with a lower T_g, the mobility of polymer chains increases, enhancing diffusion. Conversely, in membranes with a higher T_g, chain mobility is significantly restricted [14, 29]. Therefore, a lower T_g promotes greater diffusivity compared to a higher T_g, due to increased segmental dynamics driven by thermal energy that create and close temporary gaps in the polymer matrix [30, 31]. Notably, membranes containing SPMAK demonstrate higher T_g values compared to those containing MPS. Because MPS contains a branched 2-methyl-2-propene group, its structure increases free volume and enhances chain flexibility, leading to a lower T_g.

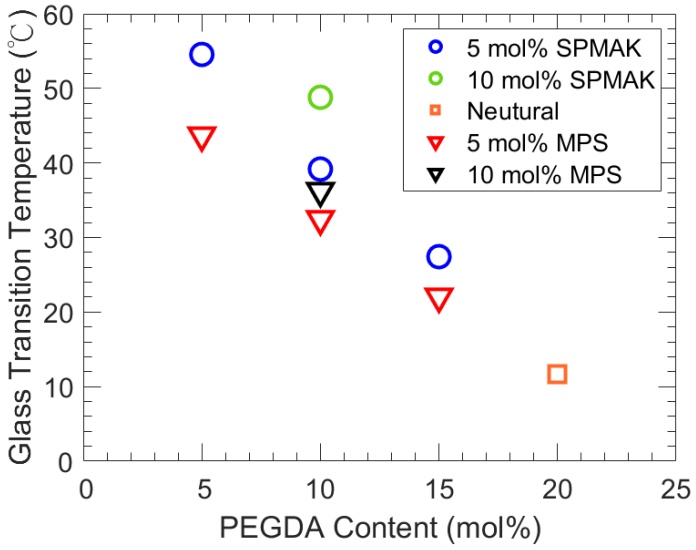

Figure 9.3. Glass transition temperature as a function of PEGDA content for all membranes.

Table 9.3 and Figure 9.4 present Young's modulus values for all membranes. While membranes with higher water volume fractions generally show lower mechanical properties, we observe that membranes with higher phenyl acrylate content can enhance mechanical strength which is observed in a previous study [10]. Interestingly, increasing crosslinker content tends to raise Young's modulus; however, in this study, we found that higher crosslinker content decreases Young's modulus but improves membrane elongation, potentially due to the longer chain length of PEGDA and difference in inherent mechanical properties compared to PA. Furthermore, membranes containing SPMAK exhibit higher Young's modulus than those containing MPS. This may be due to the linear sulfopropyl group in SPMAK, which limits molecular motion more than the branched structure of MPS, resulting in a stiffer material with a higher Young's modulus. PA80P20 shows the highest strain, while membranes with SPMAK and MPS exhibit similar elongation abilities at the same crosslinker content, which increases with PEGDA content. In

summary, when using PEGDA (n=10) as a crosslinker, membrane elongation is mainly influenced by PEGDA content, while Young's modulus is primarily determined by PA content.

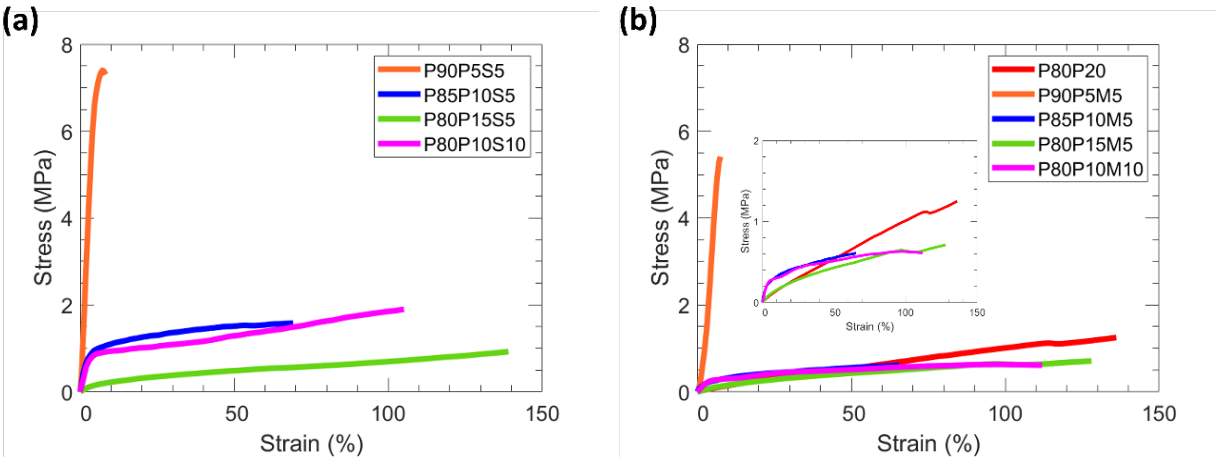

Figure 9.4. Stress-strain curves for (a) SPMAK-contained films and (b) MPS-contained films.

9.2.3. Salt Permeability

Salt permeability was characterized at 25°C using a standard diffusion cell setup, and the findings for the membranes are depicted in Figure 9.5. Generally, permeabilities across all films increase as the water volume fraction increases, consistent with findings reported elsewhere [10, 13, 32, 33]. According to free volume theory, this increase primarily stems from enhanced diffusion, as solute diffusivities typically increase with higher water volume fractions [34, 35]. The hydrated ion diameter order is OFm^- (5.9 Å) < K^+ (6.6 Å) < Na^+ (7.2 Å) < OAc^- (7.4 Å) [13]. However, this order does not correspond to the observed salt permeability. Unexpectedly, NaOFm and NaOAc demonstrate higher permeability than KOFm and KOAc most of the time. We hypothesize that sodium exhibits stronger interactions with the sulfonate group due to its higher charge density and enhanced ion-dipole attraction. Interestingly, although MPS has a higher water

volume fraction, the permeability of P90P5M5 and P80P10M10 is lower than that of P90P5S5 and P80P10S10. Additionally, previous research indicates that lower water volume fraction generally leads to higher selectivity. In contrast, as water volume fraction increases, selectivity decreases due to the corresponding rise in solute permeability [36]. Here we observe membranes with a water volume fraction above 0.2 exhibit better salt selectivity, as indicated by the dispersion salt permeability to membranes. In contrast, membranes with a water volume fraction below 0.2 show lower salt selectivity. This may be attributed to the membranes having smaller free volume elements and more tortuous structures, which would hinder solute transport.

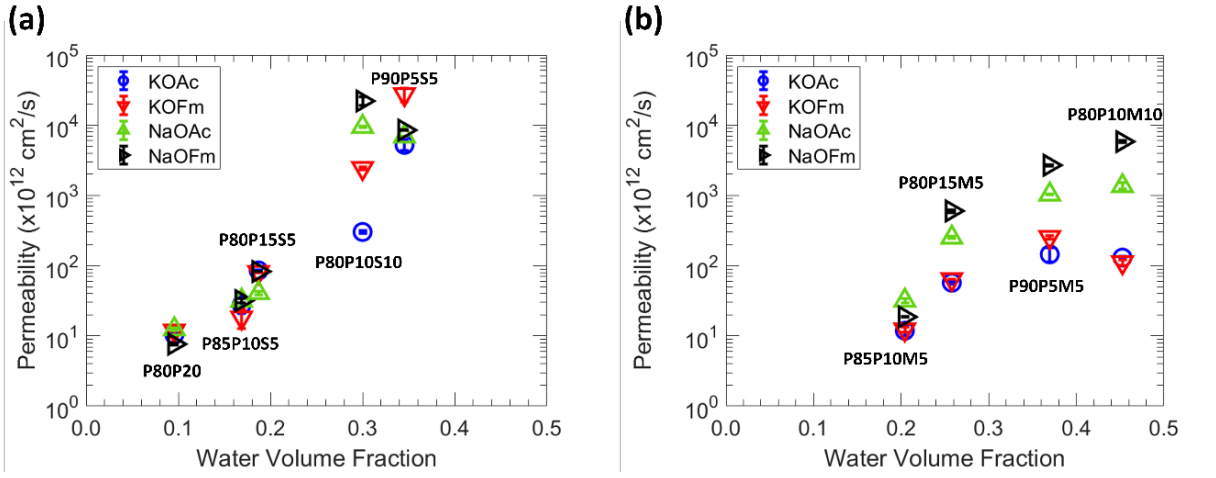

Figure 9.5. (a) Permeabilities of charge neutral film and films containing SPMAK to KOAc, KOFm, NaOAc, and NaOFm. (b) Permeabilities of films containing MPS to KOAc, KOFm, NaOAc, and NaOFm. Each data point represents the average of three experiments, with error bars indicating the standard deviation.

9.2.4. Salt Solubility

The solubilities of all salts were calculated using the previously reported Equation 8, with the results shown in Figure 9.6. We observe a correlation between solubility and water volume

fraction. Despite the salts being ordered by size as KOFm < NaOFm < KOAc < NaOAc, there is no significant trend indicating higher solubility for smaller salts. We find that membranes with the same crosslinker and charge monomer generally exhibit similar solubility, except for P90P5M5 and P90P5S5. This is very interesting since compared to other membranes containing the same crosslinker and charge monomer, P90P5M5 and P90P5S5 have a comparable water volume fraction, but show significantly different solubility.

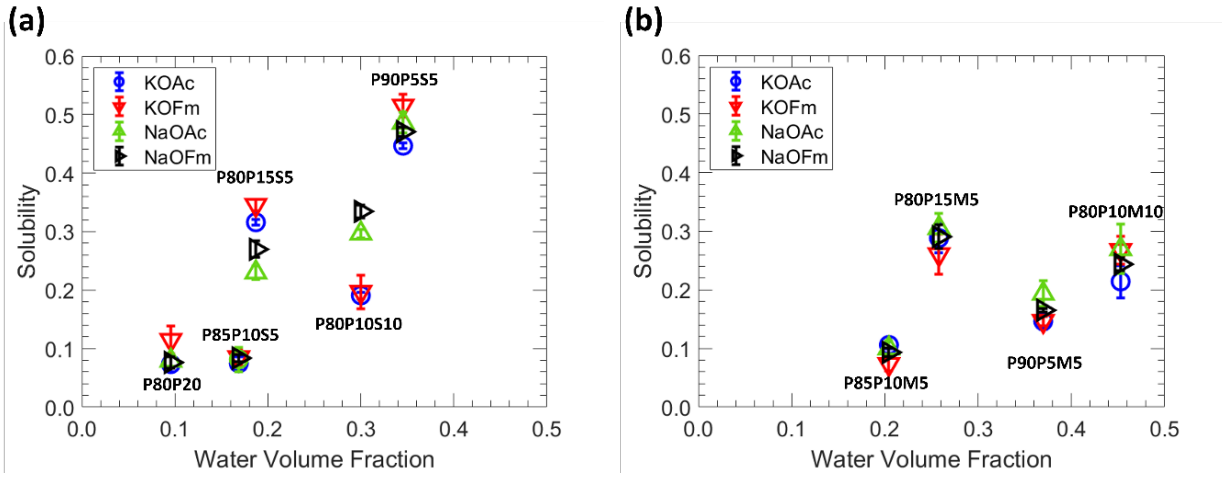

Figure 9.6. (a) Solubilities of charge neutral film and films containing SPMAK to salts. (b) solubility of films containing MPS to salts. Each data point represents the average of three experiments, with error bars indicating the standard deviation.

9.2.5. Salt Diffusivity

In this study, we characterized the permeability and solubility of various salts in these membranes, which enables diffusivity to be calculated using the solution–diffusion model, as shown in Figure 9.7. While solubility shows a slight dependence on the water volume fraction, diffusivity exhibits a much stronger dependence. We observe that when the water volume fraction

in the membrane exceeds 0.2, the salt diffusivity data becomes more dispersed, which can enhance diffusivity selectivity. Some studies suggest that reducing the water volume fraction improves selectivity by enabling better discrimination of salts [15, 36, 37]. However, when the water volume fraction is too low, salt diffusion is restricted, ultimately reducing selectivity. Thus, achieving optimal selectivity requires a balanced water volume fraction—not too high or too low. Each material (and membrane fabrication process) has its own optimal water volume fraction for selectivity due to its unique structural properties and physicochemical properties, highlighting the need for exploring more materials and combinations. Interestingly, despite Na^+ having a larger hydration diameter than K^+, Na^+ exhibits higher diffusivity than K^+. Moreover, it was observed that the diffusivity of the membrane containing SPMAK exhibits a steeper slope in diffusivity versus water volume fraction compared to the membrane with MPS. This suggests that the water volume fraction has a greater influence on the diffusivity of SPMAK-containing membranes than on those with MPS.

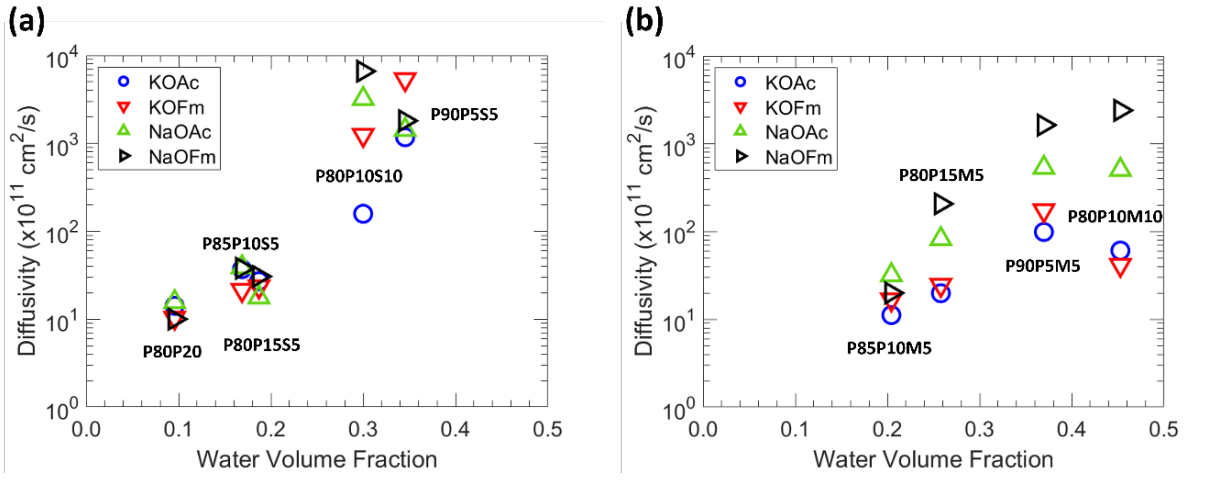

Figure 9.7. Diffusivity of (a) charge neutral film and films containing SPMAK (b) films containing MPS to all salts. Each data point represents the average of three experiments, with error bars indicating the standard deviation**.**

9.3. Conclusions

This study highlights the critical role of Cation Exchange Membranes (CEMs) in photoelectrochemical CO2 reduction cells (PEC-CRC), particularly in the challenge of preventing carboxylate ion crossover while facilitating ion transport for efficient CO2 conversion. By comparing membranes based on 3-sulfopropyl methacrylate potassium (SPMAK) and 2-methyl-2-propene-1-sulfonic acid sodium (MPS), we demonstrate that membrane performance is strongly influenced by the interplay of monomers, crosslinkers, and charge monomers. MPS-containing membranes exhibit higher water volume fractions, lower glass transition temperatures, and Young's modulus compared to SPMAK-containing membranes, leading to differences in their permeability, solubility and diffusivity. Moreover, SPMAK-containing membranes show a steeper diffusivity increase with water volume fraction than MPS-containing ones, indicating a stronger influence of water volume on SPMAK membranes. These findings reinforce the importance of optimizing membrane composition and structure to balance water uptake, mechanical stability, and transport properties. Understanding these structure-property relationships provides valuable insights for designing tailored membranes, where adjusting factors such as crosslinking density, charge monomer type, and water content can enhance membrane selectivity and mechanical performance. Future work should continue to explore new materials and compositions to further refine CEMs for artificial photosynthesis and sustainable CO2 conversion applications.

9.4. References

[1] W. Zhong, J.D. Haigh, The greenhouse effect and carbon dioxide, Weather 68(4) (2013) 100-105.

[2] T.R. Anderson, E. Hawkins, P.D. Jones, CO2, the greenhouse effect and global warming: from the pioneering work of Arrhenius and Callendar to today's Earth System Models, Endeavour 40(3) (2016) 178-187.

[3] J.F. Mitchell, The "greenhouse" effect and climate change, Reviews of Geophysics 27(1) (1989) 115-139.

[4] J.S. Sawyer, Man-made carbon dioxide and the "greenhouse" effect, Nature 239(5366) (1972) 23-26.

[5] Y. Liu, L. Guo, On factors limiting the performance of photoelectrochemical CO2 reduction, The Journal of Chemical Physics 152(10) (2020).

[6] D.A. Salvatore, C.M. Gabardo, A. Reyes, C.P. O'Brien, S. Holdcroft, P. Pintauro, B. Bahar, M. Hickner, C. Bae, D. Sinton, Designing anion exchange membranes for CO2 electrolysers, Nature Energy 6(4) (2021) 339-348.

[7] A.L. Bachmann, B. Hunter, B.S. Beckingham, Development of Structure–Property Relationships for Ammonium Transport through Charged Organogels, Membranes 14(3) (2024) 71.

[8] A. Kusoglu, A.Z. Weber, New insights into perfluorinated sulfonic-acid ionomers, Chemical reviews 117(3) (2017) 987-1104.

[9] K.A. Mauritz, R.B. Moore, State of understanding of Nafion, Chemical reviews 104(10) (2004) 4535-4586.

[10] Y.-h. Lin, J.M. Kim, B.S. Beckingham, Salt Transport in Crosslinked Hydrogel Membranes Containing Zwitterionic Sulfobetaine Methacrylate and Hydrophobic Phenyl Acrylate, Polymers 15(6) (2023) 1387.

[11] J.M. Kim, Y. Wang, Y.-h. Lin, J. Yoon, T. Huang, D.-J. Kim, M.L. Auad, B.S. Beckingham, Fabrication and Characterization of Cross-Linked Phenyl-Acrylate-Based Ion Exchange Membranes and Performance in a Direct Urea Fuel Cell, Industrial & Engineering Chemistry Research 60(41) (2021) 14856-14867.

[12] J.M. Kim, Y.-h. Lin, S.M. Bannon, G.M. Geise, B.S. Beckingham, Improved Structural Stability of Charged Hydrogels under Organic CO2 Reduction Products: Effect of Acrylate and

Methacrylate Backbone Linkages, The Journal of Physical Chemistry C 127(22) (2023) 10826-10832.

[13] J.M. Kim, Y.-h. Lin, B. Hunter, B.S. Beckingham, Transport and co-transport of carboxylate ions and ethanol in anion exchange membranes, Polymers 13(17) (2021) 2885.

[14] J.M. Kim, Y.-H. Lin, P.P. Aravindhan, B.S. Beckingham, Impact of hydrophobic pendant phenyl groups on transport and co-transport of methanol and acetate in PEGDA-SPMAK cation exchange membranes, Chemical Engineering Research and Design 185 (2022) 418-429.

[15] H. Ju, A.C. Sagle, B.D. Freeman, J.I. Mardel, A.J. Hill, Characterization of sodium chloride and water transport in crosslinked poly (ethylene oxide) hydrogels, Journal of Membrane Science 358(1-2) (2010) 131-141.

[16] A.C. Sagle, H. Ju, B.D. Freeman, M.M. Sharma, PEG-based hydrogel membrane coatings, Polymer 50(3) (2009) 756-766.

[17] X. Gong, A. Bandis, A. Tao, G. Meresi, Y. Wang, P. Inglefield, A. Jones, W.-Y. Wen, Self-diffusion of water, ethanol and decafluropentane in perfluorosulfonate ionomer by pulse field gradient NMR, Polymer 42(15) (2001) 6485-6492.

[18] E.-S. Jang, J. Kamcev, K. Kobayashi, N. Yan, R. Sujanani, T.J. Dilenschneider, H.B. Park, D.R. Paul, B.D. Freeman, Influence of water content on alkali metal chloride transport in cross-linked Poly (ethylene glycol) Diacrylate. 1. Ion sorption, Polymer 178 (2019) 121554.

[19] J. Mahler, I. Persson, A study of the hydration of the alkali metal ions in aqueous solution, Inorganic chemistry 51(1) (2012) 425-438.

[20] W. Xie, J. Cook, H.B. Park, B.D. Freeman, C.H. Lee, J.E. McGrath, Fundamental salt and water transport properties in directly copolymerized disulfonated poly (arylene ether sulfone) random copolymers, Polymer 52(9) (2011) 2032-2043.

[21] M. Paul, H.B. Park, B.D. Freeman, A. Roy, J.E. McGrath, J. Riffle, Synthesis and crosslinking of partially disulfonated poly (arylene ether sulfone) random copolymers as candidates for chlorine resistant reverse osmosis membranes, Polymer 49(9) (2008) 2243-2252.

[22] G. Geise, B. Freeman, D. Paul, Characterization of a sulfonated pentablock copolymer for desalination applications, Polymer 51(24) (2010) 5815-5822.

[23] S. Chen, L. Li, C. Zhao, J. Zheng, Surface hydration: Principles and applications toward low-fouling/nonfouling biomaterials, Polymer 51(23) (2010) 5283-5293.

[24] A. Mehta, A.L. Zydney, Permeability and selectivity analysis for ultrafiltration membranes, Journal of membrane science 249(1-2) (2005) 245-249.

[25] G. Belfort, R.H. Davis, A.L. Zydney, The behavior of suspensions and macromolecular solutions in crossflow microfiltration, Journal of membrane science 96(1-2) (1994) 1-58.

[26] A.W. Adamson, A.P. Gast, Physical chemistry of surfaces, Interscience publishers New York1967.

[27] R. Kingsbury, K. Bruning, S. Zhu, S. Flotron, C. Miller, O. Coronell, Influence of water uptake, charge, manning parameter, and contact angle on water and salt transport in commercial ion exchange membranes, Industrial & Engineering Chemistry Research 58(40) (2019) 18663-18674.

[28] N.G. McCrum, C.P. Buckley, C.B. Bucknall, Principles of polymer engineering, Oxford University Press1997.

[29] L. Kwisnek, J. Goetz, K.P. Meyers, S.R. Heinz, J.S. Wiggins, S. Nazarenko, PEG containing thiol–ene network membranes for CO2 separation: effect of cross-linking on thermal, mechanical, and gas transport properties, Macromolecules 47(10) (2014) 3243-3253.

[30] M.L. Greenfield, D.N. Theodorou, Geometric analysis of diffusion pathways in glassy and melt atactic polypropylene, Macromolecules 26(20) (1993) 5461-5472.

[31] R.W. Baker, Membrane technology and applications, John Wiley & Sons2023.

[32] J.M. Kim, B.M. Dobyns, R. Zhao, B.S. Beckingham, Multicomponent transport of methanol and acetate in a series of crosslinked PEGDA-AMPS cation exchange membranes, Journal of Membrane Science 614 (2020) 118486.

[33] M. Galizia, D.R. Paul, B.D. Freeman, Liquid methanol sorption, diffusion and permeation in charged and uncharged polymers, Polymer 102 (2016) 281-291.

[34] H. Yasuda, A. Peterlin, C. Colton, K. Smith, E. Merrill, Permeability of solutes through hydrated polymer membranes. Part III. Theoretical background for the selectivity of dialysis membranes, Die Makromolekulare Chemie: Macromolecular Chemistry and Physics 126(1) (1969) 177-186.

[35] H. Yasuda, C. Lamaze, L. Ikenberry, Permeability of solutes through hydrated polymer membranes. Part I. Diffusion of sodium chloride, Die Makromolekulare Chemie: Macromolecular Chemistry and Physics 118(1) (1968) 19-35.

[36] G.M. Geise, D.R. Paul, B.D. Freeman, Fundamental water and salt transport properties of polymeric materials, Progress in Polymer Science 39(1) (2014) 1-42.

[37] H. Ju, B.D. McCloskey, A.C. Sagle, V.A. Kusuma, B.D. Freeman, Preparation and characterization of crosslinked poly (ethylene glycol) diacrylate hydrogels as fouling-resistant membrane coating materials, Journal of Membrane Science 330(1-2) (2009) 180-188.

Chapter 10: Isolating the Impact of Water Volume Fraction in AEMs

10.1. Introduction

Addressing global warming and the energy crisis requires a dual focus on reducing carbon emissions and expanding sustainable energy sources. The urgent need to lower atmospheric CO_2 and secure energy resources points to an essential shift from hydrocarbon fuels toward greener, renewable options. PEC-CRC presents a promising solution for addressing global warming and the energy crisis by converting CO_2 into valuable chemical fuels like methanol and ethanol [1]. Ion exchange membranes (IEMs) are essential components in PEC-CRC systems [2, 3] and a range of electrochemical applications, including fuel cells [4, 5], electrodialysis [6, 7], and redox flow batteries [8, 9]. Their primary role within these systems is to separate the chemical reactions occurring at the electrodes while enabling selective ion transport between compartments [10]. The intricate balance between membrane properties, such as water volume fraction, fixed charge density, and ion transport behavior, is pivotal for optimizing their function. However, the complex dynamics of ion transport in hydrated, dense polymer membranes, particularly under multicomponent systems, remain poorly understood. This gap in knowledge limits the development of advanced membranes tailored for specific electrochemical applications. In this

study, we systematically investigate the interplay between solute-membrane interactions, water volume fraction, and fixed charge density by synthesizing neutral membranes and quaternary ammonium-functionalized AEMs based on phenyl acrylate backbones. By isolating the impact of water content, this work analyzes the transport behavior of potassium formate, acetate, and bicarbonate, both individually and in combination, to elucidate the other physiochemical properties and mechanisms governing ion transport. Here, we observe higher single-solute permeability in AEMs than neutral membranes, with potassium formate exhibiting the highest permeability, followed by acetate and bicarbonate. Co-permeation experiments find minimal differences between single-solute and two-solute permeabilities. Moreover, solubility analysis indicated that fixed charge density influences ion retention, with an increase generally reducing solubility likely due to intensified Donnan exclusion. Notably, potassium acetate shows an unusual solubility increase with rising fixed charge density. These results underscore the importance of fixed charge density and solute-membrane interactions in influencing ion transport and solubility, offering opportunities for tailoring ion exchange membrane design in PEC-CRC and other electrochemical systems.

10.2. Results and Discussion

The materials, membrane synthesis methods, and experimental procedures are detailed in Chapter 3. A total of six AEMs and one charge-neutral membrane were prepared via thermally initiated free radical copolymerization of pre-polymer mixtures, as detailed in Table 10.1 and the synthetic scheme depicted in Figure 10.1. The membranes are designated as P(w)M(x)AP(y) and

PA(w)P(x)AE(z), where w, x, y, and z represent the molar percentages of PA, MBAA, APTA, and AETAC, respectively. The crosslinker and solvent content affect the membrane's water content by altering the crosslink density. Dissolving hydrophilic charged monomers and hydrophobic crosslinkers in a shared solvent is a notable challenge. To achieve a homogeneous solution and consistent water volume fraction across all membranes, the solvent content was adjusted accordingly. And each pre-polymerization solution contains 0.1 wt.% AIBN. This arrangement facilitated a comparative analysis of the different charged monomers and fixed charge densities, isolating the effects of water volume fraction on physicochemical and transport properties. Moreover, we found that the APTA charge monomer has a greater ability to attract water molecules than AETAC. When controlling the membrane's water volume fraction to a specific value, the APTA monomer requires less solvent content to reach that target compared to AETAC.

Table 10.1. Composition of Pre-polymerization mixtures.

Name	PA (mol%)	MBAA (mol%)	APTA (mol%)	DMSO(wt%)
P55M20AP25	55	20	25	42
P65M15AP20	65	15	20	45
P80M10AP10	80	10	10	60
Name	**PA (mol%)**	**MBAA (mol%)**	**AETAC (mol%)**	**DMSO(wt%)**
P55M20AE25	55	20	25	50
P65M15AE20	65	15	20	59
P80M10AE10	80	10	10	62
P80M20	80	20	0	69

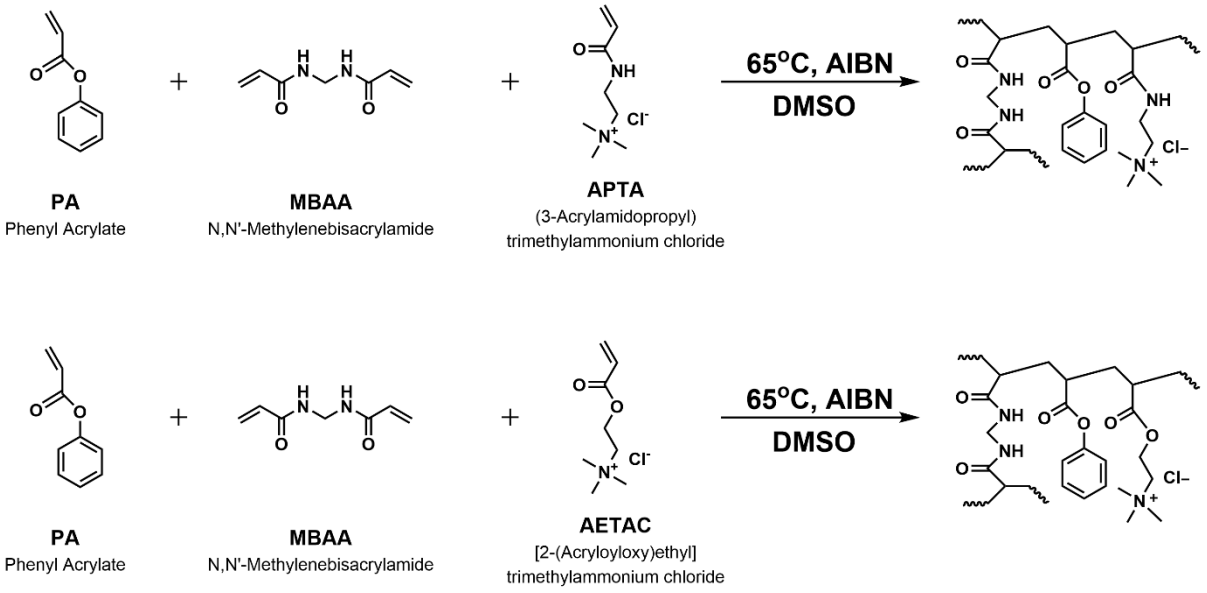

Figure 10.1. Synthetic scheme of PA/MBAA/APTA and PA/MBAA/AETAC

10.2.1. Membrane water content and charge content

In our previous research, we have synthesized several series of ion exchange membranes (IEMs) with various charged monomers and solvent contents [2-4, 11-15]. Generally, membranes with higher water volume fractions exhibit increased permeability, solubility, and diffusivity, attributed to the greater free volume available for water transport [2, 3, 12, 16]. This finding, consistent with free volume theory and other reports, highlights that water volume fraction is a critical factor influencing ion transport in hydrated membranes [17, 18]. However, varying water volume fractions between membranes make it difficult to isolate and examine the specific effects of charged monomers and charge content. Since most charged monomers are hydrophilic, there is a tradeoff between water content and charge content [19]. The increased interactions between

water molecules and charged groups make it challenging to synthesize a series of membranes with varying charge content but comparable water volume fractions. To address this, we prepared membranes with similar water volume fractions, approximately 0.4, by adjusting the solvent content and monomer-to-crosslinker ratio in the homogeneous pre-polymerization solutions. Table 10.2 provides the characterized membrane water content, dry polymer density, ionic conductivity, fixed charge concentration, and fixed charge density for the membranes in this study. Figure 10.2 illustrates the relationship between volumetric charge density and water volume fraction against the mol % of charged monomer in the pre-polymerization solution. The IEC is expected to increase as the charged monomer content increases. Here, we observed that membranes with the same charged monomer content exhibited similar IEC, fixed charge concentration, and fixed charge density values, as APTA and AETAC have comparable molecular weights (206.7 g/mol and 193.7 g/mol, respectively) and comparable water content within membranes. Moreover, this study primarily uses fixed charge density, rather than IEC, to represent the relationship between charged monomer content and transport behavior, as it accounts for membrane volume, which can significantly influence transport properties.

Table 10.2. Water uptake, dry polymer density, water volume fraction, ionic conductivity, fixed charge concentration, and fixed charge density.

Name	ω_u	ρ_p (g/mL)	$\emptyset_w$	IEC (mmol/g)	$C_A^{m,w}$	$C_A^{m,\mathrm{p}}$
P55M20AP25	0.52 ± 0.01	1.242 ± 0.005	0.393 ± 0.003	1.78	3.43	1.35
P65M15AP20	0.54 ± 0.01	1.250 ± 0.002	0.404 ± 0.004	1.47	2.73	1.10
P80M10AP10	0.56 ± 0.01	1.228 ± 0.005	0.408 ± 0.005	0.79	1.37	0.56
P55M20AE25	0.52 ± 0.01	1.271 ± 0.009	0.398 ± 0.004	1.75	3.36	1.34
P65M15AE20	0.55 ± 0.01	1.240 ± 0.006	0.407 ± 0.006	1.46	2.64	1.07
P80M10AE10	0.53 ± 0.01	1.238 ± 0.003	0.398 ± 0.003	0.71	1.34	0.53
P80M20	0.52 ± 0.01	1242 ± 0.006	0.393 ± 0.004	N/A	N/A	N/A

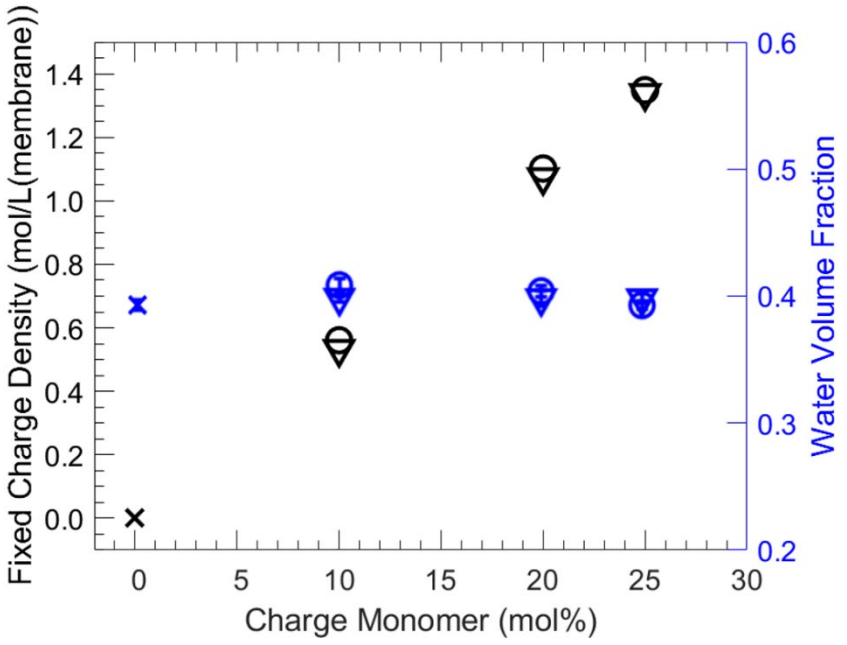

Figure 10.2. Fixed charge density and water volume fraction are plotted against the mol% of charge monomer in the pre-polymerization solution. Fixed charge density is shown in black color, while water volume fraction is depicted in blue color. Circles (◯) represent membranes containing APTA, triangles (▽) represent membranes containing AETAC, and crosses (╳) denote neutral membranes.

10.2.2. Membrane Characterization

Glass transition temperature, ionic conductivity, and Young's modulus are critical parameters in polymer membranes, reflecting the flexibility of the polymer chains, ion transport capacity, and mechanical properties of the membrane, respectively. Table 10.3 presents data on the glass transition temperature, ionic conductivity, and Young's modulus. We observe the T_g of AEMs increases with higher crosslinker content which can be attributed to a higher T_g of MBAA; the T_g values for PA, MBAA, APTA, and AETAC are 32.8℃, 150.3℃, 48.7℃, and 2.4℃, respectively. Poly(AETAC) was synthesized using 50 wt% AETAC and 50 wt% water, with AIBN

as the initiator at 0.1 wt% relative to AETAC. After synthesis, the polymer was dried in a vacuum oven at 50°C for 24 hours, followed by characterization using DSC. Typically, the ionic conductivity increases with a higher charged monomer content, as it is closely linked to the membrane water content and fixed charge concentration [20]. Higher fixed charge concentrations introduce more counter ions as charge carriers into the polymer, thereby enhancing ionic conductivity. In this study, the influence of water volume fraction is excluded, and the membranes containing APTA exhibit higher ionic conductivity compared to those with AETAC at the same charged monomer content. This could be due to the slightly higher IEC and the stronger ion-dipole interactions of the amide group in APTA compared to the ester group in AETAC [21]. These stronger interactions may create more efficient ion pathways, resulting in better ionic mobility and enhanced ion transport efficiency within the membrane. Interestingly, while Young's Modulus typically increases with higher crosslinker content, the Young's Modulus for both AEMs decreases as the crosslinker content increases. We attribute to this to the corresponding decrease in phenyl acrylate content as phenyl acrylate has been previously found to increase Young's Modulus [16, 22]. The benzene ring in phenyl acrylate is rigid and stiff, which restricts the flexibility of the polymer chains, and leads to an increase in the stiffness of the polymer membrane [23]. Moreover, the increased APTA and AETAC content could lead to more flexible polymer chains, reducing the overall rigidity of the membrane and lowering the Young's Modulus.

Table 10.3. Glass transition temperature, ionic conductivity, and Young's modulus.

Name	T_g (°C)	Ionic conductivity (mS/cm))	Young's Modulus (MPa)
P55M20AP25	131.33	7.50 ± 0.08	0.353 ± 0.020
P65M15AP20	88.31	6.35 ± 0.08	0.843 ± 0.050
P80M10AP10	71.28	3.24 ± 0.03	1.250 ± 0.010
P55M20AE25	144.9	6.68 ± 0.02	0.584 ± 0.021
P65M15AE20	87.23	5.22 ± 0.02	0.873 ± 0.018
P80M10AE10	83.29	1.95 ± 0.02	1.080 ± 0.032
P80M20	118.58	N/A	1.384 ± 0.035

10.2.3. Salt Permeability

The permeability of a total of 1 mol of single solute and two-solute mixtures was measured at 25°C using a standard diffusion cell. Figure 10.3 illustrates the single-solute permeability of neutral membranes and both AEMs to potassium formate, potassium acetate, and potassium bicarbonate. Again, permeability is closely related to the water volume fraction, higher permeability is observed as the water volume fraction increases due to more free volume available for ion transport [2, 3, 12, 16, 19]. However, the effect of water volume fraction is excluded in this study as all membranes have essentially the same water volume fraction. The neutral membrane demonstrates significantly lower permeability compared to the AEMs. Interestingly, both AEMs exhibit comparable single-solute permeability across various fixed charge densities, which deviates from expectations. Theoretically, at a constant water volume fraction, an increase in fixed charge density enhances the Donnan potential [19], which should lead to a rise in solute permeability. We hypothesize that counter-ion condensation occurs, reducing the strength of electrostatic attraction. Moreover, the permeability trend among the tested solutes—potassium

formate > potassium acetate > potassium bicarbonate—does not directly align with the order of the ions' hydrated diameters: formate (5.9 Å), acetate (7.4 Å), and bicarbonate (7.3 Å) [2, 24, 25]. This suggests that factors beyond hydrated ion size, such as solute-membrane interactions, solubility, and diffusivity are influencing the observed transport behavior. These findings underscore the complexity of solute transport in membranes and highlight the need for a more detailed investigation into the interplay between membrane structure, solute properties, charge groups, and transport mechanisms. Moreover, our previous study on AEMs, composed of 49 mol% PA and 30 mol% MBAA with the incorporation of 21 mol% AETAC or 2-(Methacryloyloxy)ethyl trimethylammonium chloride (MAETAC), demonstrated water volume fractions of 0.39 and 0.43, respectively. The study also revealed 1M permeability values for KOFm of approximately 0.3×10^{-7} cm²/s.

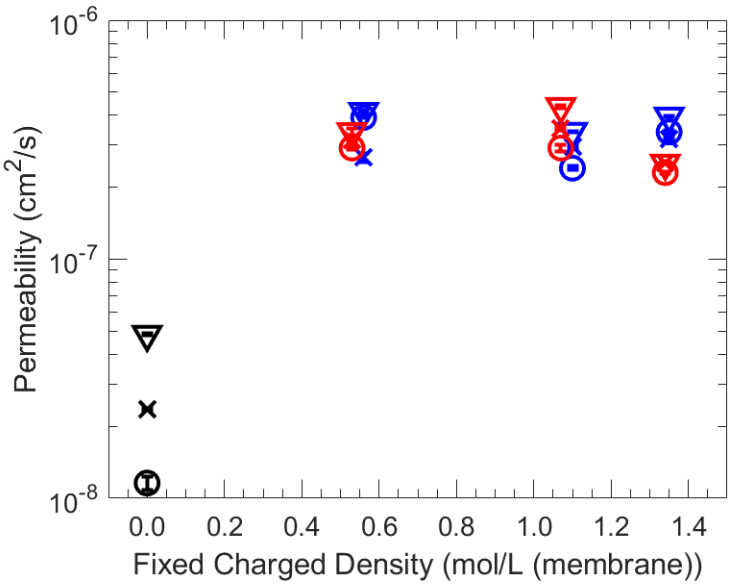

Figure 10.3. Single solute permeability as a function of fixed charge density is presented. Blue markers indicate APTA-containing membranes, red markers indicate AETAC-containing membranes, and black markers represent neutral membranes. Potassium formate is represented by triangles (▽), potassium acetate by crosses (╳), and potassium bicarbonate by circles (○).

To mitigate the effects of total concentration changes—such as dimensional swelling, Donnan potential, and fluctuations in the driving force—this study employed a solute mixture containing 0.5 mol of one solute and 0.5 mol of another. Figure 10.4 illustrates the co-permeation behavior of neutral membranes and both AEMs for potassium formate, potassium acetate, and potassium bicarbonate. The relative permeability order between the two solutes remains largely unchanged compared to their single-solute permeability. Typically, salt flux decreases as the upstream solute concentration decreases, leading to slower accumulation of solute in the downstream compartment. This occurs because the weaker driving force results in lower membrane permeability to the solute [4, 26]. However, an intriguing observation in this study is

that no significant difference was found between the single-solute and two-solute permeability values, despite the expectation of reduced co-permeation in the mixed-solute system. This expectation stems from reducing individual solute concentrations from 1 M to 0.5 M in the mixture. One explanation for this behavior is that the total solute concentration in the upstream solution remains constant at 1 M in both scenarios, maintaining a relatively stable osmotic driving force across the membrane. This could mitigate the expected decrease in permeability caused by the lower concentration of each solute. Moreover, electrostatic interactions among multiple solutes, particularly in mixtures of non-ideal, highly polar solutes (e.g., electrolytes), can result in unexpected flux behaviors. Phenomena such as flux coupling and competitive sorption complicate the prediction of multicomponent transport behavior based solely on single-component data, emphasizing the need for direct measurement of multicomponent transport parameters [27, 28]. To fully understand these unexpected outcomes, further studies are necessary. These should include varying the total solute concentration, investigating the effects of different solute pairs, and examining microstructural changes within the membrane during transport.

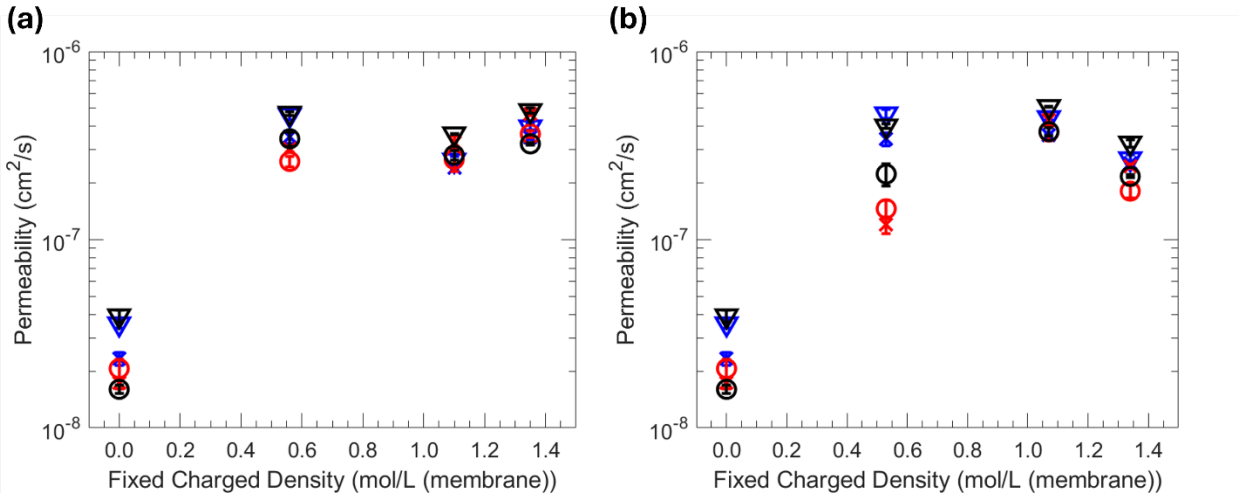

Figure 10.4. The co-permeation of two solutes is illustrated as a function of fixed charge density. (a) APTA-containing and neutral membrane (b) AETAC-containing and neutral membrane. Co-permeation results for potassium acetate and potassium formate are shown in blue, potassium acetate and potassium bicarbonate in red, and potassium formate and potassium bicarbonate in black. Symbols represent each solute: potassium formate with triangles (▽), potassium acetate with crosses (╳), and potassium bicarbonate with circles (○).

10.2.4. Salt Solubility

Previous studies have shown that membrane solubility typically correlates with water content, with more hydrated membranes absorbing more ions than those with lower water content [2, 3, 12, 16, 29]. Figure 10.5 illustrates the swelling ratio of membranes in response to equilibration with 1 M of each solute. This measures the membrane's volume change after being saturated in a salt solution, indicating how much space the membrane can take in the solution.

$$\text{Swelling Ratio} = \frac{\text{Volume of saturated film}}{\text{Volume of hydrate film}} \tag{10.1}$$

Swelling ratio typically depend on the membrane's mechanical properties and osmotic pressure caused by solution concentration; at high salt concentrations, the external osmotic

pressure increases. Water molecules move out of the membrane to balance this pressure, leading to reduced water content and membrane shrinkage. As water content decreases, the fixed charge density increases, meaning the charged sites within the membrane become more concentrated. This higher fixed charge density intensifies Donnan exclusion, where the membrane's internal electrostatic forces more effectively repel co-ions and retain counter-ions [30-32]. As a result, the solute concentration in the membrane decreases, since the membrane is less able to accommodate additional ions [30, 33]. Here, we observe that as the fixed charge density increases, swelling ratio decreases, which may lead to a reduction in water content within the membrane. This reduction in water content results in decreased free volume available in membranes and an increase in fixed charge density [30]. Additionally, membranes containing AETAC exhibit lower dimensional swelling compared to those with APTA.

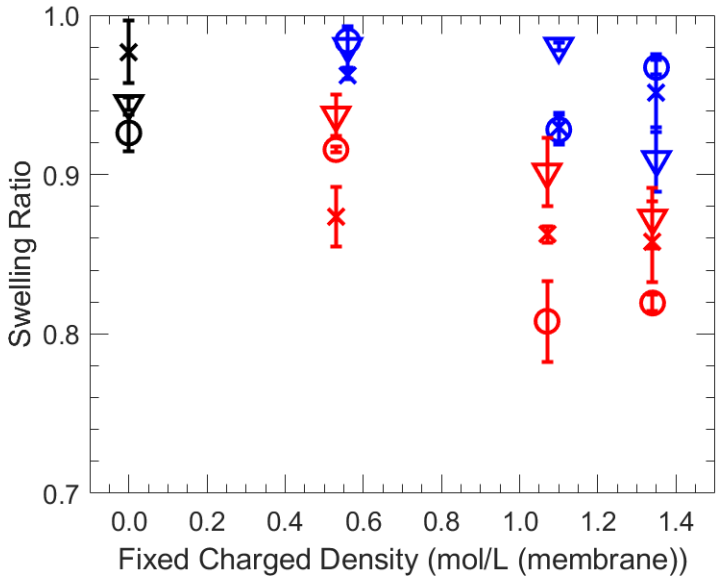

Figure 10.5. The deswelling ratio of membranes conducting single-solute solubility is shown, with blue markers for APTA-containing membranes, red markers for AETAC-containing membranes,

and black markers for neutral membranes. Potassium formate is indicated by triangles (▽), potassium acetate by crosses (╳), and potassium bicarbonate by circles (○).

Figure 10.6 shows the calculated solubility of potassium acetate, potassium formate, and potassium bicarbonate in both AEMs and an uncharged membrane from the 1M sorption-desorption experiments. The solubilities in the neutral membrane remain relatively similar, likely due to the absence of fixed charge groups, leading to fewer interactions between the membrane and ions. In contrast, both AEMs exhibit stronger interactions between the fixed charge groups and the ions, impacting solubility behavior. Specifically, the solubility of potassium formate and potassium bicarbonate in both AEMs decreases as the fixed charge density increases. This decrease may be due to the reduced membrane swelling. On the other hand, the solubility of potassium acetate in both AEMs shows an increase with rising fixed charge density. This unexpected trend may be due to specific interactions between the acetate anion and the membrane. Acetate may interact more favorably with the hydrophobic regions within the membrane or form stable ion pairs with the fixed charge groups. Moreover, membranes containing AETAC exhibit higher solubility compared to those with APTA, despite having lower dimensional swelling.

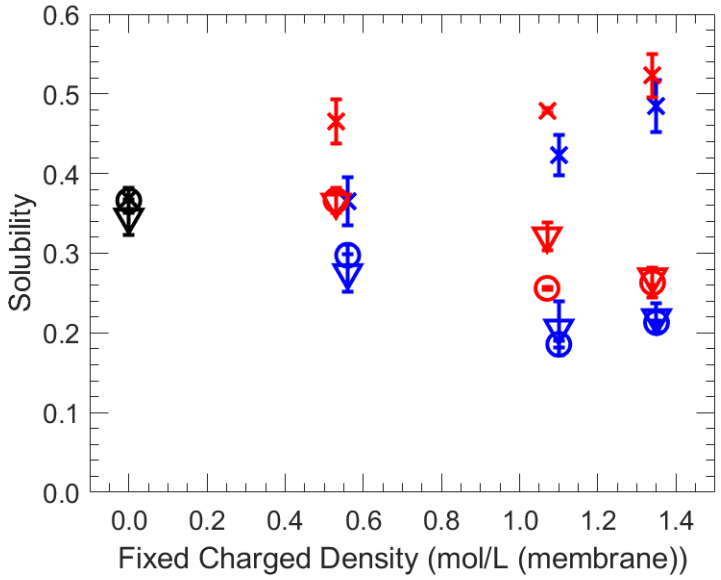

Figure 10.6. Single solute solubility as a function of fixed charge density is presented. Blue markers indicate APTA-containing membranes, red markers indicate AETAC-containing membranes, and black markers represent neutral membranes. Potassium formate is represented by triangles (▽), potassium acetate by crosses (╳), and potassium bicarbonate by circles (○).

The concentration of the solution greatly affects the solubility of AEMs, as the Donnan exclusion and dimensional swelling can be disrupted by the concentration of the solution [34, 35]. To maintain a consistent concentration, 0.5 M of one solute and 0.5 M of another solute are used for measuring co-sorption. Figure 10.7 illustrates the dimensional swelling of membranes in response to 0.5/0.5 M co-sorption. In this case, the neutral membrane exhibits a slightly higher swelling ratio compared to single-solute sorption. Membranes containing APTA show a higher swelling ratio compared to those with AETAC, following a similar trend observed with single-component sorption. For AETAC-containing membranes, dimensional swelling decreases as the fixed charge density increases, whereas APTA-containing membranes exhibit a slight increase in swelling with higher fixed charge density, which is unexpected.

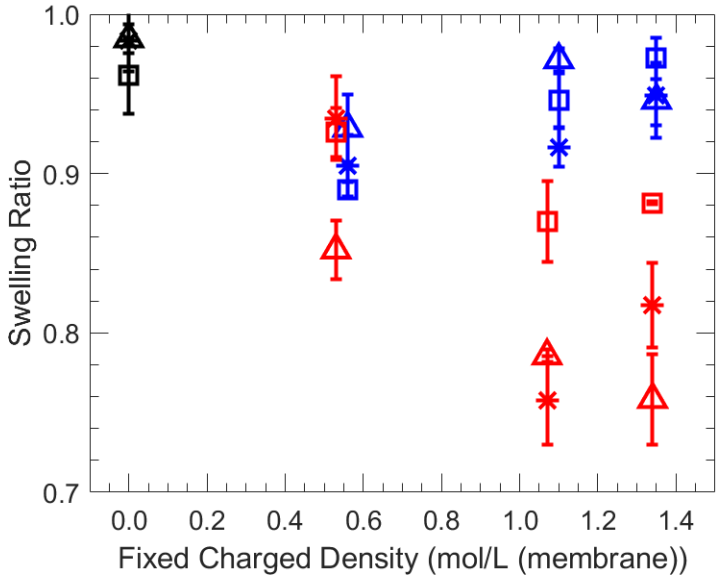

Figure 10.7. The deswelling ratio of membranes during co-sorption is illustrated, with blue markers representing APTA-containing membranes, red markers for AETAC-containing membranes, and black markers for neutral membranes. A square (□) indicates potassium acetate and potassium formate, a star (✻) represents potassium acetate and potassium bicarbonate, and a triangle (△) stands for potassium formate and potassium bicarbonate.

Figure 10.8 shows the 0.5/0.5 M two-solute solubility of potassium acetate, potassium formate, and potassium bicarbonate in both AEMs and the uncharged membrane. Generally, the co-sorption of two AEMs and uncharged membranes to potassium acetate, potassium formate, and potassium bicarbonate is lower than single solute solubility as in a membrane there is a finite free volume where solutes can interact and be retained. In a two-solute system, both solutes compete for the same free volume. This competition can reduce the sorption of each solute, leading to lower overall solubility compared to a single-solute scenario, as observed in this and prior studies [2, 36]. Here, potassium bicarbonate shows the highest co-sorption in neutral membranes, unlike its behavior in AEMs. In both AEMs, potassium bicarbonate exhibits the lowest solubility in the two-

solute system, which decreases further as the fixed charge density increases. This trend is likely due to the intensified Donnan exclusion effect and the lower charge density of bicarbonate compared to the acetate and formate. However, in both AEMs, the co-sorption of potassium acetate increases with higher fixed charge density as it might have a specific interaction with the membrane. In terms of the co-sorption of potassium formate, when it is mixed with potassium acetate its solubility decreases as fixed charge density increases due to encounter higher competition, whereas the co-sorption of potassium formate increases with potassium bicarbonate due to higher charge density than bicarbonate.

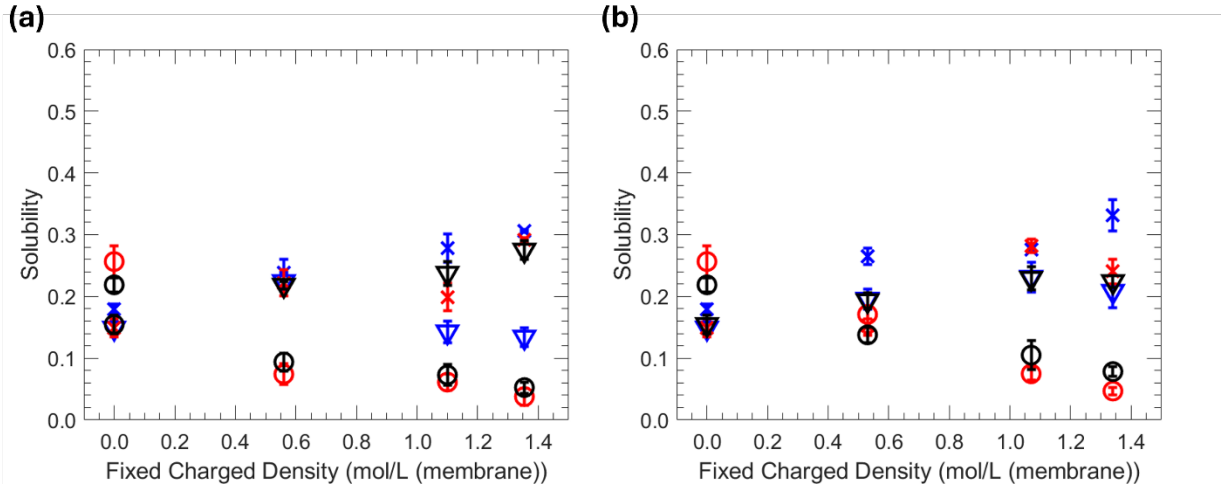

Figure 10.8. The co-sorption of two solutes as a function of fixed charge density is illustrated. (a) APTA-containing and neutral membrane (b) AETAC-containing and neutral membrane. Co-sorption results for potassium acetate and potassium formate are shown in blue, potassium acetate and potassium bicarbonate in red, and potassium formate and potassium bicarbonate in black. Symbols represent each solute: potassium formate with triangles (▽), potassium acetate with crosses (╳), and potassium bicarbonate with circles (○).

10.2.5. Salt Diffusivity

Figure 10.9 illustrates the single-solute diffusivity of potassium formate, potassium acetate, and potassium bicarbonate through the neutral membrane and AEMs. The lower diffusivity in the neutral membrane compared to both AEMs may be due to the absence of fixed charges, which means there is no electrostatic driving force to facilitate ion transport. However, no clear trend of increasing diffusivity with higher fixed charge density is observed. APTA-containing membranes exhibit slightly higher diffusivity compared to AETAC-containing membranes. This difference may be due to AETAC's ester group, which tends to form stronger ion-dipole interactions and hydrogen bonds with water molecules compared to the amide group in APTA. These stronger interactions in AETAC create a more tightly bound water structure within the membrane, reducing the mobility of solute ions and leading to lower diffusivity. Moreover, the diffusivity of the solutes in the neutral membrane follows the order of potassium formate> potassium acetate> potassium bicarbonate, which aligns with the single solute permeability. However, in AEMs, this order shifts for potassium acetate and potassium bicarbonate, likely due to differences in their interactions with the charged functional groups of the membrane. The smaller size of bicarbonate ions may reduce electrostatic interactions with the AEM's fixed charges, allowing them to diffuse more efficiently compared to acetate ions.

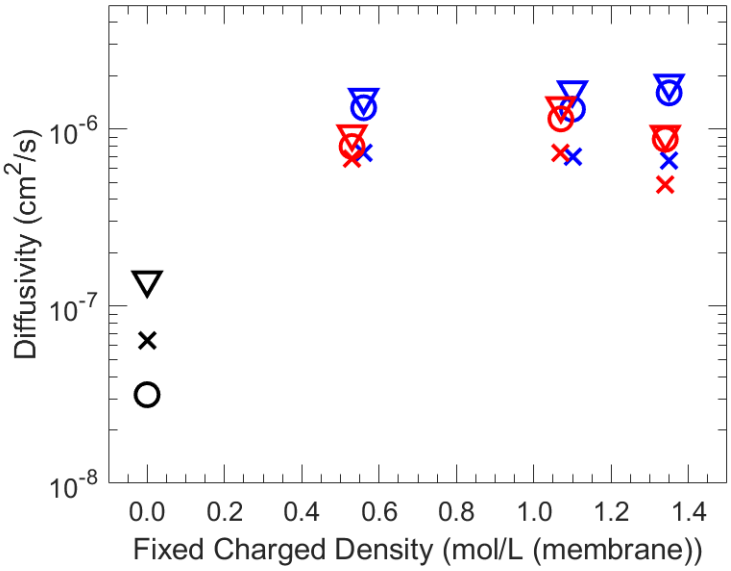

Figure 10.9. Single solute diffusivity as a function of fixed charge density is presented. Blue markers indicate APTA-containing membranes, red markers indicate AETAC-containing membranes, and black markers represent neutral membranes. Potassium formate is represented by triangles (▽), potassium acetate by crosses (╳), and potassium bicarbonate by circles (○).

Figure 10.10 illustrates the co-diffusion of potassium formate, potassium acetate, and potassium bicarbonate for the neutral membrane and AEMs. Co-diffusion exhibits higher diffusivity compared to single-solute diffusivity. This phenomenon has been observed in one of our previous reports, including PEGDA-AMPS membranes containing sulfonate groups (SO_3^-) and Nafion® 117 cation exchange membranes (CEMs) during the co-transport of carboxylate ions and alcohols [15]. The same trend is apparent in neutral membranes, where co-diffusion also leads to increased diffusivity. We hypothesize that the co-transport of carboxylate ions enhances the mobility of both solutes through a synergistic effect. Interestingly, the diffusivity hierarchy changes in AEMs compared to neutral membranes. Specifically, the co-diffusion of potassium bicarbonate exhibits higher diffusivity than its single-solute diffusivity. However, this trend does

not extend to neutral membranes, where the order of diffusivity remains consistent across solutes. This may be attributed to the lower charge density, which reduces competition with other solutes in solubility and decreases interactions with the membrane, resulting in higher diffusivity. In contrast, potassium acetate exhibits specific interactions with the functional groups, leading to the lowest diffusivity in co-diffusion.

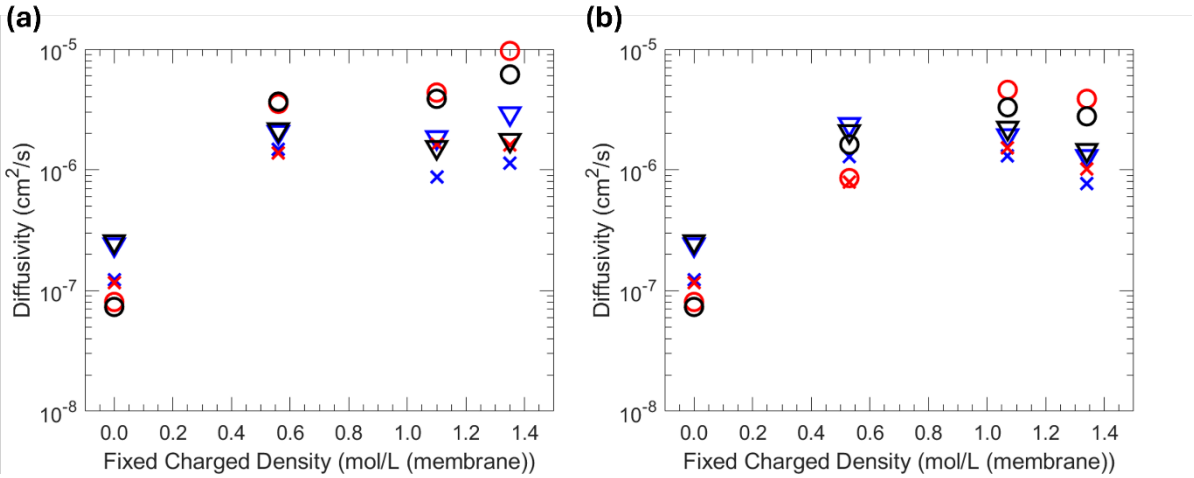

Figure 10.10. The co-diffusion of two solutes as a function of fixed charge density is illustrated. (a) APTA-containing and neutral membrane (b) AETAC-containing and neutral membrane. Co-diffusion results for potassium acetate and potassium formate are shown in blue, potassium acetate and potassium bicarbonate in red, and potassium formate and potassium bicarbonate in black. Symbols represent each solute: potassium formate with triangles (▽), potassium acetate with crosses (╳), and potassium bicarbonate with circles (○).

10.3. Conclusions

This study investigated single and dual solute transport in 1 neutral membrane and 6 different AEMs based on two different quaternary ammonium-containing comonomers, focusing on the impact of fixed charge density and charge group chemistry for membranes with water volume fraction. We found that the APTA charge monomer attracts more water molecules than

AETAC, and membranes containing APTA exhibit higher ionic conductivity due to the stronger ion-dipole interactions of APTA's amide group. Moreover, in co-sorption membrane solubility to all solutes decreases compared to sing solute solubility due to the competition of finite space for solutes to retain in the membrane. In terms of solute solubility order, it was observed that potassium bicarbonate shows the highest solubility but shows the lowest solubility in AEMs. We hypothesize that the solute charge density affects membrane solubility to solute. Since potassium bicarbonate has a lower charge density compared to other solutes, it shows the lowest solubility in co-sorption. This effect becomes more significant as fixed charge density increases. In co-sorption experiments, membrane solubility to all solutes decreases compared to single-solute conditions, likely due to competition for the finite space available for solute retention. Regarding solute solubility trends, potassium bicarbonate exhibits the highest solubility in the neutral membrane but the lowest solubility in AEMs. We hypothesize that solute charge density plays a key role in membrane solubility, as potassium bicarbonate, having a lower charge density than other solutes, demonstrates reduced solubility in co-sorption conditions. This effect becomes more pronounced as the membrane's fixed charge density increases. Therefore, membrane diffusivity to solutes is also influenced by the interaction between the solute and the membrane. In general, solutes that interact more strongly with the membrane exhibit slower diffusivity. These findings highlight the importance of synthesizing membranes with comparable water volume fractions to investigate other factors affecting transport behavior. Future research, such as exploring the interplay of concentration changes in mixed transport systems and ion-membrane interactions, could further enhance our understanding of membrane transport behavior in practical applications.

10.4. References

[1] D. Li, K. Yang, J. Lian, J. Yan, S. Liu, Powering the world with solar fuels from photoelectrochemical CO2 reduction: basic principles and recent advances, Advanced Energy Materials 12(31) (2022) 2201070.

[2] J.M. Kim, Y.-h. Lin, B. Hunter, B.S. Beckingham, Transport and co-transport of carboxylate ions and ethanol in anion exchange membranes, Polymers 13(17) (2021) 2885.

[3] J.M. Kim, Y.-H. Lin, P.P. Aravindhan, B.S. Beckingham, Impact of hydrophobic pendant phenyl groups on transport and co-transport of methanol and acetate in PEGDA-SPMAK cation exchange membranes, Chemical Engineering Research and Design 185 (2022) 418-429.

[4] J.M. Kim, Y. Wang, Y.-h. Lin, J. Yoon, T. Huang, D.-J. Kim, M.L. Auad, B.S. Beckingham, Fabrication and Characterization of Cross-Linked Phenyl-Acrylate-Based Ion Exchange Membranes and Performance in a Direct Urea Fuel Cell, Industrial & Engineering Chemistry Research 60(41) (2021) 14856-14867.

[5] J. Yoon, J.M. Kim, Y.-h. Lin, G.M. Geise, B.S. Beckingham, D.-J. Kim, Impact of a Novel Nickel-Based Catalyst and Phenyl-Acrylate-Based Anion-Exchange Membrane in a Direct Urea Fuel Cell, Energy & Fuels 38(13) (2024) 12274-12281.

[6] S. Al-Amshawee, M.Y.B.M. Yunus, A.A.M. Azoddein, D.G. Hassell, I.H. Dakhil, H.A. Hasan, Electrodialysis desalination for water and wastewater: A review, Chemical Engineering Journal 380 (2020) 122231.

[7] R. Nagarale, G. Gohil, V.K. Shahi, Recent developments on ion-exchange membranes and electro-membrane processes, Advances in colloid and interface science 119(2-3) (2006) 97-130.

[8] A.Z. Weber, M.M. Mench, J.P. Meyers, P.N. Ross, J.T. Gostick, Q. Liu, Redox flow batteries: a review, Journal of applied electrochemistry 41 (2011) 1137-1164.

[9] X. Li, H. Zhang, Z. Mai, H. Zhang, I. Vankelecom, Ion exchange membranes for vanadium redox flow battery (VRB) applications, Energy & Environmental Science 4(4) (2011) 1147-1160.

[10] C. Espinoza, J.C. Díaz, D. Kitto, H.K. Kim, J. Kamcev, Bound water enhances the ion selectivity of highly charged polymer membranes, ACS Applied Materials & Interfaces 16(34) (2024) 45433-45446.

[11] J.M. Kim, B.S. Beckingham, Comonomer effects on co-permeation of methanol and acetate in cation exchange membranes, European Polymer Journal 147 (2021) 110307.

[12] J.M. Kim, Y.-h. Lin, S.M. Bannon, G.M. Geise, B.S. Beckingham, Improved Structural Stability of Charged Hydrogels under Organic CO2 Reduction Products: Effect of Acrylate and Methacrylate Backbone Linkages, The Journal of Physical Chemistry C 127(22) (2023) 10826-10832.

[13] J.M. Kim, B.M. Dobyns, R. Zhao, B.S. Beckingham, Multicomponent transport of methanol and acetate in a series of crosslinked PEGDA-AMPS cation exchange membranes, Journal of Membrane Science 614 (2020) 118486.

[14] B.M. Dobyns, J.M. Kim, B.S. Beckingham, Multicomponent transport of methanol and sodium acetate in poly (ethylene glycol) diacrylate membranes of varied fractional free volume, European Polymer Journal 134 (2020) 109809.

[15] J.M. Kim, B.S. Beckingham, Transport and co-transport of carboxylate ions and alcohols in cation exchange membranes, Journal of Polymer Science 59(21) (2021) 2545-2558.

[16] Y.-h. Lin, J.M. Kim, B.S. Beckingham, Salt Transport in Crosslinked Hydrogel Membranes Containing Zwitterionic Sulfobetaine Methacrylate and Hydrophobic Phenyl Acrylate, Polymers 15(6) (2023) 1387.

[17] M.A. Hickner, Ion-containing polymers: new energy & clean water, Materials Today 13(5) (2010) 34-41.

[18] F.G. Helfferich, Ion exchange, Courier Corporation1995.

[19] G.M. Geise, M.A. Hickner, B.E. Logan, Ionic resistance and permselectivity tradeoffs in anion exchange membranes, ACS applied materials & interfaces 5(20) (2013) 10294-10301.

[20] P. Długołęcki, K. Nymeijer, S. Metz, M. Wessling, Current status of ion exchange membranes for power generation from salinity gradients, Journal of Membrane Science 319(1-2) (2008) 214-222.

[21] D. Balasubramanian, B. Misra, Relative affinities of alkali metal ions to the ligands in ionophores, FEBS letters 41(1) (1974) 78-80.

[22] M.T.I. Mredha, S.K. Pathak, J. Cui, I. Jeon, Hydrogels with superior mechanical properties from the synergistic effect in hydrophobic–hydrophilic copolymers, Chemical Engineering Journal 362 (2019) 325-338.

[23] H. Wynberg, W. Nieuwpoort, H. Jonkman, Flexible aromatic rings, Tetrahedron Letters 14(46) (1973) 4623-4628.

[24] K. Leung, I.M. Nielsen, I. Kurtz, Ab initio molecular dynamics study of carbon dioxide and bicarbonate hydration and the nucleophilic attack of hydroxide on CO2, The journal of physical chemistry B 111(17) (2007) 4453-4459.

[25] A.M. Kiss, T.D. Myles, K.N. Grew, A.A. Peracchio, G.J. Nelson, W.K. Chiu, Carbonate and bicarbonate ion transport in alkaline anion exchange membranes, Journal of The Electrochemical Society 160(9) (2013) F994.

[26] G.M. Geise, D.R. Paul, B.D. Freeman, Fundamental water and salt transport properties of polymeric materials, Progress in Polymer Science 39(1) (2014) 1-42.

[27] M. Soltanieh, S. Sahebdelfar, Interaction effects in multicomponent separation by reverse osmosis, Journal of Membrane Science 183(1) (2001) 15-27.

[28] B.S. Beckingham, N.A. Lynd, D.J. Miller, Monitoring multicomponent transport using in situ ATR FTIR spectroscopy, Journal of Membrane Science 550 (2018) 348-356.

[29] H. Ju, A.C. Sagle, B.D. Freeman, J.I. Mardel, A.J. Hill, Characterization of sodium chloride and water transport in crosslinked poly (ethylene oxide) hydrogels, Journal of Membrane Science 358(1-2) (2010) 131-141.

[30] N. Yan, R. Sujanani, J. Kamcev, M. Galizia, E.-S. Jang, D.R. Paul, B.D. Freeman, Influence of fixed charge concentration and water uptake on ion sorption in AMPS/PEGDA membranes, Journal of Membrane Science 644 (2022) 120171.

[31] G.M. Geise, L.P. Falcon, B.D. Freeman, D.R. Paul, Sodium chloride sorption in sulfonated polymers for membrane applications, Journal of Membrane Science 423 (2012) 195-208.

[32] J. Kamcev, M. Galizia, F.M. Benedetti, E.-S. Jang, D.R. Paul, B.D. Freeman, G.S. Manning, Partitioning of mobile ions between ion exchange polymers and aqueous salt solutions: importance of counter-ion condensation, Physical Chemistry Chemical Physics 18(8) (2016) 6021-6031.

[33] J. Kamcev, D.R. Paul, B.D. Freeman, Effect of fixed charge group concentration on equilibrium ion sorption in ion exchange membranes, Journal of Materials Chemistry A 5(9) (2017) 4638-4650.

[34] Y. Ji, H. Luo, G.M. Geise, Specific co-ion sorption and diffusion properties influence membrane permselectivity, Journal of membrane science 563 (2018) 492-504.

[35] F. Zhu, S. Feng, Z. Wang, Z. Zuo, S. Zhu, W. Yu, Y.N. Ye, M. An, J. Qian, Z.L. Wu, Co-Ion Specific Effect Aided Phase Separation in Polyelectrolyte Hydrogels toward Extreme Strengthening and Toughening, Macromolecules 56(15) (2023) 5881-5890.

[36] B.M. Carter, B.M. Dobyns, B.S. Beckingham, D.J. Miller, Multicomponent transport of alcohols in an anion exchange membrane measured by in-situ ATR FTIR spectroscopy, Polymer 123 (2017) 144-152.

Chapter 11: Phenyl Acrylate-Based IEMs for Direct Urea Fuel Cells

---

Reproduced from: Kim, J. M., Wang, Y., Lin, Y., Yoon, J., Huang, T., Kim, D.-J., Auad, M. L., & Beckingham, B. S. (2021). Fabrication and characterization of cross-linked phenyl-acrylate-based ion exchange membranes and performance in a direct urea fuel cell. Industrial & Engineering Chemistry Research, 60(41), 14856–14867. https://doi.org/10.1021/acs.iecr.1c02798.

11.1. Introduction

Ion exchange membranes (IEMs) are hydrated, dense polymeric membranes with a charged functional group that have been applied in various applications, such as direct fuel cells (direct methanol fuel cells [1-4] and direct urea fuel cells (DUFCs) [5-7]) and CO2 reduction cells [8-12]. Major roles of IEMs in these devices are to provide ion-selective transport for device operation and to minimize the crossover of charge-neutral solutes (i.e., methanol (MeOH), ethanol (EtOH), and urea), which reduce performance. While many efforts have focused on enhancing the ion selective transport through higher ionic conductivity [13-15], investigations on minimizing neutral solute crossover are relatively lacking [16-18]. Common strategies for mitigating this type of solute crossover are (1) to engineer the surface of the membrane with functional groups or chemistry that inhibit transport [9] and (2) to incorporate solid additive materials (silica nanoparticles and carbon nanotubes [19, 20]) within the membrane to obstruct the transport of undesired molecules.

Recently, our group has been performing a series of investigations to identify potential pendant functional groups that suppress the transport of CO_2 reduction products, MeOH, EtOH, formate (OFm^-), and acetate (OAc^-), that dissolve in catholyte and whose transport through the IEM is undesirable [18]. For instance, we prepared a series of cross-linked copolymeric cation exchange membranes (CEMs) with a cross-linker, poly(ethylene glycol) diacrylate (PEGDA), a sulfonated ionomer, 2-acrylamido-2-methyl-1-propanesulfonic acid (AMPS [21-23]), and a comonomer, either acrylic acid, hydroxyethyl methacrylate, or poly(ethylene glycol) methacrylate (PEGMA) [18, 24-27]. While the diffusion of all solutes in these cross-linked copolymeric CEMs in one-component diffusion cell experiments exhibited conventional diffusive behavior (dependent on the free volume and the solute size [28-35]), we observed the diffusivities of OFm^- and OAc^- to be suppressed in codiffusion with either MeOH or EtOH in PEGDA-AMPS/PEGMA CEMs. To rationalize this behavior, we conjectured that flux coupling (between two solutes, alcohol and carboxylate, that assist the carboxylate diffusivity) is suppressed by the presence of the relatively long pendant PEG chains from PEGMA [18]. Although this series of investigations provided valuable insights into understanding the impact of various pendant groups on the transport and cotransport of solutes, the applicability of this strategic approach upon membrane modification remained in doubt as a cross-linked IEM must be mechanically stable (cross-linked IEMs with PEGDA are quite fragile).

Here, we introduce a class of cross-linked IEMs that are significantly enhanced in mechanical properties with relatively low water content [36]. Recently, Mredha et al. introduced a hydrogel with great mechanical properties (i.e., modulus and strength), where they prepared a series of copolymeric organogels with a cross-linker, N,N'-methylenebis(acrylamide) (MBAA), a

hydrophobic comonomer, phenyl acrylate (PA), and a hydrophilic comonomer, acrylamide (AAm) in an organic solvent, dimethyl sulfoxide (DMSO), and converted the organogels to hydrogels by a solvent exchange from DMSO to water [36]. Here, we take inspiration from this approach to improving mechanics but vary the chemistry to prepare IEMs. In lieu of AAm, we utilize an ionomer, either AMPS or methacroylcholine chloride (MACC, bearing a quaternary ammonium (QA^+)), and prepare cross-linked MBAA-PA/AMPS CEMs (briefly PA/A) and MBAA-PA/MACC (briefly PA/M). Further, we also replace PA with phenyl methacrylate (PMA/A and PMA/M) to understand the effect of the additional methyl group on the polymer backbone [37] on membrane properties. From these IEMs, we select an AEM with a low water volume fraction (PA/M prepared with 30 mol % of MBAA, briefly PA/M-30) to examine the applicability of these membranes in a fuel cell (i.e., DUFC). DUFC is an emerging type of direct fuel cell, which converts urea (from industrial wastewater and urine) to electrical power [38] with a relatively high energy density and a low operating temperature [39-41]. One of the challenges of these devices is a lack of IEMs (either CEM [42] or AEM [7]) that minimize crossover of urea to the cathode side of the cell (especially at higher concentrations) as this crossover can suppress the overall reaction (sweeping effect). To further examine the likelihood of urea crossover, we measure urea permeability of PA/M-30. Finally, we perform similar experiments on a commercial AEM (Fumasep FAA-3-50, briefly FAA) to validate our cross-linked IEMs as competitive with commercial IEMs for such devices.

11.2. Results and Discussion

The materials, membrane synthesis methods, and experimental procedures are detailed in Chapter 3. A total of 8 cross-linked CEM organogels were prepared by thermal copolymerization of prepolymerization mixtures, as shown in Figure 11.1 and Table 11.1. A series of crosslinked PA-AMPS films (PA/A) and cross-linked PMA-AMPS films (PMA/A) were prepared. Both PA/A and PMA/A contain 70 mol% of either PA or PMA (a hydrophobic comonomer) and 30 mol % of AMPS (a sulfonated comonomer). Each film contains from 5 to 30 mol % of MBAA (a cross-linker) and 0.1 wt % of AIBN (thermal initiator), where both mol % and wt % are the sum of a hydrophobic comonomer (either PA or PMA) and the sulfonated comonomer (AMPS). Each prepolymerization mixture was prepared with 50 wt % of DMSO (solvent) content. Moreover, a total of 7 cross-linked AEM organogels (PA-MACC (PA/M) and PMA-MACC (PMA/M)) were prepared by thermal copolymerization of prepolymerization mixtures, as shown in Figure 11.1 and Table 11.1. Both PA/M and PMA/M contain 70 mol % of either PA or PMA and 30 mol % of MACC (a quaternary ammonium (QA^+)-containing comonomer). PA/M films contain from 5 to 30 mol % of MBAA, and PMA/M films contain from 5 to 20 mol % of MBAA, where the mol % is the sum of a hydrophobic comonomer (either PA or PMA) and the QA^+-containing comonomer (MACC). We note that phase separation was observed in the prepolymerization mixture prepared analogously for PMA/M-30, such that a homogeneous cross-linked film could not be prepared. All films contain 0.1 wt % of AIBN, where the wt % is based on the sum of the two comonomers. Each prepolymerization mixture was prepared with 50 wt % of solvent content, where the solvent is composed of water (~8 wt %) from the MACC solution and the remaining DMSO (~92 wt %).

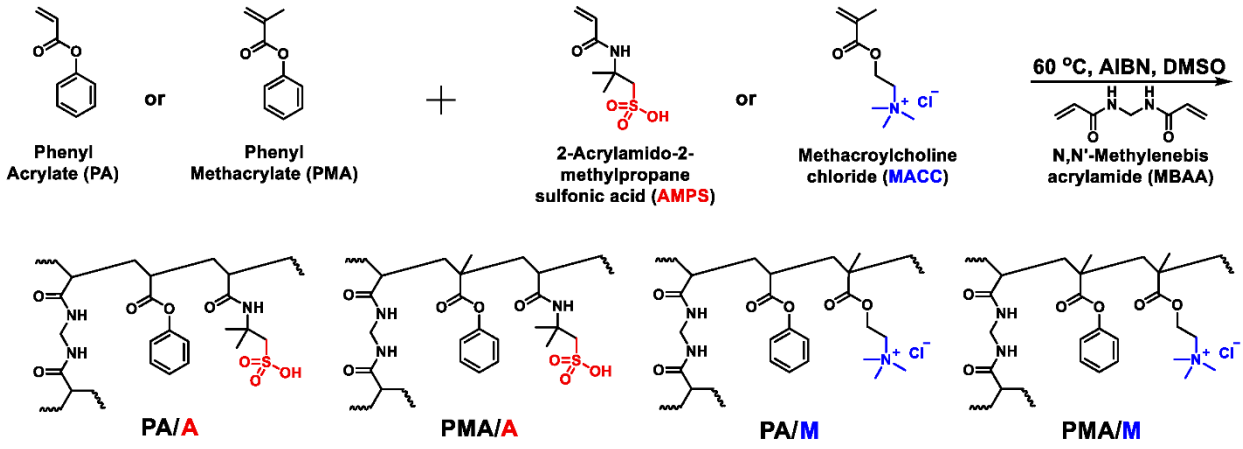

Figure 11.1. Scheme of prepared PA/A, PMA/A, PA/M, and PMA/M organogels.

Table 11.1. Membrane characteristics from pre-polymerization mixtures.

Cation Exchange Membranes

Name	MBAA[a] (mol%)	AMPS[b] (mol%)	PA or PMA (g)	AMPS (g)	AIBN (g)	MBAA (g)	DMSO (g)
PA/A-5	5	30	1.492	0.894	0.003	0.111	2.500
PA/A-10	10	30	1.428	0.856	0.003	0.212	2.500
PA/A-20	20	30	1.317	0.789	0.003	0.391	2.500
PA/A-30	30	30	1.221	0.732	0.002	0.545	2.500
PMA/A-5	5	30	1.541	0.844	0.003	0.112	2.500
PMA/A-10	10	30	1.475	0.808	0.003	0.214	2.500
PMA/A-20	20	30	1.359	0.744	0.003	0.394	2.500
PMA/A-30	30	30	1.260	0.690	0.002	0.547	2.500

Anion Exchange Membranes

Name	MBAA[a] (mol%)	MACC[c] (mol%)	PA or PMA (g)	MACC (g)	AIBN (g)	MBAA (g)	DMSO (g)	Water[d] (g)
PA/M-5	5	30	1.491	0.896	0.003	0.111	2.276	0.224
PA/M-10	10	30	1.427	0.858	0.003	0.212	2.286	0.214
PA/M-20	20	30	1.316	0.790	0.003	0.391	2.302	0.198
PA/M-30	30	30	1.220	0.733	0.002	0.544	2.317	0.183
PMA/M-5	5	30	1.540	0.845	0.003	0.112	2.289	0.211
PMA/M-10	10	30	1.474	0.809	0.003	0.214	2.298	0.202
PMA/M-20	20	30	1.358	0.745	0.003	0.394	2.314	0.186

[a]MBAA = mol of MBAA/(mol of PA or PMA + mol of AMPS or MACC) × 100 %
[b]AMPS = mol of AMPS/(mol of PA or PMA + mol of AMPS) × 100 %
[c]MACC = mol of MACC/(mol of PA or PMA + mol of MACC) × 100 %
[d]Water, from the MACC solution as 20 % of the solution is water.

11.2.1. Young's Modulus and Storage Modulus

Tensile experiments of all films were performed in triplicate, and an exemplary stress−strain curve from all films is shown in Figure 11.2 (where (A-E) are scaled differently). The Young's moduli are shown in Figure 11.3 and Table 11.2.

Generally, commercial films show a higher toughness (both strong and ductile) over cross-linked films. A contribution to the relatively higher ductility of these commercial films is that they are thermoplastic polymers (cross-link-free) such that they can freely elongate, whereas the cross-linked films undergo irreversible damage to the film upon breaking of the internal network under strain [43]. For cross-linked IEMs, films prepared with less MBAA (cross-linker) were more ductile than the films prepared with higher MBAA contents, as would be expected. In the case of PA/M-30, the toughness of the film was significantly decreased after ion exchange to the OH-form (PA/M-30-OH) (see Figure 11.2D).

The Young's modulus within each series (PA/A, PMA/A, PA/M, or PMA/M) of membranes increases with increasing MBAA (cross-linker) content (see Figure 11.3). This is due to the increase in the cross-link density (number of cross-links per volume; see Table 11.2), which reduces the ductility of each film [21, 24, 43]. Moreover, the Young's moduli of PMA-containing films (PMA/A and PMA/M) are higher than those of PA containing films (PA/A and PA/M), which can be attributed, in part, to an increase in polymer backbone rigidity from the additional methyl groups (Figure 11.1) [37]. Again, the Young's modulus of PA/M-30-OH was less than PA/M-30 (in Cl form) (see Figure 11.3 (B)). Similarly, the storage modulus of all films increased with increasing MBAA content (see Table 11.2). This is likely due to the increase in the cross-link

density (Flory's rubber elasticity relationship, eq 3.8) with increasing MBAA content (see Table 11.2).

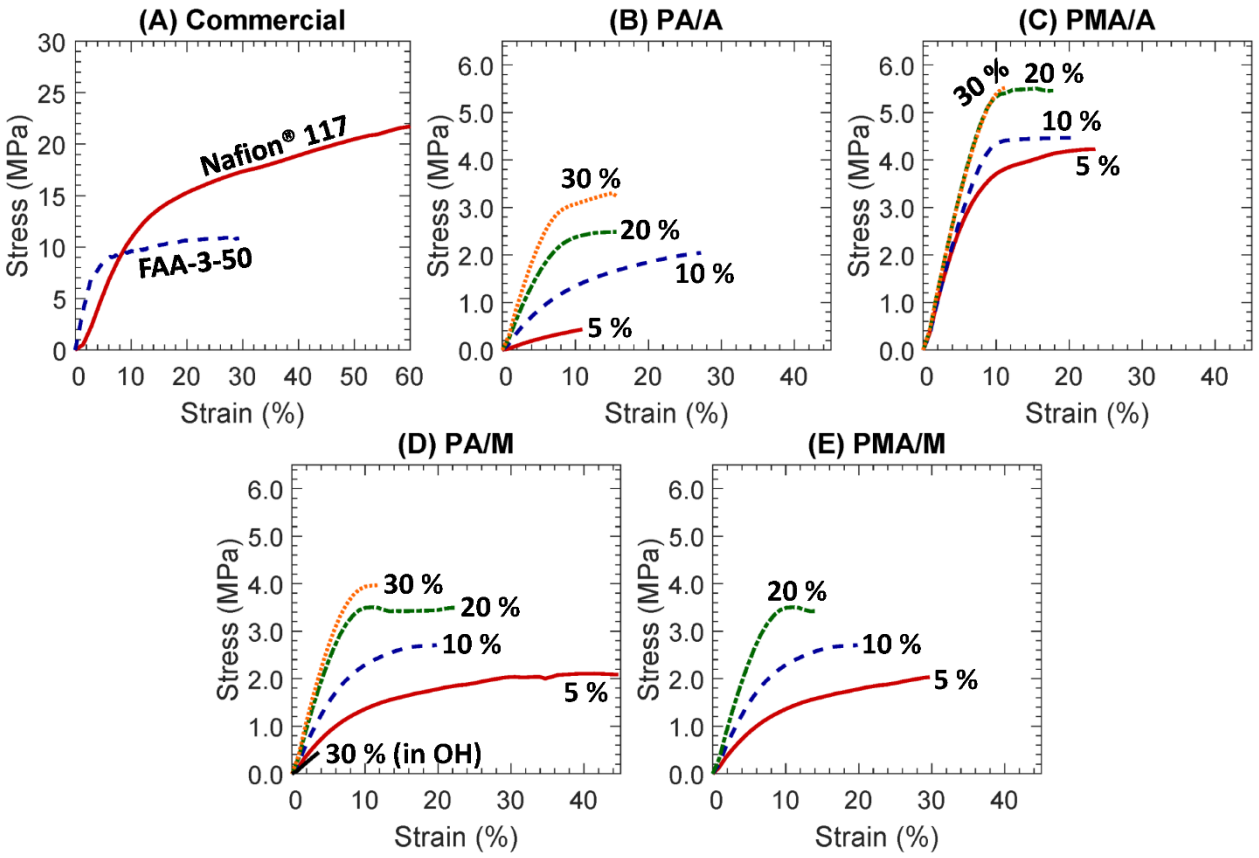

Figure 11.2. Stress-strain curves of (A) commercial CEM(Nafion 117, red solid) and AEM (FAA-Br, blue dashed), (B) PA/A, (C) PMA/A, (D) PA/M, and (E) PMA/M, where the MBAA (cross-linker) contents are specified as 5 (red solid), 10 (blue dashed), 20 (green dot-dashed), and 30 (orange dotted) mol %.

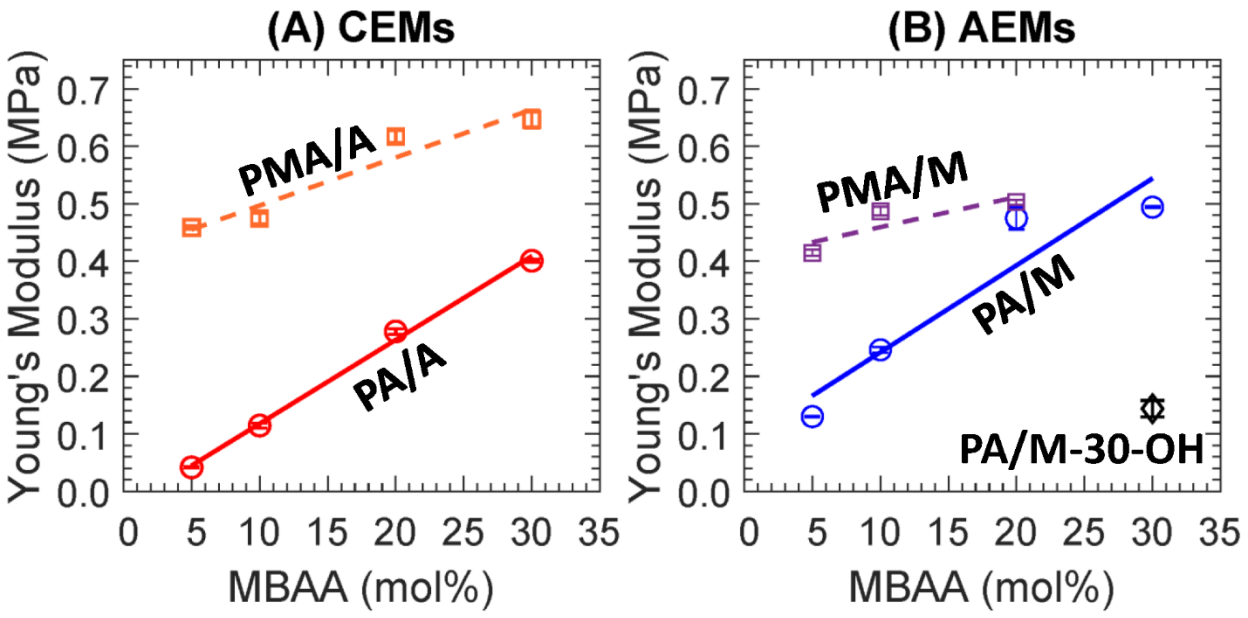

Figure 11.3. Young's modulus of (A) CEMs, PA/A (○, red, solid line) and PMA/A (□, orange, dashed line). Young's modulus of (B) AEMs, PA/M(○, blue, solid line) and PMA/M (□, purple, dashed line). Each data point is the average of three membranes with error bars corresponding to the standard deviation. Lines are present as a guide to the eye.

Table 11.2. Young's modulus, dry polymer density, water volume fraction, ionic conductivity, and ion exchange capacity of CEMs and AEMs**.**

Cation Exchange Membranes					
Name	**Young's Modulus (MPa)[a]**	**Storage Modulus E'(GPa)[b]**	**Estimate Crosslink Density, v_e (mmol/cm^3)**	**Density (g/mL)**	**Water Volume Fraction**
Nafion® 117	1.0 ± 0.0	-	-	1.80 ± 0.01	0.25 ± 0.00[c]
PA/A-5	0.04 ± 0.00	0.06 ± 0.04	8 ± 6	1.30 ± 0.05	0.66 ± 0.00
PA/A-10	0.11 ± 0.00	0.28 ± 0.07	38 ± 9	1.30 ± 0.03	0.49 ± 0.03
PA/A-20	0.28 ± 0.01	0.40 ± 0.13	54 ± 18	1.30 ± 0.00	0.45 ± 0.00
PA/A-30	0.40 ± 0.00	0.42 ± 0.04	57 ± 5	1.32 ± 0.03	0.46 ± 0.01
PMA/A-5	0.46 ± 0.00	0.29 ± 0.11	39 ± 15	1.25 ± 0.02	0.59 ± 0.03
PMA/A-10	0.47 ± 0.01	0.35 ± 0.07	47 ± 10	1.27 ± 0.00	0.52 ± 0.01
PMA/A-20	0.62 ± 0.01	0.43 ± 0.19	58 ± 25	1.26 ± 0.02	0.43 ± 0.00
PMA/A-30	0.65 ± 0.02	0.35 ± 0.09	47 ± 13	1.27 ± 0.01	0.41 ± 0.00
Anion Exchange Membranes					
Name	**Young's Modulus (MPa)[a]**	**Storage Modulus E'(GPa)[b]**	**Estimate Crosslink Density, v_e (mmol/cm^3)**	**Density (g/mL)**	**Water Volume Fraction**
FAA	2.0 ± 0.0	-	-	1.34 ± 0.02	0.12 ± 0.02
FAA-OH	-	-	-	1.27 ± 0.08	0.58 ± 0.06
PA/M-5	0.13 ± 0.00	0.63 ± 0.17	84 ± 23	1.23 ± 0.00	0.48 ± 0.01
PA/M-10	0.25 ± 0.00	0.46 ± 0.08	62 ± 11	1.22 ± 0.01	0.43 ± 0.01
PA/M-20	0.47 ± 0.02	1.02 ± 0.15	137 ± 20	1.23 ± 0.00	0.39 ± 0.01
PA/M-30[d]	0.49 ± 0.00	-	-	1.24 ± 0.00	0.40 ± 0.01
PA/M-30-OH[d]	0.14 ± 0.01	-	-	1.43 ± 0.02	0.67 ± 0.01
PMA/M-5	0.41 ± 0.01	0.25 ± 0.08	33 ± 10	1.20 ± 0.02	0.53 ± 0.04
PMA/M-10	0.49 ± 0.01	0.46 ± 0.11	62 ± 15	1.22 ± 0.01	0.50 ± 0.00
PMA/M-20	0.50 ± 0.00	0.40 ± 0.12	54 ± 16	1.23 ± 0.02	0.44 ± 0.00

[a] The thickness of the films was ~0.35 mm.
[b]The thickness of the films was ~1 mm.
[c] Literature [23].
[d] Could not prepare the film (PA/M-30) for 1 mm thickness due to phase separation.

11.2.2. Water Volume Fraction

The water volume fractions of all films were measured as shown in Figure 11.4 and Table 11.2. Generally, the water volume fraction of all films decreases with increasing MBAA content. For instance, the water volume fraction of the films prepared with 30 mol % of MBAA is less than those prepared with 5, 10, and 20 mol % of MBAA by 1.33, 1.14, and 1.01 times, on average, respectively. The water volume fractions of CEMs are slightly higher than those of AEMs. This is likely because the higher sulfonate anion hydration numbers (λ_i, H_2O/ion (i)) of the sulfonate anion (λ_{sulf}: 12−16 [44]) is higher than that of quaternary ammonium cations (λQA: 4 [45]). The difference in the water volume fraction of films prepared with PA and PMA was not apparent, where the water volume fractions of PA/A films were slightly higher than those of PMA/A films and those of PMA/M films were slightly higher than those of PA/M films (see Figure 11.4 (A and B)).

The water volume fraction of PA/M-30 in Cl form (λ_{cl}, = 1 [46]) was significantly higher than that of FAA in Br form (λ_{Br}, = 1 [46]). One possible cause is the difference in the polymer structure such that FAA is more tightly structured via its poly(phenylene oxide) backbone52 than PA/M-30 with a cross-linked poly-(phenyl acrylate-co-MACC) backbone. However, the water volume fraction of FAA is much closer to that of PA/M-30 after exchange of the counterion to the OH form (λOH = 3[46]) (see Figure 11.4 (C)). Two primary factors likely contribute to this behavior: the higher ion exchange capacity for FAA (IEC, 2.02 meq/g) compared to PA/M-30 (1.41 meq/g) and the higher hydration number for OH (λOH = 3 [46]) compared to the Br^- and Cl^- anions.

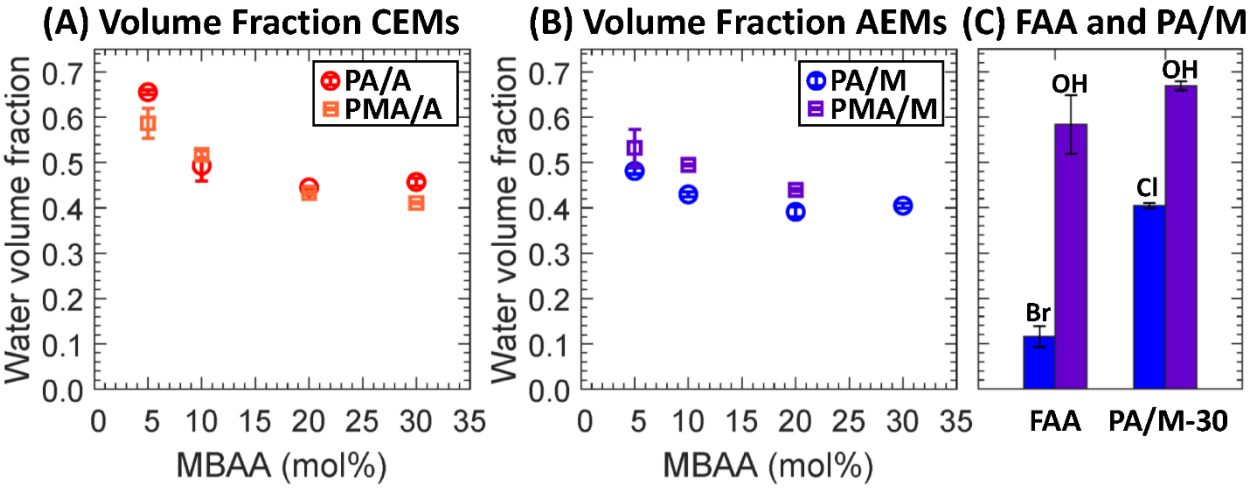

Figure 11.4. Water volume fractions of (A) CEMs, PA/A (○, red) and PMA/A (□, orange). Water volume fractions of AEMs, (B) PA/M (○, blue) and PMA/M (□, purple) and (C) FAA-Br, FAA-OH, PA/M-30-Cl, and PA/M-30-OH. Each data point is the average of three membranes with error bars corresponding to the standard deviation.

11.2.3. IEC and Ionic Conductivity of Membranes

The IEC of CEMs (PA/A and PMA/A) and AEMs (PA/M and PMA/M) was measured yielding the results shown in Table 11.3 and Figure 11.5. IECs of each series of films decrease with increasing MBAA content, which is likely due to the decrease in the ionomer content. The measured IECs of all films were closely matched with the theoretical IECs.

The ionic conductivities of all films were measured at 25 °C as shown in Table 11.3 and Figure 11.6, where Figure 11.6A-C is scaled differently. Generally, the ionic conductivities of the AEMs were lower than the CEMs. Here, the difference in molar conductivities of the counterion play a role, where the molar conductivity of H^+ (for PA/A and PMA/A) is 350 × 10^{-4} m^2·S/mol and that of Cl^- (for PA/M and PMA/M) is 76 × $10^{-4}$$m^2$·S/mol [47]. We observed the ionic conductivities of PA-containing CEMs (PA/A) to be higher than those of PMA-containing CEMs

(PMA/A), whereas ionic conductivities of PA-containing AEMs (PA/M) are less than those of PMA-containing AEMs (PMA/M) (see Figure 11.6 (A, B)). This is likely related to the measured IEC (dotted lines in Figure 11.5), where the IECs of PA/A films are higher than those of PMA/A films, when those of PA/M films are equal to or less than those of PMA/M films.

The ionic conductivities of FAA and PA/M-30 are significantly increased after the counterion conversion to OH form (see Figure 11.6 (C)). This is due to the molar conductivity of OH^- (198×10^{-4} $m^2 \cdot S/mol$) being significantly higher than those of Br^- (78×10^{-4} $m^2 \cdot S/mol$) and Cl^-[47]. Another contribution is the increase in water volume fraction as the ionic conductivity of IEMs often increases with increasing water volume fraction (upper bound relationship [48]).

Table 11.3. Ionic Conductivity and Ion Exchange Capacity of CEMs and AEMs.

Cation Exchange Membranes			
Name	**Conductivity (σ, mS/cm)**	**Theoretical IEC (meq/g dry polymer)[a]**	**Measured IEC (meq/g dry polymer)**
Nafion® 117	78 ± 1[b]	≥0.90[c]	-
PA/A-5	91.0 ± 0.0	1.73	1.48
PA/A-10	88.1 ± 0.0	1.65	1.42
PA/A-20	65.2 ± 0.0	1.52	1.35
PA/A-30	56.4 ± 0.1	1.41	1.19
PMA/A-5	61.5 ± 0.1	1.63	1.20
PMA/A-10	53.9 ± 0.5	1.56	1.21
PMA/A-20	35.7 ± 0.2	1.44	1.08
PMA/A-30	33.5 ± 0.0	1.33	0.96
Anion Exchange Membranes			
Name	**Conductivity (σ, mS/cm)**	**Theoretical IEC (meq/g dry polymer)[a]**	**Measured IEC (meq/g dry polymer)**
FAA	2.9 ± 0.0	2.02[c]	-
FAA-OH	16.2 ± 0.1	-	-
PA/M-5	15.6 ± 0.3	1.72	1.78
PA/M-10	14.3 ± 0.0	1.65	1.80
PA/M-20	9.1 ± 0.0	1.52	1.48
PA/M-30[d]	6.0 ± 0.0	1.41	1.41
PA/M-30-OH[d]	55.0 ± 0.1	-	-
PMA/M-5	19.6 ± 1.2	1.63	1.91
PMA/M-10	16.2 ± 0.2	1.56	1.56
PMA/M-20	12.7 ± 0.5	1.44	1.44

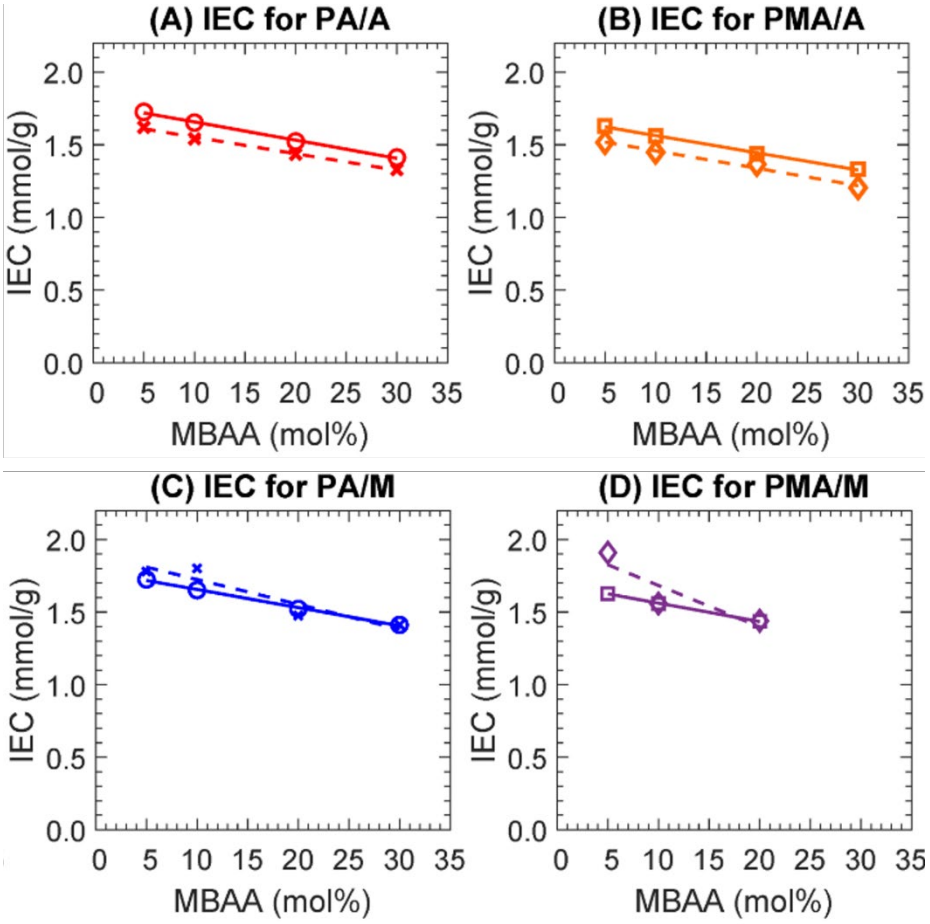

Figure 11.5. Theoretical IECs (solid lines) of (A) PA/A (red, ○) and (B) PMA/A (orange, □) and (C) PA/M (○, blue) and (D) PMA/M (□, purple). Measured IECs (dashed lines) of (A) PA/A (red, ×), (B) PMA/A (orange, ◊), (C) PA/M (×, blue), and (D) PMA/M (◊, purple). Lines are present as a guide to the eye.

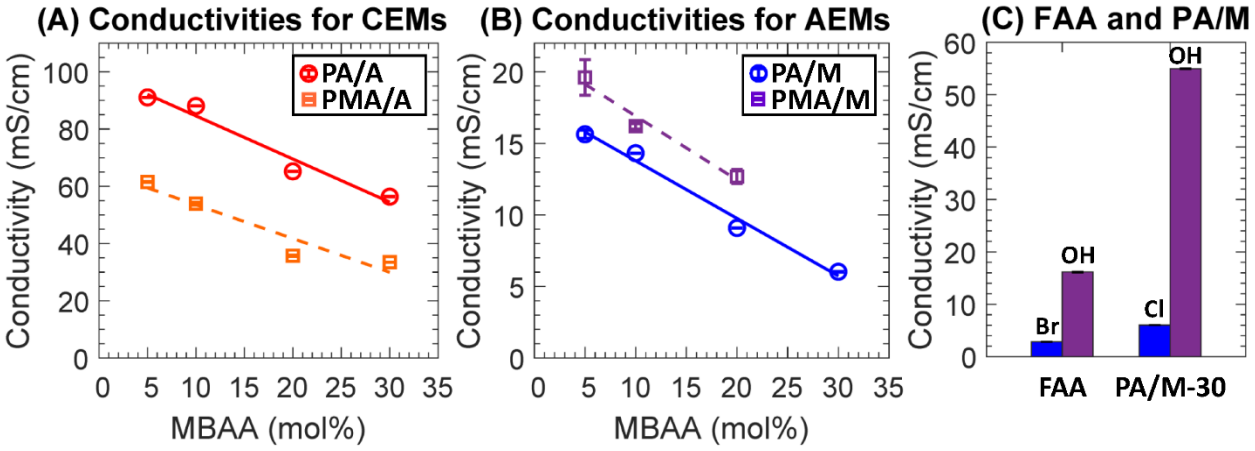

Figure 11.6. Ionic conductivities of (A) CEMs, PA/A (○, red, solid line) and PMA/A (□, orange, dashed line), and (B) AEMs, PA/M (○, blue, solid line) and PMA/M (□, purple, dashed line). Lines are present as a guide to the eye. (C) Ionic conductivities of FAA in Br^- form (blue) and OH^- form (purple) and PA/M-30 in Cl^- form (blue) and OH^- form (purple). Each data point is the average of three membranes with error bars corresponding to the standard deviation.

11.2.4. Direct Urea Fuel Cell

Two membrane electrode assemblies (MEAs), prepared with FAA-OH and PA/M-30-OH, were used in analogous fuel feeds of 1 M KOH containing 0.33Murea and humidified air (relative humidity: 100%) as the electron− and donor−acceptors [7]. The anode and cathode reactions in the fuel cell are as follows [5]:

$$(\text{Anode}): CO(NH_2)_2 + 6OH^- \rightarrow CO_2 + 5H_2O + N_2 + 6e^- \quad (R1)$$

$$(\text{Cathode}): 3/2O_2 + 3H_2O + 6e^- + 6OH^- \quad (R2)$$

The $Ni(OH)_2$ catalysts on the anode will adsorb the urea molecules, followed by urea oxidation under alkaline media. As a result of the urea oxidation reaction, six electrons flow to the cathode through the external circuit, forming a hydroxide ion (OH^-) with the humidification at the cathode (see Figure 11.7).

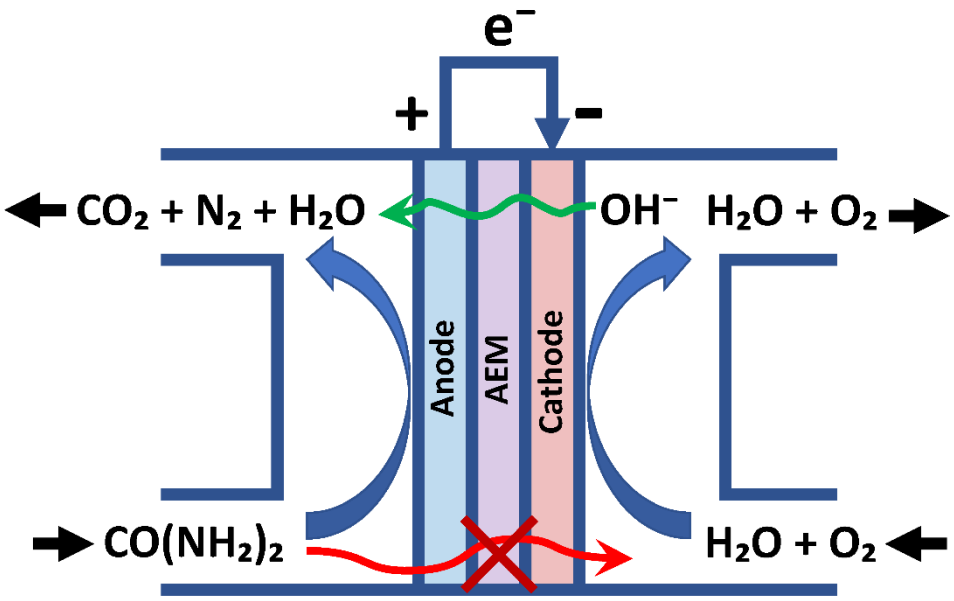

Figure 11.7. Schematic diagram of a direct urea fuel cell.

The relative DUFC performance of both MEAs was investigated in a DUFC utilizing a $Ni(OH)_2$/C anode and Ag/C cathode at 20 °C, as shown in Figure 11.8 A, B. After the activation process, the initial difference of electrical potential between the two electrodes was read as the open-circuit voltage (OCV). The power output, P, of the fuel cell is also determined through the product of voltage, V, and current, I (P = V/I). The OCV and power densities were evaluated, reaching 0.89 V and 2.16 mW/cm^2 at FAA-OH and 0.89 V and 2.19 mW/cm^2 at PA/ M-30-OH, respectively (see Table 11.4 and Figure 11.8). The two prominent roles of the membrane in a DUFC are (1) restricting the urea flow from the anode to cathode to improve urea oxidation efficiency and (2) transferring OH^- from the cathode to the anode in alkaline media. Critically, the obtained OCV and power density using the PA/M-30-OH membrane were comparable to those obtained for the commercially available FAA-OH membrane.

As the DUFC efficiency improves at higher working temperatures due to diminished polarization resistances, analogous tests were performed in a DUFC system at moderate elevated temperature (50 °C) under the same feed conditions, as shown in Figure 11.8 C, D. At this elevated temperature, FAA-OH exhibits an OCV of 0.97 V and maximum power density of 2.53 mW/cm^2, and PA/M-30-OH demonstrated an OCV of 0.99 V and a maximum power density of 3.40 mW/cm2 (see Table 11.4). These differences in operation at elevated temperature are presumably linked with the crossover of urea ($CO(NH_2)_2$) and OH^- from the anode to the cathode, which diminishes the anodic reaction and interferes with the cathodic reaction (eq 3.6). In addition, AEMs undergo the loss of ion conductivity as the OH^- ion flow is hindered by the direct contact of anode and urea molecules in the urea-based environment [49]. More details on the urea crossover will be discussed in the next section.

Table 11.4. Maximum Power Density and Voltage at the Maximum Power Density.

Name	Temperature (°C)	Maximum power density (mW/cm^2)	Voltage at the maximum power density (V)
FAA-OH	20	2.16	0.327
	50	2.53	0.301
PA/M-30-OH	20	2.19	0.449
	50	3.40	0.404

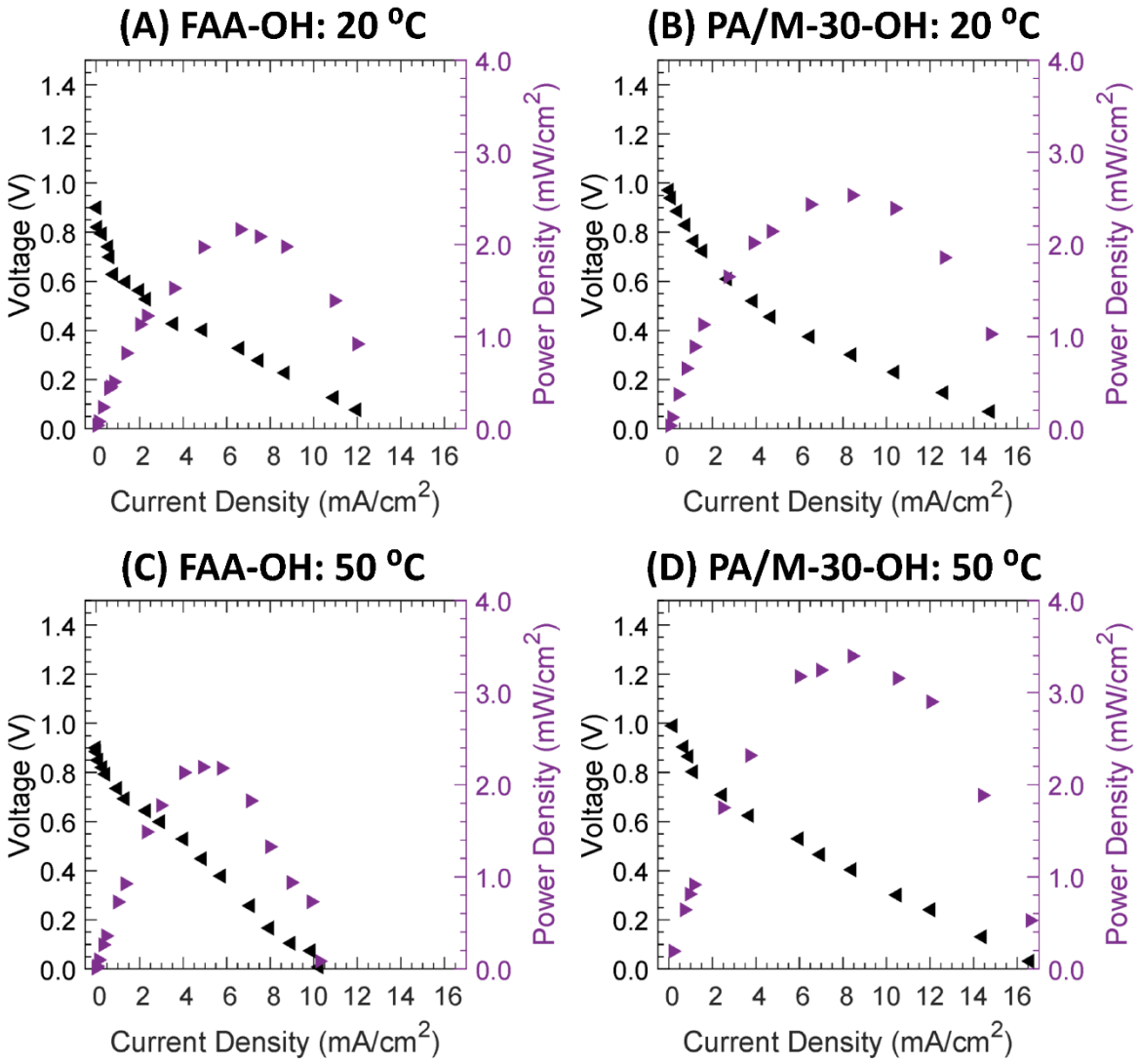

Figure 11.8. Power density and OCV, in initial voltage, of (A, C) FAA-OH and (B, D) PA/M-30-OH at (A, B) 20 and (C, D) 50 °C.

11.2.5. Urea Permeability

The diffusive permeabilities of FAA-OH and PA/M-30-OH to urea at 25 and 55 °C at 1, 2, and 3Mwere measured via diffusion cell experiments (see Figure 11.9).

Generally, the permeabilities of both FAA-OH and PA/M-30-OH to urea measured at 55 °C were higher than those measured at 25 °C by a factor of 2, on average. This is due to the increase in the diffusivity (Stokes−Einstein [50]) with temperature [51]. While PA/M-30-OH permeabilities to urea were essentially consistent under different concentrations (1, 2, and 3 M, with a slight decrease observed from 1 to 2 M at 55 °C), FAA-OH permeabilities were increased with increasing urea concentrations. This is presumably because the solubility (dependent on the affinity between the solute and polymer) of the FAA-OH to urea is a function of concentration. As a dense membrane, the permeabilities of FAA-OH can be explained by the solution-diffusion relationship (permeability = solubility × diffusivity [35, 52]). Since the solute diffusivity is dependent on the free volume, we calculated the ratios between the solvated film (after 2 days in 0.33, 1, 2, and 3 M urea) and hydrated film to understand the volume changes (as the change in volume can be a proxy for the change in free volume) (see Table 11.5 for values). We observed negligible changes in film volumes under all concentrations, which indicates the change in permeability is presumably due to the changes in sorption. Further investigation on FAA-OH (such as sorption−desorption63 and relative permittivity [53-55]) can be considered for a better understanding of this behavior. Based on the higher permeability to urea, a higher urea crossover is expected during DUFC operation with FAA-OH than with PA/M-30-OH, which likely contributes to the lower FAA-OH power densities. Nevertheless, more investigations on the cross-

linked IEMs introduced here and their chemically similar analogues are underway (compositional optimization, other fuel tests, and further characterizations) to validate and integrate the broad applicability of this class of cross-linked IEMs.

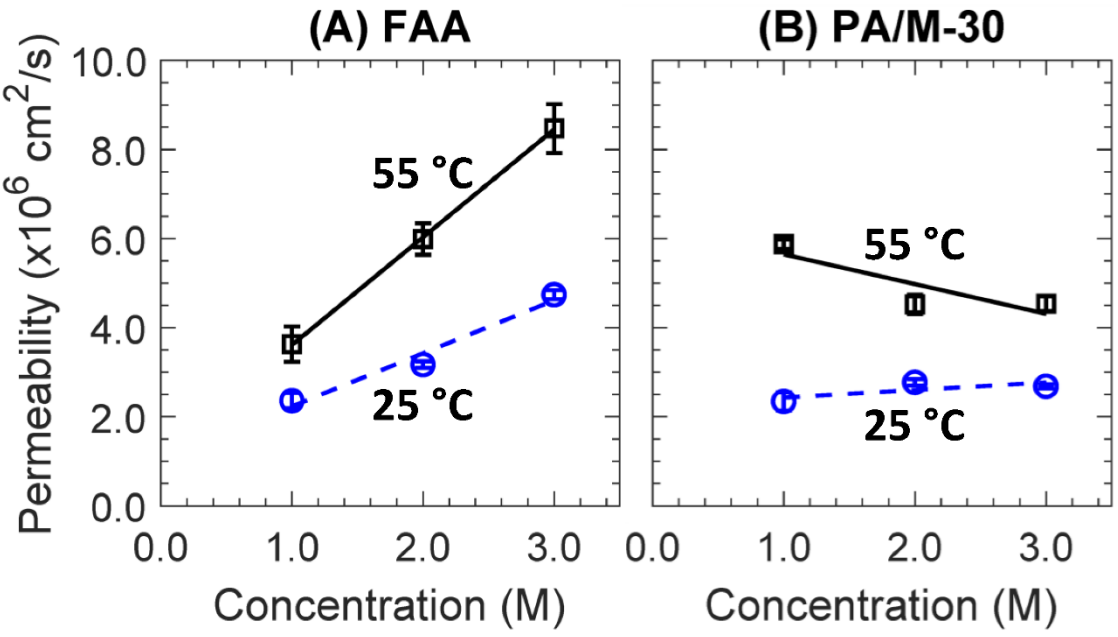

Figure 11.9. Urea permeabilities of (A) FAA-OH and (B) PA/M-30-OH at 25 °C (dashed, blue,○) and 55 °C (solid line, black, □) at 1, 2, and 3 M urea. Lines are present as a guide to the eye.

Table 11.5. The volumetric ratio between solvated films (Solutions: 0.33, 1, 2, and 3 M Urea) and hydrated films (VS/VH) was measured via the photograph-caliper method at 25 °C, where the surface area of each film was measured from a digital photograph coupled with the ImageJ software and the film thickness was measured with a digital caliper by taking the average of 5 random points.

	$V_{0.33M}/V_H$	V_{1M}/V_H	V_{2M}/V_H	V_{3M}/V_H
FAA-OH	0.996 ± 0.007	1.010 ± 0.007	1.000 ± 0.000	1.014 ± 0.031
PA/M-30-OH	1.000 ± 0.006	0.995 ± 0.004	0.996 ± 0.002	1.010 ± 0.011

11.3. Conclusions

A new class of cross-linked CEMs (PA/A and PMA/A) and AEMs (PA/M and PMA/M) were prepared and characterized. As the cross-linker (MBAA) content increases, Young's modulus increases, and water volume fraction decreases, both desirable improvements. An AEM composition with a low water volume fraction (PA/M-30) was selected to validate the applicability of the film in a direct fuel cell (i.e., DUFC), and the performance was compared with a commercial anion exchange membrane (FAA-3-50). The power density from the DUFC prepared with PA/M-30-OH was slightly higher than that with Fumasep FAA- 3-50-OH. This is likely due to a higher ionic conductivity (55 > 16 mS/cm) and presumably less urea crossover. This new class of cross-linked IEM can be a promising candidate for various energy devices upon target-specific compositional optimization.

11.4. References

[1] M. Galizia, D.R. Paul, B.D. Freeman, Liquid methanol sorption, diffusion and permeation in charged and uncharged polymers, Polymer 102 (2016) 281-291.

[2] A. Heinzel, V. Barragan, A review of the state-of-the-art of the methanol crossover in direct methanol fuel cells, Journal of Power sources 84(1) (1999) 70-74.

[3] K. Matsuoka, Y. Iriyama, T. Abe, M. Matsuoka, Z. Ogumi, Alkaline direct alcohol fuel cells using an anion exchange membrane, Journal of Power Sources 150 (2005) 27-31.

[4] D.T. Hallinan, Y.A. Elabd, Diffusion and sorption of methanol and water in nafion using time-resolved Fourier transform infrared− attenuated total reflectance spectroscopy, The Journal of Physical Chemistry B 111(46) (2007) 13221-13230.

[5] E.T. Sayed, T. Eisa, H.O. Mohamed, M.A. Abdelkareem, A. Allagui, H. Alawadhi, K.-J. Chae, Direct urea fuel cells: Challenges and opportunities, Journal of Power Sources 417 (2019) 159-175.

[6] J. Yoon, Y.S. Yoon, D.-J. Kim, Silver-nanoparticle-decorated NiOOH nanorods for electrocatalytic urea sensing, ACS Applied Nano Materials 3(8) (2020) 7651-7658.

[7] J. Yoon, D. Lee, Y.N. Lee, Y.S. Yoon, D.-J. Kim, Solid solution palladium-nickel bimetallic anode catalysts by co-sputtering for direct urea fuel cells (DUFC), Journal of Power Sources 431 (2019) 259-264.

[8] M.R. Singh, E.L. Clark, A.T. Bell, Effects of electrolyte, catalyst, and membrane composition and operating conditions on the performance of solar-driven electrochemical reduction of carbon dioxide, Physical Chemistry Chemical Physics 17(29) (2015) 18924-18936.

[9] D.A. Salvatore, C.M. Gabardo, A. Reyes, C.P. O'Brien, S. Holdcroft, P. Pintauro, B. Bahar, M. Hickner, C. Bae, D. Sinton, Designing anion exchange membranes for CO2 electrolysers, Nature Energy 6(4) (2021) 339-348.

[10] D.M. Weekes, D.A. Salvatore, A. Reyes, A. Huang, C.P. Berlinguette, Electrolytic CO2 reduction in a flow cell, Accounts of chemical research 51(4) (2018) 910-918.

[11] D.J. Miller, F.A. Houle, Membranes for Solar Fuels Devices, (2018).

[12] B.S. Beckingham, N.A. Lynd, D.J. Miller, Monitoring multicomponent transport using in situ ATR FTIR spectroscopy, Journal of Membrane Science 550 (2018) 348-356.

[13] Z. Yin, H. Peng, X. Wei, H. Zhou, J. Gong, M. Huai, L. Xiao, G. Wang, J. Lu, L. Zhuang, An alkaline polymer electrolyte CO 2 electrolyzer operated with pure water, Energy & Environmental Science 12(8) (2019) 2455-2462.

[14] Z. Liu, H. Yang, R. Kutz, R.I. Masel, CO2 electrolysis to CO and O2 at high selectivity, stability and efficiency using sustainion membranes, Journal of the Electrochemical Society 165(15) (2018) J3371.

[15] L. Li, J. Zhang, T. Jiang, X. Sun, Y. Li, X. Li, S. Yang, S. Lu, H. Wei, Y. Ding, High ion conductivity and diffusivity in the anion exchange membrane enabled by tethering with multication strings on the poly (biphenyl alkylene) backbone, ACS Applied Energy Materials 3(7) (2020) 6268-6279.

[16] M. Krödel, B.M. Carter, D. Rall, J. Lohaus, M. Wessling, D.J. Miller, Rational design of ion exchange membrane material properties limits the crossover of CO2 reduction products in artificial photosynthesis devices, ACS applied materials & interfaces 12(10) (2020) 12030-12042.

[17] P. Leung, Q. Xu, T. Zhao, L. Zeng, C. Zhang, Preparation of silica nanocomposite anion-exchange membranes with low vanadium-ion crossover for vanadium redox flow batteries, Electrochimica Acta 105 (2013) 584-592.

[18] J.M. Kim, B.S. Beckingham, Comonomer effects on co-permeation of methanol and acetate in cation exchange membranes, European Polymer Journal 147 (2021) 110307.

[19] L. Cui, Q. Geng, C. Gong, H. Liu, G. Zheng, G. Wang, Q. Liu, S. Wen, Novel sulfonated poly (ether ether ketone)/silica coated carbon nanotubes high-performance composite membranes for direct methanol fuel cell, Polymers for Advanced Technologies 26(5) (2015) 457-464.

[20] Y.-H. Su, Y.-L. Liu, Y.-M. Sun, J.-Y. Lai, D.-M. Wang, Y. Gao, B. Liu, M.D. Guiver, Proton exchange membranes modified with sulfonated silica nanoparticles for direct methanol fuel cells, Journal of Membrane Science 296(1-2) (2007) 21-28.

[21] N. Yan, D.R. Paul, B.D. Freeman, Water and ion sorption in a series of cross-linked AMPS/PEGDA hydrogel membranes, Polymer 146 (2018) 196-208.

[22] Y. Yu, N. Yan, B.D. Freeman, C.-C. Chen, Mobile ion partitioning in ion exchange membranes immersed in saline solutions, Journal of Membrane Science 620 (2021) 118760.

[23] J.M. Kim, B.M. Dobyns, R. Zhao, B.S. Beckingham, Multicomponent transport of methanol and acetate in a series of crosslinked PEGDA-AMPS cation exchange membranes, Journal of Membrane Science 614 (2020) 118486.

[24] A.C. Sagle, H. Ju, B.D. Freeman, M.M. Sharma, PEG-based hydrogel membrane coatings, Polymer 50(3) (2009) 756-766.

[25] H. Ju, A.C. Sagle, B.D. Freeman, J.I. Mardel, A.J. Hill, Characterization of sodium chloride and water transport in crosslinked poly (ethylene oxide) hydrogels, Journal of Membrane Science 358(1-2) (2010) 131-141.

[26] S. Kalakkunnath, D.S. Kalika, H. Lin, B.D. Freeman, Segmental relaxation characteristics of cross-linked poly (ethylene oxide) copolymer networks, Macromolecules 38(23) (2005) 9679-9687.

[27] H. Lin, E. Van Wagner, J.S. Swinnea, B.D. Freeman, S.J. Pas, A.J. Hill, S. Kalakkunnath, D.S. Kalika, Transport and structural characteristics of crosslinked poly (ethylene oxide) rubbers, Journal of Membrane Science 276(1-2) (2006) 145-161.

[28] H. Yasuda, C. Lamaze, L. Ikenberry, Permeability of solutes through hydrated polymer membranes. Part I. Diffusion of sodium chloride, Die Makromolekulare Chemie: Macromolecular Chemistry and Physics 118(1) (1968) 19-35.

[29] J. Mackie, P. Meares, The diffusion of electrolytes in a cation-exchange resin membrane I. Theoretical, Proceedings of the Royal Society of London. Series A. Mathematical and Physical Sciences 232(1191) (1955) 498-509.

[30] E.-S. Jang, J. Kamcev, K. Kobayashi, N. Yan, R. Sujanani, T.J. Dilenschneider, H.B. Park, D.R. Paul, B.D. Freeman, Influence of water content on alkali metal chloride transport in cross-linked Poly (ethylene glycol) diacrylate. 2. Ion diffusion, Polymer 192 (2020) 122316.

[31] J. Kamcev, D.R. Paul, G.S. Manning, B.D. Freeman, Ion diffusion coefficients in ion exchange membranes: significance of counterion condensation, Macromolecules 51(15) (2018) 5519-5529.

[32] B.M. Carter, B.M. Dobyns, B.S. Beckingham, D.J. Miller, Multicomponent transport of alcohols in an anion exchange membrane measured by in-situ ATR FTIR spectroscopy, Polymer 123 (2017) 144-152.

[33] B.M. Dobyns, J.M. Kim, J. Li, Z. Jiang, B.S. Beckingham, Multicomponent transport of alcohols in Nafion 117 measured by in situ ATR FTIR spectroscopy, Polymer 209 (2020) 123046.

[34] B.M. Dobyns, J.M. Kim, B.S. Beckingham, Multicomponent transport of methanol and sodium acetate in poly (ethylene glycol) diacrylate membranes of varied fractional free volume, European Polymer Journal 134 (2020) 109809.

[35] J.G. Wijmans, R.W. Baker, The solution-diffusion model: a review, Journal of membrane science 107(1-2) (1995) 1-21.

[36] M.T.I. Mredha, S.K. Pathak, J. Cui, I. Jeon, Hydrogels with superior mechanical properties from the synergistic effect in hydrophobic–hydrophilic copolymers, Chemical Engineering Journal 362 (2019) 325-338.

[37] K. Chang, T. Xue, G.M. Geise, Increasing salt size selectivity in low water content polymers via polymer backbone dynamics, Journal of Membrane Science 552 (2018) 43-50.

[38] N. Senthilkumar, G. Gnana Kumar, A. Manthiram, 3D hierarchical core–shell nanostructured arrays on carbon fibers as catalysts for direct urea fuel cells, Advanced Energy Materials 8(6) (2018) 1702207.

[39] N. Kakati, G. Li, P.-Y.A. Chuang, Insights into the Ni/C-based thin-film catalyst layer design for urea oxidation reaction in a three-electrode system, ACS Applied Energy Materials 4(4) (2021) 4224-4233.

[40] A. Modak, R. Mohan, K. Rajavelu, R. Cahan, T. Bendikov, A. Schechter, Metal–organic polymer-derived interconnected Fe–Ni alloy by carbon nanotubes as an advanced design of urea oxidation catalysts, ACS Applied Materials & Interfaces 13(7) (2021) 8461-8473.

[41] D. Yang, L. Yang, L. Zhong, X. Yu, L. Feng, Urea electro-oxidation efficiently catalyzed by nickel-molybdenum oxide nanorods, Electrochimica Acta 295 (2019) 524-531.

[42] F. Guo, K. Cheng, K. Ye, G. Wang, D. Cao, Preparation of nickel-cobalt nanowire arrays anode electro-catalyst and its application in direct urea/hydrogen peroxide fuel cell, Electrochimica Acta 199 (2016) 290-296.

[43] J. Ferry, Viscoelastic Properties of Polymers, Wiley, 1980.

[44] A. Kusoglu, A.Z. Weber, New insights into perfluorinated sulfonic-acid ionomers, Chemical reviews 117(3) (2017) 987-1104.

[45] D.R. Dekel, Review of cell performance in anion exchange membrane fuel cells, Journal of Power Sources 375 (2018) 158-169.

[46] J.N. Israelachvili, Intermolecular and surface forces, Academic press2011.

[47] P. Vanýsek, Ionic conductivity and diffusion at infinite dilution, CRC handbook of chemistry and physics 94 (1993).

[48] L.M. Robeson, H.H. Hwu, J.E. McGrath, Upper bound relationship for proton exchange membranes: Empirical relationship and relevance of phase separated blends, Journal of Membrane Science 302(1-2) (2007) 70-77.

[49] W. Xu, H. Zhang, G. Li, Z. Wu, A urine/Cr (VI) fuel cell—Electrical power from processing heavy metal and human urine, Journal of Electroanalytical Chemistry 764 (2016) 38-44.

[50] J.T. Edward, Molecular volumes and the Stokes-Einstein equation, Journal of chemical education 47(4) (1970) 261.

[51] S.P. Cadogan, G.C. Maitland, J.M. Trusler, Diffusion coefficients of CO2 and N2 in water at temperatures between 298.15 K and 423.15 K at pressures up to 45 MPa, Journal of Chemical & Engineering Data 59(2) (2014) 519-525.

[52] R.W. Baker, Membrane technology and applications, John Wiley & Sons2023.

[53] K. Chang, G.M. Geise, Dielectric permittivity properties of hydrated polymers: measurement and connection to ion transport properties, Industrial & Engineering Chemistry Research 59(12) (2019) 5205-5217.

[54] K. Chang, H. Luo, G.M. Geise, Influence of salt concentration on hydrated polymer relative permittivity and state of water properties, Macromolecules 54(2) (2021) 637-646.

[55] K. Chang, H. Luo, G.M. Geise, Water content, relative permittivity, and ion sorption properties of polymers for membrane desalination, Journal of membrane science 574 (2019) 24-32.

Chapter 12: Conclusion and Recommendations

12.1. Conclusions

Ion exchange membranes are essential components in a variety of membrane-based technologies. This dissertation focuses on enhancing the understanding of ion transport mechanisms by synthesizing membranes and conducting concentration-gradient-driven transport experiments. The presented research encompasses a range of membranes, including charge-neutral membranes, IEMs, and zwitterionic membranes, to explore ion transport behavior under single and binary solute conditions. In Chapter 4, a notable finding is the observation of charge screening effects during co-transport with alcohol. A charge screening effect is hypothesized, assuming that the diffusion of carboxylate salts is more influenced by the carboxylate anion than by the cation. The diffusivities of carboxylate salts in AEMs decrease when co-diffusing with ethanol. This reduction is attributed to the screening of electrostatic attractions by the co-diffusing EtOH, demonstrating a charge screening phenomenon. The permeability order is determined by the size differences between two carboxylate anions and two cations. Additionally, AEMs in the HCO_3^- form exhibit higher water uptake compared to those in the Cl^- form due to differences in hydration numbers. However, AEMs in the HCO_3^- form demonstrate lower ionic conductivity than their Cl^- counterparts.

In Chapter 5, P-E and P-G films, the water volume fractions remain essentially unchanged because the reduction in crosslinking is counterbalanced by the incorporation of hydrophobic phenyl-containing pendant groups. In ternary films (P-S/E and P-S/G), the water volume fraction increases with higher SPMAK content due to the rise in hydrophilic sulfonate group content and the reduction in hydrophobic phenyl group content. MeOH permeability increases with higher SPMAK content (due to increased water volume fraction) and slightly decreases with more phenyl-containing comonomers. During co-permeation with KOAc, MeOH permeabilities slightly decrease. For binary films (P-S, P-E, P-G), KOAc permeability decreases with increasing comonomer content (both sulfonate and phenyl). In P-S, this reduction is attributed to electrostatic repulsion between mobile OAc^- ions and bound sulfonate anions, which intensifies with higher IEC. In P-E and P-G, the hydrophobicity of phenyl groups and the hydrophilicity of KOAc may cause repulsive interactions. In ternary films (P-S/E, P-S/G), KOAc permeability increases with higher SPMAK content. Under co-permeation with MeOH, KOAc permeability increases in P-S films, likely due to charge screening by MeOH reducing electrostatic interactions. For P-E and P-G films, KOAc permeability during co-permeation is similar and higher, respectively, compared to single permeation, potentially due to changes in polymer segmental dynamics induced by MeOH.

In Chapter 6, sulfonate-containing films (PA/S and PA/SM) had higher water volume fractions than quaternary ammonium-containing films (PA/A and PA/MA) due to the higher hydration number of sulfonate compared to ammonium. Methacrylate-containing films (PA/MA and PA/SM) exhibited greater water volume fractions than methacrylate-free films (PA/A and PA/S), likely because the quaternary carbons in the polymer backbone reduce osmotic deswelling

through steric hindrance. Membranes with higher water volume fractions generally had higher solute permeabilities. KOFm permeability was unaffected by the presence or absence of MeOH. However, MeOH permeability during co-permeation with KOFm differed from its single-solute permeability, suggesting that co-permeating KOFm impacts MeOH transport. This behavior may stem from a relationship between water volume fraction and flux coupling (MeOH−KOFm). Lower water volume fractions (narrower chain spacing) likely increase solute-solute interactions, enhancing flux coupling and MeOH diffusion with KOFm. Conversely, higher water volume fractions (wider chain spacing) reduce these interactions, leading to weaker flux coupling and less MeOH diffusion.

In Chapter 7, increasing SBMA content leads to a more compact structure due to its linear shape, while the bulkier phenyl ring in PA increases fractional free volume. Higher SBMA content likely enhances ionic interactions between ammonium and sulfonate groups, acting as dynamic crosslinks that reduce water uptake and water volume fraction. These structural differences influence water volume fraction and membrane properties. Membrane ionic conductivity increases with SBMA content due to higher ion content. The Young's modulus increases with increasing PA or MBAA content, attributed to PA's hydrophobicity, the rigid benzene ring, and increasing crosslink density, which enhance the film's inner structure and strength but reduce strain at break. Ion permeability increases with higher water volume fractions, as salt permeability aligns with water sorption behavior. According to Yasuda's model, higher water content in zwitterionic polymer membranes corresponds to increased salt permeability.

In Chapter 8, water volume fractions in the films generally increase with higher APTA content due to lower crosslink densities and the presence of charged quaternary ammonium (QA^+)

groups. PEGDA-crosslinked films exhibit higher water volume fractions than MBAA-crosslinked films, attributed to PEGDA's hydrophilic backbone and longer crosslinker chain. Dimensional swelling increases with decreasing crosslinker content, reflecting a more open network structure. MBAA-crosslinked films swell less due to their shorter chain length and superior mechanical properties. Interestingly, PEGDA-crosslinked films show higher water contact angles (indicating more hydrophobicity) than MBAA-crosslinked films, contrary to expectations based on their chemical structures and water solubilities. PEGDA lowers PEGDA-crosslinked films' T_g as its content increases, whereas MBAA-crosslinked films' T_g and stiffness decrease with less MBAA. MBAA-crosslinked films are glassy at room temperature, contributing to their higher Young's modulus and lower strain at break compared to PEGDA films. Salt permeability increases with higher APTA content (lower crosslinker content), correlated with fractional free volume. However, A0/P20's permeability is 82 times higher than A0/M20, despite similar water volume fractions, indicating water volume fraction alone doesn't dictate solute permeability. This study reveals that while water volume fraction influences permeability, polymer structure also plays a crucial role. Additionally, solute permeability trends align with the order of their hydrated diameters.

In Chapter 9, membranes containing MPS exhibited a higher water volume fraction compared to those with SPMAK, likely due to differences in polymer structure. SPMAK membranes may face greater steric hindrance and structural obstacles, reducing their water content. Increased PA content correlated with reduced WVF, likely due to the higher hydrophobicity of PA compared to PEGDA. Additionally, membranes with higher charge monomer content attracted more water, attributed to the interactions between charge groups and polar water molecules. The ion exchange capacity of the films increased with lower PEGDA content and higher SPMAK or

MPS content, reflecting greater WVF and charge monomer content. Membranes containing SPMAK displayed higher T_g than those with MPS, while higher PEGDA content lowered T_g. Increased crosslinker content reduced Young's modulus but improved elongation at break, possibly due to the longer chain length of PEGDA compared to PA. SPMAK-containing membranes showed a higher Young's modulus than MPS membranes. Among the tested membranes, PA80P20 exhibited the highest strain. SPMAK and MPS membranes at the same crosslinker content show similar elongation at break, which improved (larger elongation at break) with PEGDA content. Salt permeability did not align with the order of hydrated ion diameter size. Notably, NaOFm and NaOAc often showed higher permeability than KOFm and KOAc.

In Chapter 10, seven membranes with similar water volume fractions were synthesized. Membranes containing APTA demonstrated higher ionic conductivity than those with AETAC at the same charged monomer content. This difference is likely due to APTA's slightly higher IEC and the stronger ion-dipole interactions of its amide group compared to the ester group in AETAC. These interactions may create more efficient ion pathways, enhancing ionic mobility and transport efficiency. Interestingly, Young's modulus decreased with increasing crosslinker content for both AEMs, contrary to typical trends. This behavior might result from a decrease in phenyl acrylate content, whose rigid benzene rings stiffen the polymer structure, combined with an increase in flexible charged monomers like APTA and AETAC, which reduce membrane rigidity. Neutral membranes showed significantly lower permeability than AEMs. Despite variations in fixed charge density, both AEMs displayed similar single-solute permeability, deviating from theoretical expectations. At constant water volume fractions, higher fixed charge density should enhance the Donnan potential and reduce solute permeability. This discrepancy suggests additional factors,

such as solute-membrane interactions or microstructural changes, influence permeability. Moreover, the relative permeability order between solutes remained consistent across single- and mixed-solute systems.

In Chapter 11, hydrogel-based CEMs, PA/A and PMA/A, and AEMs, PA/M and PMA/M, were prepared. PA/M-30 the film's toughness significantly decreased after ion exchange to the OH^- form (PA/M-30-OH). The Young's modulus increased with higher MBAA content due to increased crosslink density, which reduced film ductility. PMA-containing films showed higher Young's moduli than PA-containing films, likely due to the added rigidity from PMA's methyl groups. Notably, PA/M-30-OH had a lower modulus compared to PA/M-30 in the Cl^- form. Water volume fraction generally decreased with increasing MBAA content. CEMs exhibit slightly higher water content than AEMs. This difference is attributed to the higher hydration number of sulfonate anions compared to quaternary ammonium cations. No significant difference in water volume fraction was observed between PA- and PMA-based films. CEMs displayed higher ionic conductivities than AEMs, mainly due to the higher molar conductivity of H^+ compared to Cl^-. Counterion conversion to OH^- form significantly increased the ionic conductivities of FAA and PA/M-30, attributed to the high molar conductivity of OH^- and an increased water volume fraction. The urea permeability of FAA-OH and PA/M-30-OH doubled at 55 °C compared to 25 °C due to increased diffusivity with temperature. PA/M-30-OH showed slightly decreased permeability with increasing concentration, while FAA-OH exhibited increased permeability with higher urea concentrations.

12.2. Recommendations for Future Work

12.2.1. Multi-Solute Transport in IEMs

Solute transport is one of the most critical properties of membranes, as it directly impacts their performance in separation and purification processes. Sodium chloride is widely used for transport testing due to its prevalence as the most common salt in everyday life. However, different applications demand specific solute transport characteristics. Numerous research studies have investigated the transport of various solutes in polymer membranes, each offering valuable insights into membrane performance and behavior [1-7].

Single-solute transport experiments are widely conducted because they are easier to measure and simplify the analysis by excluding interactions between multiple solutes. While this approach is beneficial for isolating specific transport mechanisms, it often falls short of reflecting real-world conditions, where solutions typically contain multiple solutes. Multi-solute transport experiments, although more complex, are essential for accurately understanding membrane performance in practical applications. These experiments introduce challenges such as overlapping solute interactions, differences in solute properties, and potential variations in transport behavior, making analysis significantly more difficult. To bridge this gap, more multi-solute transport studies are necessary to elucidate the transport behaviors of solutes in membranes. The following approaches are proposed to advance our understanding of this topic:

1. **Transport of Different Solute Combinations**

- Investigate the simultaneous transport of two alcohols (e.g., methanol and ethanol) or two carboxylate ions (e.g., KOAc and NaOAc, or KOFm and KOAc) to study the competitive transport and cation and anion effect on transport.
- Study transport behavior with different electrolyte combinations to explore interactions between solutes of varying ionic strengths, charges, and under different pH conditions.

Here, further investigation of whether a particular solute dominates the observed permeability behavior and the underlying reason(s) it does so is needed. Further investigation to identify the prominent interactions or solute competition that should be either avoided or encouraged depending on the application. There remains much to learn in this space and improving understanding of these interactions and driving forces is needed to enhance the overall efficiency of the device and assist in design of new materials and device architectures for the target product.

Effect of Solute Concentrations

- Vary the concentrations of each solute in multi-solute systems (e.g., 1 M with 1 M, 0.5 M with 0.5 M, or 1 M with 2 M) to study how concentrations influence transport behavior.
- Compare the effects of total solute concentration in multi-solute systems to those in single-solute transport. For example, evaluate the transport characteristics of a binary solute system (0.5 M methanol and 0.5 M ethanol) against a single-solute system (1 M methanol), focusing on differences in permeability, diffusivity, and solute interaction effects.

This investigation is more relevant to real-world applications, as solute concentrations in a solution are not usually equal. While certain products or solutes may be unavoidable in the solution, we may be able to control their concentrations to either inhibit or enhance specific solutes, ultimately improving the permeability of our target product. Therefore, it is essential to study the impact of different solute concentrations on transport behavior and how the myriad of interactions are influenced.

12.2.2. Isolating Water Volume Fraction Effect

Water content is one of the most fundamental and influential factors affecting ion transport within membranes, as it directly determines the free volume available for ion mobility. This critical parameter can be finely tuned by adjusting the solvent content in the pre-polymerization solution, providing precise control over the hydration levels of the resulting membrane. Isolating the influence of water volume fraction is essential for accurately analyzing solute transport behavior, as variations in water content can obscure or confound the effects of other important factors, such as polymer structure, electrostatic effect, flexibility of polymer chain, and charge density. These overlapping influences make it difficult to discern their individual contributions to permeability and transport performance. While controlling solvent content is a key strategy for predicting and regulating water content in membranes, using too little solvent can lead to immiscible solutions. This challenge can be addressed by modifying other components, such as charge monomers and crosslinkers. For example, increasing the amount of charge monomer typically increases water content, while increasing crosslinker concentration reduces it. By systematically isolating the effects of water content, its influence can be separated from other variables, allowing for a deeper

understanding of different factors affecting ion transport. This approach facilitates the design of membranes with optimized transport properties, tailored to meet the demands of specific applications, and advances the development of high-performance IEMs.

12.2.3. Next Generation of IEMs

The majority of applications utilizing IEMs require membranes with high selectivity for ion transport, excellent ionic conductivity, and robust durability and stability. Achieving these goals necessitates the discovery of new preparation methods or innovative membrane compositions. Below are several suggestions to guide future development efforts:

1. **Optimize Solvent Usage and Control Water Content**

   Minimizing solvent usage and identifying a solvent capable of dissolving all components at low solvent content is critical for controlling the water volume fraction within the membrane. A miscibility ternary plot incorporating monomer, crosslinker, and charge monomer compositions, combined with different solvents, could be a valuable tool for understanding miscibility and ensuring homogenous membrane formation. For example, dimethylformamide (DMF), tetrahydrofuran (THF), N-methyl-2-pyrrolidone (NMP), and acetone are highly polar solvents with significant potential. This approach allows for better water content control and reduces immiscibility issues.

2. **Maximize Ionic Functional Group Content**

   Increasing the content of ionic functional groups within the membrane can significantly enhance ionic conductivity. Careful tuning of charge monomer concentration is necessary to balance conductivity improvements with mechanical stability and water content. For

example, choosing a crosslinker with multiple reactive sites, such as trimethylolpropane triacrylate (TMPTA), trimethylolpropane trimethacrylate (TMPTMA), pentaerythritol tetraacrylate (PETA), or pentaerythritol tetramethacrylate (PETMA), can reduce crosslinker usage, increase charge monomer content, and facilitate network formation.

3. **Explore Novel Charge Monomers**

   Investigating new charge monomers and leveraging their structural variations can minimize the adverse effects of increased water content associated with higher charge densities. For example, vinylbenzyl trimethylammonium and styrene sulfonic acid are ideal charge functional group for AEMs and CEMs. Both are short-chain charged monomers with a styrene backbone, which enhances mechanical properties and helps reduce water content. This exploration could lead to membranes that maintain high ionic conductivity while offering improved selectivity and controlled water content.

4. **Incorporate Mechanically Robust Monomers**

   Selecting monomers that enhance mechanical properties is essential for real-world applications. Membranes that are too brittle may fail under operational stresses, limiting their usability. Conducting comprehensive mechanical testing, such as tensile strength and Young's modulus evaluations, will ensure that membranes meet the durability requirements for practical applications.

12.3. References

[1] L. Ni, J. Meng, G.M. Geise, Y. Zhang, J. Zhou, Water and salt transport properties of zwitterionic polymers film, Journal of membrane science 491 (2015) 73-81.

[2] Y. He, J. Liu, G. Han, T.-S. Chung, Novel thin-film composite nanofiltration membranes consisting of a zwitterionic co-polymer for selenium and arsenic removal, Journal of Membrane Science 555 (2018) 299-306.

[3] H. Luo, J. Aboki, Y. Ji, R. Guo, G.M. Geise, Water and salt transport properties of triptycene-containing sulfonated polysulfone materials for desalination membrane applications, ACS applied materials & interfaces 10(4) (2018) 4102-4112.

[4] T. Tran, C. Lin, S. Chaurasia, H. Lin, Elucidating the relationship between states of water and ion transport properties in hydrated polymers, Journal of Membrane Science 574 (2019) 299-308.

[5] R. Kingsbury, K. Bruning, S. Zhu, S. Flotron, C. Miller, O. Coronell, Influence of water uptake, charge, manning parameter, and contact angle on water and salt transport in commercial ion exchange membranes, Industrial & Engineering Chemistry Research 58(40) (2019) 18663-18674.

[6] E.-S. Jang, J. Kamcev, K. Kobayashi, N. Yan, R. Sujanani, T.J. Dilenschneider, H.B. Park, D.R. Paul, B.D. Freeman, Influence of water content on alkali metal chloride transport in cross-linked Poly (ethylene glycol) diacrylate. 2. Ion diffusion, Polymer 192 (2020) 122316.

[7] M.S. Islam, R.J. Vogler, S.M. Abdullah Al Hasnine, S. Hernández, N. Malekzadeh, T.P. Hoelen, E.S. Hatakeyama, D. Bhattacharyya, Mercury removal from wastewater using cysteamine functionalized membranes, ACS omega 5(35) (2020) 22255-22267.